

**APPLICATION OF PROBABILITY THEORY TO
INTEGRATED GEOLOGICAL MAPPING FROM
REMOTELY SENSED DATA OF THE
PRECAMBRIAN SHIELD (MANITOBA, CANADA)**

Govindaraju Suresh Kumar Rao

A Thesis

Submitted to the University of Manitoba
in Partial Fulfillment of the Requirements
for the Degree of

DOCTOR OF PHILOSOPHY

Department of Geological Sciences
The University of Manitoba
Winnipeg, Manitoba

© Govindaraju S.K. Rao, 1994



National Library
of Canada

Acquisitions and
Bibliographic Services Branch

395 Wellington Street
Ottawa, Ontario
K1A 0N4

Bibliothèque nationale
du Canada

Direction des acquisitions et
des services bibliographiques

395, rue Wellington
Ottawa (Ontario)
K1A 0N4

Your file *Votre référence*

Our file *Notre référence*

The author has granted an irrevocable non-exclusive licence allowing the National Library of Canada to reproduce, loan, distribute or sell copies of his/her thesis by any means and in any form or format, making this thesis available to interested persons.

L'auteur a accordé une licence irrévocable et non exclusive permettant à la Bibliothèque nationale du Canada de reproduire, prêter, distribuer ou vendre des copies de sa thèse de quelque manière et sous quelque forme que ce soit pour mettre des exemplaires de cette thèse à la disposition des personnes intéressées.

The author retains ownership of the copyright in his/her thesis. Neither the thesis nor substantial extracts from it may be printed or otherwise reproduced without his/her permission.

L'auteur conserve la propriété du droit d'auteur qui protège sa thèse. Ni la thèse ni des extraits substantiels de celle-ci ne doivent être imprimés ou autrement reproduits sans son autorisation.

ISBN 0-612-13472-5

Canada

**APPLICATION OF PROBABILITY THEORY TO INTEGRATED GEOLOGICAL MAPPING
FROM REMOTELY SENSED DATA OF THE PRECAMBRIAN SHIELD (MANITOBA, CANADA)**

BY

GOVINDARAJU SURESH KUMAR RAO

A Thesis submitted to the Faculty of Graduate Studies of the University of Manitoba in partial fulfillment of the requirements for the degree of

DOCTOR OF PHILOSOPHY

© 1994

Permission has been granted to the LIBRARY OF THE UNIVERSITY OF MANITOBA to lend or sell copies of this thesis, to the NATIONAL LIBRARY OF CANADA to microfilm this thesis and to lend or sell copies of the film, and UNIVERSITY MICROFILMS to publish an abstract of this thesis.

The author reserves other publications rights, and neither the thesis nor extensive extracts from it may be printed or otherwise reproduced without the author's permission.

Dedicated to

My parents,

members of my family,

and particularly to

my wife and our son.

Their faith in my ability to complete
this research, at times, far exceeded my own.

I hereby declare that I am the sole author of this thesis. I authorize the University of Manitoba to lend this thesis to other institutions or individuals for the purpose of scholarly research.

G.S.K. Rao

I further authorize the University of Manitoba to reproduce this thesis by photocopying or by other means, in total or in part, at the request of other institutions or individuals for the purpose of scholarly research.

G.S.K. Rao

Abstract

Investigation of earth resource potential requires the integration of various information obtained from different survey techniques. Such information is commonly represented as two-dimensional digital map layers. The ability to selectively combine, by spatial data integration processes, diverse data types, is increasingly becoming a mainstay of geological exploration programs. Such automated mapping of a terrain usually requires some previous knowledge of the terrain. This knowledge is used to constrain the mapping algorithm or to formulate a set of rules that govern the integration process. However, in cases where a completely unknown terrain is being investigated, the lack of prior knowledge can be a serious obstacle.

The present research addresses the fundamental problem of integrating remotely sensed satellite and geophysical data, in the absence of an initial data base. Three types of integration techniques, based on probability theory, are presented: algebraic probability, spatial index, and Bayesian probability. The target proposition is the mapping of the boundary zone between the Proterozoic Churchill Province and Archean Superior Province.

In an hitherto unmapped study area, the algebraic probability method demonstrates the assignment of probabilities to input data sets, based on the target proposition and visual interpretation. The input data are integrated by an algebraic additive process. The probability assignment and the algebraic additive process are validated by application to another area of known geology. Once validated, the results of the algebraic probability method are treated as an *a priori* indicator for the next two methods.

The spatial index method is developed to quantify the spatial correlation in

the input data sets with the *a priori* information. This correlation is then converted into a probability measure, and the integration process is carried out.

The Bayesian method uses a pairwise integration of input data with *a priori* information being provided by the algebraic probability method. The result of the Bayesian integration is an *a posteriori* probability map. This map reflects the revised estimate of the probability of occurrence of the target proposition.

The analysis was carried out on two test sites located in central Manitoba. The Wabowden test site has sparse and widely separated rock exposures. This site was treated as analogous to an unknown area. The Lake Wekusko test site, with a much greater density of outcrops and therefore of better control, was used to validate the method developed.

The results show that the probability method is a useful technique for data integration. Based on the results of this study, a revised geological map was compiled, which shows that the NE trend of the Churchill-Superior boundary zone changes to an approximate N-S trend in the southern part of the study area, where Paleozoic rocks mask the Precambrian Shield. The results also show that the boundary zone as located by the present analysis, is about 11 km east of the the currently estimated eastern edge of the boundary zone as defined by surface geology. One possible explanation of this discrepancy is to invoke a shallow SE dip for the boundar zone, as opposed to the NW dip advocated by most workers. Independent investigations using latest seismic reflection data also support a SE dip for the Thompson Belt.

Acknowledgements

I would like to acknowledge a profound debt of gratitude to:

Prof. W.M. Moon, my thesis supervisor, for initiating this research project and for his constant guidance and encouragement.

Prof. L.D. Ayres; his painstaking, critical review of my thesis, constructive comments and suggestions were instrumental in making the thesis a cohesive document.

Dr. Vijay Singh, who introduced me to the Vax computer and ARIES image processing system, patiently reviewed earlier drafts of the thesis, and provided phenomenal amounts of support and encouragement.

Profs. W.C. Brisbin, N.M. Halden, L.P. Stene and G.S. Clark; members of my thesis advisory committee, who showed unflagging and constant interest in my progress, and were readily available for extended discussions at crucial stages in my research.

The Ministry of Education, Government of India and The Canadian Commonwealth Scholarship and Fellowship Administration for the Commonwealth Scholarship award, which made my stay in Canada possible.

Prof. K. Gopal Rao, I.I.T. Bombay, who initiated me into the field of remote sensing and taught me the intricacies of digital image processing.

Jeff Young, Eva Zaleski, Sebastian Lau; for offering the kind of support that only a fellow graduate student can and knows how.

Mulu Serzu, John Morrish, Joong Sun Won, Ji Soo Kim, Li Bo, Henry Odwar and Kiwon Lee; colleagues from the Geophysics Group, for the many discussions and tips on eliminating obscure software bugs.

Hartley Pokrant, Roy Dixon, Dave Busch, Gerry Lux; from the Manitoba Remote Sensing Centre, for help with data purchase, data transfer, and for providing a cordial working atmosphere, complete with an unceasing radio and a generous dose of camaraderie.

F.P. Agterberg, G.F. Bonham-Carter, D.F. Wright, R.K.T. Reddy and C. F. Chung; from the Geological Survey of Canada, who took the time to unravel the technical knots in my work.

Jim Bamburak from the Manitoba Energy and Mines for his patient, uncomplaining, relentless searches that invariably located the long-forgotten report I needed.

Prof. A.C. Turnock, R.W. Ferguson and J.T. Teller; my resident counsellors, for their compassion and moral support.

Administrative and Support Staff of the Dept. of Geological Sciences for attending to myriad details during my program.

Neharika, Laxman, Imogene, Yogesh, Prasad, Raji, Alok and Sandhya; a special group of friends on whom I relied extensively during dark depressing times.

My wife Veena and our son Aditya; who endured, for virtually an eternity, in stoic silence, and gave of their support even when there was no more left to give; their sacrifice graces every page of this document.

CONTENTS

CHAPTER	PAGE NO.
Abstract	iv
Acknowledgements	vi
1. INTRODUCTION	1
1.1 General	1
1.2 Location of Study Area	4
1.2.1 Selection of Test Sites	4
1.3 Data Sets	7
1.4 Scope of Investigation	8
1.4.1 Methodology	8
1.4.2 Algebraic Probability Method	10
1.4.3 Spatial Index Method	10
1.4.4 The Bayesian Approach	11
1.5 Structure of the Thesis	12
2. GEOLOGY OF THE STUDY AREA	13
2.1 Introduction	13
2.2 Gravity Anomalies	16
2.3 Aeromagnetic Anomalies	19
2.4 The Superior Province	19
2.5 The Pikwitonei Subprovince	24
2.6 The Churchill Province	24
2.7 Churchill-Superior Boundary Zone	27
2.8 Structure and Tectonics	31

2.9 Geology of the Test Sites	36
3. PREPROCESSING OF DATA SETS	44
3.1 Gravity Anomaly Data	46
3.2 Aeromagnetic Anomaly Data	47
3.3 Radar Data	53
3.4 Satellite Data (MSS, TM and SPOT)	57
4. METHODOLOGY: RATIONALE	82
5. DIGITAL IMAGE ANALYSIS OF LAKE WEKUSKO SITE	88
5.1 Introduction	88
5.2 Training Area Signature Generation	91
5.3 Principal Component Transform	94
5.4 Maximum Likelihood Classification	97
5.5 Interpretation of Images	112
6. ALGEBRAIC PROBABILITY METHOD	114
6.1 Algebraic Probability Method	114
6.2 Application of the Method	117
6.2.1 Interpretation of Results	120
6.3 Validation of the Method	135
6.3.1 Integration of Aeromagnetic and Filtered Satellite Data ..	137
6.3.2 Integration of Aeromagnetic and Clustered Satellite Data	139
6.3.3 Interpretation of Results	160
7. SPATIAL INDEXING METHOD	166
7.1 Development and Application	166
7.2 Interpretation of Results	170

8. BAYESIAN PROBABILITY METHOD	173
8.1 Introduction	173
8.2 Application of Bayesian Probability Theory	176
8.2.1 Bayesian Integration	177
8.3 Interpretation of Results	182
9. CONCLUSIONS	183
BIBLIOGRAPHY	193

LIST OF FIGURES

FIGURE NO.	PAGE NO.
1.1 Location of test sites	5
2.1 Precambrian tectonic elements of Laurentia	14
2.2 Lithotectonic domains of the Canadian Shield of Manitoba and Saskatchewan	15
2.3 Bouguer gravity anomaly patterns	18
2.4 Subdivision of aeromagnetic anomaly patterns	20
2.5 Generalised geology map of the study area	23
2.6 Proposals for the Churchill-Superior boundary zone	28
2.7 Double indentation tectonic model	35
2.8 Proposed tectonic model	37
2.9 Generalised geology map of Wabowden test site	40
2.10 Generalised geology map of Lake Wekusko test site	42
3.1 Rasterised gravity anomaly map for Wabowden test site	48
3.2 Rasterised gravity anomaly map for Lake Wekusko test site	49
3.3 Total field aeromagnetic anomaly map for Wabowden test site	54
3.4 Stretched aeromagnetic anomaly map for Wabowden test site	55
3.5 Total field aeromagnetic anomaly map for Lake Wekusko test site	56
3.6 Geometry of side-looking airborne radar (SLAR)	59
3.7 The synthetic-aperture radar (SAR) system	59
3.8 Stereo and off-nadir viewing capability of SPOT satellite	63
3.9 MSS Band 4 image for Wabowden test site	72

3.10	MSS Band 5 image for Wabowden test site	73
3.11	MSS Band 6 image for Wabowden test site	74
3.12	MSS Band 7 image for Wabowden test site	75
3.13	TM Band 3 image for Lake Wekusko test site	76
3.14	TM Band 5 image for Lake Wekusko test site	77
3.15	TM Band 7 image for Lake Wekusko test site	78
3.16	TM Band 3 image for Lake Wekusko test site (After filtering)	79
3.17	TM Band 5 image for Lake Wekusko test site (After filtering)	80
3.18	TM Band 7 image for Lake Wekusko test site (After filtering)	81
4.1	General scheme for data integration	87
5.1	False colour composite from TM data of Lake Wekusko test site	90
5.2(a)	C-SAR data overlain on TM Band 7 and Band 5	92
5.2(b)	Preliminary interpretation of 5.2(a)	92
5.3	Schematic diagram of PCT axes for two band data	96
5.4(a)	False colour composite of Lake Wekusko site from PCT images of TM data	99
5.4(b)	Interpretation of 5.4(a)	99
5.5	Result of maximum likelihood classification of SPOT data for Lake Wekusko test site	110
5.6	Geology of the area corresponding to Figure 5.5	111
6.1	Result of algebraic probability integration (Expt. 1)	124
6.2	Result of algebraic probability integration (Expt. 2)	125
6.3	Result of algebraic probability integration (Expt. 3)	126

6.4	Result of algebraic probability integration (Expt. 4)	127
6.5	Result of algebraic probability integration (Expt. 5)	128
6.6	Result of algebraic probability integration (Expt. 6)	129
6.7	Result of algebraic probability integration (Expt. 7)	130
6.8	Result of algebraic probability integration (Expt. 8)	131
6.9	Profiles along line A-A	132
6.10	Profiles along line B-B	133
6.11	Profiles along line C-C	134
6.12	Integration of aeromagnetic with filtered TM Band 5 (Expt. 1)	141
6.13	Integration of aeromagnetic with filtered TM Band 5 (Expt. 2)	142
6.14	Integration of aeromagnetic with filtered TM Band 5 (Expt. 3)	143
6.15	Integration of aeromagnetic with filtered TM Band 5 (Expt. 4)	144
6.16	Integration of aeromagnetic with filtered TM Band 7 (Expt. 1)	145
6.17	Integration of aeromagnetic with filtered TM Band 7 (Expt. 2)	146
6.18	Integration of aeromagnetic with filtered TM Band 7 (Expt. 3)	147
6.19	Integration of aeromagnetic with filtered TM Band 7 (Expt. 4)	148
6.20	TM band 5 image (After clustering)	149
6.21	TM Band 7 image (After clustering)	150
6.22	Integration of aeromagnetic with clustered TM Band 5 (Expt. 1)	...	152
6.23	Integration of aeromagnetic with clustered TM Band 5 (Expt. 2)	...	153
6.24	Integration of aeromagnetic with clustered TM Band 5 (Expt. 3)	...	154
6.25	Integration of aeromagnetic with clustered TM Band 5 (Expt. 4)	...	155
6.26	Integration of aeromagnetic with clustered TM Band 7 (Expt. 1)	...	156
6.27	Integration of aeromagnetic with clustered TM Band 7 (Expt. 2)	...	157
6.28	Integration of aeromagnetic with clustered TM Band 7 (Expt. 3)	...	158

6.29	Integration of aeromagnetic with clustered TM Band 7 (Expt. 4)	... 159
6.30	Reproduction of Figure 2.10 facing 161
6.31	Interpretation of integration results 161
6.32	Interpretation of integration results 162
7.1	Flowchart for the spatial index method 167
7.2	Result of integration using spatial index method 171
8.1	Flowchart for the Bayesian integration procedure 179
8.2	A posteriori probability map from the integration of aeromagnetic and satellite (MSS Band 7) data 181
9.1	Proposed locations of the boundary and their significance 188
9.2	geological section interpreted from LITHOPROBE data 190
9.3	Revised geology map of Wabowden test site 191

LIST OF TABLES

TABLE NO.	PAGE NO.
2.1 Interpretation of Aeromagnetic Anomalies	21
2.2 Timing of tectonic and metamorphic events in the Churchill and Superior Provinces	32
2.3 Lithological units in Wabowden test site	41
2.4 Lithological units in Lake Wekusko test site	43
3.1 Number of pixels in each grey level	53
3.2 Bands used in radar data acquisition	58
3.3 LANDSAT and SPOT sensor characteristics	61
3.4 Listing of GCPs used in the geometric correction of MSS data (Wabowden test site)	68
3.5 Listing of GCPs used in the geometric correction of TM data (Lake Wekusko test site)	70
5.1 Statistics for PCT of TM data for Lake Wekusko test site	98
5.2 Training area statistics for SPOT data of Lake Wekusko test site	102
5.3 Interclass distance measure of seven classes for SPOT data of Lake Wekusko test site	109
6.1 List of probability values assigned to data sets	121
6.2 Probability values assigned to aeromagnetic and filtered satellite data	140

6.3 Probability values assigned to aeromagnetic and clustered satellite data	151
7.1 Spatial index values for different data sets	170
8.1 Table of parameters in the Bayesian integration procedure	178

CHAPTER 1

Introduction

1.1 General

Remote Sensing—the acquiring of information about an object without coming into actual physical contact with it—takes many forms. In general the term connotes orbital acquisition platforms which record data that can be processed for information about the earth's environment and its natural resources.

Besides the ease with which inaccessible areas can be imaged, spectral, spatial and temporal resolution are the primary advantages of remotely sensed data. That is, an image can be acquired in different portions of the electromagnetic spectrum (spectral resolution); the ground resolution represented by the pixel dimensions can vary with type of sensor (spatial resolution); and the same image can be acquired at different times (temporal resolution). Besides these, synoptic coverage and availability of data in digital form, which permits rapid computer-aided analysis of large areas, are added benefits. Discriminating between surface features is largely depen-

dent on variation in spectral reflectance both between different features and between spectral bands for the same feature (Mather, 1987).

Remotely sensed data have been used in a diverse variety of applications. Perhaps a single common factor in such analyses is that they are, by necessity, interdisciplinary in nature. Thus, for instance, a forestry application involves knowledge of physics (spectral characteristics of the canopy), soil sciences, botany, meteorology (rainfall distribution) and statistics (data processing). Consequently a virtual plethora of literature deals with different aspects of remote sensing applications. Perhaps the closest to a single compendium covering many of these aspects is the Manual of Remote Sensing (Colwell, 1983). One of the earliest benefits of remote sensing has been its proven effectiveness in geological investigations (Goetz and Rowan, 1981; Goetz *et al.*, 1983).

Given the interdisciplinary nature of remote sensing investigations, the analyst is required to use ancillary data sets to complement the results obtained from space-borne or air-borne images. Non-spatial ancillary data has been used, for example, in classification of satellite images to produce thematic maps (Strahler *et al.*, 1976, 1980; Richards *et al.*, 1982).

The relevance of spatial characteristics of image data is becoming increasingly apparent. Results from conventional digital image processing techniques were significantly improved by incorporating spatial attributes at various stages of processing (Bolstad and Lillesand, 1992). However, complications arise from differences in the form in which these data sets are available, differences in scale between data sets, different formats and media of storage, and non-availability of crucial information,

particularly for inaccessible areas.

Nevertheless, to arrive at a cumulative result the analyst has to devise a means of integrating the information from all the different data sets. The simplest technique would be to generate maps on transparent sheets and to overlay them for a visual interpretation. However, this method is generally subjective, prone to errors related to accuracy of registration between maps, and not easily given to quantification. Measurement of attributes such as lengths and areas, commonly done manually, is subject to operator error.

With the advent of computer technology and digital processing methods this technique has been superseded by computer-aided integration. Transformations in scale and in data type are easily accomplished and stringent statistical controls can be implemented to reduce registration and analytical errors. Also, data sets can be individually enhanced prior to integration to improve the information extraction process (Fabbri and Kushigbor, 1989; Walsh *et al.*, 1990).

In the current study, airborne geophysical and satellite data constitute the input data. The primary thrust of this research is the development of a method of computer-aided integration. The objective is to test the efficacy of combining different types of remotely sensed data sets as an aid in geological mapping. The method of integration is developed for an area of poor bedrock exposure and therefore of poorly known geology. This area can be considered as analogous to an unmapped area. Then the method is validated by testing over another nearby test site of better exposure and well documented geology.

The methodology developed here with some modification may be applicable to

similar analysis in other areas that require integration of data sets.

1.2 Location of the Study Area

The Precambrian Shield of Manitoba can be divided into the Archean Superior Province and the early Proterozoic Churchill Province. The former underlies the north-central and southeastern parts of Manitoba and the latter the northern part. The boundary between these two provinces is probably a tectonic suture; it is partly exposed in the central and northern parts of Manitoba along a zone known as the Thompson Belt, which has a north-northeasterly trend. The southwest part of the Thompson Belt is poorly exposed and is overlain by Paleozoic sedimentary rocks. The area of study is centered approximately over this poorly exposed area and is in effect the junction of the Superior Province, the Churchill Province and Paleozoic strata.

The area of study is one frame of Landsat imagery derived from the Landsat 4 index map (Track and Frame no. 33-22) covering an approximate area of 185 km² (Figure 1.1). The approximate co-ordinates of this area are N 53° 50' - N 55° 30' and W 97° 50' - W 100° 30' (NTS 63 J). Preliminary regional analyses were conducted for this entire area. For the purpose of detailed analysis two smaller test sites each covering an area of 30 minutes of longitude × 30 minutes of latitude were chosen.

1.2.1 Selection of Test Sites

The primary objective of this research is devising a mathematical method of integration of geophysical and remotely sensed data sets. The result should enable refinement of known geology, prediction of lithological contacts masked by overly-

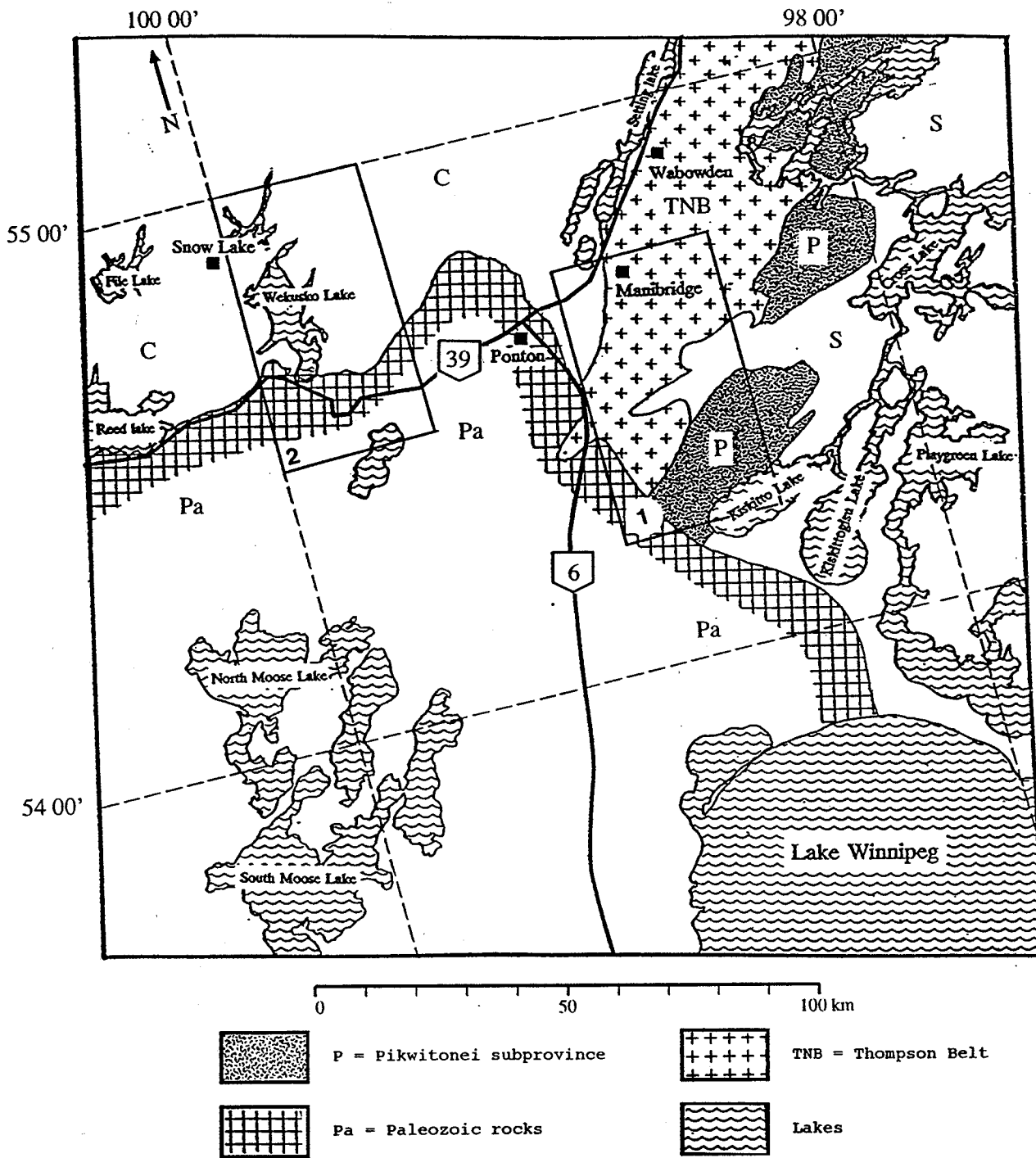


Figure 1.1 Location of Test Sites

Geology shown is simplified after Corkery, 1987

S = Superior Province, C = Churchill Province

(1) Wabowden Test Site; (2) Lake Wekusko Test Site

ing deposits and mapping of tectonic and structural features. Two test sites were selected in which the available knowledge base has widely differing degrees of uncertainty.

The Wabowden test site straddles the boundary between Archean (Superior Province) and Proterozoic (Churchill Province) rocks. At the junction of the two provinces is a major tectonic feature (Thompson Nickel Belt). To the southwest the younger Paleozoic rocks mask the continuation of the older rocks. Northeast of the Paleozoic cover, vast clay, sand, and gravel deposits resulting from Pleistocene glaciation result in a very low frequency of bedrock exposure, thus preventing compilation of a detailed geologic map. Furthermore, the size of the outcrops is very small requiring a considerable amount of extrapolation and inference in the location of geological contacts. All these factors lead to a high degree of uncertainty. This site is a good candidate for the development and testing of the integration procedure.

The Lake Wekusko test site to the west is composed of Proterozoic rocks (Churchill Province) and younger Paleozoic rocks to the south. Here the Proterozoic rocks are well exposed and the degree of uncertainty associated with their spatial location is relatively low. Well defined structures exist in the northern portion of the site.

For both sites, aeromagnetic, gravity and satellite data coverage were acquired.

1.3 Data Sets

The following data sets were used in this study:

1. Topographic maps
2. Geological maps
3. Satellite data (Landsat MSS, Landsat TM, SPOT MLA, C-SAR)
4. Aeromagnetic anomaly data
5. Gravity anomaly data

Topographic maps were treated as the base map to achieve registration between information layers. Thus all layers were geometrically corrected and transferred with respect to control points obtained from topographic maps.

Geological maps were obtained from the Geological Survey of Canada, Manitoba Energy and Mines (Geological Services Branch), or from published literature. Due to the paucity of outcrops in the study area and difficulty in field mapping many of the maps contain boundaries of lithological units that are inferred and extrapolated. The problem is also compounded by lack of concensus between different workers on the classification of lithological units.

Landsat Multi Spectral Scanner (MSS) and Landsat Thematic Mapper (TM) digital data, stored on computer compatible tapes, were obtained from the Canada Centre for Remote Sensing (CCRS). The SPOT Multi Linear Array (MLA) data was obtained from Radarsat International Incorporated and the C-Band Synthetic Aperture Radar (C-SAR) data from CCRS.

Digital aeromagnetic anomaly data were obtained from the Geological Survey of Canada and gravity data from published literature.

1.4 Scope of the Investigation

As indicated earlier, this study deals with the integration of geological, geophysical and ancillary data sets for the purpose of mapping lithologic units and structures in a poorly exposed area that straddles a major geotectonic boundary. Methods of integration have, over the years, evolved from simple overlaying and visual interpretation to more sophisticated computer-aided registration of information in digital form. In the present work the emphasis is on the latter type of integration techniques. Such techniques provide for a wide range of processing such as scale transformations and conversion of data from one form to another. Further, they also facilitate storage and retrieval of individual and combined data layers.

The geological maps used in this study do not constitute an input data set in the integration process. Rather, they are used for comparison with the final results to evaluate the efficacy of the method for geological mapping. Further, the assignment of probabilities to the geophysical and satellite data is predicated on the analyst's judgement of the spatial characteristics of geological features in a typical Precambrian terrane. This subjectivity is an inherent part of the integration process and cannot be entirely dispensed with. Nevertheless, such assignment of probabilities is valid, since it is based on well established geological principles.

1.4.1 Methodology

The general approach in computer-aided integration techniques is to devise a statistically valid and rigorous means of integrating different information layers. Since the data layers are almost always geo-referenced, the technique has come to

be known as Geographic Information Systems (GIS) and is primarily intended for manipulating and displaying large volumes of geographically referenced data sets. In its essence GIS represents a system for handling spatial data with particular emphasis on spatial entities and relationships (Marble and Peuquet, 1983). A GIS has four components; a data input system, a data storage and retrieval subsystem, a data manipulation and analysis subsystem, and a data reporting subsystem.

Since satellite images contain a vast amount of data (more than 7 million pixels in each band for MSS data) with inherent spatial characteristics, they are well suited for integration with other geographic based data sets (such as topographic, landuse, forestry, and geophysical maps, for example). Indeed satellite images are rapidly becoming an integral part of GIS (Barker, 1988; Zhou, 1989). Such integration must, however, deal with different modes of representation and must provide for geometric registration between the different data sets. Several case studies demonstrating registration to significant levels of accuracy have been documented (Goodenough, 1988 and references listed therein). The most fundamental consideration is that of the type of projection used. Snyder (1978, 1981, 1987) has pointed out the errors attendant in matching Space Oblique Mercator projection (used for satellite imagery) with Universal Transverse Mercator projection (used for topographic maps). These can however be overcome by using well established mathematical relationships (Newton, 1985).

Published reports demonstrate the effectiveness of GIS in land- and forest-resource management (Burrough, 1986; Goodenough, 1988), gold exploration (Bonham-Carter et al, 1988), exploration for copper deposits (Agterberg, 1989a),

and a variety of other applications (Marble and Peuquet, 1983). The techniques of integration are as varied as the applications; symbolic reasoning (Goodenough, 1988), fuzzy set theory (An *et al.*, 1991), binary coding, and the method of Bayesian statistics (Bonham-Carter *et al.*, 1988; Agterberg *et al.*, 1990).

In the present research the method of integration is based on probability theory. To begin with, in the algebraic probability method, probability assignment is done without benefit of previous knowledge from field-based investigations. The results obtained from this are used to constrain the formulation of the spatial index method and the Bayesian approach. Thus the evolution of the method is a logical progression of probability assignment.

1.4.2 Algebraic Probability Method

In geological investigation it is not uncommon to encounter areas where, mostly due to inaccessibility, no field studies have been done. In such cases, remotely sensed data are generally the only means available to perform a preliminary analysis. The algebraic probability method developed in this study can be used in such cases because it does not call for any pre-existing database on which to construct the integration procedure.

The method makes use of a visual analysis of the remotely sensed data to identify anomalies of significance. These are assigned relative probability values, known as local probability. It is also possible to assign a probability to each data set as a whole, known as global probability, which reflects the analyst's estimate of the efficacy of that data set in mapping the feature of interest. Integration of the

data sets is a matter of algebraic summation. The results from this integration are used as initial information in the subsequent methods.

1.4.3. Spatial Index Method

Commonly it is necessary to establish the correlation between the anomalies or patterns in remotely sensed data and features of interest on the ground. By comparing the spatial distribution of the anomalies with that of the ground feature, such a correlation can be determined. The Spatial Index is one such measure of the correlation.

Using the results obtained in the algebraic probability step, one or more significant anomalies, directly related to a ground feature can be identified. This forms the reference anomaly against which the spatial distribution of the other anomalies are compared. By quantifying the degree of overlap, the Spatial Index can be computed.

1.4.4 The Bayesian Approach

The classical concept of probability was developed in relation to prediction of the occurrence of events in games of chance (Bayes, 1764). Thus it was designed to study random occurrences as opposed to the prediction of deterministic phenomena. Some reservations are likely to be expressed about the use of probability to model occurrences that could not be regarded as being generated by random processes. Regardless of whether a geological process is truly random, subjectivist Bayesian probability holds that probability statements can be made about any potentially verifiable hypothesis, whether or not a chance mechanism can be imagined (Spiegelhalter, 1986).

A single information layer can be said to be comprised of a collection of several smallest units of measure commonly referred to as a cell. To begin with each cell has a certain *a priori* probability of being associated with the feature of interest (a mineralized zone, a fault etc.). After information from an additional second layer is integrated with the first, a new *a posteriori* probability results which is governed by the laws of Bayesian probability.

Thus with the addition of each subsequent layer the probability is revised. After completion of the integration the final *a posteriori* probability value for each cell will reflect the degree of association between the cell and the feature of interest.

1.5 Structure of the Thesis

After the Introduction (Chapter 1), the geology of the study area is described in detail in Chapter 2. Preprocessing of the data sets for the purpose of generating data sets compatible for integration is discussed in Chapter 3. Preprocessing involves geometric correction of satellite images; interpolation and rasterisation of aeromagnetic anomaly maps; and digitisation and rasterisation of geological and gravity anomaly maps. Chapter 4 gives an overall view of the rationale behind the methodology. After conventional digital image processing techniques (Chapter 5), three methods of integration – algebraic probability, spatial index and Bayesian approach – are presented in Chapters 6, 7 and 8. The results obtained, their implications and conclusions are treated in Chapter 9.

The International System of units are used in this thesis (A.S.P.R.S., 1978).

CHAPTER 2

Geology of the Study Area

2.1 Introduction

The Canadian Shield, occupying nearly half of Canada, consists of Precambrian rocks. Initially the shield was divided into a number of structural provinces based on internal structural trends and styles of folding (Stockwell *et al.*, 1970). However, with advances in isotopic geochronology in recent years it has become possible to rigorously subdivide the Canadian Shield in terms of age of igneous and metamorphic events (Figure 2.1).

The study area straddles the boundaries between the Archean Superior Province on the east, the Proterozoic Trans-Hudson Orogen of the former Churchill Province on the northwest, and overlying Paleozoic platformal rocks of the Interior Plains on the southwest (Figure 2.2). The Precambrian terrane is lithologically and structurally diverse.

As in many other parts of the Canadian Shield, geological investigation of the

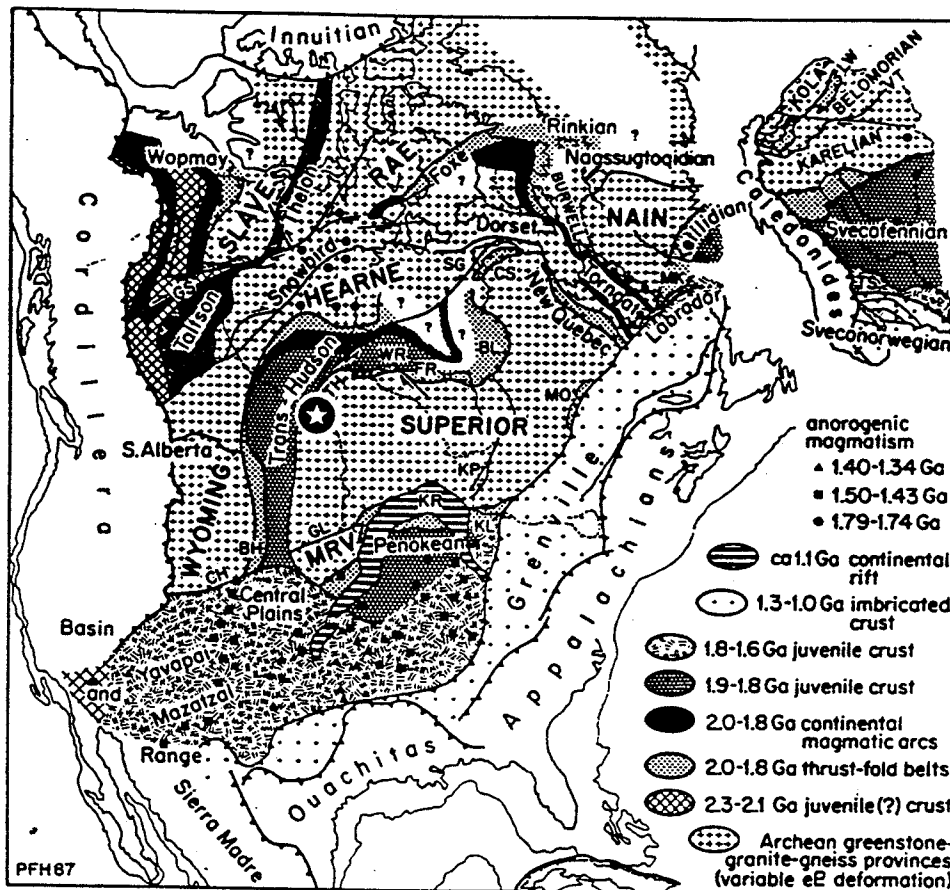


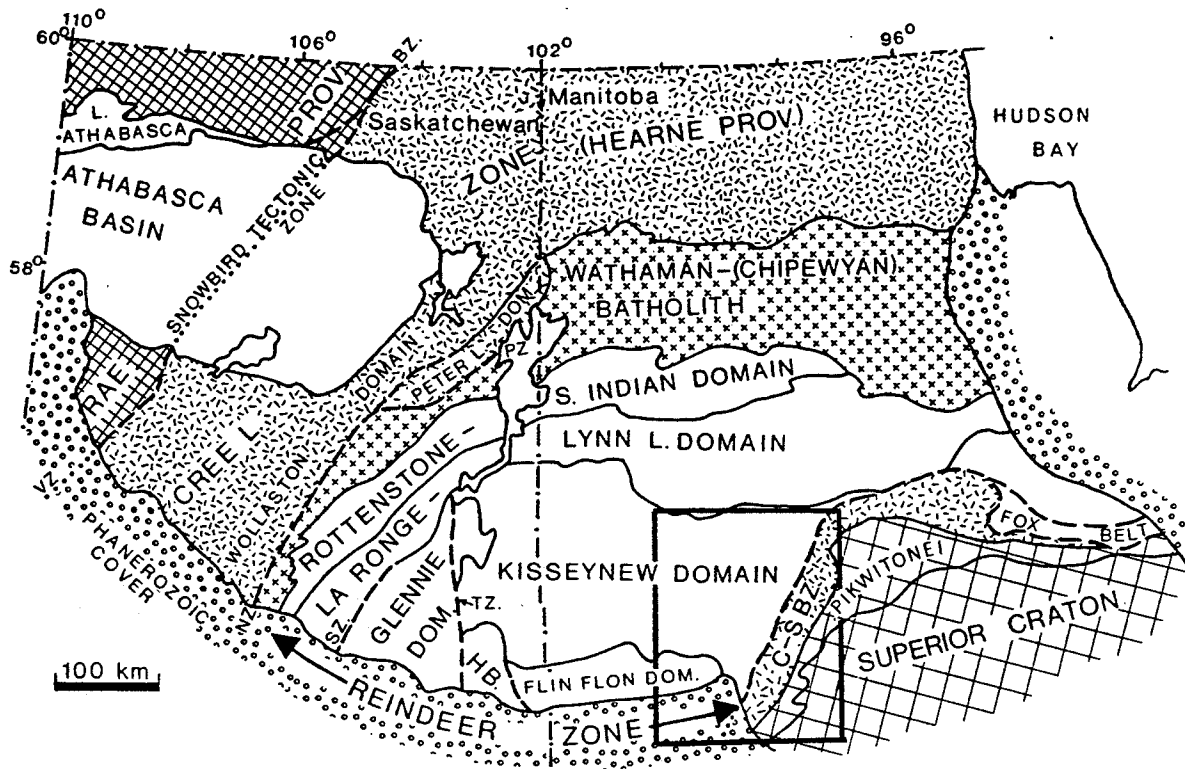
Figure 2.1 Precambrian tectonic elements of Laurentia (After Hoffman, 1988)

Uppercase names are Archean Provinces, lowercase names are Proterozoic and Phanerozoic orogens

BH Black Hills inlier; BL Belcher belt; CH Cheyenne belt; CS Cape Smith belt; FR Fox River belt; GL Great Lakes tectonic zone; GS Great Slave Lake shear zone; KL Killarney magmatic zone; KP Kapuskasing uplift; KR Keweenaw rift zone; LW Lapland-White Sea tectonic zone; MK Makkovik orogen; MO Mistassini-Otish basins; MRV Minnesota River Valley terrane; SG Sugluk terrane, TH Thompson belt; TS Transscandinavian magmatic zone; VT Vetrenny tectonic zone; WR Winisk River fault

The Churchill Province is here divided into the Archean Rae and Hearne Provinces and various 2.0-1.8 Ga orogenic belts of which the Trans-Hudson orogen is relevant to this study.

Star denotes location of study area.



Previously published lithotectonic domains of the Reindeer Zone, and other elements of the Trans-Hudson Orogen in Saskatchewan and Manitoba. Ornamented Precambrian components are mainly "ensialic" elements of the orogen and bounding cratons. Unornamented domains are mostly juvenile Early Proterozoic crustal elements. Heavy dashed lines indicate major ductile shear zones or brittle-ductile faults. Abbreviations: C-S BZ, Churchill-Superior Boundary Zone; HB, Hanson Lake Block; TZ, Tabbernor fold/fault zone; SZ, Stanley fault/shear zone; NZ and PZ, Needle Falls and Parker Lake shear zones; and VZ and BZ, Virgin River and Black Lake shear zones (parts of Snowbird tectonic zone).

Figure 2.2 Lithotectonic domains of the Canadian Shield of Manitoba and Saskatchewan (After Lewry et al., 1990)

Box shows approximate study area

Precambrian terrane in Manitoba is adversely affected by the Paleozoic cover and by locally thick and extensive Quaternary deposits. In such terrains, regional ground and airborne geophysical techniques (Gibb, 1968; Kiss, 1989) and various types of satellite imagery have proven to be useful aids in refining the lithology and structure (Kowalik and Glenn, 1987; Masouka *et al.*, 1988).

Beginning in the early 1960s, gravity measurements were being made in the Canadian Shield of Manitoba (Innes, 1960) and by the mid-1980s an aeromagnetic survey of most of the Canadian Shield in Manitoba had been completed (Kiss, 1989). Gravity surveys provide information on the broad crustal distribution of rock types based on changes in average densities and on regional structural features. Aeromagnetic data can be used to differentiate rock types by discriminating between differing magnetic properties. Commonly it is possible, by using aeromagnetic data, to locate the extension of rock types under overburden, under lakes and under non-magnetic sedimentary cover.

In conjunction with detailed geological and geochemical mapping, geophysical data compiled from these surveys have helped refine the structure of the Precambrian rocks in Manitoba.

2.2 Gravity Anomalies

Gravity studies of the Canadian Shield (Wilson and Brisbin, 1961, 1962; Gibb, 1983; Green *et al.*, 1985a) reveal definite linear trends that can be closely related to major geological features, especially boundaries between structural provinces. The Bouguer gravity anomaly map shown in Figure 2.3 (after Gibb, 1968), covers

northern Manitoba and northeastern Saskatchewan. The anomalies range from a high of 14 mgals over the Fox River ultramafic sill (No. 7 on Fig. 2.3) to a low of -84 mgals in the northwestern corner of the map area. In the south-central part Gibb (1968) has identified a northeasterly trending anomalous zone flanked by large regional gravity lows. The study area straddles this anomalous zone.

The boundary between Archean rocks of the Superior Province and early Proterozoic and Archean rocks of the Churchill Province is within the anomalous zone which comprises a central belt of gravity lows flanked by somewhat continuous strips of gravity highs. The southern Nelson River high (No. 1 in Fig. 2.3) is underlain by Archean granulite facies rocks of the Pikwitonei subprovince of the Superior Province. The northern strip of discontinuous gravity highs consists of the Burntwood River high (No. 4 in Fig. 2.3) underlain by early Proterozoic granulite facies rocks and the Owl River high (No. 9 in Fig. 2.3), which reflects an undetermined Precambrian basement lithology covered by Paleozoic sedimentary rocks. The central negative anomalies consist of the Setting Lake low, the Mystery Lake low, the Split Lake low and the Weir Lake low, and they define a more or less continuous northeasterly trending belt about 50 km wide that increases to 80 km wide near Hudson Bay. Gibb (1968) hypothesised that three subjacent bodies of granite, of lower density than the surrounding rocks, underlie the Split Lake low, the Mystery Lake low and the Setting Lake low.

Crustal models derived from gravity profiles suggest that, in general, the younger (Proterozoic) Churchill Province is thicker and denser than the older (Archean) Superior Province (Gibb and Thomas, 1976).

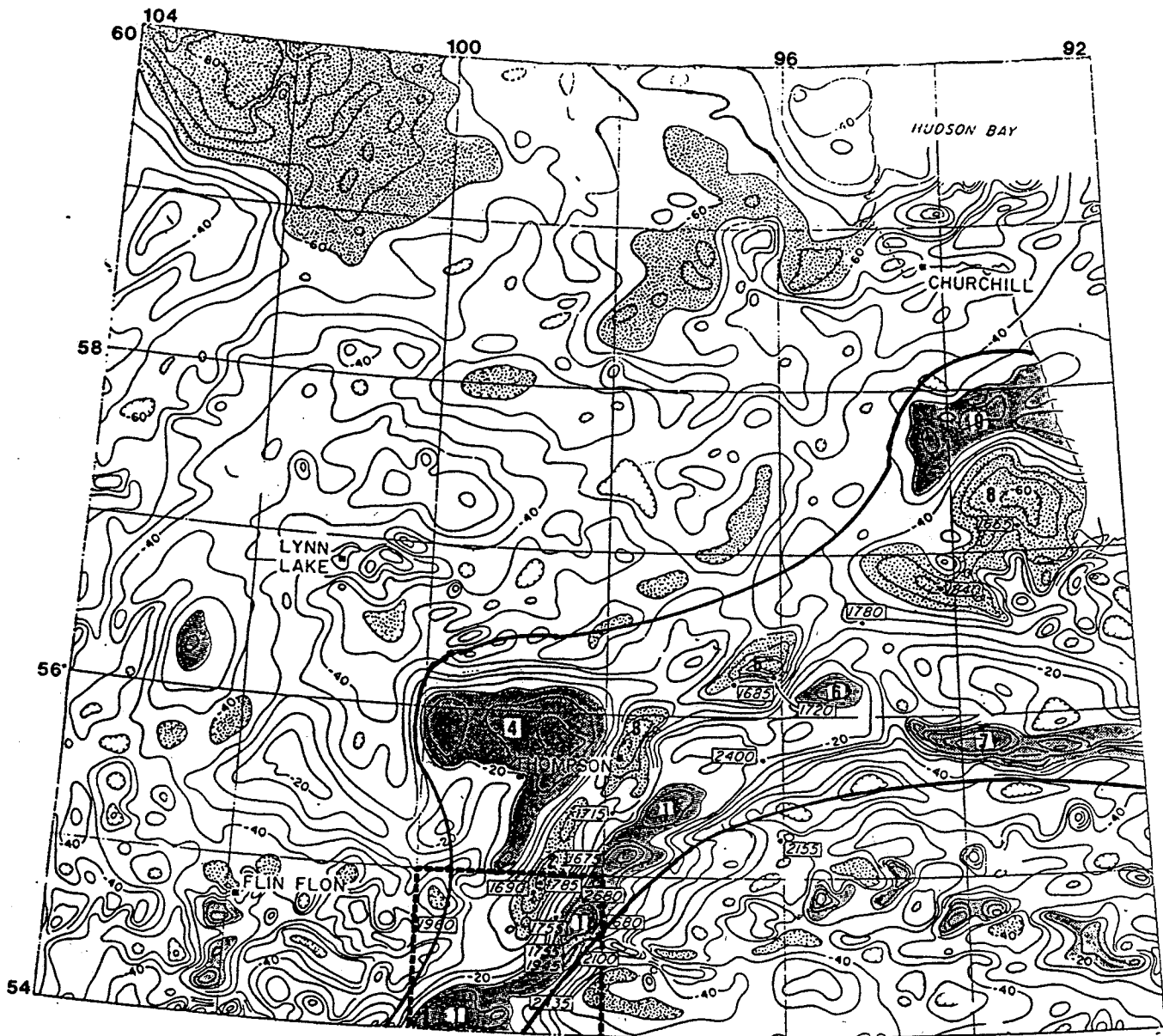


Figure 2.3 Bouguer gravity anomaly patterns (After Gibb, 1968.) Light stipple – gravity low; heavy stipple – gravity high; thick lines outline the anomalous zone
 1. Nelson River high; 2. Setting Lake low; 3. Mystery Lake low;
 4. Burntwood River high; 5. Split Lake low; 6. Kettle River high;
 7. Fox River high; 8. Weir River low; 9. Owl River high
 Box shows approximate study area.

2.3 Aeromagnetic Anomalies

Studies of aeromagnetic anomalies (Kornik and MacLaren, 1966; Kornik, 1971; Green *et al.*, 1979, 1985a) indicate that magnetic linear trends reflect the pattern of geological structures. The dominantly easterly trends in the Superior Province are clearly seen as are the northeast to east trends in the southwest part of the Churchill Province. The magnetic patterns over Paleozoic sedimentary cover also reflect the structural trends of the underlying basement.

When interpreting the aeromagnetic anomaly map of Manitoba, Kornik and MacLaren (1966) and Kornik (1971) recognised several subdivisions each characterised by differing magnetic features such as magnetic trends, patterns and distributions of anomalies. In a general sense these subdivisions can be correlated with geological variations in rock type (Figure 2.4; Table 2.1). However, in detail, there is considerable discrepancy between the geology inferred by Kornik (1971) and the current geological map of Manitoba (Corkery, 1987).

2.4 The Superior Province

The Superior Province is characterised by dominantly easterly trending structures. The rocks of the Superior Province are mostly granitic with interspersed metavolcanic and metasedimentary belts and can be subdivided into many sub-provinces on the basis of distinctive rock assemblages, structural configuration and metamorphic grade (Card, 1990). The subprovinces are separated either by faults or by a steep metamorphic gradient.

Amongst rocks in the Superior Province, the volcanic and sedimentary rocks

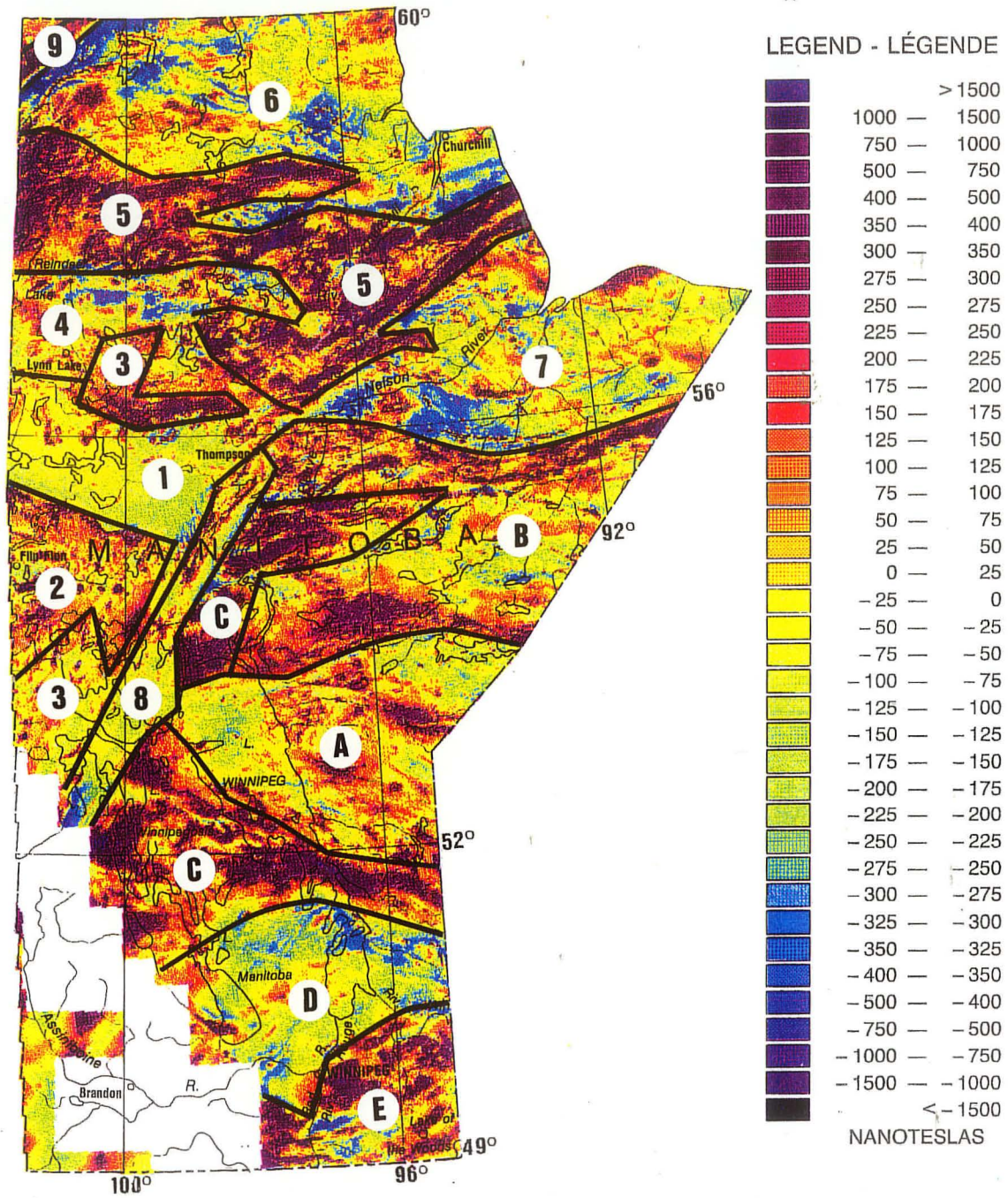


Figure 2.4 Subdivisions of aeromagnetic anomaly patterns (After Kornik, 1971)
 (Letters refer to Superior province and numbers to Churchill province)
 (See Table 2.1 for explanation of symbols)
 (Source of Map: GSC Map 1255 A, 1987; 1:5,000,000)

CODE	CHARACTERISTICS
A	northwesterly magnetic trend; large broad anomalies associated with granitic and gneissic areas
B,D	easterly trend; volcanic and sedimentary belts occur in areas of lower magnetic intensity; local high anomalies within these belts indicate presence of iron formation
C	readily recognised due to its peculiar pattern of small interspersed circular- or semi-circular-shaped local high and low anomalies; underlain by charnockite and pyroxene-granulite rocks
E	underlain by granitic and gneissic material
1	underlain by granitic rocks containing numerous large and small inclusions of sedimentary gneiss
2	complexly folded, regionally metamorphosed, stratiform gneisses; cause local anomalies of moderate intensity
3	volcanic-sedimentary areas; small discontinuous anomalies; do not contain large gneissic belts and also have less magnetic iron formation (in contrast to B, D)
4	mostly granitic rocks; irregular shaped, small to medium sized anomalies of low to moderate relief
5	intense and areally large anomalies; underlain by granitic and gneissic material; some of the gneisses have a mafic character; closely correlates with the North American Central Plains Conductivity Anomaly
6	poorly developed anomalies; volcanic-sedimentary belts and basins; abundant metasedimentary rocks in all grades up to granulite facies
7	mainly Paleozoic rocks; where exposed the Precambrian rocks are gneissic; covered areas have large magnetic anomalies suggesting presence of volcanic-sedimentary belts
8	occurs adjacent to Churchill-Superior boundary zone; complex area subjected to several metamorphic events and faulting
9	granitic rocks causing a broad high anomaly

Table 2.1 Interpretation of aeromagnetic anomalies

(Letter code refers to the Superior Province and number code to the Churchill Province as shown in Figure 2.4)

(Compiled after Kornik, 1971).

of Archean age are oldest and are generally interpreted to represent island arc-like volcanoes and flanking sedimentary aprons (Cross Lake Subprovince, Figure 2.5). These were folded, faulted, metamorphosed and intruded by granitic rocks during the Kenoran orogeny between 2.73 and 2.68 Ma (Card, 1990). They now form easterly trending greenstone belts bordered by large granitic batholiths; metamorphic grade is mostly greenschist and amphibolite facies. The volcanic rocks are generally older than, and are conformably overlain by, the sedimentary rocks. In some belts there are several such cycles of deposition (Stott and Corfu, 1991).

The volcanic rocks comprise mafic to felsic lava flows and volcanoclastic units. Mafic flows predominate in the lower two-thirds of most sequences whereas felsic volcanoclastic rocks form the upper parts. Sills, dykes and irregularly shaped intrusions of gabbro and diorite are present within the volcanic sequence, particularly in the mafic parts.

The sedimentary aprons typically comprise interbedded greywacke and shale. Conglomerates occur within the greywacke sequences but are commonly spatially associated with volcanic rocks. In terms of aeromagnetic data, an important minor sedimentary lithology is iron formation consisting of thin chert layers interbedded with magnetite-rich layers. The sedimentation commonly appears to be contemporaneous with the buildup of the felsic volcanic rocks, erosion of which may have provided the bulk of the detritus (Ojakangas, 1985). Thus the major source of the detrital material for the sedimentary rocks was the volcanic rocks flanking the basins of sedimentation.

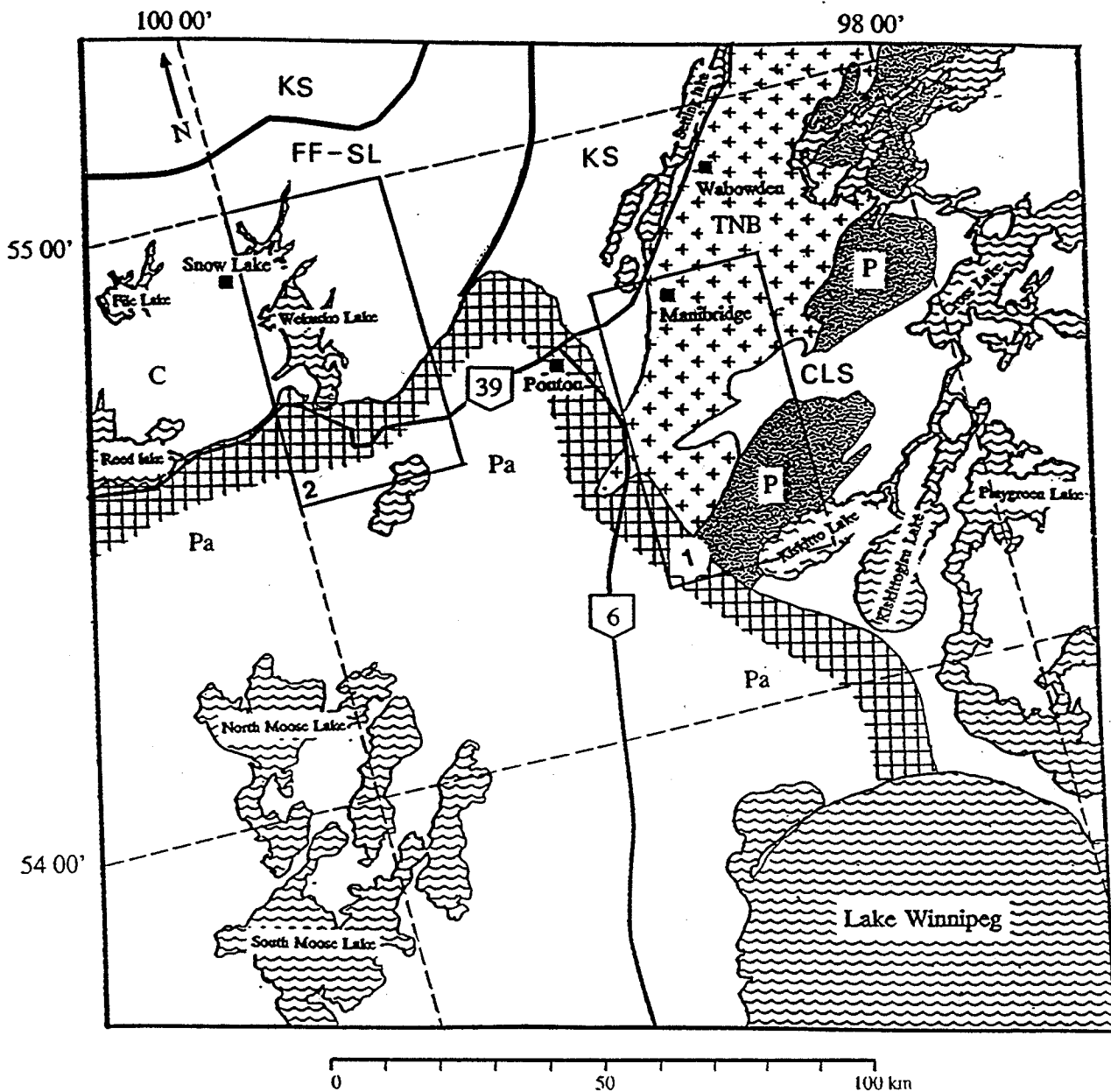


Figure 2.5 Generalised geology map of the study area

Geology shown is simplified after Corkery, 1987

P=Pikwitonei Subprovince, CLS=Cross Lake Subprovince, FF-SL=Flin Flon-Snow Lake Belt, KS=Kisseynew Domain, TNB=Thompson Belt

(1) Wabowden Test Site; (2) Lake Wekusko Test Site

2.5 The Pikwitonei Subprovince

In the northwestern Superior Province the granite-greenstone rocks grade into the Pikwitonei Subprovince (Figure 2.5) which forms the northwest edge of the Superior Province and is characterised by higher grade, granulite facies metamorphism, higher density and higher average magnetic susceptibility. The predominant rocks in the Pikwitonei Subprovince are layered to massive granulite facies gneisses with enderbitic and charnockitic affinities. These are locally interlayered with amphibolite facies gneisses that vary from amphibolite to plagioclase-quartz-biotite gneiss. An orthopyroxene isograd demarcates the boundary between the Pikwitonei Subprovince and the lower grade rocks of the Superior Province on the southeast. This isograd is oblique to the typical easterly trending structures of the Superior Province (Hubregtse, 1980a)

Bell (1978) suggested that the Pikwitonei Subprovince is a basement complex upon which the younger Archean rocks of the Cross Lake Subprovince (Superior Province) were deposited. Hubregtse (1980a), however, showed that the Pikwitonei granulite complex represents a more highly metamorphosed segment of the Superior Province, separated from the greenschist-amphibolite facies greenstone belt-gneiss terrane by an orthopyroxene isograd as opposed to an unconformity (Bell, 1978). Hence he considered the Pikwitonei to be a lower crustal equivalent of the granite-greenstone terrane (Hubregtse, 1980a) and a part of the Superior Province.

2.6 The Churchill Province

Recent work by Hoffman (1988) has led some workers to subdivide rock units

formerly assigned to the Churchill Province into several new provinces: in Manitoba and adjacent parts of Saskatchewan and the Northwest Territories these are the Rae Province, Hearne Province, and the Trans-Hudson Orogen (Figure 2.1). The Rae and Hearne Provinces, which occur well beyond the study area, are dominantly high metamorphic grade Archean rocks that were reworked during several Proterozoic orogenic events. The Trans-Hudson Orogen, which occurs between the Hearne Province on the northwest and the Superior Province on the southeast, is composed largely of early Proterozoic rocks that were apparently deposited in an oceanic setting between two Archean cratons (Figures 2.1 and 2.2; Green *et al.*, 1985b; Lewry *et al.*, 1990). These early Proterozoic rock units underlie the Churchill Province part of the study area (Figure 2.2).

Along the southeastern edge of the Hearne Province, in the Wollaston Domain (Figure 2.2) early Proterozoic sedimentary rocks were deposited on a basement of deeply eroded Archean rocks and granitic gneisses. In general the sedimentary rocks are shallow-water to subaerial shelf sequences composed of fluvial quartzites with minor dolomite, argillite, and stromatolitic dolomite; deeper water facies are represented by siltstone, shale and greywacke (Stockwell *et al.*, 1970).

The shelf sequence is separated from early Proterozoic volcanic and sedimentary terranes to the southeast by a major shear zone and granitoid rocks of the Wathaman-Chipewyan batholith (Figure 2.2). These volcanic and sedimentary rocks are interpreted to be former island arcs and intervening sedimentary basins that developed on Proterozoic oceanic crust (Green *et al.*, 1985b; Lewry *et al.*, 1990). In the study area, three separate lithotectonic elements have been defined: the Flin

Flon Domain, the Kiseynew Domain, and the Thompson belt which is within the Churchill-Superior Boundary zone (Figure 2.2; Lewry *et al.*, 1990; Weber, 1990).

The Flin Flon Domain, which is also known as the Flin Flon – Snow Lake Belt (Figure 2.5), is a typical greenstone-granitoid terrane. The lower part of the volcanic sequence is largely submarine volcanic flows and volcanoclastic rocks ranging in composition from basalt to rhyolite. These are overlain by, and interfinger laterally with, greywacke, siltstone and mudstone turbidites. The sequence has undergone greenschist to amphibolite facies metamorphism and multiphase deformation (Green *et al.*, 1985a).

The Kiseynew Domain on the north mainly comprises greywackes, siltstones and mudstones that have been subjected to high grades of metamorphism to form paragneiss, migmatites and anatectic granitic bodies. These rocks originated as volcanic detritus from nearby volcanic island arcs, transported by turbidity currents (Bailes, 1980).

One of the most important applications of remote sensing is the identification of favourable areas of mineral exploration. In the study area and the immediate vicinity there are a number of known mineral deposits. Polymetallic sulphide deposits occur in the Flin Flon belt. Nickel-copper sulphide ores are associated with mafic to ultramafic intrusions (e.g. Thompson Belt). Gold-bearing quartz veins occur in sheared volcanic and sedimentary rocks in the vicinity of porphyritic granite intrusions. Varying grades of iron ores occur in the iron-formations, and smaller bands of iron-formation, including iron-sulphide concentrations are present in some narrow belts of metamorphosed volcanic and sedimentary rocks. Uranium deposits

occur in early Proterozoic sediments and in some granitic rocks.

2.7 Churchill-Superior Boundary Zone

Identification of the boundary between the Archean Superior Province and the Proterozoic Churchill Province in Manitoba has been a topic of investigation for the past five decades. Given the complex geology, deformation and metamorphic history of the area, the boundary has been variously interpreted by different workers.

Initial studies (e.g. Gill, 1949) were based on the concept of structural provinces and subprovinces. Later, gravity data (Wilson and Brisbin, 1961,1962) revealed a significant low that was identified as a boundary; this boundary was postulated to have evolved from an orogenic episode and was the remnant root of a mountain zone. Structural studies (Rance, 1966) identified a lineament as being the trace of an unconformity between the two provinces. More recent work suggests the boundary is more a wide transitional zone (Weber, 1990) than an abrupt demarcation. Figure 2.6 is a schematic summary of the evolution of proposals for the location of the boundary between the Churchill and Superior Provinces (Bell, 1971). The prevailing opinion at present is that the Thompson Belt is a complex transition zone between the Churchill and Superior Provinces (Weber, 1990).

The Thompson Belt is underlain by amphibolite- to granulite-facies polymetamorphic ortho- and paragneiss of Archean age (Cranstone and Turek, 1976). These gneisses are largely derived from Pikwitonei type granulites through selective retrogression and recrystallization, migmatization, and structural reconstruction under amphibolite-grade conditions during the Hudsonian orogeny (Weber, 1990). Re-

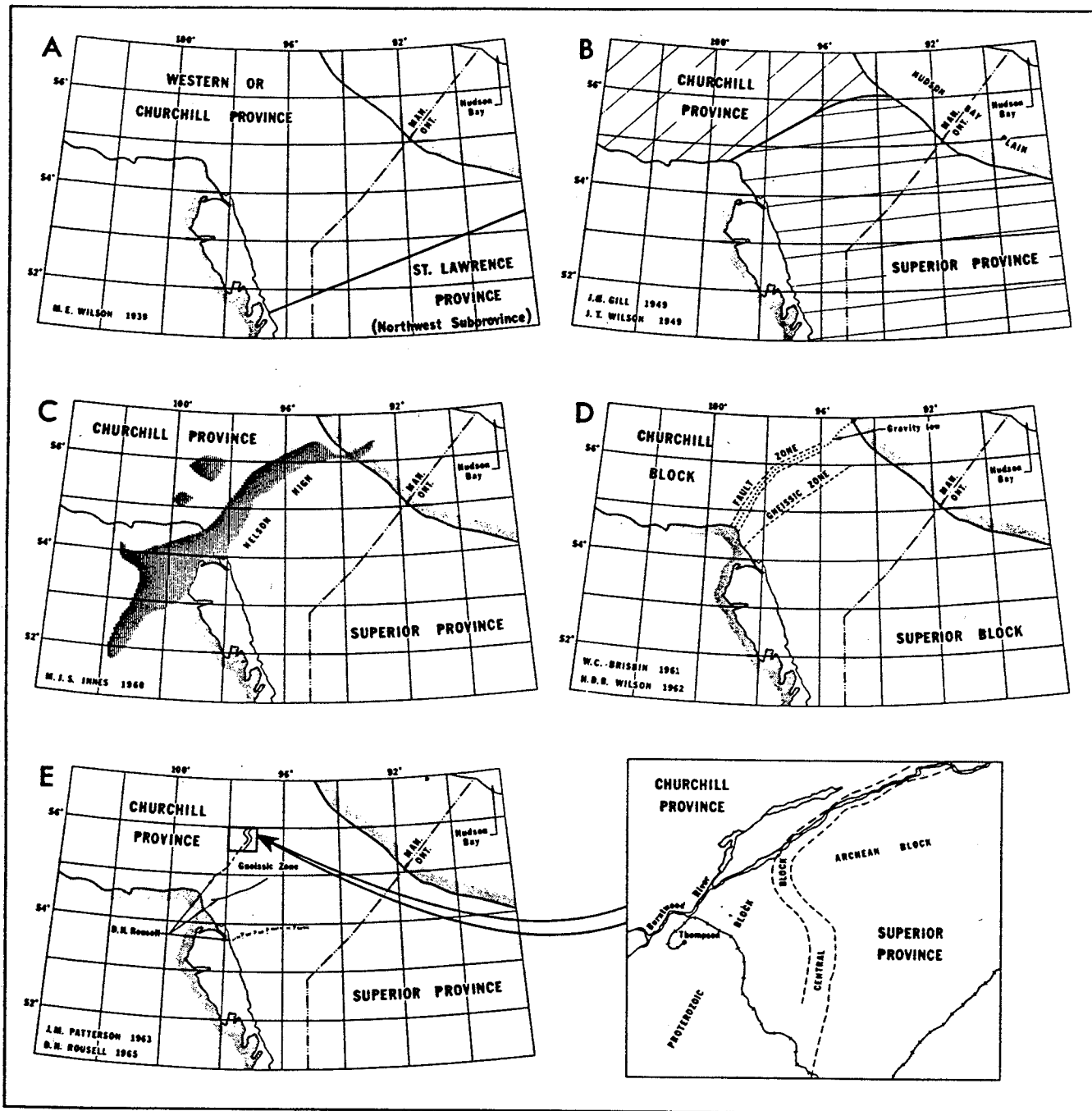


Figure 2.6 Proposals for the Churchill-Superior boundary zone (Bell, 1971)

(D) is after Wilson and Brisbin, 1961,1962

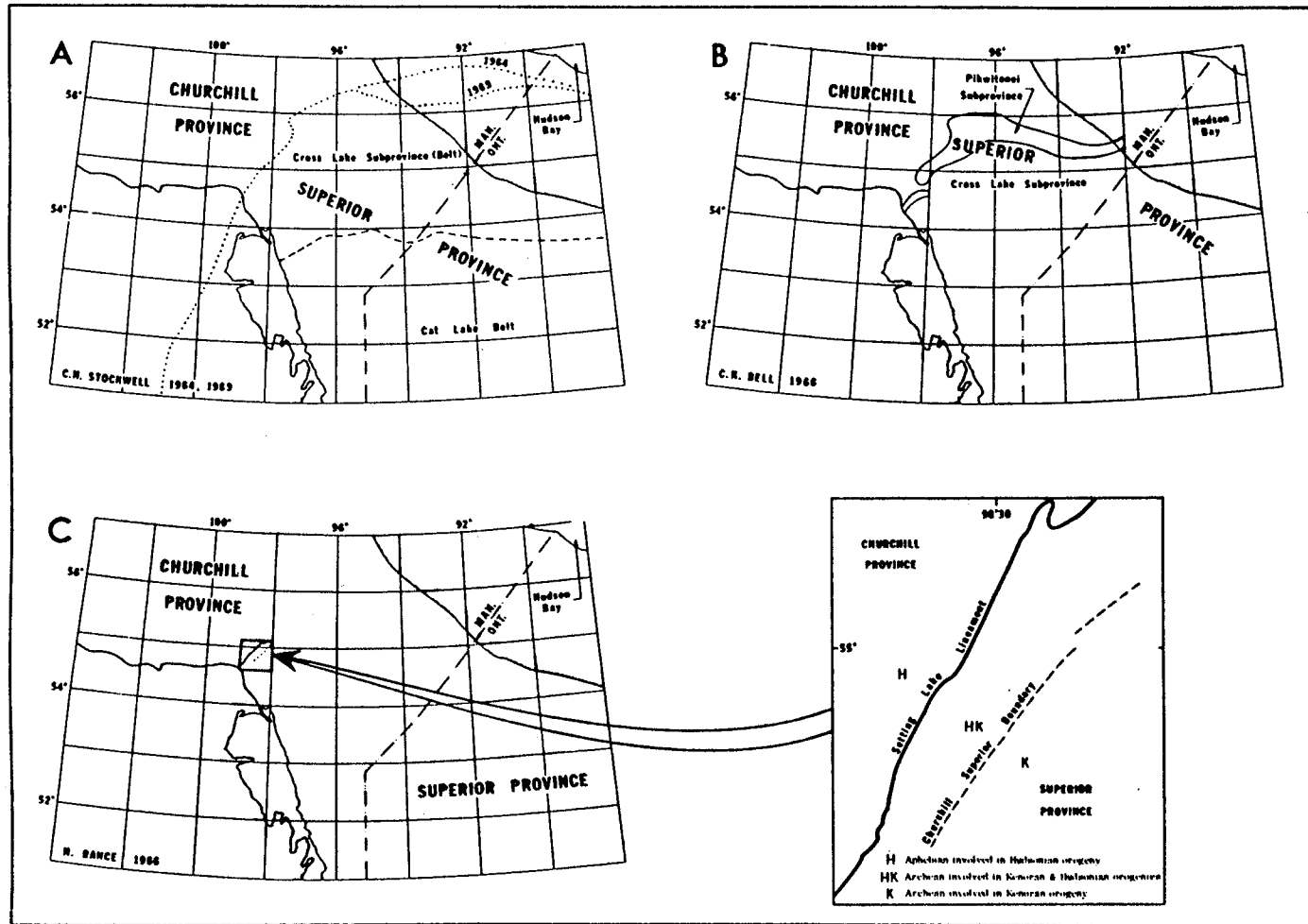


Figure 2.6 (Contd.) Proposals for the Churchill-Superior boundary zone (Bell, 1971)

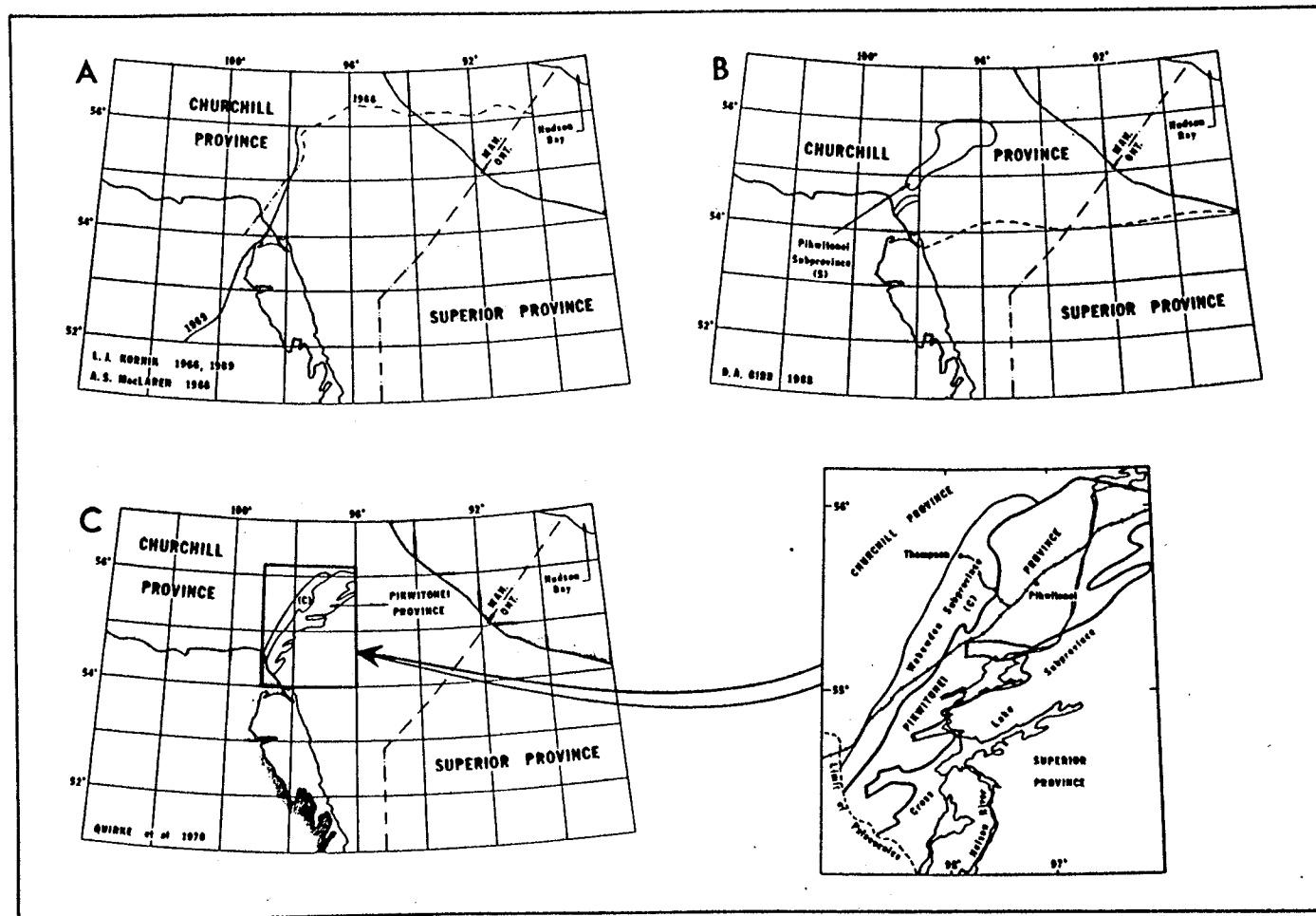


Figure 2.6 (Contd.) Proposals for the Churchill-Superior boundary zone (Bell, 1971)

(A) is after Kornik and MacLaren, 1966

worked gneisses in the Churchill-Superior Boundary zone were affected by a structural and metamorphic overprint, the eastern limit of which has been mapped in terms of a garnet isograd (Hubregtse, 1980a).

Along the western margin of the Thompson Belt, early Proterozoic metasediments and metavolcanics of the Ospwagan Group occur in narrow belts. The metasediments are composed of arenites, marbles, pelites, chert, oxide- and sulphide-facies iron formations with associated apatite-rich horizons, and greywackes. Overlying the metasediments are ultramafic to mafic volcanic rocks, serpentinites and ultramafic amphibolites (Bleeker, 1990). The serpentinites are the host rock for nickel mineralization. The metasediments and metavolcanics are intruded by minor granitoid plutons (Peredery, 1982).

Baragar and Scoates (1981) considered the supracrustal rocks to be rift sequences; igneous material of oceanic origin underplated a tectonically thinned continental margin (Superior Province) and derived magmas were intruded and extruded into a marginal basin or back-arc basin tectonic setting (Weber, 1990). Kinematic indicators in the bounding mylonites indicate that the Superior Province has moved up relative to the Churchill Province (Bleeker, 1990).

2.8 Structure And Tectonics

A variety of depositional and deformational events have been identified by geological and geochronologic studies in the Superior and Churchill Provinces. These are summarised in Table 2.2 (Green *et al.*, 1985a; Gordon *et al.*, 1990).

The Pikwitonei Subprovince has undergone two periods of folding. In the first

	AGE (Ga)
Age of the Archean cratons	
Superior craton (including the Pikwitonei granulites and the Thompson belt) [I,IV,V]	2.5-3.1
Churchill craton (including the Cree Lake zone) [I,IV]	2.5-2.7
Uplift of the Pikwitonei granulites [*]	2.3-2.5
Rifting of the Archean cratons	
Superior craton (Thompson and Fox River belts and the Molson dykes) [II,III,V]	2.3-2.4
Churchill craton (Cree Lake zone)	1.9-2.5
Island arc and related magmatism	
Flin Flon-Snow Lake belt [I]	1.8-1.9
La Ronge-Lynn Lake belt [I,IV]	> 1.9
Wathaman-Chipewyan batholith and related intrusives [I,IV]	1.8-1.9
Hudsonian orogenic activity	
Thompson belt [II,IV,V]	1.6-1.9
Fox River belt [II,IV]	1.7
Flin Flon-Snow Lake belt [I,IV]	1.7-1.9
La Ronge-Lynn Lake belt [IV]	1.6-2.0
Wathaman-Chipewyan batholith and related intrusives [I,IV,V]	1.7-1.9
Kisseynew belt [IV]	1.7-1.8
Reindeer-South Indian Lakes belt [IV]	2.0
Cree Lake zone [IV]	1.7-1.9

Table 2.2 Timing of Tectonic and Metamorphic Events in the Churchill and Superior Provinces (Modified from Green et al., 1985a; Gordon et al., 1990)

Techniques: I - U/Pb zircon; II - Pb/Pb; III - Sr/Sr; IV - Rb/Sr;
V - K/Ar; * - inferred

phase the gneissosity developed in the granulite facies gneisses. Subsequent open flow folding produced an average regional foliation that strikes N 65° E and dips 80° northwest with fold axes plunging 35° towards N 60° E (Bell, 1978). The lower metamorphic grade greenstone belt sequences of the Superior Province also have undergone two periods of folding as a result of which the regional northeast-trending fold axes have been bent by subsequent folding of the axial plane in which they lie (Bell, 1978). There is evidence that the geometry of Archean folds was modified by the early Proterozoic Hudsonian Orogeny. The Thompson Belt rocks are deformed into tightly compressed similar folds with planar limbs and axial planes that strike north-northeast and dip steeply to the southeast. At least three deformational phases of folding affected this area. Subsequent to the second phase of folding, intense shearing, faulting and mylonitisation occurred throughout the entire length of the Thompson Belt (Bell, 1978). The final phase of folding is interpreted as sinistral wrench folds (Bleeker, 1990). In the Flin Flon Subprovince the folds are more open (Bell, 1978).

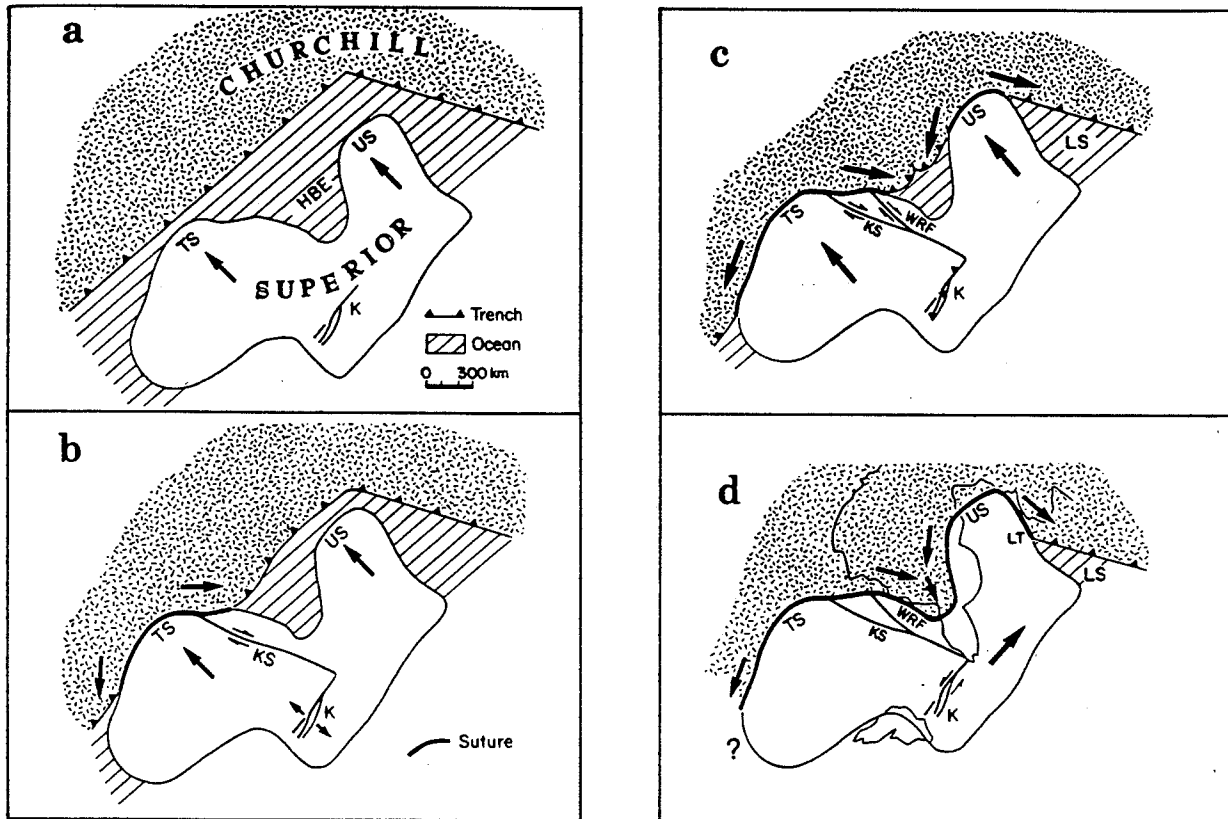
Most recent workers have interpreted the Trans-Hudson Orogen to be an area of juvenile crust formed in an ocean between two Archean cratons now represented by the Superior and Hearne Provinces. Volcanism in the Trans-Hudson Orogen is interpreted to be the result of subduction of oceanic crust, and the Hudsonian deformation in the Trans-Hudson Orogen and bounding areas is interpreted to be the result of collision of the two cratons; the boundary between the Churchill and Superior Provinces is considered to be an ancient suture zone. Workers differ in the nature of the deformation, the relationship of the volcanic belts to subduction,

and the nature of the collision. Two representative but controversial hypotheses are presented here without any prejudice about the validity of either model, or indeed of other models presented by other workers (e.g. Lewry *et al.*, 1990).

Symmetrical distribution of linear, positive gravity anomalies near the southern and eastern perimeter of Hudson Bay, led Gibb (1983) to suggest a model in which subduction of oceanic lithosphere led to suturing of the Superior and Churchill protoplates. Two major promontories on the north margin of the northwesterly moving Superior protoplate resulted in progressive "double indentation" of the Churchill craton by the Superior protoplate (Figure 2.7). Following complete suturing the direction of motion of the Superior plate, relative to the Churchill plate, may have changed by about 90°, from northwesterly to northeasterly, enabling complete closure of the predecessor of the Labrador Sea. The regional faults and their sense of motion correlates with that predicted by the theoretical pattern of slip lines associated with a wedge shaped indenter. Further, the various domains are narrowest in the area near the apex of the proposed wedge, which seems to support such a model (Figure 2.7).

Another tectonic model for the study area has been proposed by Green *et al.* (1985a) which has the following features:

- the rifting and rupturing of Archean cratons in the early Proterozoic;
- formation of oceanic basins between the Superior and Churchill cratons;
- closing of the oceanic basins by subduction;
- collision of the Superior craton with the Flin Flon-Snow Lake arc which was marginal to the Churchill craton;



Stages in the double indentation of the Churchill Craton by salients of the converging Superior plate and the filling of the Hudson Bay embayment (HBE) (after Gibb, 1983). a) Pre-collision stage. TS = Thompson salient; US = Ungava salient; K = Kapuskasing Structural Zone. b) Initial collision and suturing of Thompson salient. Indentation progresses by displacement of Churchill material and filling of the embayment commences as the trench migrates. Dextral slicing of western Superior craton develops (KS = Kenyon structure) causing local tensional component in Kapuskasing Zone. c) Collision of Ungava salient and extension of suturing. Double indentation progresses by displacement of Churchill material from the paths of both salients. Dextral slicing of western Superior craton continues with development of Winisk River Fault (WRF). Thrust component develops along margin of Kapuskasing Zone. LS = Labrador Sea predecessor now isolated from Hudson Bay embayment. d) Completion of filling of Hudson Bay embayment. Kapuskasing Structural Zone receives sinistral component of dislocation during final stages of closing of Labrador Sea predecessor and Labrador Trough (LT) forms. Motion of Superior plate relative to Churchill is changed by about 90°E as Labrador Sea is closed.

Figure 2.7 Double indentation tectonic model (Thomas and Gibb, 1985)

- major sinistral faulting and related shear folding along the Thompson belt;
and
- cessation of all relevant plate motions and major isostatic readjustments.

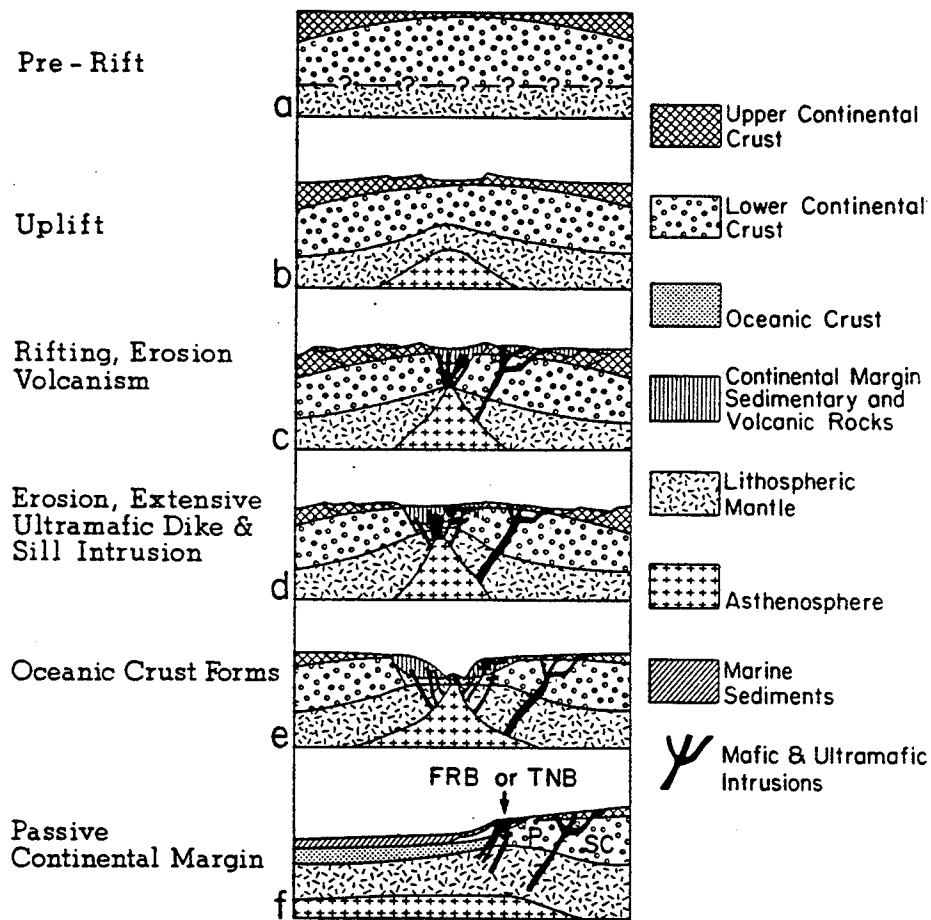
In this model (Figure 2.8) Green *et al.* (1985a) envisaged an Archean Superior Craton separated from Archean Churchill (and Wyoming) cratons by a broad region of mostly Proterozoic oceanic crust in which one or more volcanic island arcs and associated fore-arc and back-arc basins developed. The Thompson nickel belt is regarded as a remnant of the western continental margin of the Superior craton.

2.9 Geology of the Test Sites

Two test sites were selected for the purpose of this study; the main selection criterion was the amount of geological control available. The Wabowden test site has only sparse surface outcrop and geologic contacts are based on extrapolation and inference. The high degree of uncertainty in positions of many geologic contacts makes it possible to treat the site as an approximation of unknown terrain. This site is a good candidate for the development of the integration procedure used in the present study.

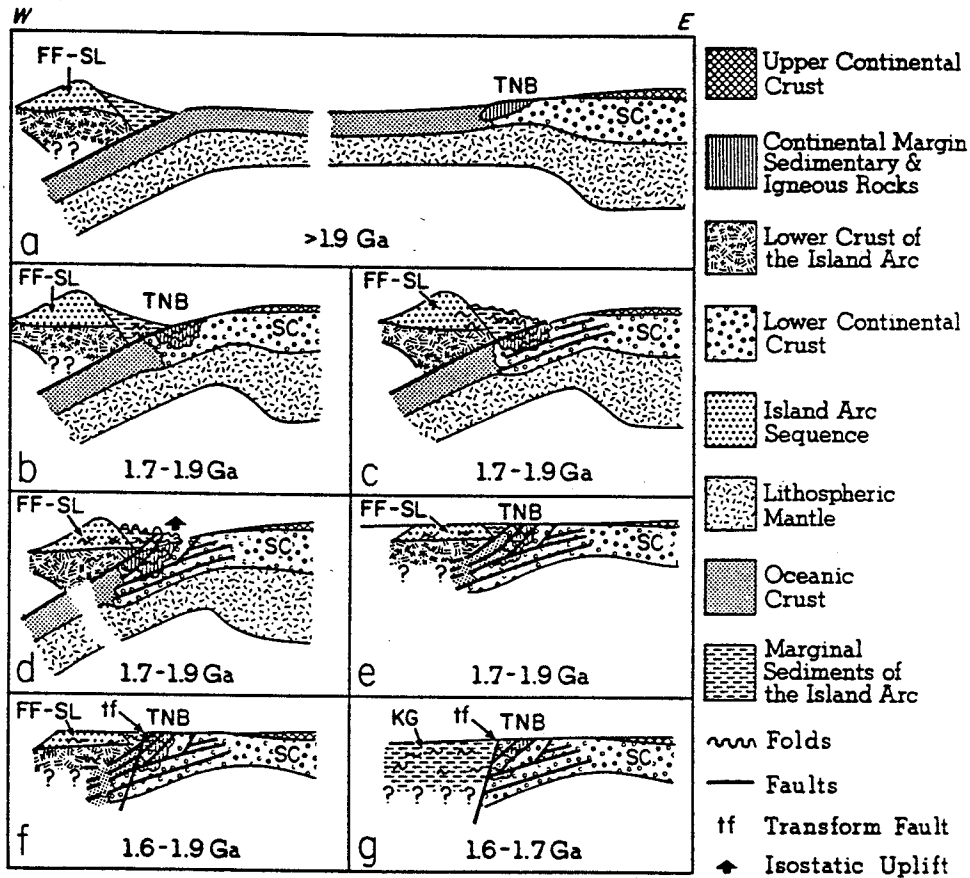
To test the integration procedure developed in this research, the Lake Wekusko test site farther west was also selected. Here, the degree of uncertainty of location of geologic contacts is significantly lower on account of better and more frequent surface exposures.

The dimensions of both test sites are 32.75 km in the E-W direction and 55.25 km in the N-S direction.



Suggested evolution of the northwestern Superior craton margin up until 2.3–2.4 Ga. *P*, *FRB* and *TNB* are the Pikwitonei, Fox River and Thompson belts respectively; *SC* is the Superior craton.

Figure 2.8 Proposed Tectonic Model (Green et al., 1985a)



Suggested evolution of the Thompson belt (TNB). FF-SL—Flin Flon-Snow Lake belt, KG—Kisseynew belt, SC—Superior craton. Evolution up to diagram (f) also applies to the Superior craton margin in southern Canada and in the northern United States.

Figure 2.8 (Contd.) Proposed Tectonic Model (Green et al., 1985a)

The geology of the Wabowden test site is shown in Figure 2.9. and lithological descriptions of rock units are summarised in Table 2.3. Except for the southwest corner, where Paleozoic rocks occur, the rest of the site consists of Precambrian rocks. The test site straddles the boundary between the Superior and Churchill Provinces. The Pikwitonei Subprovince and the Cross-Lake Subprovince of the Superior Province dominate most of the map. The rocks of the Churchill Province occur in the northwest part of the site.

The Lake Wekusko test site (Figure 2.10) is in the greenstone belt of the Flin Flon domain of the Churchill Province but the southern part of the area is covered by dolomitic limestone. Lithological descriptions of the rock types are summarised in Table 2.4.

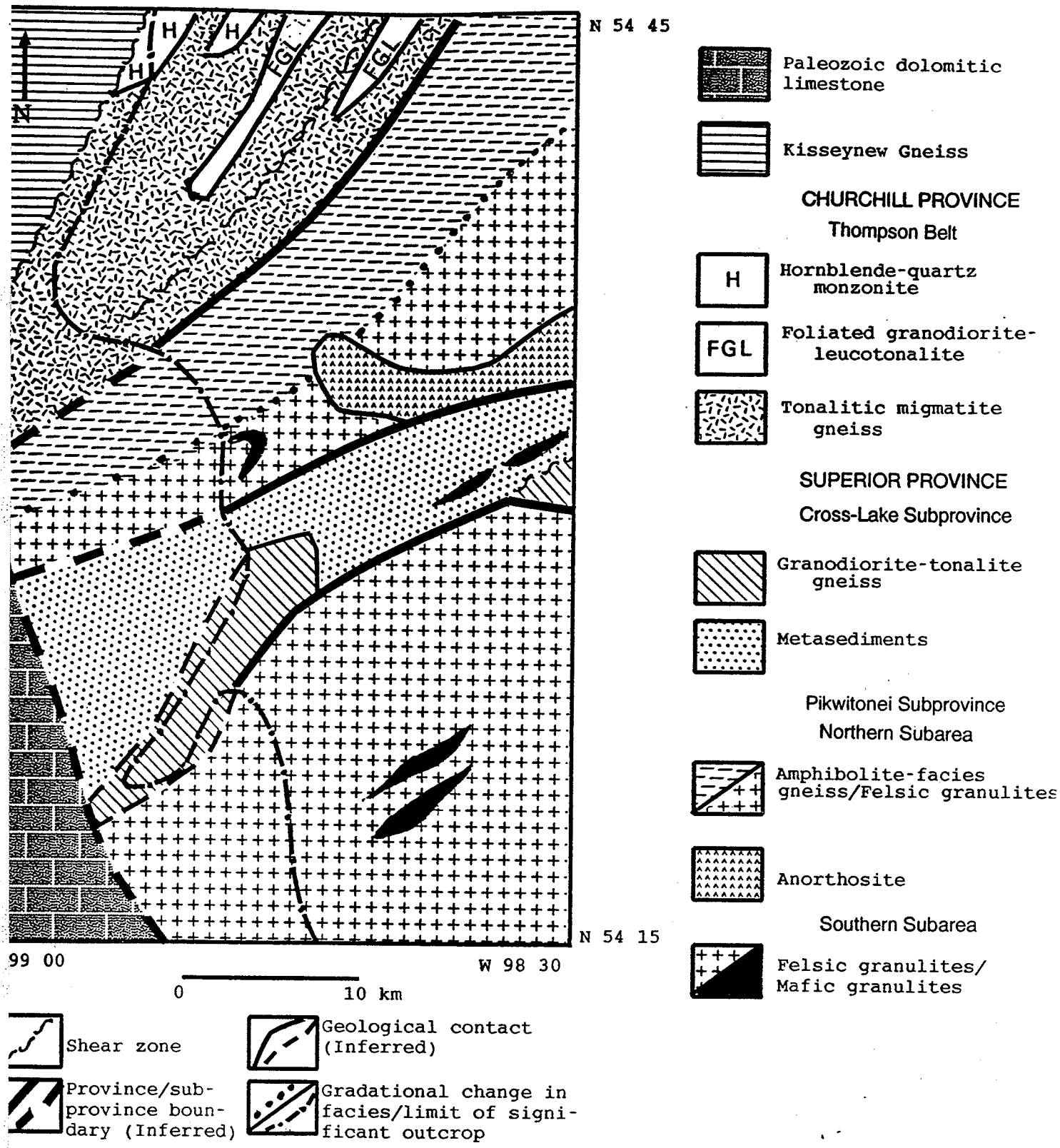


Figure 2.9 Generalised geology of Wabowden Test Site (Compiled after Bell, 1978; Hubregtse, 1980b)

ROCK UNIT	DESCRIPTION
Paleozoic (Ordovician)	Mottled dolomitic limestone, dolomite, cherty limestone (Average thickness = 11 m)
Kisseynew gneiss	Metasedimentary; dark quartz-rich biotite-plagioclase gneiss with reddish quartz-plagioclase pegmatite steaks; minor amphibolite-plagioclase gneiss
Hornblende-quartz monzonite	Foliated to massive, medium-grained hornblende-quartz monzonite; epidote veins, accessory apatite
Foliated granodiorite-leucotonalite	Foliated granodiorite-leucotonalite, pegmatite and minor granite, locally migmatite with granitized components
Tonalitic migmatite gneiss	Leucocratic transitional migmatite; augen-cataclastite and minor porphyritic quartz diorite sills; mesocratic migmatite and hybrid migmatite
Granodiorite-tonalite gneiss	Grey to pink foliated tonalitic gneiss; massive tonalite (with mafic inclusions); locally compositional variations of quartz monzonite, tonalite, trondhjemite, quartz diorite and hornblende diorite
Metasediments	Metasomatic rocks; granoblastic biotite-quartz-plagioclase paragneiss
Amphibolite-facies gneiss/ Felsic granulites	Layered granoblastic, biotite-quartz-plagioclase gneiss
Anorthosite	Massive, well jointed, greenish, coarse- to very coarse-grained anorthosite; locally varies to gabbroic anorthosite
Mafic granulites/ felsic granulites	Mafic orthopyroxene granulite and amphibolite; minor metapyroxenite and metadiorite; orthopyroxene-sillimanite gneiss

Table 2.3 Lithological units in Wabowden test site (Compiled after Bell, 1978; Hubregtse, 1980b)

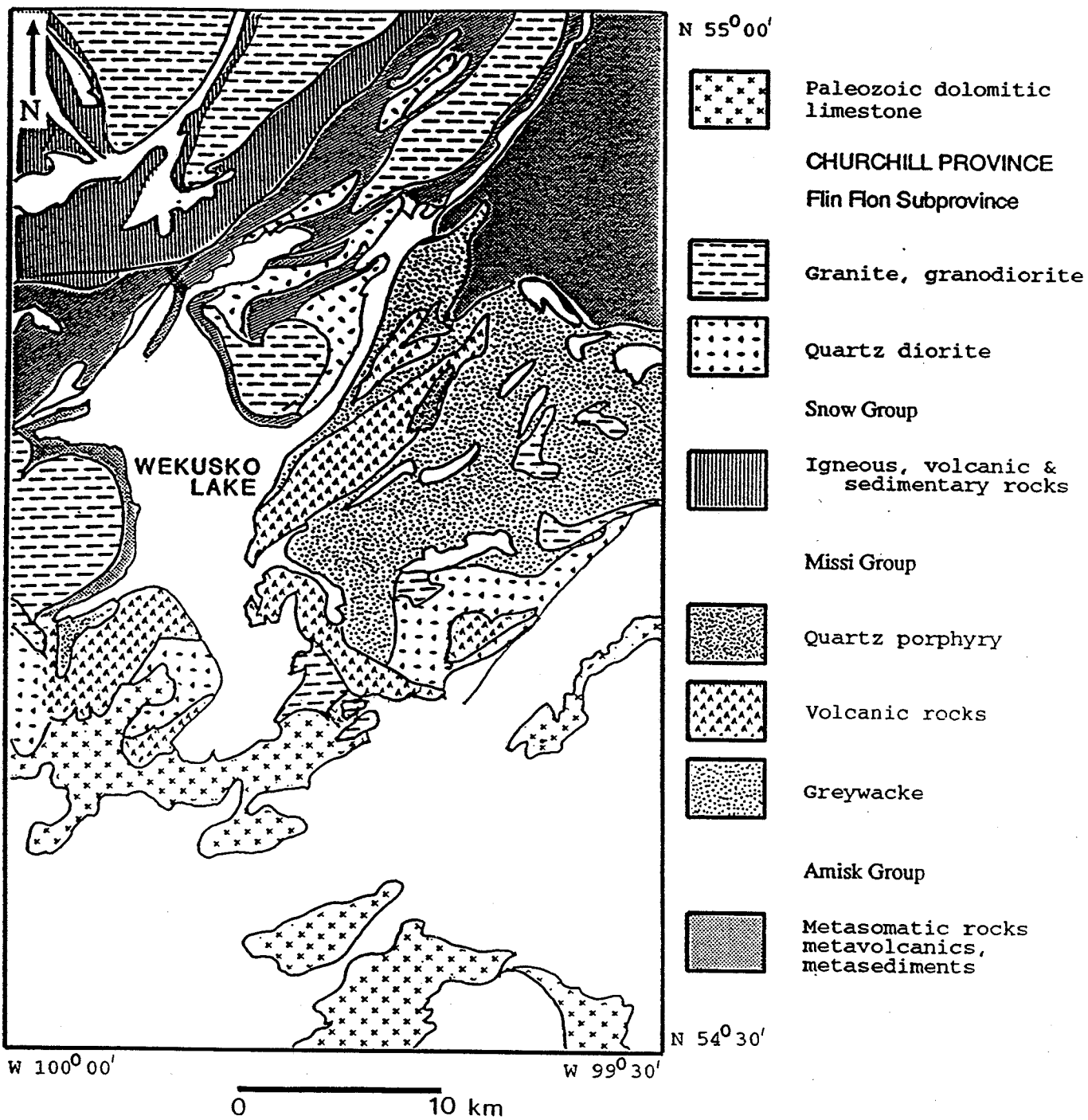


Figure 2.10 Generalised geology of Lake Wekusko Test Site (Compiled after Bell, 1978; Gordon et al, 1990)

Unornamented area in the south is Paleozoic rocks overlain by glacial deposits

ROCK UNIT	DESCRIPTION
Paleozoic (Ordovician)	Mottled dolomitic limestone, dolomite, cherty limestone (11 m to 41 m thick)
Granite, granodiorite	Granite, granite porphyry, quartz monzonite, granodiorite
Quartz diorite	Quartz diorite, diorite, quartz gabbro and anorthositic gabbro
Igneous, volcanic and sedimentary rocks	Felsic volcanic rocks; feldspathic sedimentary rocks; tuff and breccia; hornblende gabbro and diorite; mafic flows, arkose, minor greywacke
Quartz porphyry	Quartz feldspar porphyry, quartz porphyry
Volcanics	Mafic and felsic metavolcanic rocks, interlaminated feldspathic chert and greywacke
Greywacke	Greywacke, in part metamorphosed to biotite gneiss; minor arkose
Metasomatic, metavolcanic, metasedimentary rocks	Quartz-eye gneiss, garnetiferous biotite-quartz-plagioclase-gneiss; mafic volcanics, volcanic breccia, agglomerate and tuff; greywacke, argillite, quartzite, schist

Table 2.4 Lithological units in Lake Wekusko test site (Compiled after Bell, 1978; Hubregtse, 1980b; Gordon et al, 1990)

CHAPTER 3

Preprocessing of Data Sets

This chapter describes the characteristics and the steps involved in the preliminary processing of the different data sets. The geological and geophysical data were processed on the AMDAHL mainframe system and the satellite data on the VAX-based DIPIX ARIES (Applied Resource Image Exploitation System, Letts, 1978) image analysis system (Geophysical Imaging Laboratory) at the University of Manitoba.

In general the preprocessing is oriented towards the generation of data sets compatible for integration. In the case of analogue maps, the maps are digitised and stored as vector coded files in the computer. With the aid of plotting software, the vector coded files are transformable to a two-dimensional plot of any desired scale. The scale (size) of the plot is only limited by plotting hardware and memory capacity available in the computer. Alternatively, as was done in this study, the map is rasterised to a required grid dimension

The selection of the grid dimension is dictated by the aspect ratio of the test sites, measured by computing the ratio between the ground distance for 30' of latitude (55250 m) and 30' of longitude (32750 m). This ratio is 1.7. Hence the grid dimensions was determined as 128 columns (E-W direction) and 256 rows (N-S direction) giving an aspect ratio of 2.0, which is a close approximation of the actual ground aspect ratio.

One of the most important problems about acquiring satellite data for areas in the northern latitudes is the very limited time window available for data acquisition. The period from November to May is ruled out because of snow cover. Vegetation is in full bloom from July to September and masks the spectral signature of the rocks. During Autumn (September to November) the trees shed their foliage which lies on the ground and is likely to contaminate the spectral signature. Therefore the ideal time period is a brief three months from May to July, immediately after the snow cover has melted and before the vegetation blooms. Even in this short time frame, there must be a fortuitous occurrence of cloud-free days when the orbiting satellite is directly overhead the area of study.

Due to unpredictable variations in satellite orbital parameters, the one frame of satellite data that has been recorded may not necessarily cover the entire area of study. In such cases it is possible to use two adjacent frames and perform a seamless joining of the two to obtain the required coverage. But this option is not always feasible, mainly due to financial constraints.

In the present study the TM data for the Lake Wekusko test site are not a perfect rectangle (§Figure 3.14). The MSS data were expected to provide coverage

of both the Wabowden and the Lake Wekusko test sites. Only the former area is fully covered (§3.11); while more than 30% of the northwestern corner of the Lake Wekusko area was missing and MSS data for this area were therefore not used in this research. Spot data were available only for the northern half of Lake Wekusko test site

Although the aeromagnetic data were made available in digital form on magnetic tapes, repeated attempts to procure the digital gravity data were unsuccessful. As a last resort, published gravity maps were digitised.

3.1 Gravity Anomaly Data

Gravity prospecting is a reconnaissance tool, which involves the measurement of variations in the gravitational field of the earth. Local variations in the density of rocks cause fluctuations in the main gravity field. Measurements of these fluctuations results in a gravity anomaly map. Thus in gravity measurements it is not the earth's true gravitational field that is measured but its variation from one point to another. Measurement stations are usually closely located along the earth's surface, and interstation differences can be recorded with greater precision than the total gravitational field.

Variations in the measured values depend on the lateral changes in the density near the station. For instance, sedimentary rocks usually have a lower density than basement rocks. This density contrast makes mapping of sedimentary basins viable with gravity anomaly data. Hence gravity data has long been used in locating potential hydrocarbon deposits in oil exploration.

Gravity anomalies are smaller and smoother than magnetic anomalies because density variations are relatively small and uniform compared to changes in magnetic susceptibility. Gravity surveys are usually ground based, but measurements can be made also from low-altitude aircrafts and helicopters.

A regional gravity survey over central Manitoba and Saskatchewan was carried out using a total of 4100 stations. Of these, 3200 stations were spaced approximately 12 km apart. In the Churchill Superior Boundary Zone, data from 900 stations with an approximate interval of 6 km were used. From the gravity anomaly maps obtained from Gibb (1968) for the two test sites, the contours were table digitised using a Talos Systems digitiser. The maps were stored in the computer as a vector coded file. The contour interval in both maps is 5 milligals.

The vector-coded gravity anomaly maps obtained by digitisation were rasterised by means of a conversion algorithm (Steneker and Bonham-Carter, 1988). The grid dimensions were maintained the same as in other data sets. The rasterised version of the gravity anomaly maps for the Wabowden and the Lake Wekusko test sites are shown in Figures 3.1 and 3.2 respectively.

3.2 Aeromagnetic Anomaly Data

Geophysical data provide an effective mapping tool for lithology and structure and are commonly used in conjunction with conventional mapping techniques (Telford *et al.*, 1976). In order to provide accurate and detailed systematic magnetic coverage, the Geophysical Data Centre of the Geological Survey of Canada (GSC) carried out several aeromagnetic surveys in Manitoba. These were largely support-

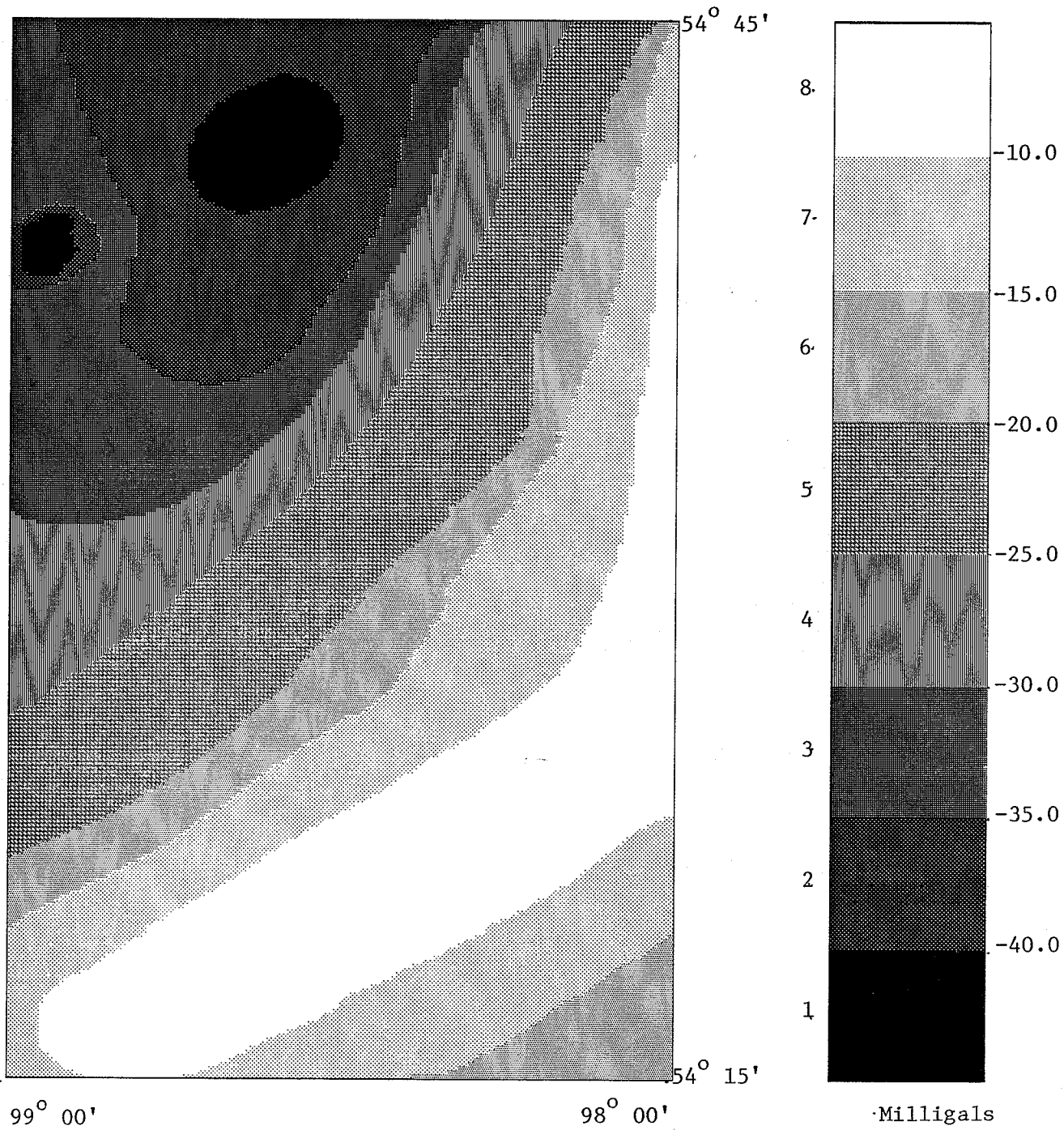


Figure 3.1 Rasterised gravity anomaly map for Wabowden test site

Distance = 55250 m (N-S), 32750 m (E-W)

Pixel size = 216 m (N-S), 257 m (E-W)

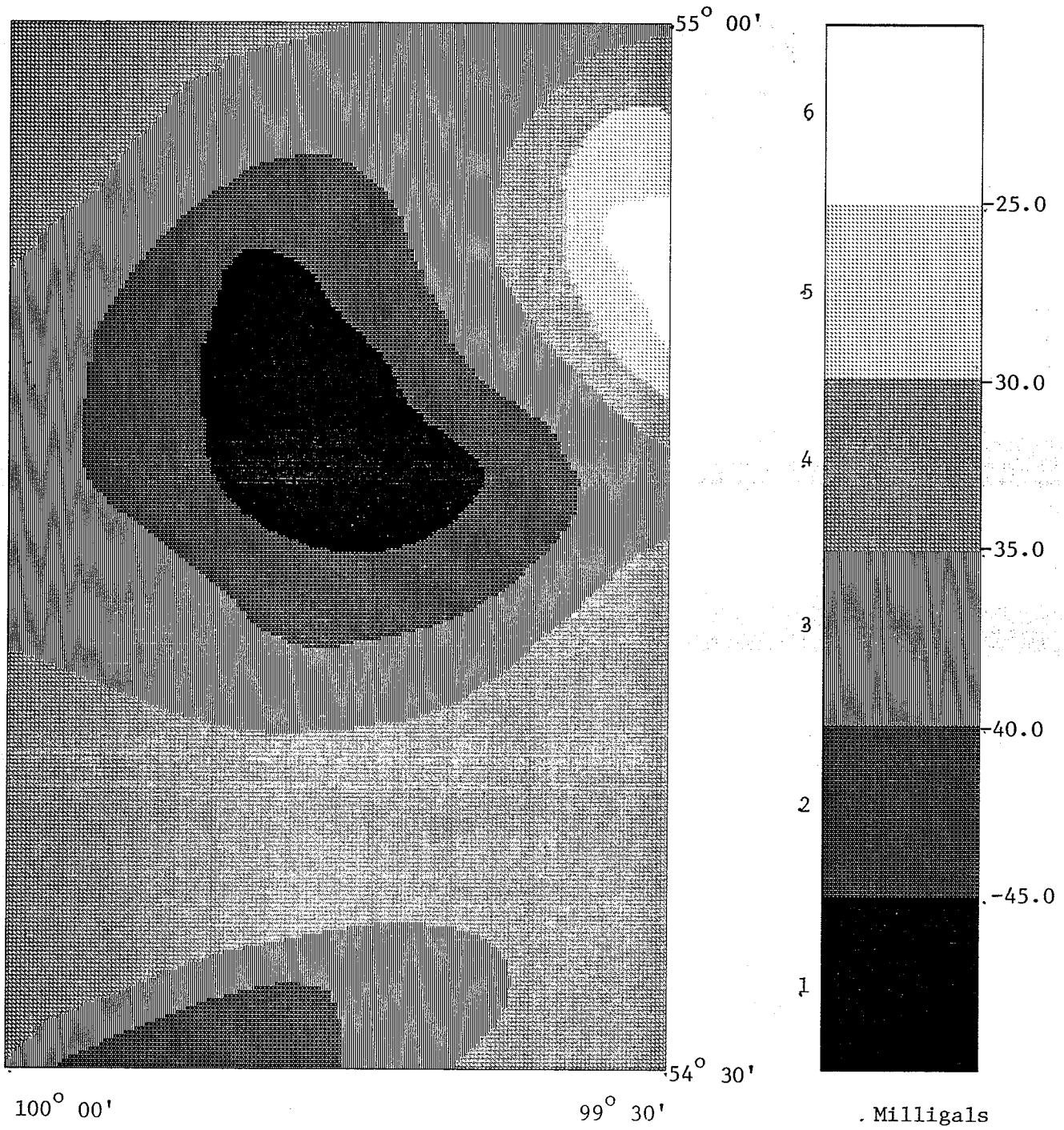


Figure 3.2 Rasterised gravity anomaly map for Lake Wekusko test site

Distance = 55250 m (N-S), 32750 m (E-W)

Pixel size = 216 m (N-S), 257 m (E-W)

ed by the Canada-Manitoba Mineral Development Agreement. The aeromagnetic anomaly data used in this study were obtained from this source. The acquisition parameters and other details given here are adapted from Kiss (1989).

The data were acquired by means of light aircraft equipped with an optically pumped cesium vapour Varian magnetometer. The altitude of the aircraft was maintained at 150 m above ground level and the spacing between survey lines at 300 m. The digital data were recorded at the rate of 4 samples per second and stored on magnetic tapes in ASCII format.

Magnetic tapes containing the total field aeromagnetic survey data covering a portion of the study area were procured from the GSC. The data were written in sixteen segmented blocks, each block covering a ground area of 15 minutes of latitude \times 30 minutes of longitude. On an average, each block contained about 1800 data points.

The digital total field aeromagnetic anomaly data were downloaded from magnetic tape onto the AMDAHL mainframe system. A simple two dimensional x-y plot of the data points revealed gaps in the data and an irregular grid presumably caused by aircraft drift and instrument fatigue during data acquisition. In order to correct for this it was necessary to interpolate the data to eliminate the gaps and to make it compatible for integration.

Given a set of data points each having a corresponding x, y, z value in the Cartesian co-ordinate system, it is possible to compute the new z value for a pair of new x and y values, by the process of 2-D interpolation. For instance, if x_i, y_i, z_i and x_j, y_j, z_j are known, then the value of z_n for a new point x_n, y_n can be com-

puted. Different mathematical procedures of interpolation are available depending on whether the original data are regularly or irregularly gridded. In the present case an IMSL subroutine (IQHSCV) was used.

IQHSCV calculates an interpolating function which is a fifth degree polynomial in each triangle of a triangulation of the $x - y$ projection of the surface. The interpolating function is continuous and has continuous first-order partial derivatives. Interpolation of z values in a triangle is based on three assumptions (Akima, 1978a, b):

- i) The value of the function at point (x, y) in a triangle is interpolated by a bivariate fifth-degree polynomial in x and y ; *i.e.*

$$z(x, y) = \sum_{j=0}^5 \sum_{k=0}^{5-j} q_{jk} x^j y^k \quad (3.1)$$

- ii) The values of the function and its first-order and second-order partial derivatives (*i.e.* z , z_x , z_y , z_{xy} and z_{yy}) are given at each vertex of the triangle.
- iii) The partial derivative of the function differentiated in the direction perpendicular to each side of the triangle is, at most, a polynomial of the third-degree.

The interpolation algorithm uses a five stage procedure (Akima, 1978a, b):

1. Partitioning into a number of triangles in the $x - y$ plane.
2. Determination or selection of several data points that are closest to each data point and are used for estimating the partial derivative.
3. Location of the output point at which bivariate interpolation is to be

performed (i.e., determination of the triangle in which the point lies), or organisation of the output grid points for smooth surface fitting by sorting them with respect to triangle members.

4. Estimation of partial derivatives at each data point.
5. Interpolation at each output point.

After each block was individually interpolated a mosaic of the 16 blocks was generated where the edges of adjacent blocks were reinterpolated to eliminate seams. Then an aeromagnetic anomaly map was generated by means of a grey level plotting program.

The data corresponding to Wabowden and Lake Wekusko test sites were segregated and assigned to separate data sets for use in the integration procedure and for further processing. These were individually plotted as grey level maps.

A frequency distribution of the aeromagnetic anomaly map for the Wabowden test site shows that about 83% of the pixels fall within the lower grey levels (Level 4 to 7). To enhance the information present in these levels a piece-wise linear contrast stretch was carried out. This technique takes advantage of the dynamic range of the display medium and a near-Gaussian frequency distribution is obtained. Table 3.1 shows the number of pixels in each grey level before and after stretching.

The frequency distribution of the Lake Wekusko anomaly data (Table 3.1) is near-Gaussian and consequently does not need to be stretched.

The aeromagnetic anomaly map for Wabowden test site before stretching is shown in Figure 3.3 and after stretch in Figure 3.4. The Lake Wekusko test site aeromagnetic anomaly map is shown in Figure 3.5.

Greylev Number	Number of Pixels		
	Before Stretch (a)	After Stretch (a)	Unstretched (b)
16	78	95	397
15	17	89	143
14	43	83	182
13	46	225	250
12	83	530	307
11	225	1411	529
10	530	1751	974
9	1411	2822	1384
8	1751	4133	1880
7	2822	3455	4010
6	4087	5549	5859
5	8986	7201	8398
4	11362	4097	7025
3	1129	1129	1211
2	91	91	115
1	107	107	104
Total	32768	32768	32768

Table 3.1 Number of pixels in each grey level
(a) before and after stretch (Wabowden test site)
(b) unstretched (Lake Wekusko test site)

3.3 Radar Data

Radar, which is an active remote sensing method, propagates microwave radiation to the surface and records the returning wavefield, also known as back-scattered wavefield. Since it provides its own energy source it can operate without benefit of sunlight and can also completely penetrate clouds. Further the angle of incident energy can be controlled to enhance features of interest. Table 3.2 lists the bands of microwave spectrum used in remote sensing and the wavelengths commonly used in imaging radars.

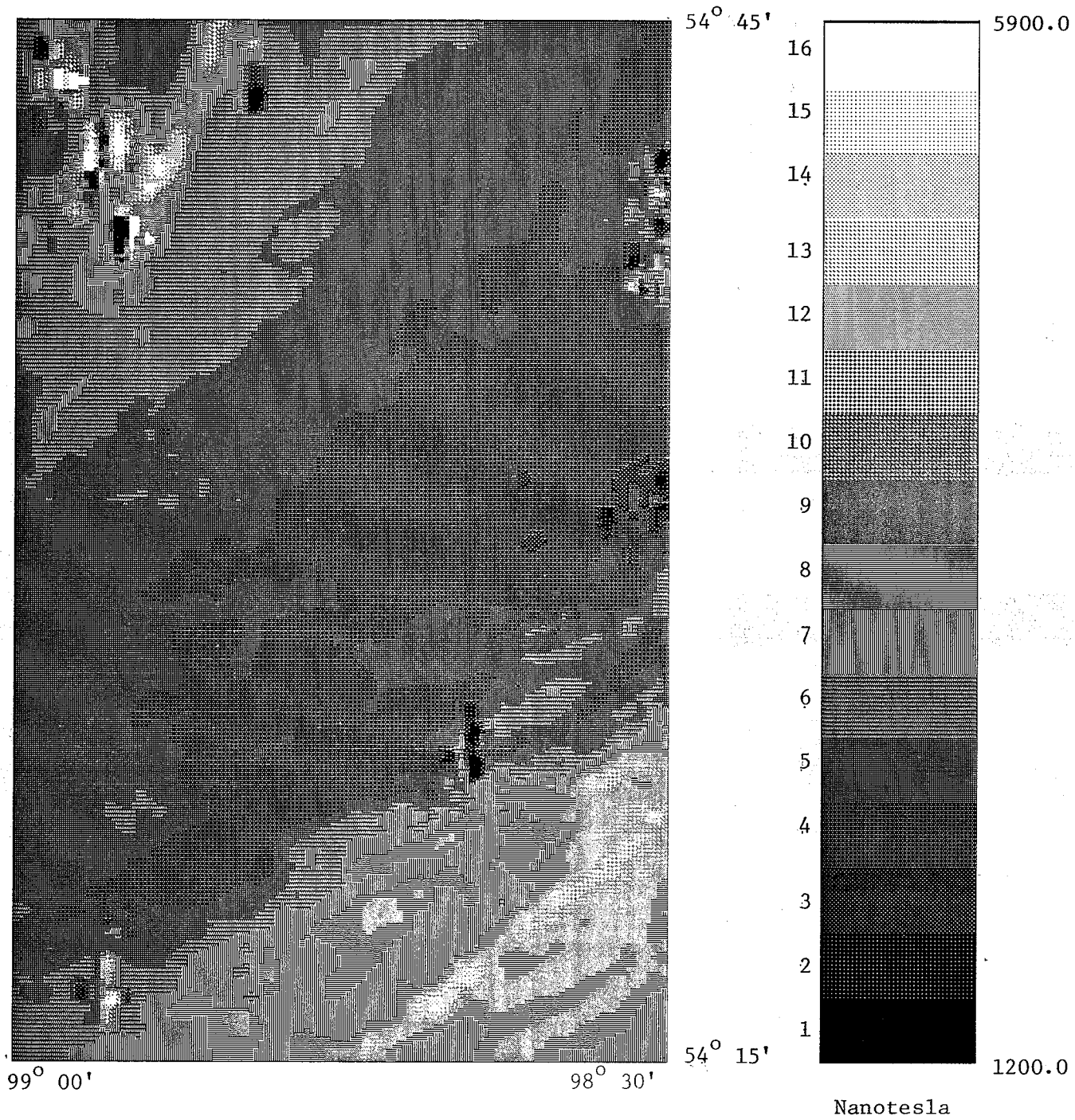


Figure 3.3 Total field aeromagnetic anomaly map for Wabowden test site

Distance = 55250 m (N-S), 32750 m (E-W)

Pixel size = 216 m (N-S), 257 m (E-W)

Grey scale bar is linear

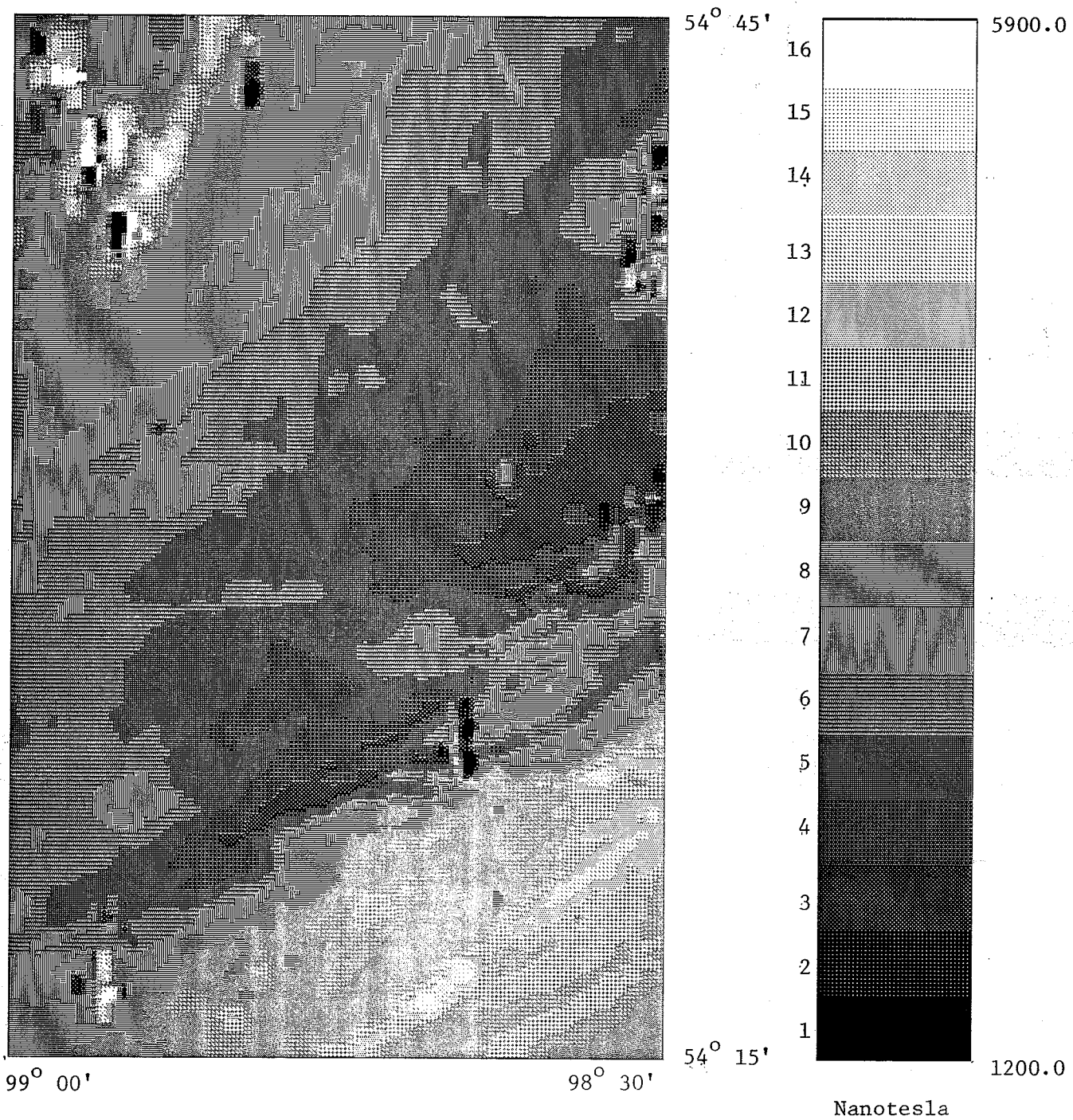


Figure 3.4 Stretched aeromagnetic anomaly map for Wabowden test site

Distance = 55250 m (N-S), 32750 m (E-W)

Pixel size = 216 m (N-S), 257 m (E-W)

Grey scale bar is linear

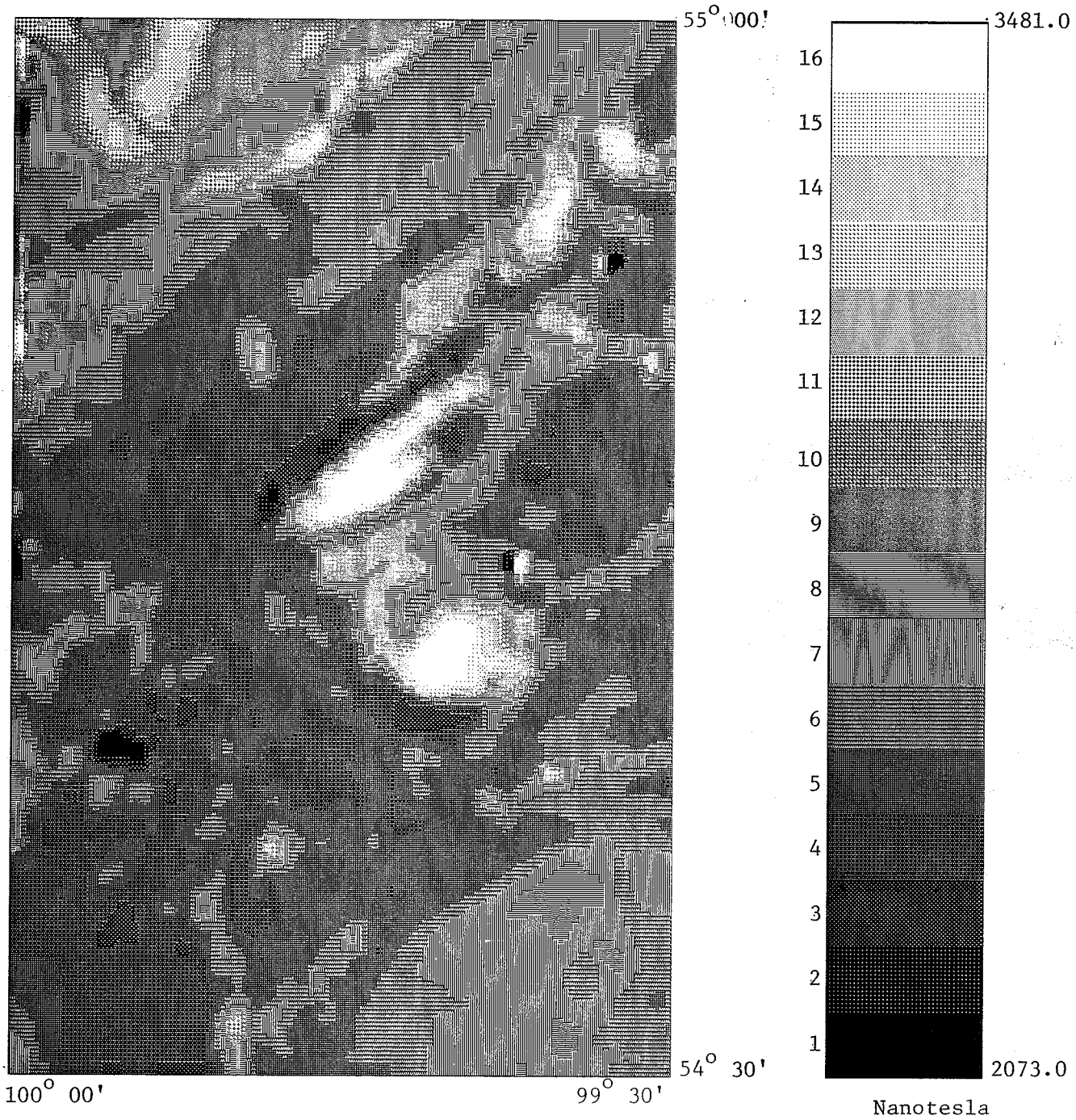


Figure 3.5 Total field aeromagnetic anomaly map for Lake Wekusko test site

Distance = 55250 m (N-S), 32750 m (E-W)

Pixel size = 216 m (N-S), 257 m (E-W)

Grey scale bar is linear

By far the most commonly used microwave sensor is the Side-Looking Airborne Radar (SLAR). The geometry of the SLAR system is shown in Figure 3.6. There are two types of SLAR; the Real-Aperture Radar (RAR) and the Synthetic-Aperture Radar (SAR). The term aperture refers to the length of the antenna. In RAR the length of the antenna is equivalent to its physical length and therefore provides a limited coarse resolution. On the other hand SAR has a fine resolution. A physically short antenna is shifted to successive positions along the flight line with each position being treated as an individual element of the antenna. Thus it produces a very long antenna synthetically by using the forward motion of the platform. This results in a synthetic beam of constant width regardless of range (Figure 3.7)

The radar data used in the present study consists of airborne Synthetic Aperture Radar data recorded in Band C (C-SAR) operating at a wavelength of 5.66 cm in both nadir and narrow swath modes. The optimum imagery used in this study was obtained in the narrow swath mode with HH polarisation. At an average aircraft altitude of 6 km the narrow swath mode produces $6 \text{ m} \times 6 \text{ m}$ resolution imagery over incidence angles from 45° to 76° which corresponds to 18 km swath width on the ground range. The entire image strip consists of 40,000 lines with 4096 pixels per line. Only a portion of this image relevant to this study, consisting of 867 lines and 1036 pixels per line was used.

3.4 Satellite Data (Landsat and SPOT)

Since the launch of the first satellite for earth observation in July 1972 the Landsat (formerly ERTS-1) series of satellites have provided a vast amount of data

Band	Wavelength (cm)	
	Range	Used for Imaging
K _a	0.8 - 1.1	0.86
K	1.1 - 1.7	
K _u	1.7 - 2.4	
X	2.4 - 3.8	3.0, 3.2
C	3.8 - 7.5	6.0
S	7.5 - 15.0	
L	15.0 - 30.0	23.5, 24.0, 25.0
P	30.0 - 100.0	68.0

Table 3.2 Bands used in radar data acquisition (After Avery and Berlin (1992))

which, in the past few decades, have been used for a diverse variety of applications. For details of launch dates, functional lifetimes, orbit parameters, payloads, data acquisition, storage, and telemetry the reader is referred to other sources such as Landsat Data Users Notes (NOAA 1975-), Colwell (1983), Jensen (1986), Richards (1986), Sabins (1987) and Drury (1987). A brief review of the satellites and their sensors is given here.

Landsat 1 through 3 were launched in near-polar, circular orbits at an altitude of about 919 km. The periodicity of the orbits was 103 minutes resulting in 14 orbits per day. Due to the sunsynchronous orbit the crossing of the equator was at approximately the same local time of 0930 - 1000 hours. The cyclicity of orbits permitted the same scene to be imaged once every 18 days. The payload comprised the Return Beam Vidicon (RBV) and the Multispectral Scanner (MSS) of which only the latter is described here.

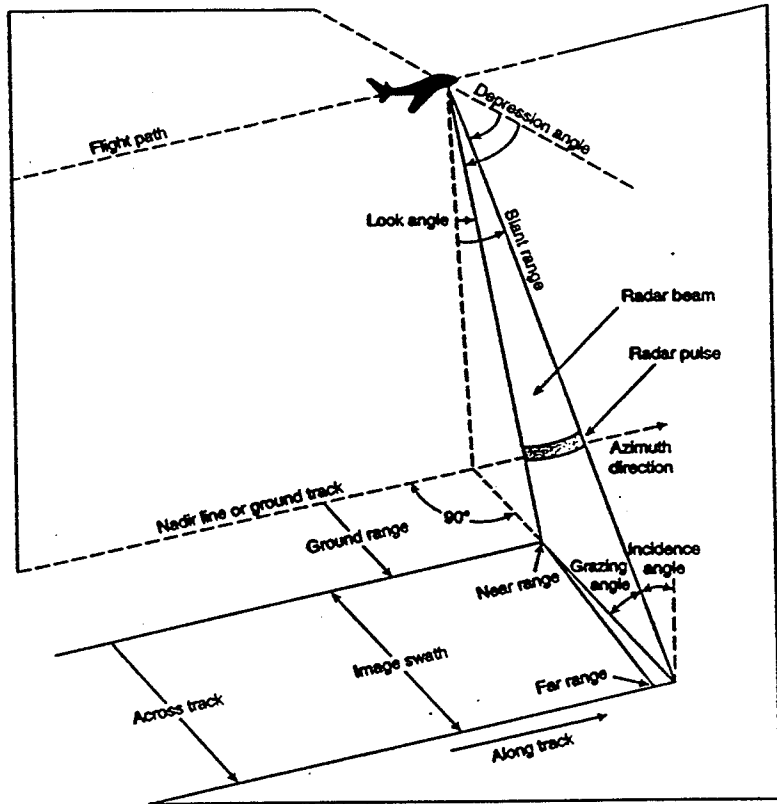


Figure 3.6 Geometry of side-looking airborne radar (SLAR) (Avery and Berlin, 1992)

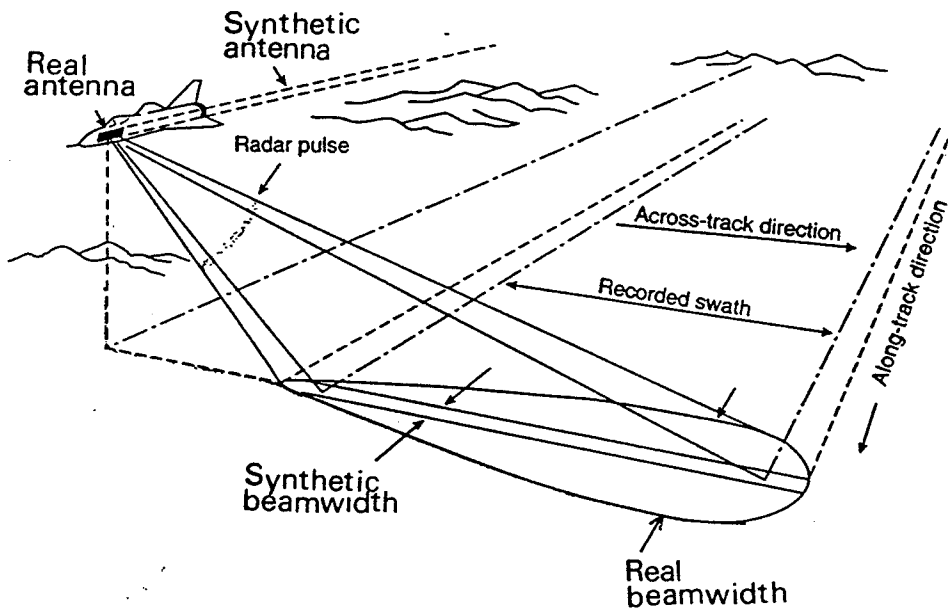


Figure 3.7 The synthetic-aperture radar (SAR) system (Avery and Berlin, 1992)

The MSS records information in four spectral bands (Table 3.3). On an average, a single frame of Landsat MSS data covers 185 km in the E-W direction and 178 km in the N-S direction. This scene is comprised of 2340 scan lines and 3240 pixels per line with a total of more than 7 million pixels per scene per band. The average pixel resolution is 82 m. But if the overlap between pixels is taken into account, the actual resolution is 56 m in the E-W direction and 79 m in the N-S direction, giving an aspect ratio of 1.41.

With the launch of Landsat 4 and later satellites, changes in orbital parameters and sensor payloads have been introduced. The orbiting altitude was lowered to 705 km, the cyclicity of the orbit changed to enable a same scene revisit of 16 days, and the equatorial crossing time altered to 1100 hours local time. The reduction in orbit coupled with improved sensors allowed for higher resolution, and the crossing time meant higher sun angles thereby reducing shadow lengths. This is useful for vegetation related studies, since the canopy is more realistically represented. However, geological applications were adversely affected since shadows commonly enhance geologic structures.

In addition to the MSS, the later Landsat satellites carry a refined sensor called Thematic Mapper (TM) (Salomonson, 1984), which records data in seven spectral bands with an enhanced pixel resolution of 30 m in six of the bands and 120 m in the remaining seventh band (Table 3.3).

Both MSS and TM sensors are equipped with an oscillating mirror that scans from west to east in the across track direction. This results in a 'down-time' during which the scanner returns to its original position for the next west-east scan. Fur-

LANDSAT 5 SENSOR				
BAND	WAVELENGTH RANGE Micrometers	PIXEL SIZE Metres	WAVELENGTH RANGE Micrometers	PIXEL SIZE Meters
Thematic Mapper		Multispectral Scanner		
1	0.45 - 0.52	30		
2	0.52 - 0.60	30		
3	0.63 - 0.69	30		
4	0.76 - 0.90	30	0.50 - 0.60	82
5	1.55 - 1.75	30	0.60 - 0.70	82
6	10.40 - 12.50	120	0.70 - 0.80	82
7	2.08 - 2.35	30	0.80 - 1.10	82
SPOT SENSOR				
Multi Linear Array		Panchromatic Linear Array		
1	0.50 - 0.59	20	0.51 - 0.73	10
2	0.61 - 0.68	20		
3	0.79 - 0.89	20		

Table 3.3 Landsat and SPOT sensor characteristics

ther, mechanical vibrations during oscillation induce errors in the data; and only ground track directly beneath the satellite pass can be imaged.

In early 1986 the SPOT (*Système Probatoire l'Observation de la Terre*) satellite developed by *Centre National d'Études Spatiales* (CNES) was launched which addressed many of the shortcomings of Landsat sensors. The SPOT satellite orbits the earth at an altitude of 832 km in a circular, near-polar, sunsynchronous orbit. The payload consists of two High Resolution Video (HRV) cameras which can image in panchromatic and multispectral modes (SPOT, 1984).

A new type of 'pushbroom' sensor (SPOT, 1984) was installed which images a complete line of the ground scene in the cross-track direction in one look. The absence of an oscillating mirror eliminates the errors described earlier for MSS and TM sensors. The Multi Linear Array (MLA) sensor of the SPOT satellite records data in three bands with a ground resolution of 20 m, while the Panchromatic Linear Array (PLA) images in a single spectral band spanning the visible portion of the electromagnetic spectrum with a resolution of 10 m (Table 3.3).

The SPOT satellite has an unique capability of providing stereo images by imaging the same scene from slightly different angles during two passes on successive days (Figure 3.8). The ratio of observation base to satellite altitude varies from 0.75 at the equator to 0.50 at 45° latitudes. This has a well-demonstrated use in cartographic applications (Welch, 1985). The off-nadir viewing capability can also be used to image scenes that are not directly beneath the satellite track (Figure 3.8).

Data that are recorded by the orbiting platforms are telemetered to ground receiving stations. Here the data are commonly preprocessed primarily to remove instrumentation induced errors. The data are then written onto magnetic tapes for eventual distribution to users. The data storage format is usually one of three types:

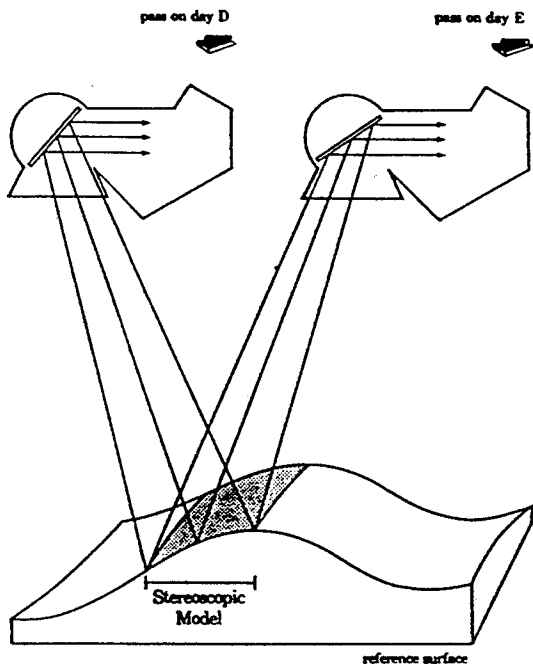
BSQ Band sequential; all the data for the first band are written to the tape

first, followed by all the data for the next band and so on,

BIL Band interleaved by line; data are written in the form line 1(band 1),

line 1(band 2), line 1(band 3), and

Stereoscopic Viewing Capabilities



Off-nadir Viewing

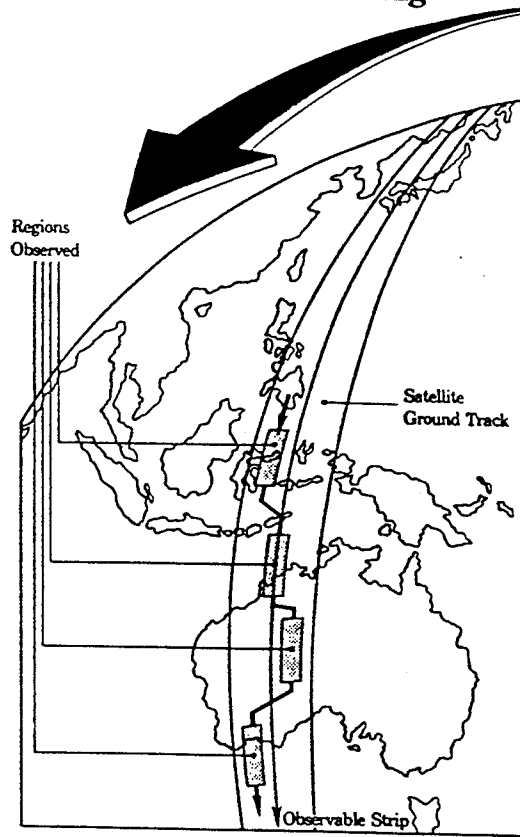


Figure 3.8 Stereo and off-nadir viewing capability of SPOT satellite (SPOT, 1984)

BIP Band interleaved by pixel; data are written in the form pixel (1,1) of band 1, pixel (1,1) of band 2, pixel (1,1) of band 3 and so on.

It may be noted in passing that, in a study by Siegrist and Schnetzler (1980), using an airborne MSS with 24 channels, it was found that the spectral range between 1.18 μm to 1.30 μm (reflective near infrared range) is the optimum range for lithological discrimination. None of the present day satellites record data in this range. The now defunct Landsat 3 recorded data in one additional channel in the emissive infrared range (10.4 μm to 12.6 μm ; Richards (1986; Table 1.7). However, these data are dependent upon numerous physical properties, variations in which led to ambiguities and errors in analysis (Price, 1981). In recent years data from airborne Multispectral Scanners such as Daedalus DS-1260 (11 bands), TIMS (6 bands) (Jensen, 1986; Table 2.2) have gained wide acceptance especially for mineral alteration mapping (Rowan and Kahle, 1982; Kahle and Goetz, 1983).

The present study involved the use of MSS, TM and SPOT data. All the data sets were acquired from the Prince Albert Satellite Station in Canada in the form of computer compatible tapes (CCTs) on which the data were stored in ASCII form using the BSQ data format. The MSS data of Band 4, Band 5, Band 6, and Band 7 contained 2244 lines per band and 3236 pixels per line (pixel resolution 82 m). The TM data for the Lake Wekusko test site in Band 3, Band 5, and Band 7 contained 2944 lines and 3500 pixels per line. The pixel resolution for TM data is 30 m. The MLA SPOT data for a portion of the Lake Wekusko test site contained a total of 2398 lines per band with 2794 pixels per band (pixel resolution 20 m). Due to a variety of problems encountered during the data acquisition stages it was not

possible to use the same sensor data for the two test sites. Therefore the data sets used were: MSS data for Wabowden test site; TM, C-SAR and SPOT data for the Lake Wekusko test site.

The initial steps in the processing of satellite data such as removal of sensor-induced noise (Crippen, 1989) were performed at the ground receiving station. Geometric correction, which involves spatial and intensity interpolation and is directed towards removal of geometric distortions in the raw image was done in the present work.

Raw satellite images commonly contain errors caused by geometric distortion which are a result of variations in altitude, attitude, and mirror scan velocity, and are also due to earth rotation. One of the first steps involved in the processing of satellite data is correction of such errors. In principle the errors are rectified by registering the raw image with a reference map (such as a topographic map) or a reference image (such as a previously corrected image). The rectification of a remotely sensed image by registration with a topographic map is briefly discussed here. Since the maps used are based on a Universal Transverse Mercator projection the image after correction is also transformed to this projection (Snyder, 1978, 1981).

First a set of ground control points (GCPs) must be identified whose coordinates on the map (northing and easting) and on the image (scan line number, pixel number) can be readily and accurately obtained. Ideally points such as road intersections and small islands which occupy about one pixel are selected; the GCPs must be uniformly distributed over the entire image (Orti, 1981). The number of

GCPs required will depend upon the relief, the frequency of change in relief and the order of the transform polynomial used. 1st, 2nd, 3rd, 4th, and 5th order polynomials require a minimum of 3, 6, 10, 15, and 21 GCPs respectively (Welch, *et al.*, 1985). In most cases 10 to 30 GCPs are sufficient.

Besides image data, satellites also transmit other ancillary data such as sensor and satellite attitudes, non-linearities in scan mirror profile, etc. (Welch *et al.*, 1985) from which their attitude and position during acquisition of an image can be inferred. This additional data can be used for geometric correction thereby eliminating the need for several GCPs (Welch, *et al.*, 1985). In some cases correction of SPOT scenes to subpixel accuracy using this method of satellite modelling has been achieved with as few as 3 GCPs (Swann *et al.*, 1988), and 4 GCPs (Friedman *et al.*, 1983).

The two basic operations to achieve geometric corrections are spatial interpolation and intensity interpolation. Spatial interpolation models the geometric distortion using least-squares criteria by means of a polynomial equation. The order of the polynomial to be used is decided by the analyst. In most cases it is sufficient to use a six coefficient parameter transformation expressed as (Jensen, 1986):

$$\begin{aligned}x_{ip} &= a_0 + a_1x_{op} + a_2y_{op}, \\y_{ip} &= b_0 + b_1x_{op} + b_2y_{op},\end{aligned}\tag{3.2}$$

where x_{ip} , y_{ip} are positions in the input image and x_{op} , y_{op} are positions in the rectified output image. Using the GCPs the six coefficients are computed and a rectified output grid is generated.

In the next step, intensity interpolation, brightness values from x_{ip} , y_{ip} in the input image are relocated to x_{op} , y_{op} in the rectified output image. Such brightness value interpolation, or resampling, can be done using nearest-neighbour interpolation, bilinear interpolation or cubic convolution. In nearest-neighbour interpolation the brightness value of the pixel closest to the x_{ip} , y_{ip} is assigned to the x_{op} , y_{op} coordinates. Bilinear interpolation and cubic convolution can be expressed as (Jensen, 1986):

$$BV_{op} = \frac{\sum_{n=1}^{\eta} (Z_n / D_n^2)}{\sum_{n=1}^{\eta} (1 / D_n^2)}, \quad (3.3)$$

where,

$\eta = 4$ for bilinear interpolation (or $= 16$ for cubic convolution),

Z_n is the brightness value of the neighbouring four or sixteen data points,

and

D_n^2 are the distances squared from x_{ip} , y_{ip} to these neighbouring data points.

For the MSS data using a 1:50,000 topographic map sheet, fifteen GCPs were selected for geometric correction. After successive trials eleven of these were retained in the calculation of the polynomial transform for spatial interpolation (Table 3.4). The final residual error in along scan direction is 10.36 metres and in the across scan direction is 12.50 metres which is less than one pixel size. After resampling, the corrected image consisted of 2751 lines per band \times 2876 pixels per line. From this a subimage for the Wabowden test site comprising 1225 lines per band \times 524 pixels per line was derived.

For the TM data of Lake Wekusko test site a total of 24 GCPs were identified

GCP No.	Slave Line	Slave Pixel	UTM North	UTM East	Line Residual	Pixel Residual
2	821.0	640.0	6078250.0	464500.0	2.5	1.8
3	662.0	1203.0	6083250.0	498750.0	-2.5	-1.8
5	826.0	2241.0	6055875.0	553000.0	2.0	1.8
6	1214.0	2221.0	6024750.0	544000.0	-20.5	-17.1
8	1857.0	1121.0	5987750.0	470250.0	-2.0	-1.6
9	1820.0	639.0	5997250.0	444125.0	2.0	1.5
10	1265.0	1318.0	6033000.0	493000.0	-22.0	-17.9
11	1268.0	1671.0	6028000.0	512500.0	34.0	28.4
12	1208.0	2856.0	6016375.0	579500.0	3.0	2.4
13	1456.0	2706.0	5998375.0	566000.0	0.5	0.9
14	1064.0	1648.0	6044625.0	515375.0	2.0	1.8

Order of transform = 3

Standard error of pixel estimate = 10.358 m

Standard error of line estimate = 12.492 m

Table 3.4 List of GCPs for geometric correction of MSS data (Wabowden test site)

from a 1:50,000 scale topographic map of which 19 were considered to give the desired sub-pixel accuracy in geometric correction. The residual error was 19.05 metres along scan and 18.72 metres across scan (Table 3.5). From the corrected image, a subimage of the test site was derived consisting of 2634 lines per band \times 2132 pixels per line.

In both cases a 3rd order transform was adequate to obtain sub-pixel residuals. Higher orders, due to the uncertainties of higher order coefficients, do not necessarily decrease the error (Ford and Zanelli, 1985) and were therefore not attempted.

A subimage consisting of 648 lines \times 1068 pixels per line of the C-SAR data was registered to the TM image of Lake Wekusko test site.

Similarly for the SPOT data from the original image of 2398 lines per band \times 2794 pixels per line, a geometrically corrected image of 1517 lines per band \times 1685 pixels per line was obtained.

MSS images for Wabowden test site in all four bands are shown in Figures 3.9, 3.10, 3.11 and 3.12. TM image in Bands 3, 5 and 7 for Lake Wekusko test site are shown in Figures 3.13, 3.14 and 3.15.

The TM images for the Lake Wekusko site show a high degree of spatial variability. This is partly due to the salt-and-pepper noise introduced as an artifact during the process of resampling. To correct for this, a low-frequency filter was applied to the images. To prevent blurring, commonly caused by the application of a low-frequency filter, an unequal weighted smoothing kernel (Wang *et al.*, 1983)

GCP No.	Slave Line	Slave Pixel	UTM North	UTM East	Line Residual	Pixel Residual
1	1402.0	2917.0	6080450.0	437350.0	9.5	-13.3
2	1010.0	2304.0	6091075.0	443600.0	-4.0	4.2
3	1283.0	2745.0	6079600.0	454150.0	19.5	-12.6
4	1097.0	3057.0	6082600.0	464700.0	-22.0	0.6
6	1143.0	3031.0	6081500.0	463550.0	20.5	-29.5
7	1226.0	3026.0	6079100.0	462825.0	6.5	43.7
9	1481.0	3145.0	6070650.0	464225.0	12.5	3.1
10	1579.0	3102.0	6068050.0	462150.0	-31.0	-42.6
11	1547.0	3020.0	6069700.0	460100.0	3.0	28.3
12	1577.0	2917.0	6069650.0	456850.0	15.0	1.8
14	1528.0	2858.0	6071500.0	455525.0	-41.0	2.4
15	1554.0	2688.0	6072100.0	450350.0	1.0	-35.1
16	1468.0	2525.0	6075850.0	446350.0	-26.5	19.8
17	1638.0	2445.0	6071550.0	442675.0	28.5	3.5
18	1579.0	2316.0	6074275.0	439400.0	13.0	6.9
19	1674.0	2280.0	6071725.0	437600.0	-30.0	5.9
20	2195.0	2442.0	6055300.0	438200.0	3.0	-2.9
21	1731.0	3040.0	6064100.0	459200.0	19.5	14.8
24	2575.0	2824.0	6041075.0	446200.0	-2.0	0.6

Order of transform = 3

Standard error of pixel estimate = 19.047 m

Standard error of line estimate = 18.722 m

Table 3.5 List of GCPs for geometric correction of TM data (Lake Wekusko test site)

was used. The coefficients of the 3×3 kernel are:

$$L = \begin{bmatrix} 1.00 & 1.00 & 1.00 \\ 1.00 & 2.00 & 1.00 \\ 1.00 & 1.00 & 1.00 \end{bmatrix} \quad (3.4)$$

The kernel is moved over the entire image in successive steps. The products of the pixel brightness values, covered by the kernel at a particular position, and the coefficients are summed to give a new brightness value for the pixel currently at the centre of the kernel. This technique has been variously referred to as template method, moving box-car filter, or window method.

The TM images after filtering are shown in Figures 3.16, 3.17, and 3.18.

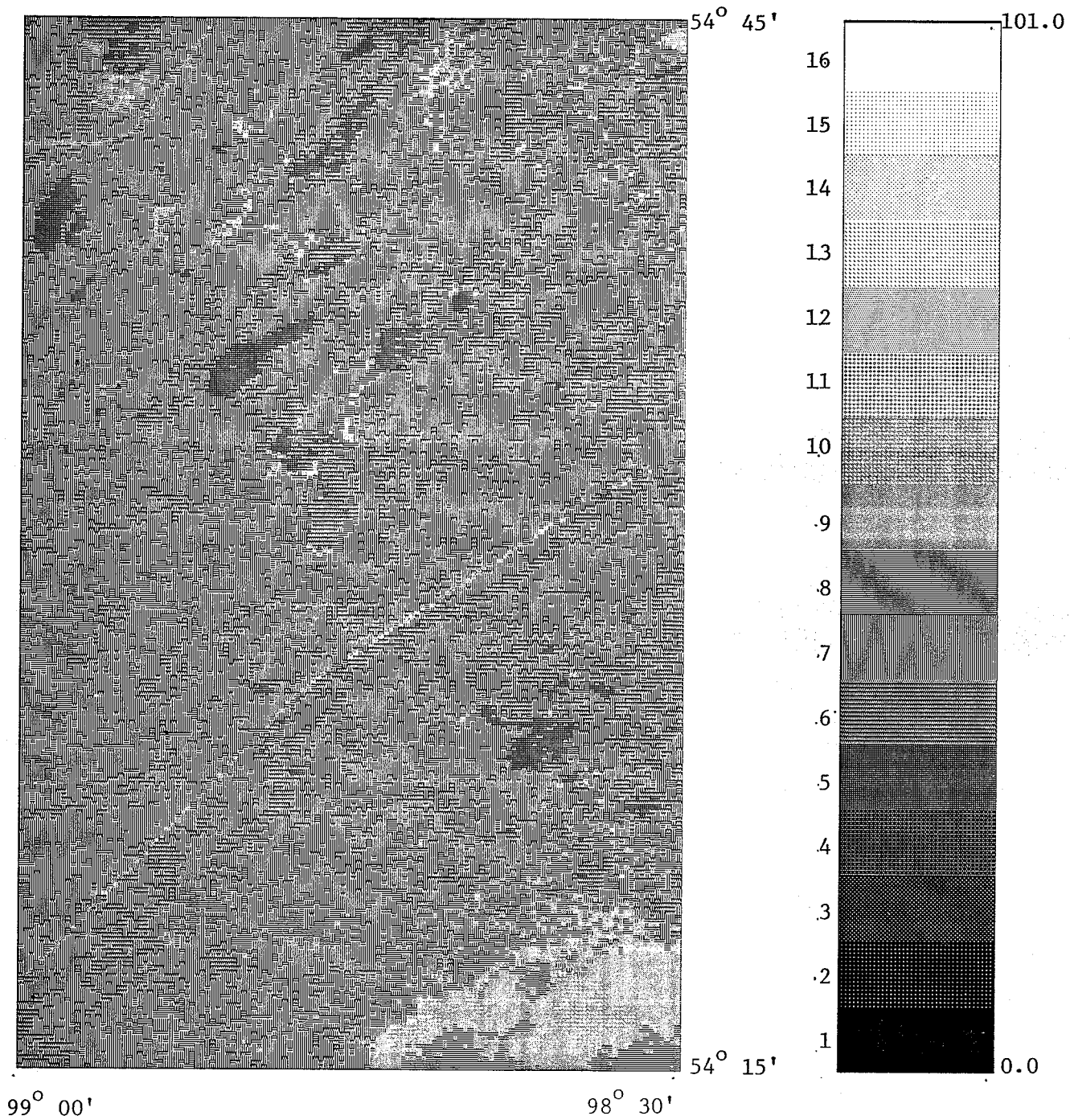


Figure 3.9 MSS Band 4 image for Wabowden test site

Distance = 55250 m (N-S), 32750 m (E-W)

Pixel size = 216 m (N-S), 257 m (E-W)

Grey scale bar is linear

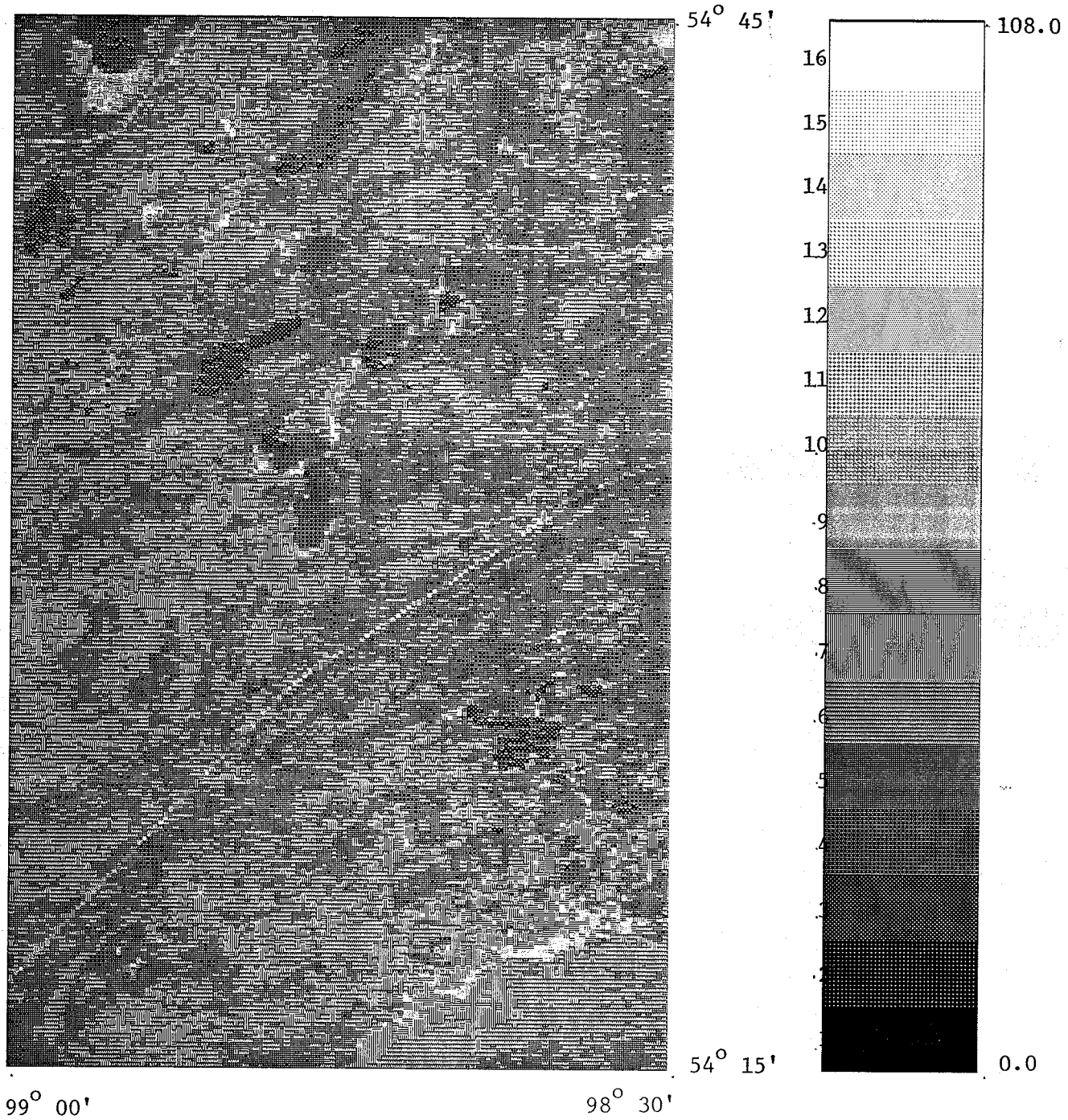


Figure 3.10 MSS Band 5 image for Wabowden test site

Distance = 55250 m (N-S), 32750 m (E-W)

Pixel size = 216 m (N-S), 257 m (E-W)

Grey scale bar is linear

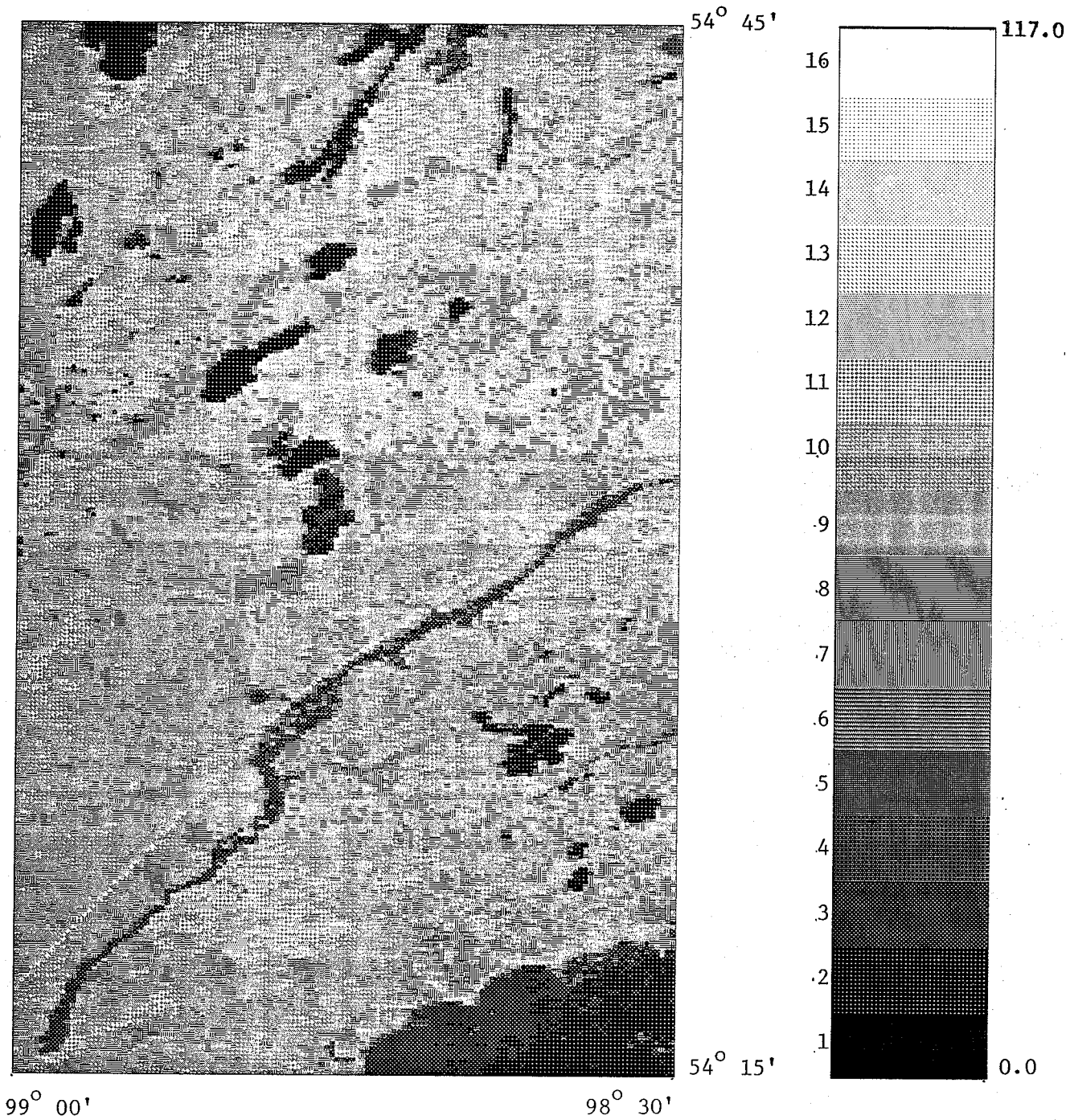


Figure 3.11 MSS Band 6 image for Wabowden test site

Distance = 55250 m (N-S), 32750 m (E-W)

Pixel size = 216 m (N-S), 257 m (E-W)

Grey scale bar is linear

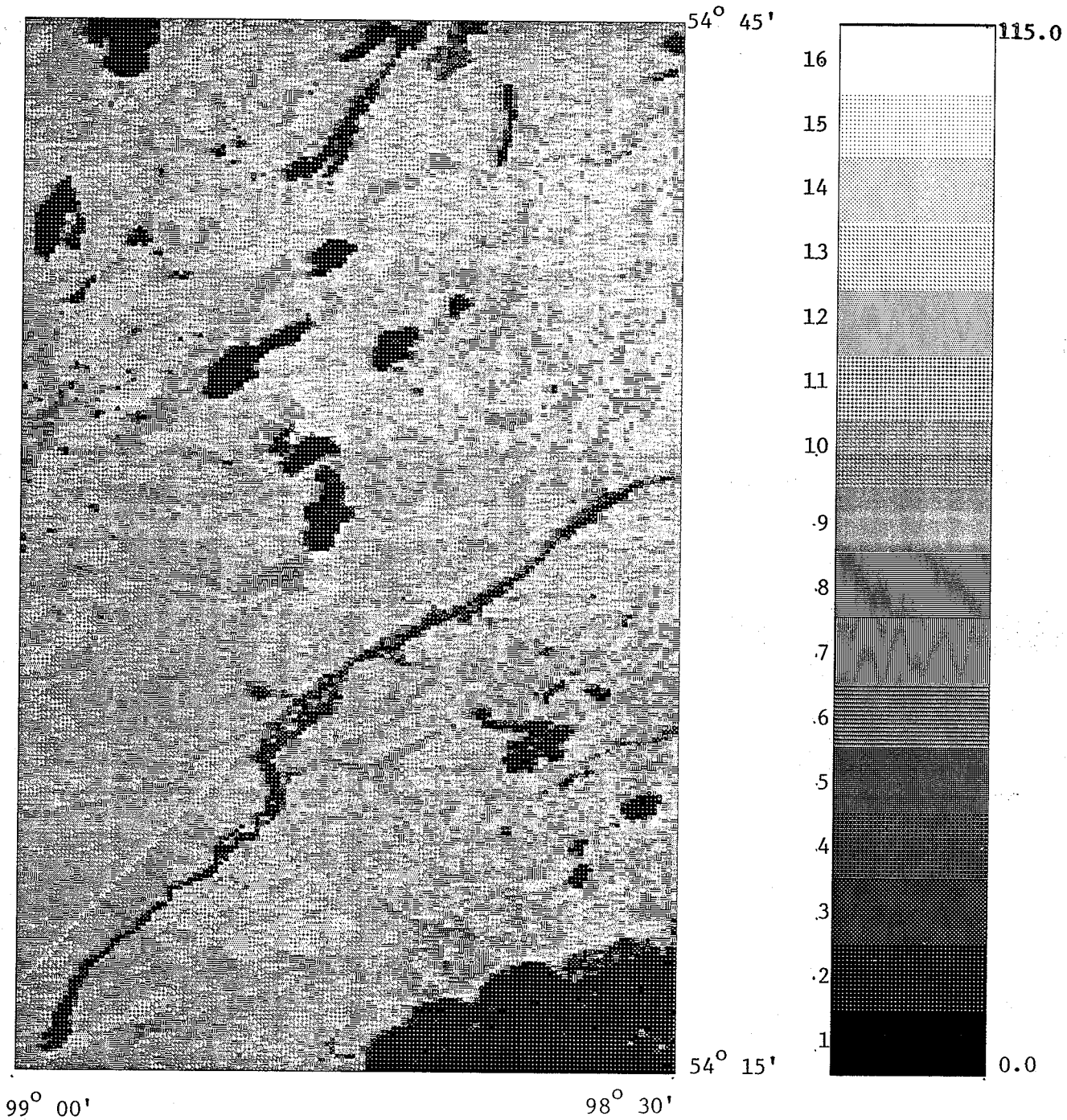


Figure 3.12 MSS Band 7 image for Wabowden test site

Distance = 55250 m (N-S), 32750 m (E-W)

Pixel size = 216 m (N-S), 257 m (E-W)

Grey scale bar is linear

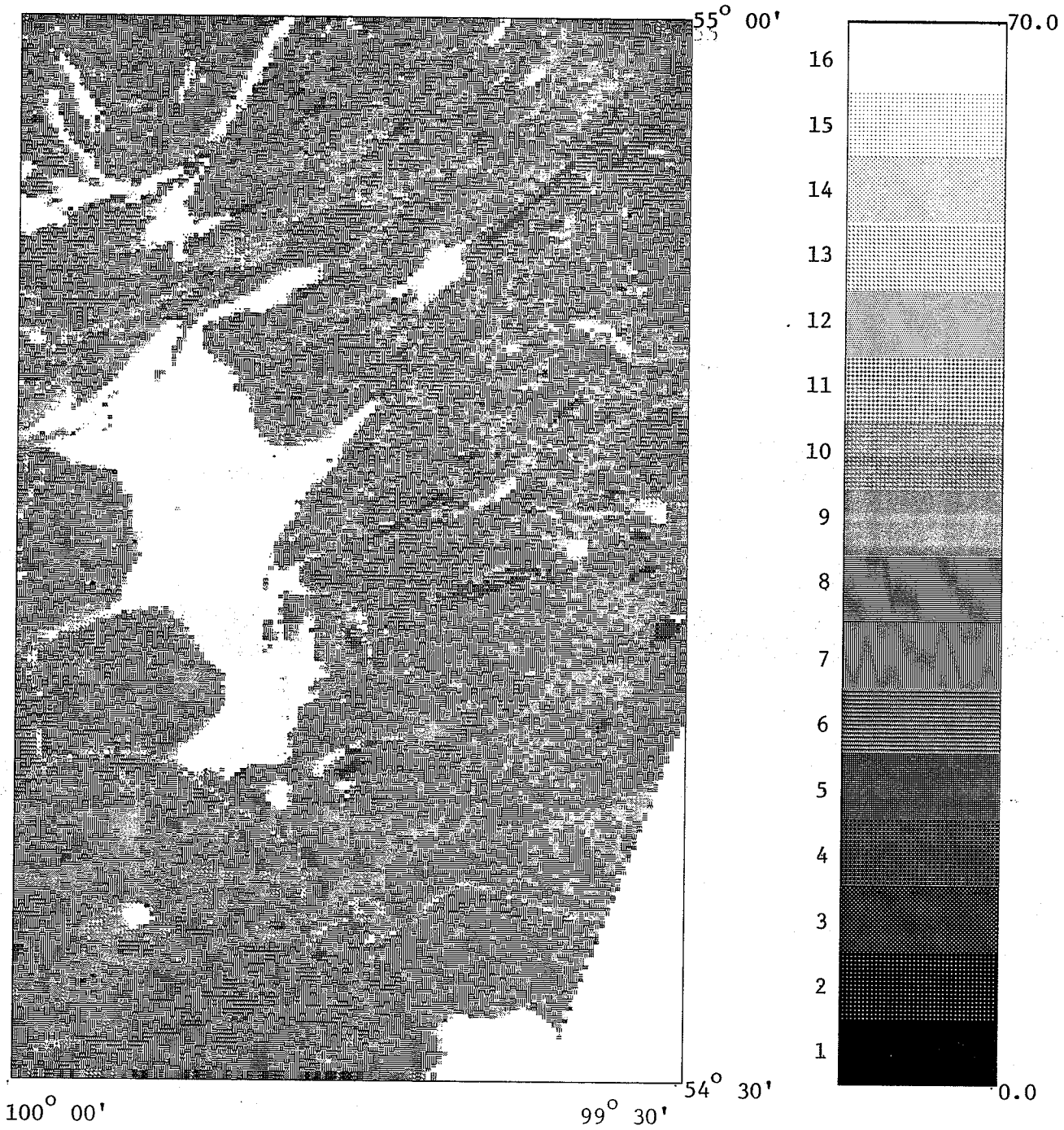


Figure 3.13 TM Band 3 image for Lake Wekusko test site

Distance = 55250 m (N-S), 32750 m (E-W)

Pixel size = 216 m (N-S), 257 m (E-W)

Grey scale bar is linear

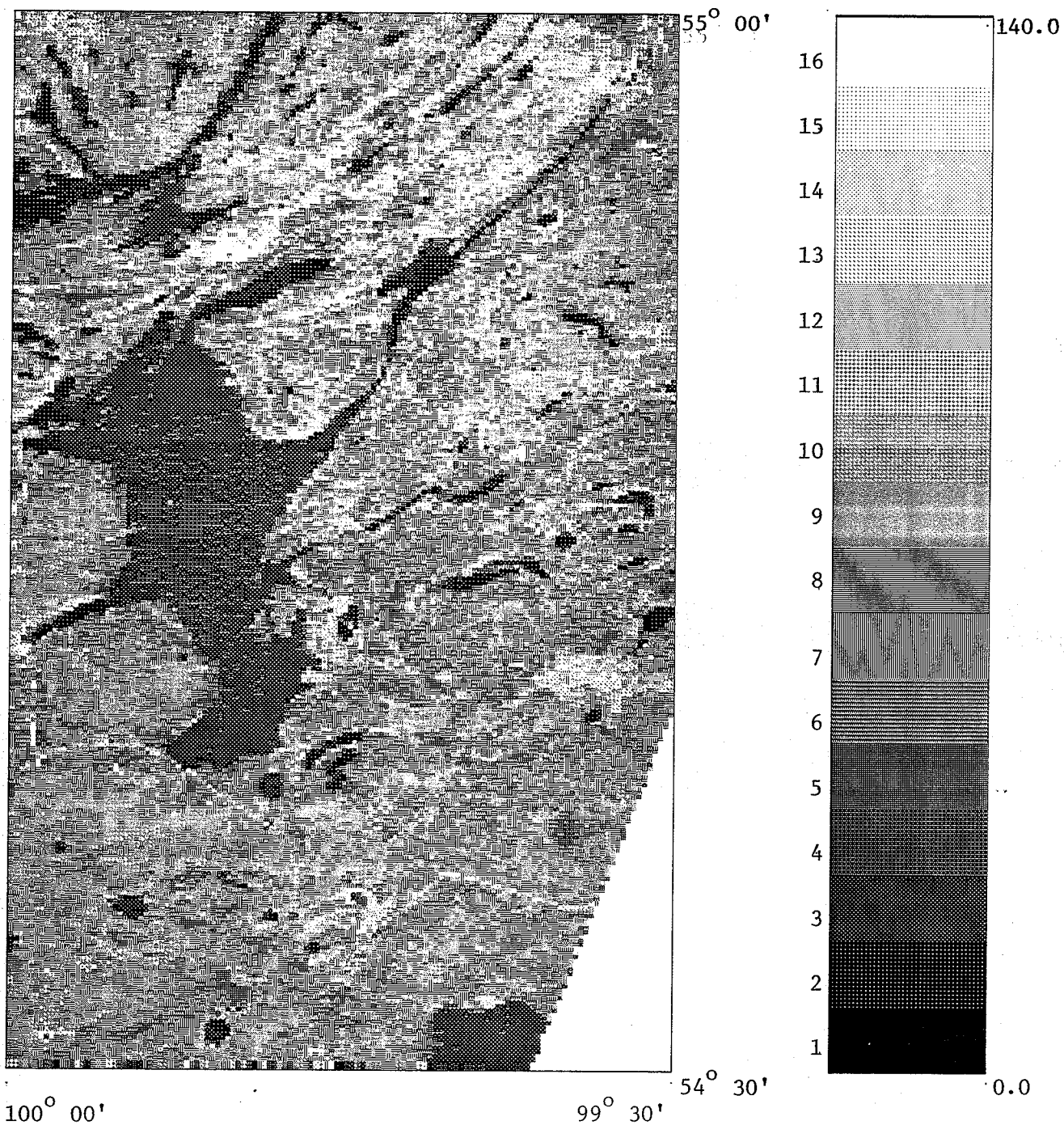


Figure 3.14 TM Band 5 image for Lake Wekusko test site

Distance = 55250 m (N-S), 32750 m (E-W)

Pixel size = 216 m (N-S), 257 m (E-W)

Grey scale bar is linear

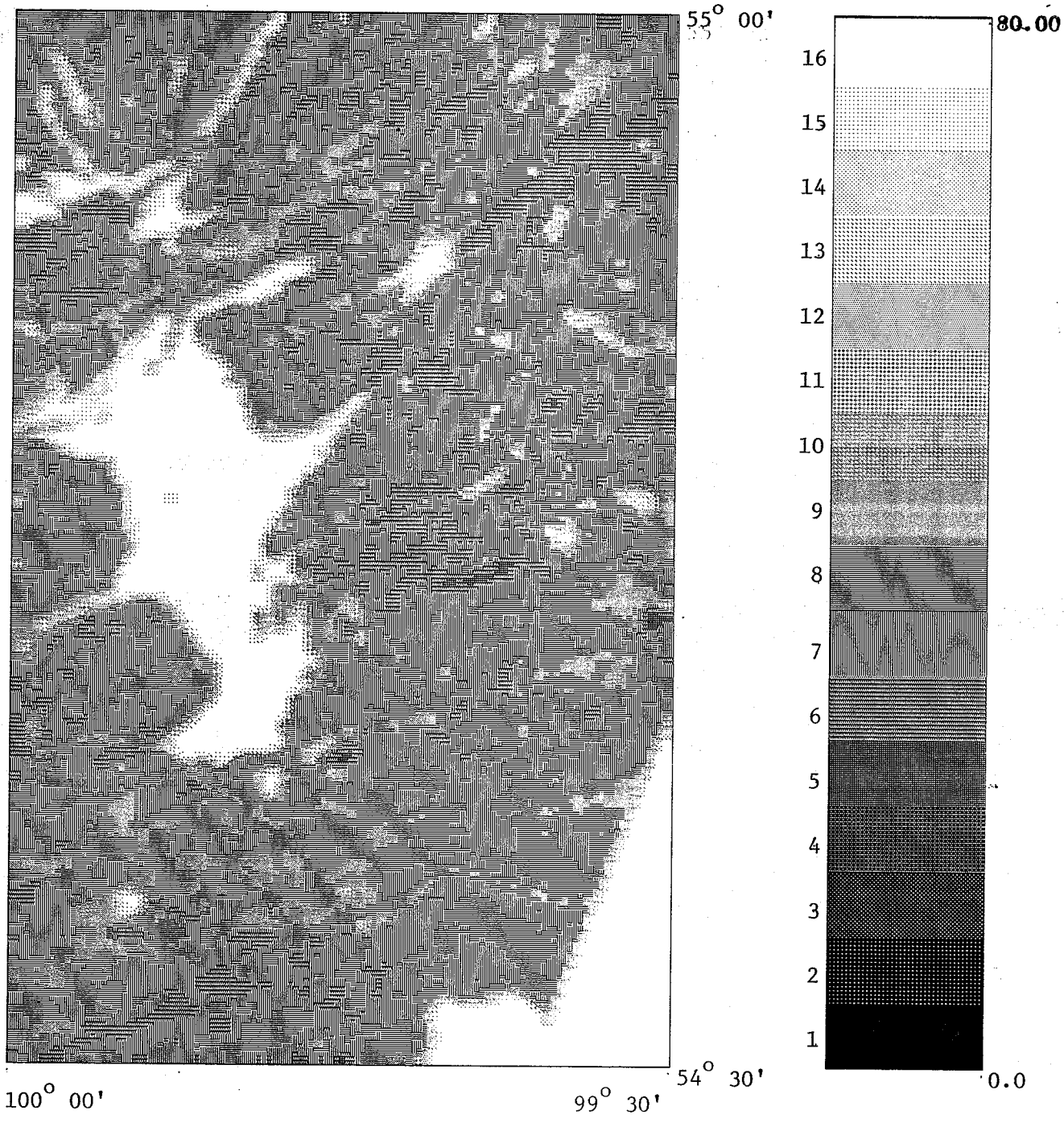


Figure 3.16 TM Band 3 image for Lake Wekusko test site (After filtering)

Distance = 55250 m (N-S), 32750 m (E-W)

Pixel size = 216 m (N-S), 257 m (E-W)

Grey scale bar is linear

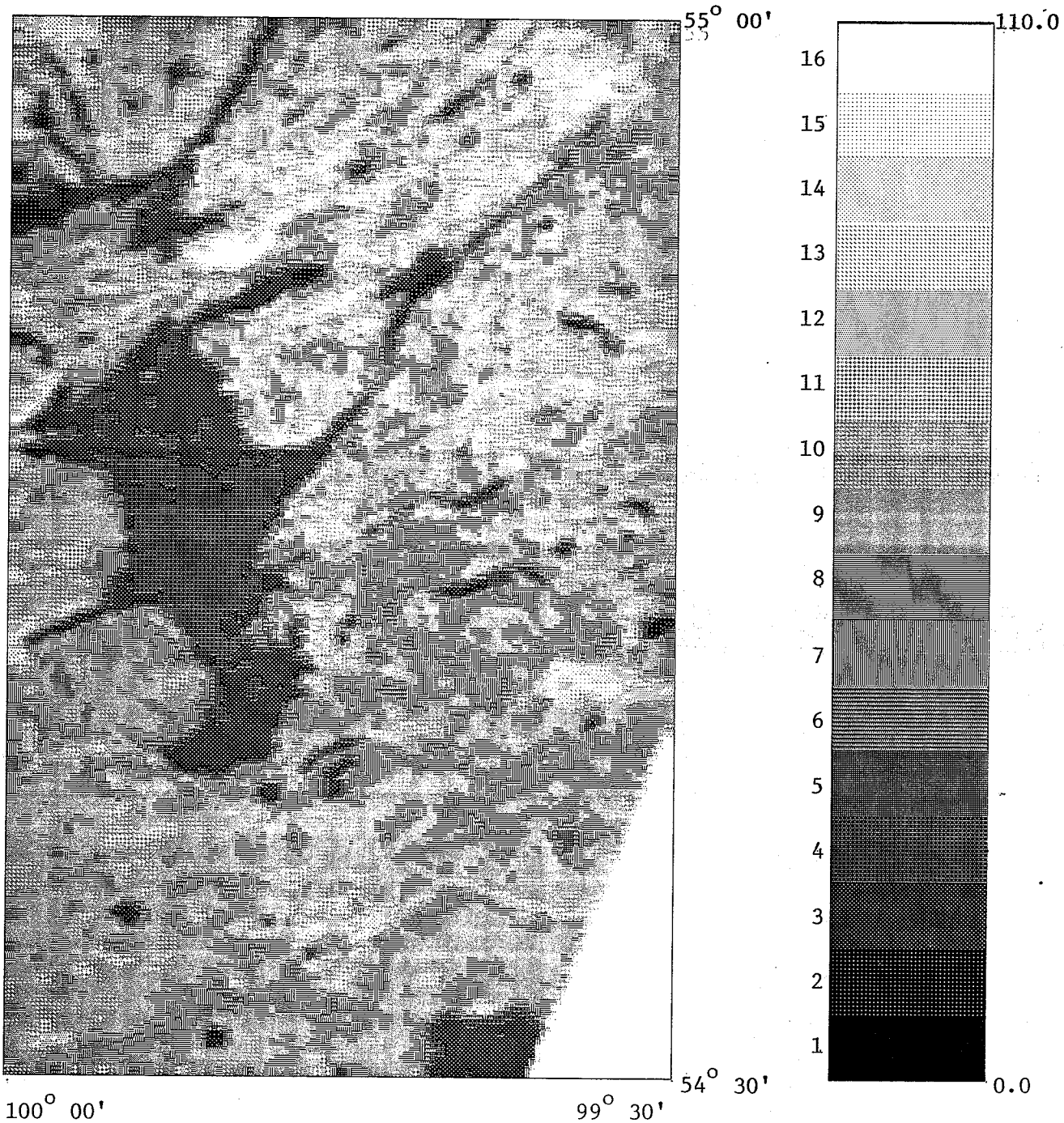


Figure 3.17 TM Band 5 image for Lake Wekusko test site (After filtering)

Distance = 55250 m (N-S), 32750 m (E-W)

Pixel size = 216 m (N-S), 257 m (E-W)

Grey scale bar is linear

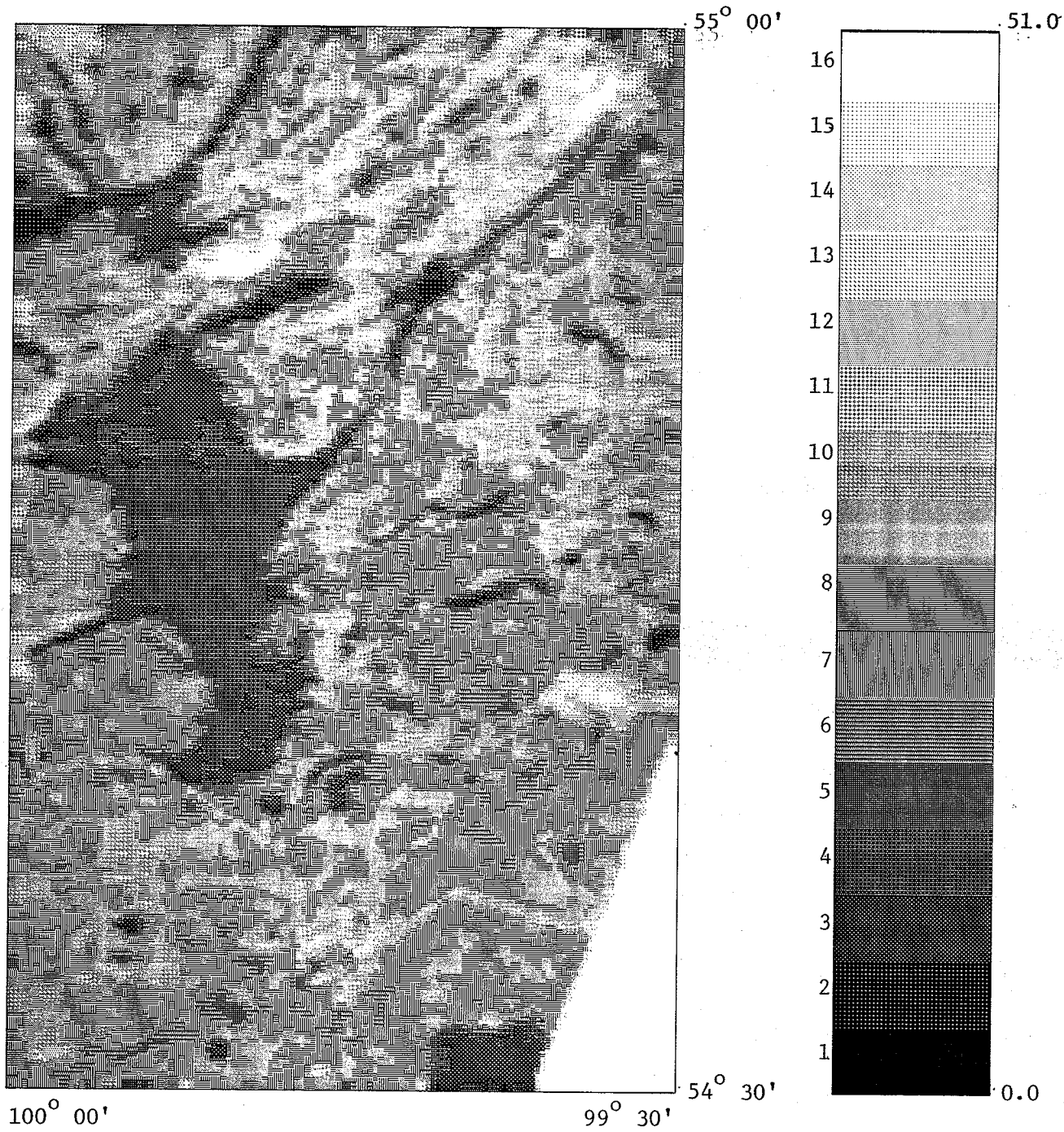


Figure 3.18 TM Band 7 image for Lake Wekusko test site (After filtering)

Distance = 55250 m (N-S), 32750 m (E-W)

Pixel size = 216 m (N-S), 257 m (E-W)

Grey scale bar is linear

CHAPTER 4

Methodology: Rationale

Earth science research commonly requires the integration of a number of layers of spatial information derived from different sources. Such information is commonly represented as two-dimensional maps and forms digital map layers. The ability to selectively and accurately combine digital information from two or more layers is advantageous in that an individual data layer usually does not contain all the necessary information for a full-fledged analysis. This approach of combining diverse data types has long been an essential activity of geological exploration programs. However, integration of digital spatial data has seen great advances in the past decade.

Traditionally, integration has been accomplished on an analog basis by overlaying maps and generating a composite that could be visually interpreted. Registration was achieved by aligning, as accurately as possible, features common to the base map. The errors involved in this technique were most frequently caused by,

among others, scale differences and operator errors. Moreover, spatial attributes could not be readily quantified and were at best visually estimated; mathematical manipulations and the ability to experiment with different possible combinations were extremely difficult.

With the advent of computer-aided digital analyses it became possible to store large maps in digital format. This also meant that a wide range of processing including scale transformation could be done with considerably improved accuracy and efficiency. Further, the computational facility enabled mathematically rigorous integration techniques to be developed. Sources of error such as, operator error, scale mismatch, etc. were significantly reduced. With increasing availability and refinement of computer graphics technology, Geographic Information Systems (GIS) came into being which is primarily intended for manipulating and displaying large volumes of geographically referenced data sets. It is this method of digitally combining different maps that has attracted wide attention in the past two decades. An overview of modern techniques in use is given in Agterberg (1989b).

The mathematical/statistical operations that can be performed on each data set are dependent upon the characteristics of the data, particularly on the level of measurement, viz: nominal, ordinal, interval or ratio (Stevens, 1946). Geological maps display data that are nominal in nature. The numerical values representing each rock type serve merely as symbols, without involving any implied ordering or distance measure. Hence, operations that do not assume any ordering or distance measure, such as frequency counts can be readily performed. In addition, the spatial distribution of the measures, information representation and integer operations can

be subjected to mathematical investigation (Moon, 1993).

In many studies utilizing remotely sensed data sets, the starting point for the study is some specific information; this information forms the foundation upon which the subsequent integration of data sets can be based. Empirical relations between lake sediment geochemistry and gold occurrences (Wright *et. al*, 1988), is an example of such information. In another study using a geobotanical approach, elements detected in spruce bark samples were correlated with gold occurrences (George and Bonham-Carter, 1989). Relating drainage patterns to potential planes of weakness allowed Goodacre *et. al* (1991) to map zones of seismic activity using spatial statistics. Similarly, ground based mapping provided details about regional structure and stratigraphy that were quantified and integrated with other data sets to locate new volcanogenic massive sulphide deposits (Reddy *et. al*, 1991).

In mineral exploration, the models for combining data layers may be based on formal rules such as in expert systems (Bolstad and Lillesand, 1992), or on simple Boolean and/or arithmetic combination using heuristic reasoning (Robinove, 1986). Heuristic models are particularly appropriate in areas where exploration is at an early stage or where known mineral occurrences provide an inadequate sample for statistical characterisation of the signatures associated with a particular mineral deposit. The process involves characterisation of the mineral deposit by means of a logical combination of features associated with that deposit (Agterberg, 1990). These features, termed prognostic indicators, can be expressed in terms of probabilities. In mineral exploration, spatial analysis is an essential requirement and the degree of association between the indicator and the mineral deposit is a

function of the proximity between the two.

The requirement for initial information is not restricted to geological investigations alone. Ecological remote sensing studies of avian habitats relied on a database of foraging characteristics and nesting habits compiled from field studies (Hodgson *et. al*, 1988). An integrated study aimed at habitat modeling of squirrels was based on a set of several ecological variables (Pereira and Itami, 1991).

In other studies, such as the present investigation, no specific starting information is available. Therefore, currently known methods of integration are not readily applicable. An alternative method must be developed so that the remotely sensed data sets can be integrated. Indeed, the result of such an integration can be treated as a starting point for further integration processes. The current study is based upon this premise.

Thus, this study addresses the fundamental question of how to integrate remotely sensed satellite and geophysical data without the need for an initial database acquired from field surveys. The method developed herein is ideally suited for completely unknown territories, both terrestrial and planetary. One factor that is common to all artificial intelligence based systems and the method developed in this study is the need for an expert. This is one need that cannot be dispensed with. An experienced analyst is required to visually interpret the remotely sensed data.

This research begins with the application of conventional digital image processing techniques to the Lake Wekusko test site, followed by the development of three types of integration methods: algebraic probability, spatial index and Bayesian approach. Figure 4.1 shows the general scheme of integration.

The first step of preprocessing includes standard techniques commonly employed in digital image analysis. For instance, satellite images are subject to geometric correction, removal of noise, seamless edge matching etc. Geophysical data may need reinterpolation to account for missing data points. In the present study, preprocessing also includes image enhancement by contrast stretching, and filtering to eliminate salt and pepper noise.

In the algebraic probability method no prior knowledge is available. A series of experimental cases are attempted and the results evaluated. As is shown later, features that are consistently mapped have a strong correspondence to the geology. Thus the algebraic probability method provides information which can be used as *a priori* input in the other two methods. Each successive step of integration increases the amount of information that can be derived from the data sets.

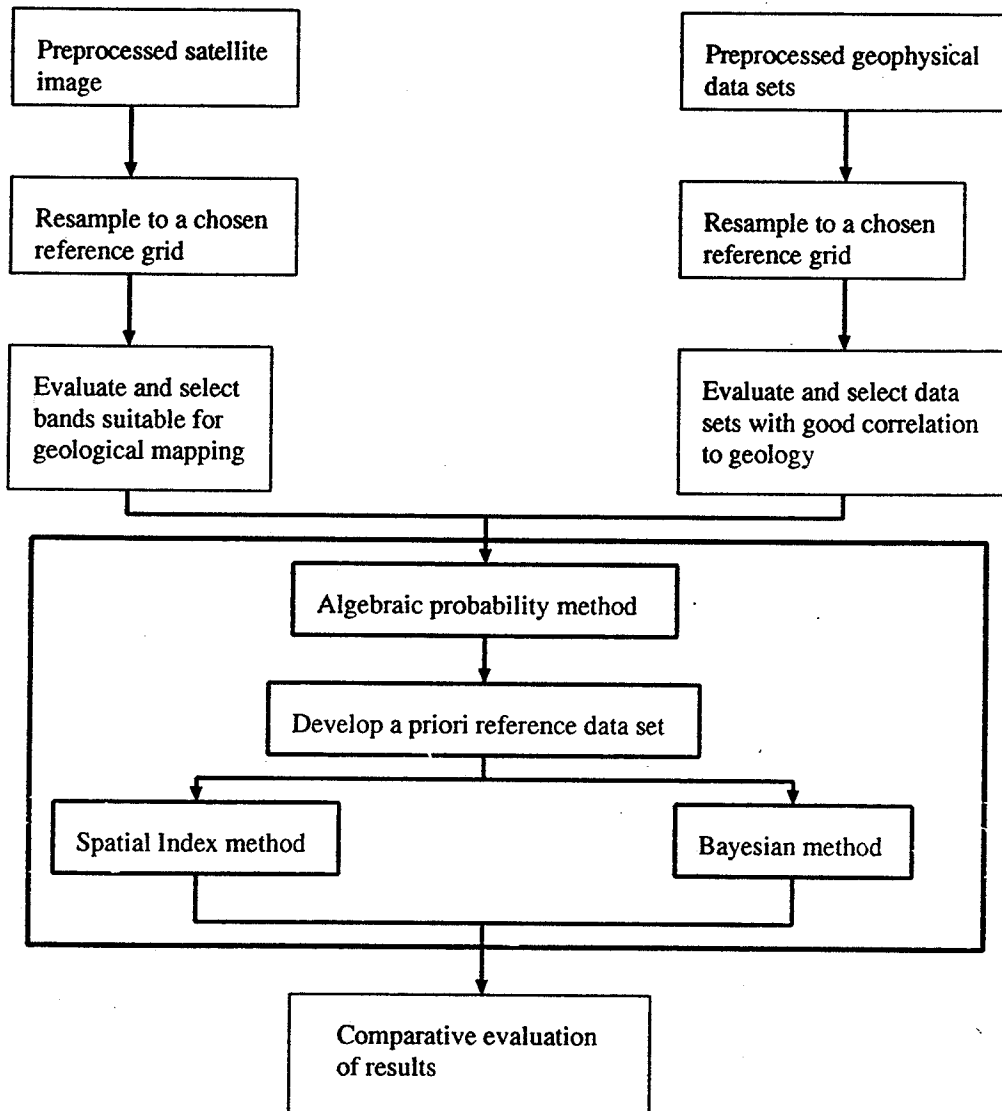


Figure 4.1 General scheme for data integration

CHAPTER 5

Digital Image Analysis of Lake Wekusko Test Site

5.1 Introduction

Availability of surface exposures and amount of differential relief are two factors, among many others, that affect the quality of the satellite image. In the case of the Lake Wekusko test site, the number and size of surface exposures are much greater than the Wabowden test site and there is also more differential relief. It is therefore reasonable to expect that conventional digital processing techniques (Jensen and Hodgson, 1986) applied to the satellite image data will prove useful in mapping the rock type distribution. On the other hand the Wabowden test site has a much lower density of surface outcrop exposures. Visual analysis of the MSS data for the Wabowden test site showed that digital image processing techniques would not produce useful results, and were therefore not done for the site.

In this chapter the results obtained from conventional digital processing of

satellite images are discussed. The satellite images were processed on the Dipix ARIES image analysis system.

After the satellite image has been geometrically corrected it can be further processed to extract the relevant information. The means by which satellite data are transformed into information are varied. The underlying premise in all of the methods is that each type of surface feature (rocks, vegetation, water bodies) has an unique spectral signature. It is this characteristic that can be used to identify the ground features either in individual or in composite images.

The first step in the analysis is generation of a false colour composite (FCC). In this method each one of three bands of the image is projected onto a viewing device through a filter which allows a specific colour to pass through. When projected onto a video imaging device, such as a cathode ray tube, each band is transmitted as a separate signal to each of the three guns. Each band is thus assigned a colour by projection through a red, green or blue gun. When the three projected images are exactly superimposed a FCC is generated. The FCC is advantageous because a wide range of colours can be displayed (256 colours in an 8 bit system) and because it seeks to mimic the natural colours of the ground surface, enabling ease of visual interpretation. Where appropriate, one of the three bands can be replaced by ancillary data such as digital elevation data or data from a different sensor. Since a FCC is generated only from three colours, a judicious selection of three bands must be made when more than three bands of data are available. Usually, three spectrally widely separated bands are used. Figure 5.1 is a FCC generated from TM Band 3, Band 5 and Band 7 data.

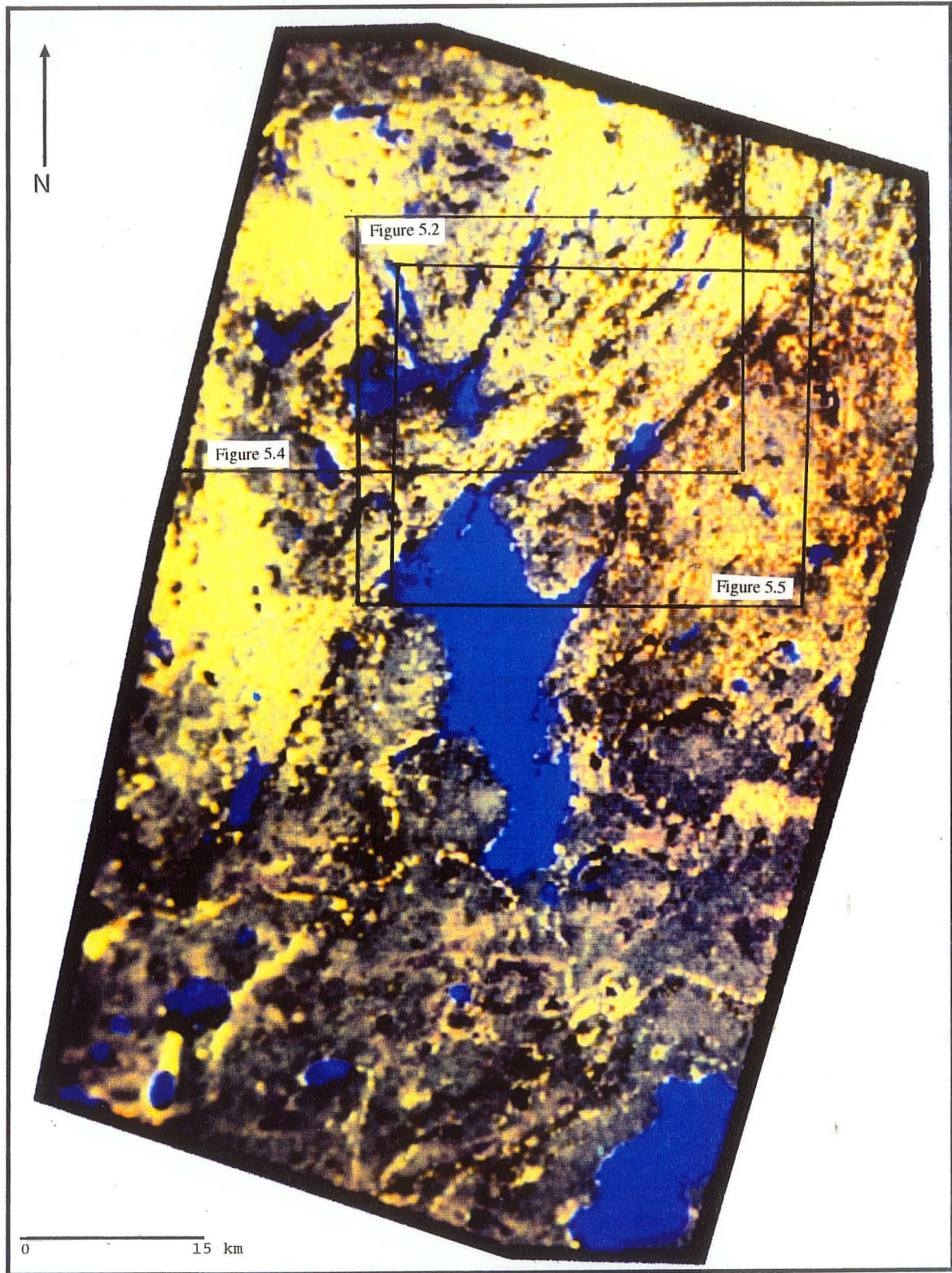


Figure 5.1 False colour composite from TM data of Lake Wekusko test site
 Band 7=red, Band 5=green, Band 3=blue
 Water bodies = blue; Proterozoic rocks = yellow; Paleozoic cover = greyish yellow
 Boxes show locations of Figures 5.2, 5.4 and 5.5

Sometimes it is advantageous to combine data from different sensors. For example, in the study of geological structures, radar data have proven to be very effective (Masuoka *et al.*, 1988). By replacing one band of satellite image with radar data a combined image can be obtained, such as shown in Figure 5.2(a) comprising C-SAR data, TM Band 7 and TM Band 5 for part of the Lake Wekusko area. Which band is replaced by the radar data, is a choice that is dictated by the quality of the three bands. In most cases a simple visual analysis is sufficient to make this decision.

Two of the most commonly used methods of information extraction are the Principal Component transform and multispectral classification techniques. These methods are based on image statistics which are computed from sample sites. When used for classification purposes, these are known as training sites because they are used to train the classification algorithm.

5.2 Training Area Signature Generation

Supervised classification techniques of satellite image processing for the identification of surface classes require some *a priori* knowledge of the occurrence of these classes. The term classes, refers to surface features on the ground such as lakes, rock types, water bodies etc. The known or reasonably known areas are used to train the classification algorithm. Training areas must be representative of the classes of interest and must be relatively homogenous. That is, the histogram of the training area should show unimodal spectral reflectance values. A multimodal histogram indicates that the training area contains more than one class and must be purified.

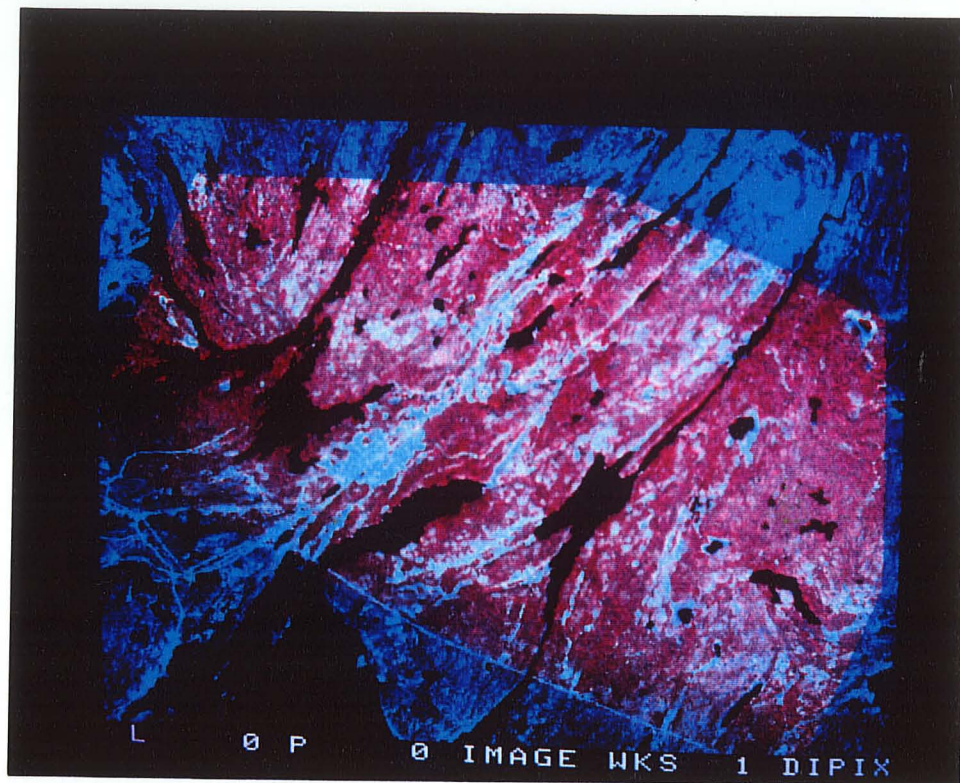


Figure 5.2(a) C-SAR data overlain on TM Band 7 and Band 5 (Part of Wekusko site)

C-SAR=red, Band 7=green, Band 5=blue

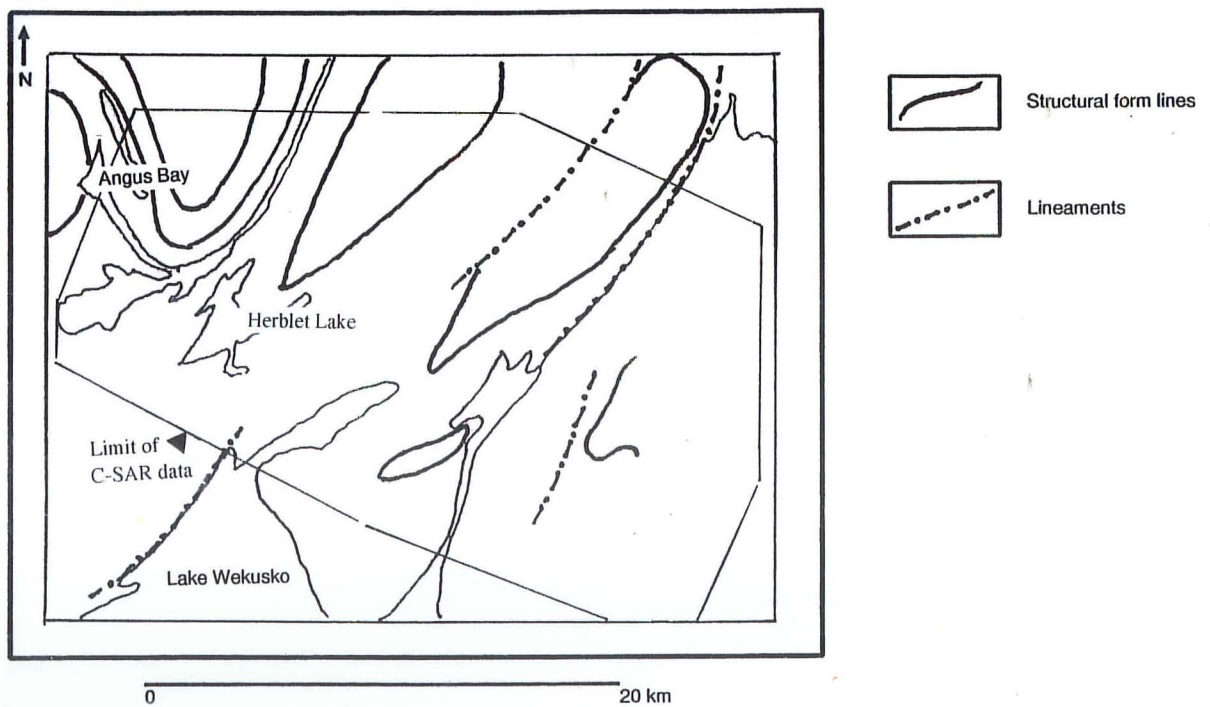


Figure 5.2(b) Preliminary interpretation based on visual inspection of (a)

In addition, each training area is generally composed of many pixels. An empirical rule is to have at least 10 N pixels per area, where N is the number of bands to be used in the classification process (Swain and Davis, 1978). The spectral reflectance values of all pixels in each training area are used to calculate important statistical parameters such as mean, standard deviation, variance, variance-covariance matrix, and correlation matrix. These represent fundamental information on the spectral characteristics of the classes.

Training statistics can also be used to assess the separability of different classes. There are many methods to achieve this such as calculation of auto-correlation distance, divergence (Jensen, 1986), Bhattacharyya distance (Haralick and Fu, 1983), also known as Jeffries-Matusita (JM) distance (Richards, 1986), and transformed divergence (Swain and Davis, 1978). In this study the auto-correlation distance method was used to determine the inter-signature spectral distance.

If p_1 and p_2 are the Gaussian probability distribution of Class 1 and Class 2 obtained from the corresponding training areas, the autocorrelation distance measure between these two classes is given by

$$D_{1,2} = -\log \int \sqrt{p_1 p_2}. \quad (5.1)$$

In this case a value of ≈ 2.0 implies a 10% correlation between the two classes and a value of ≈ 0.0 implies a 100% correlation. Thus larger values indicate more easily separable classes and lower values show that the two classes are spectrally close to each other. In the latter case the analyst may decide to refine the training areas to eliminate contaminating pixels and increase separability.

Univariate and multivariate statistics from the training area were used in the computation of principal component transforms and for classification of the SPOT image using a maximum likelihood classification algorithm.

5.3 Principal Component Transform

The Principal Component Transform, also known as Karhunen–Loève Transform, uses the vector nature of the image to derive a transformed image that makes features, not recognisable in the original data, clearly recognisable in the transformed image and also helps to preserve the essential information content of the image, while reducing its dimensionality. The transformation is applied to a correlated set of data and results in an uncorrelated set that has certain ordered variance properties.

Given a set of data points $x_1, x_2, x_3, \dots, x_n$ the mean is given by (Richards, 1986)

$$m = \frac{1}{n} \sum_{j=1}^n x_j. \quad (5.2)$$

The covariance can be expressed as (Richards, 1986)

$$\Sigma_x = \frac{1}{n-1} \sum_{j=1}^n (x_j - m)(x_j - m)^t, \quad (5.3)$$

where t denotes vector transport.

In order to find the eigenvalues the equation used is (Richards, 1986)

$$[\Sigma_x - \lambda I] = 0, \quad (5.4)$$

where I is an identity matrix.

Solving for λ , the eigenvalue, we obtain n values $\lambda_1, \lambda_2, \lambda_3, \dots, \lambda_k$ (for a k -dimensional data set) in the x component. Similarly in the y -coordinate system the covariance matrix can also be computed.

In the case of a two dimensional data set, the eigenvalues λ_1 and λ_2 are used to compute the eigenvectors e_1 and e_2 where e_1 and e_2 are mutually orthogonal vectors describing the orientation of the new coordinate axes (i.e. PCT1 and PCT2) along which the dimensionality of the data is significantly reduced because most of the information content is along the direction of the first principal component transform (Figure 5.3). The original data are then projected onto the orthogonal principal component axes.

Thus calculation of the PCT involves the following steps (Richards, 1986):

- i) Assembling a covariance matrix,
- ii) Determining eigenvalues and eigenvectors, and
- iii) Calculating the new pixel values along the components.

The newly derived transformed data points can be treated as an entirely new, artificially generated band ('neo-channel'), which can be subjected to further processing such as classification or can be used for direct interpretation.

The dimensionality of the input is limited by the availability of computational resources. In the case of the output data, even though more than three components can be generated, the first two usually account for about 95% of the variance. The third, fourth, fifth and so on, components contain monotonically decreasing amounts of the variance and consequently are seldom computed.

PCT analyses enable the estimation of the amount of total variance accounted

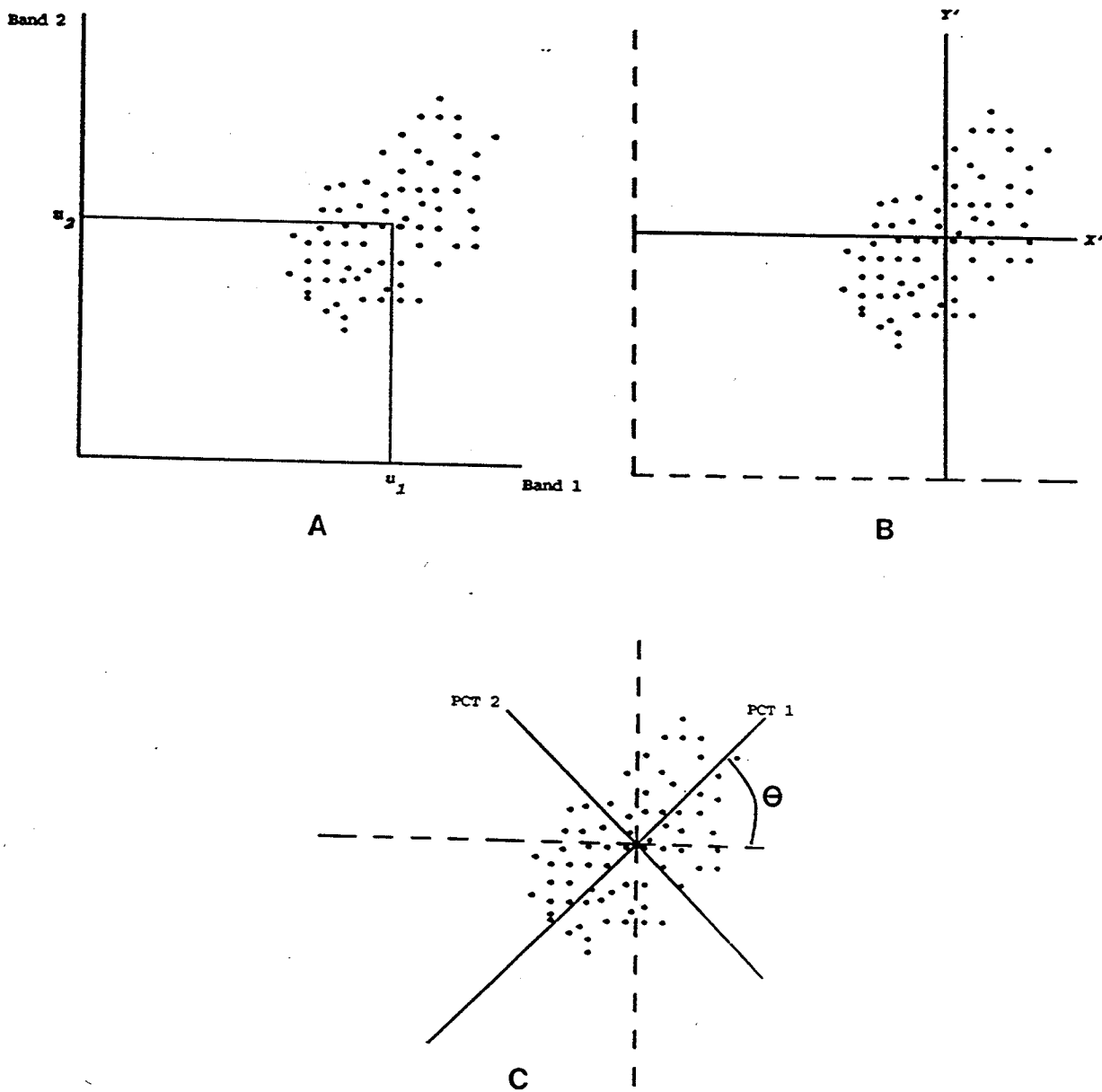


Figure 5.3 Schematic diagram of PCT axes for two band data

(A) original data from two bands with means μ_1 and μ_2 ; (B) shifted co-ordinate axes; (C) axes rotated by angle θ so that maximum variance is along PCT1

for by each of the principal components by using the relation (Jensen, 1986):

$$\% \text{contribution} = \frac{\lambda_p \times 100}{\sum_{p=1}^k \lambda_p}, \quad (5.5)$$

where p is the p th component of a total of k components.

The eigenvector can also be used to assess how much each band of data is associated with each principal component. This parameter termed 'factor loading' is computed as (Jensen, 1986):

$$R_{\beta p} = \frac{e_{\beta p} \times \sqrt{\lambda_p}}{\sqrt{\text{Var}_{\beta}}}, \quad (5.6)$$

where,

$e_{\beta p}$ is the eigenvector for band β and component p ,

λ_p is the eigenvalue of the p th component, and

Var_{β} is the variance of band β in the covariance matrix.

The statistical parameters in the computation of the PCT for TM data of the Lake Wekusko test site are shown in Table 5.1. Band 7 and 5 are highly correlated and they have the highest factor loading with PCT 1. The false colour composite from these three PCTs is shown in Figure 5.4.

5.4 Maximum Likelihood Classification

Maximum likelihood classification is the most commonly used method for remotely sensed satellite data. This method, based on Bayesian probability, is described in this section.

Let us assume that there are M classes (or ground surface features) to be identified denoted as ω_i , where $i = 1, 2, \dots, M$ and \vec{x} is a column vector of brightness

Univariate Statistics			
Band	7	5	3
Mean	62.24	112.87	54.35
Standard Deviation	8.85	12.26	10.80

Multivariate Statistics			
Correlation Matrix			
Band	7	5	3
Band 7	1.000		
Band 5	0.956	1.000	
Band 3	0.736	0.688	1.000
Covariance Matrix			
Band 7	78.247		
Band 5	103.739	150.383	
Band 3	70.334	91.140	116.586
Principal Components	1	2	3
Eigen Values	297.37	43.747	4.096
Percent Contribution	86.141	12.672	1.186
Eigenvectors			
Band 7	1.512	1.678	1.073
Band 5	5.303	0.770	-5.577
Band 3	5.058	-7.714	2.965
Factor Loadings			
Band 7	2.947	1.254	0.245
Band 5	7.457	0.415	-0.920
Band 3	8.078	-4.725	0.555

Table 5.1 Statistics of Principal component transform for TM data of

Lake Wekusko test site

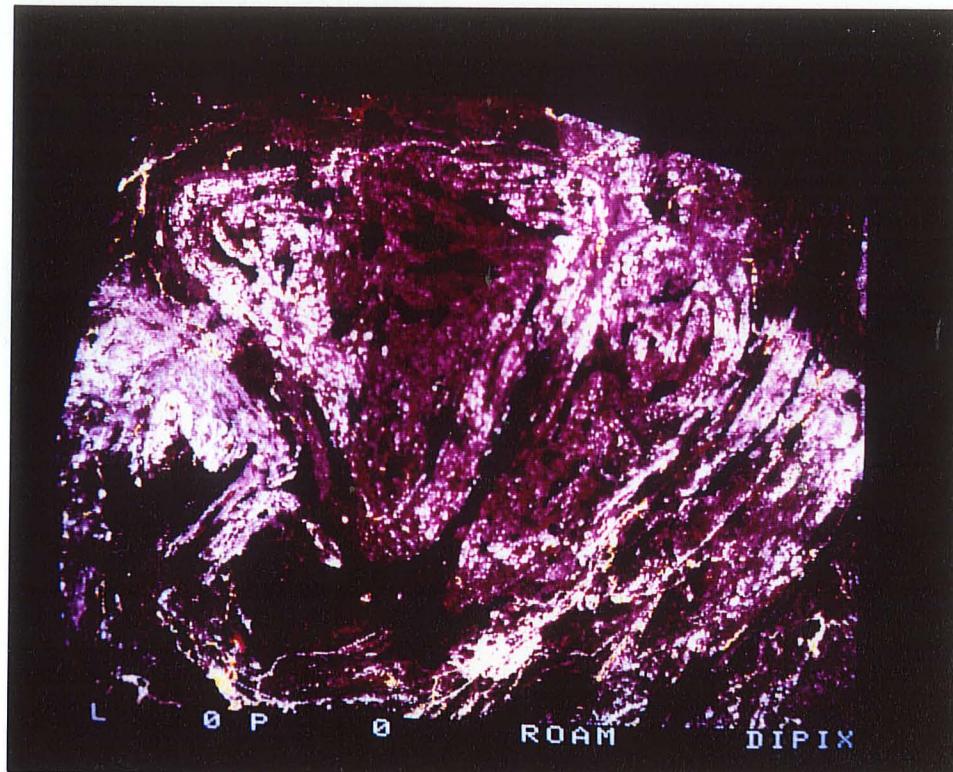


Figure 5.4(a) FCC of part of Lake Wekusko site from PCT images of TM data

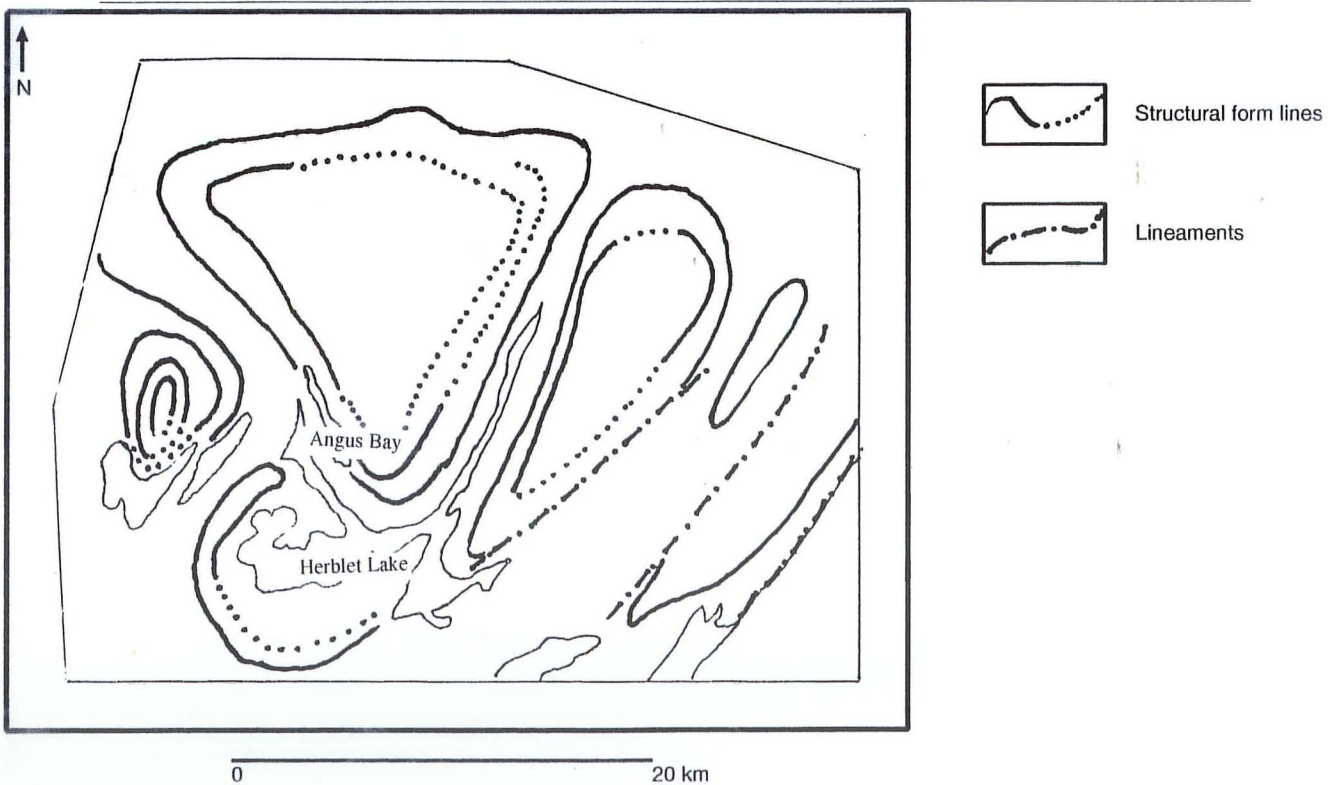


Figure 5.4(b) Visual interpretation of (a)

values for a pixel in all bands under consideration. It is now required to compute the conditional probability $p(\omega_i|\vec{x})$, i.e. the likelihood that the ω_i is the correct class for the pixel at position \vec{x} in multispectral space. From the training data we can estimate a Gaussian probability distribution that describes the likelihood of finding a pixel from class ω_1 at the position \vec{x} ; i.e. we can estimate $p(\vec{x}|\omega_i)$ according to: (Richards, 1986)

$$p(\vec{x}|\omega_i) = (2\pi)^{-\frac{1}{2}} \sigma_i^{-1} \exp\left(-\frac{1}{2}(\vec{x} - \vec{m}_i)^2 / \sigma_i^2\right), \quad (5.7)$$

where

σ_i is the standard deviation of the class ω_i ,

σ_i^2 is the variance of the class ω_i ,

\vec{m}_i is the mean vector of the pixels in that class ω_i , and

\vec{x} is the vector of pixel values.

The known quantity $p(\vec{x}|\omega_i)$ and the unknown quantity $p(\omega_i|\vec{x})$ are related by Baye's theorem as follows: (Richards, 1986)

$$p(\omega_i|\vec{x}) = \frac{p(\vec{x}|\omega_i) p(\omega_i)}{p(\vec{x})}. \quad (5.8)$$

The quantity $p(\omega_i)$ is the *prior probability*, which may be known or can be assessed by the analyst based on the knowledge of the image. Alternatively it can be assigned an equal value for all possible classes. The quantity $p(\vec{x})$ is the probability of finding a pixel from any class at location \vec{x} . The classification rule is (Richards, 1986)

$$\vec{x} \in \omega_i \quad \text{if} \quad \frac{p(\vec{x}|\omega_i) p(\omega_i)}{p(\vec{x})} > \frac{p(\vec{x}|\omega_j) p(\omega_j)}{p(\vec{x})} \quad \text{for all } i \neq j. \quad (5.9)$$

Thus the pixel is assigned to that class with which its associated probability is the highest. In other words the probability indicates the maximum likelihood of the pixel being associated with that class.

The maximum likelihood classification was carried out on the SPOT data using training areas for seven classes. SPOT data were used to take advantage of its finer resolution (20 m) as compared to TM data (30 m). The seven classes were selected on the basis of visual comparison with the geological map. For each rock type, groups of pixels were selected whose location coincided approximately with location of the rock types as shown on the map. To average out the variations in spectral reflectance, the sample sites were as widely separated as possible.

The signature statistics of the seven classes are shown in Table 5.2 and auto-correlation distance measures are shown in Table 5.3. The statistical calculations are used to confirm that representative homogeneous samples were selected for each class. This is shown by the low standard deviation for each class in all three bands. However, for water bodies the sample shows a high standard deviation in the infrared region (SPT3). This is unusual because water has uniformly low reflectance in the infrared region. The discrepancy is due to a dominant specular reflection that occurs over a large part of Lake Wekusko. It is not advisable to avoid taking samples from this part, since classification errors may ensue. Information from the interclass distance table (Table 5.3) indicates which classes are separable in spectral space. For example, comparing Class 7 with the rest shows that it can be easily differentiated from Class 2 (4.342) and is least separable from Class 3 (1.546) The result of the maximum likelihood classification is shown in Figure 5.5.

Class 1: Granite-granodiorite; a priori probability = 0.20

Univariate Statistics			
Band	SPT1	SPT2	SPT3
Mean	42.75	28.33	42.09
Standard Deviation	3.47	3.32	3.89

Multivariate Statistics			
Correlation Matrix			
Band	SPT1	SPT2	SPT3
SPT1	1.000		
SPT2	0.858	1.000	
SPT3	-0.282	-0.136	1.000

Covariance Matrix			
	SPT1	SPT2	SPT3
SPT1	12.075		
SPT2	9.904	11.037	
SPT3	-3.813	-1.753	15.123

Table 5.2 Statistics of training area for class = granite-granodiorite (SPOT data)

Class 2: Quartz diorite; a priori probability = 0.05

Univariate Statistics			
Band	SPT1	SPT2	SPT3
Mean	37.11	22.37	37.76
Standard Deviation	1.54	1.55	2.80

Multivariate Statistics			
Correlation Matrix			
Band	SPT1	SPT2	SPT3
SPT1	1.000		
SPT2	0.717	1.000	
SPT3	0.543	0.342	1.000

Covariance Matrix			
	SPT1	SPT2	SPT3
SPT1	2.370		
SPT2	1.713	2.411	
SPT3	2.344	1.490	7.867

Table 5.2 (Contd.) Statistics of training area for class = quartz diorite (SPOT data)

Class 3: Snow Group rocks; a priori probability = 0.20

Univariate Statistics			
Band	SPT1	SPT2	SPT3
Mean	37.64	22.99	33.21
Standard Deviation	2.18	2.42	6.99

Multivariate Statistics			
Correlation Matrix			
Band	SPT1	SPT2	SPT3
SPT1	1.000		
SPT2	0.756	1.000	
SPT3	0.621	0.323	1.000

Covariance Matrix			
	SPT1	SPT2	SPT3
SPT1	4.733		
SPT2	3.972	5.836	
SPT3	9.444	5.457	48.877

Table 5.2 (Contd.) Statistics of training area for class = Snow Group (SPOT data)

Class 4: Missi Group volcanic rocks; a priori probability = 0.10

Univariate Statistics			
Band	SPT1	SPT2	SPT3
Mean	38.51	23.48	36.79
Standard Deviation	2.60	2.72	4.50

Multivariate Statistics			
Correlation Matrix			
Band	SPT1	SPT2	SPT3
SPT1	1.000		
SPT2	0.816	1.000	
SPT3	0.484	0.281	1.000

Covariance Matrix			
	SPT1	SPT2	SPT3
SPT1	6.748		
SPT2	5.772	7.414	
SPT3	5.655	3.446	20.264

Table 5.2 (Contd.) Statistics of training area for class = volcanics (SPOT data)

Class 5: Missi Group greywacke; a priori probability = 0.20

Univariate Statistics			
Band	SPT1	SPT2	SPT3
Mean	37.37	22.73	35.90
Standard Deviation	1.73	1.86	3.71

Multivariate Statistics			
Correlation Matrix			
Band	SPT1	SPT2	SPT3
SPT1	1.000		
SPT2	0.696	1.000	
SPT3	0.432	0.246	1.000

Covariance Matrix			
	SPT1	SPT2	SPT3
SPT1	2.986		
SPT2	2.234	3.448	
SPT3	2.770	1.694	13.762

Table 5.2 (Contd.) Statistics of training area for class = greywacke (SPOT data)

Class 6: Amisk Group rocks; a priori probability = 0.20

Univariate Statistics			
Band	SPT1	SPT2	SPT3
Mean	38.64	23.13	37.37
Standard Deviation	1.97	2.54	3.30

Multivariate Statistics			
Correlation Matrix			
Band	SPT1	SPT2	SPT3
SPT1	1.000		
SPT2	0.822	1.000	
SPT3	0.734	0.662	1.000
Covariance Matrix			
SPT1	3.890		
SPT2	4.120	6.454	
SPT3	4.774	5.546	10.883

Table 5.2 (Contd.) Statistics of training area for class = Amisk Group (SPOT data)

Class 7: Water bodies; a priori probability = 0.05

Univariate Statistics			
Band	SPT1	SPT2	SPT3
Mean	36.49	22.86	19.08
Standard Deviation	9.13	10.23	15.47

Multivariate Statistics			
Correlation Matrix			
Band	SPT1	SPT2	SPT3
SPT1	1.000		
SPT2	0.981	1.000	
SPT3	0.907	0.893	1.000

Covariance Matrix			
SPT1	SPT2	SPT3	
83.385			
91.588	104.553		
128.175	141.270	239.263	

Table 5.2 (Contd.) Statistics of training area for class = water (SPOT data)

INTERCLASS DISTANCE FOR 7 CLASSES OF SPOT DATA

Class	1	2	3	4	5	6	7
1	0.000						
2	2.156	0.000					
3	1.626	0.668	0.000				
4	1.110	0.393	0.169	0.000			
5	2.046	0.184	0.228	0.130	0.000		
6	1.340	0.516	0.411	0.161	0.270	0.000	
7	2.352	4.342	1.546	2.450	3.028	3.597	0.000

Correlation levels: 2.0 ~ 10%, 1.0 ~ 30%, 0.5 ~ 50%, 0.0 ~ 100%

Class 1: granite-granodiorite; Class 2: quartz diorite; Class 3: Snow Group rocks; Class 4: Missi Group volcanic rocks; Class 5: Missi Group greywacke; Class 6: Amisk Group rocks; Class 7: water bodies

Table 5.3 Interclass distance measures of the seven classes (SPOT data)

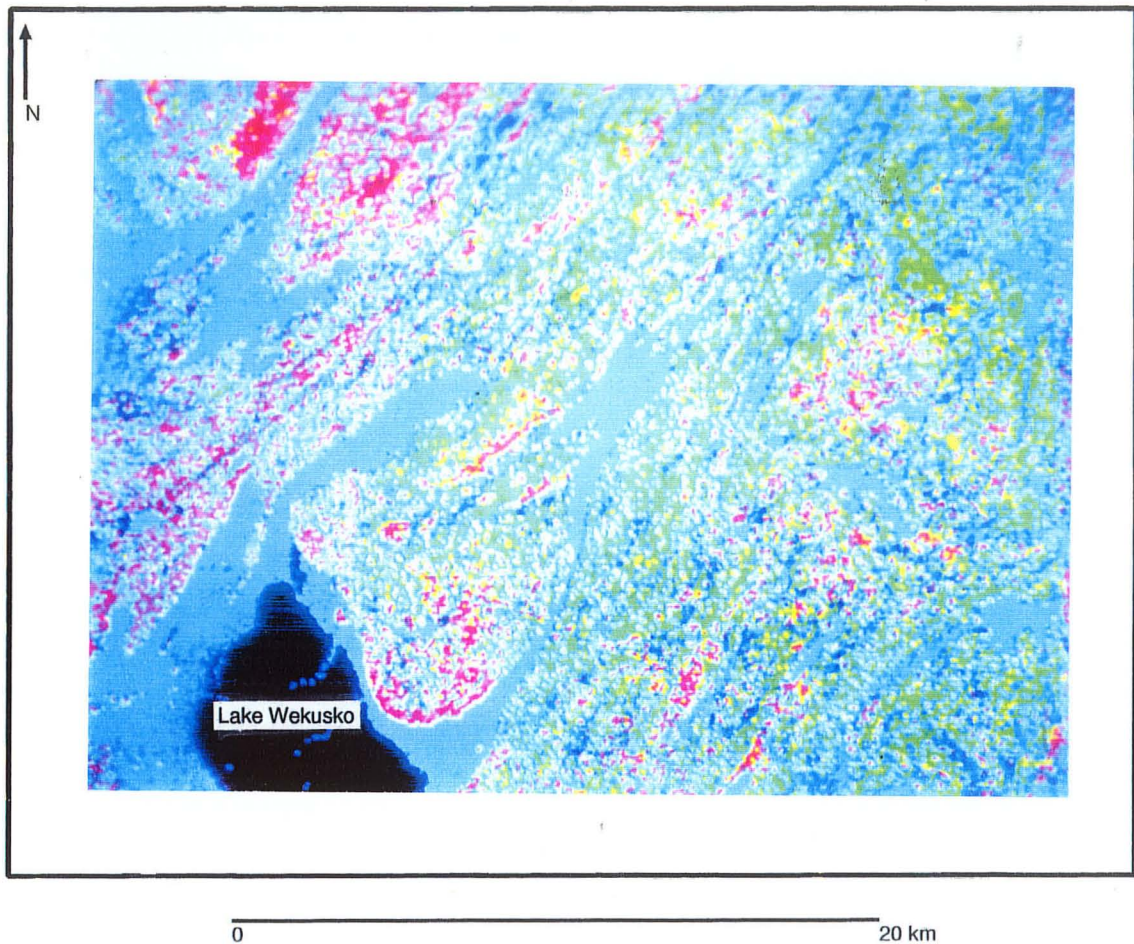


Figure 5.5 Result of Maximum likelihood classification of SPOT data
for Lake Wekusko test site (Compare with Figure 5.6)

Red = granite-granodiorite; yellow = quartz diorite; orange =
Snow Group; green = Missi Group volcanic rocks; dark-blue = Miss
Group greywacke; pink = Amisk Group; light-blue = water bodies

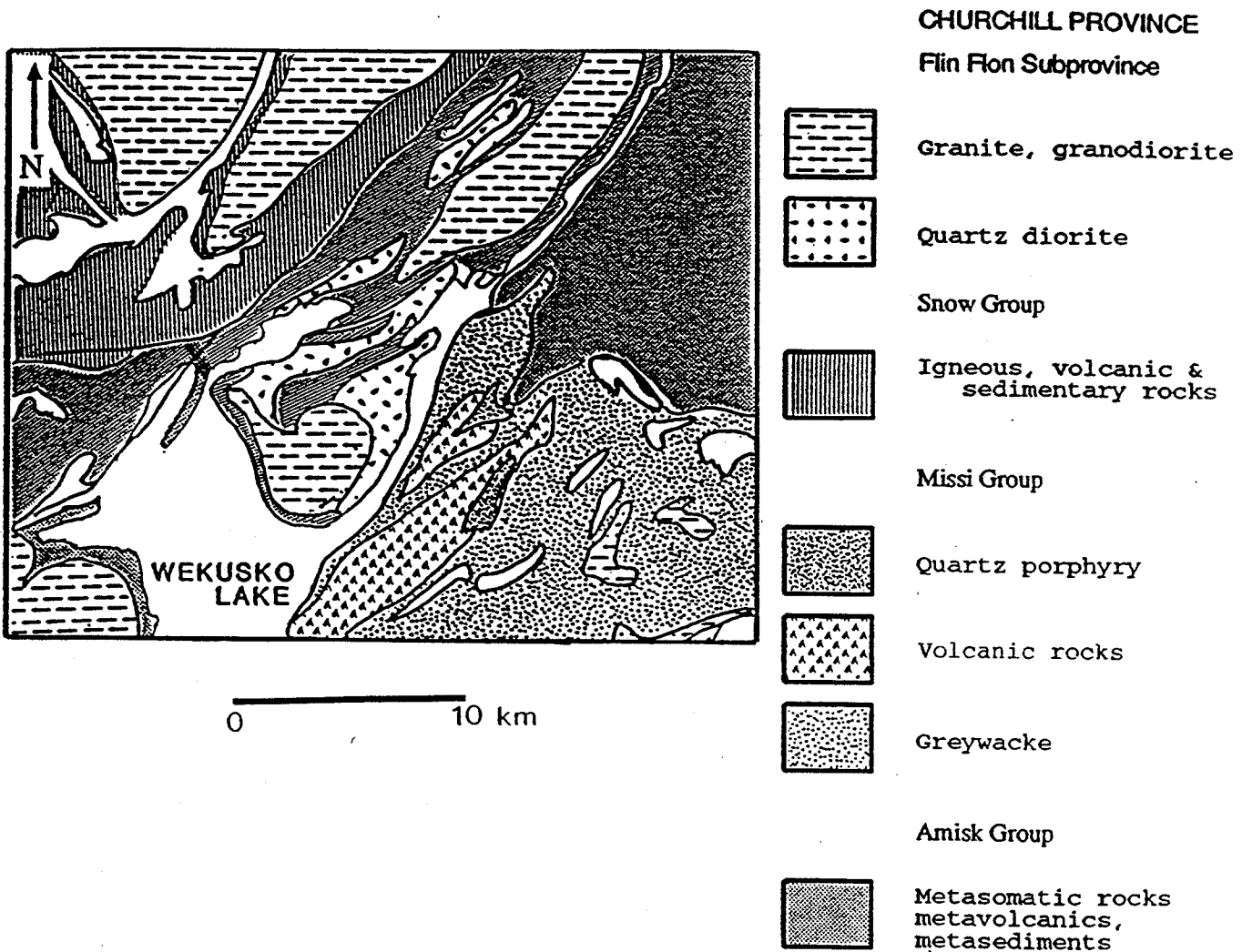


Figure 5.6 Geology of area corresponding to Figure 5.5

Compiled after Bell, 1978; Gordon et al., 1990

5.5 Interpretation of Images

The FCC shown in Figure 5.1 was generated from TM bands 3, 5 and 7. Of the three, Band 7 which covers the mid-infrared (2.08 - 2.35 μm) is considered to be "an important band for the discrimination of geologic rock formations" (Jensen, 1986, p. 34). Band 3 (0.63 - 0.69 μm) although ideally suited for vegetation discrimination is also useful for soil and geological boundary delineation. Band 5 (1.55 - 1.75 μm) is applicable to hydrological studies (Jensen, 1986) and aids in the detection of lineaments since surface water tends to flow along these planes of weakness.

The FCC shows, albeit to a limited extent, some of the geological formations in the northern part of the image. In the absence of digital enhancement the amount of detail observed in this image is limited.

On the other hand, the combined C-SAR and TM image (Figure 5.2(a)) reveals more of the structural features. As shown in Figure 5.2(b), the outlines of the structures can be easily delineated. Also some of the lineaments are clearly recognized.

Perhaps the most useful information on the complexity of folds in the northernmost part of the image is better seen in the PCT image (Figure 5.4(a)), than in the FCC generated from the original TM bands (Figure 5.1). The main reason for this is that the sample areas used in the generation of the image statistics contained a significant portion of pixels from this region. In other words information contained along the first two PCT axes has a very strong geological component. The form lines of the folded structure are clearly identifiable (Figure 5.4(b)).

The Maximum Likelihood Classifier (Figure 5.5) was performed by generating

training area signatures from known locations of various rock types as derived from the geology map (Figure 5.6). It is therefore an attempt to obtain an updated map of the distribution of rock types from the three SPOT bands. Given the spatial resolution of 10 m of SPOT data, this data are well suited for this purpose. As shown in Table 5.3 the interclass distance for granite-granodiorite (Class 1) with respect to the other classes is consistently high. This implies that this class is readily separable from the rest. Some parts of this class are very well delineated. Although it does not appear as a continuous homogeneous cluster, the overall spatial distribution of the class is evident. Class 2 (quartz diorite), however, has a very low separability and is poorly mapped. Class 3 (Snow Group) is barely visible. Class 4 (Missi Group volcanic rocks) is well mapped in the area to the east of Lake Wekusko. It also appears as widely scattered pockets in the eastern part of the area. Class 5 (Missi Group greywacke) cannot be clearly seen. Class 6 (Amisk Group) can be seen occurring sporadically in the eastern part of the area, intermingling with the Missi Group volcanic rocks (Class 5).

The results presented here show that conventional digital processing techniques are an useful tool in lithological discrimination. However, as has been demonstrated by numerous other studies (e.g. Hook, 1985; Kowalik and Glenn, 1987), incorporating ancillary data maximises the information extraction process. Others have investigated the incorporation of ancillary data in the classification process (e.g. Strahler *et al.*, 1976, 1980). The current research, as discussed earlier, focuses on the integration of different remotely sensed data using probability theory for the purpose of mapping a geological feature, which comprises the target proposition.

CHAPTER 6

Algebraic Probability Method: Development and Validation

6.1 Algebraic Probability Method

The Wabowden test site lacks extensive surface outcrop exposures. Thus geological maps for this area are poorly constrained with rock unit boundaries based on inference and extrapolation. In this sense the test site can be considered as analogous to unexplored terrain. It is ideal for the development of the method.

To validate the method, it is necessary to test it on an area where the geological control is more reliable. The Lake Wekusko test site offers such control and is used for validating the method.

It is well known that geophysical and satellite data can provide information about the geology of an area. Each data set records a physical property of the rocks. For instance the gravity reflects the density distribution, aeromagnetic data respond to magnetic susceptibility, radar data are an index of the dielectric constant

as measured by the backscatter, and satellite data record the spectral reflectance of the rock types. Since these properties are in turn influenced by the mineral composition of the rock types, the data sets are effective in geological and structural mapping (e.g. Kowalik and Glenn, 1987; Fernandez-Alonso and Tahon, 1991). However, the utility of the data sets is subject to certain limitations.

Satellite data are useful only when the rocks are exposed at the surface. For a valid spectral reflectance signature to be recorded, the size of the outcrops must far exceed the ground or spatial resolution of the sensor. In the Wabowden test site, for instance, surface outcrops are discontinuous and smaller than sensor resolution, whereas in the Lake Wekusko test site many outcrops are larger than sensor resolution. The presence of vegetation and soil cover and the extent of weathering further contaminates the spectral signature. Ideally this contamination can be reduced by refining the spectral, spatial and temporal resolution. Narrowing the band width of the sensors results in improved spectral resolution. Using low orbit satellites and better electro-optical mechanisms gives better spatial resolution. If the frequency of coverage is increased there is a better chance of obtaining an image when the foliage is at a minimum. The TM sensor of the Landsat satellite with its seven band data and 30 m pixel resolution and 16 day revisit capability is superior to the MSS sensor with its four band data, 82 m pixel resolution and 18 day orbit period.

Aeromagnetic data provide information about lithology in the upper crust and in some cases of the lower crust. Rock types with high magnetic susceptibility generate strong signatures, whereas those with weak susceptibility are not readily recorded. To better record the weak signals, the aircraft altitude is optimised, and

the spacing between flight lines is reduced; a technique that can be used in cases where the expenses involved in processing the enormous amount of additional data can be justified by exemplary results. Similar constraints apply to gravity surveys. Where density differences are marginal, closely spaced surveys will be required to differentiate between rock types.

In the case of radar data, features that are not normal to the incident beam are less likely to be effectively recorded; the texture of the image may be contaminated by speckle which is a system induced artifact; in mountainous terrain the large amount of shadow, an area of no data, results in large areas of unimaged terrain (Trevett, 1986).

Bearing all these limitations in mind it is possible to assess the relative merits of the data sets for a given study area. This assessment can be done by means of a visual interpretation of the data sets and can also be quantified. Along similar lines of reasoning, individual anomalies in a data set can be evaluated for their significance. All these estimates are converted to a numerical value which represents a probability measure.

In the present study, two types of probabilities were assigned, global and local probability with values of 0.0 and 1.0 at the lowest and highest extremes. The global probability refers to the efficacy of the dataset as a whole and is denoted by *gp*. The local probability is assigned to individual anomalies and is denoted by *lp*.

The data sets are integrated according to:

$$P(i, j) = \sum_{k=1}^K lp_k(i, j) \times gp_k \quad (6.1)$$

where $P(i, j)$ is the resultant probability value

$k=1, 2, 3, \dots, K$ is the number of data sets,

i, j is the location of each pixel ,

lp is the local probability for each anomaly, and

gp is the global probability.

6.2 Application of the Method

Although aeromagnetic, gravity and satellite data have, in their own right, proven to be useful in geological mapping, this usefulness is to a large measure influenced by the area of study, the quality of the data, and the purpose of the mapping. In the present case, it is necessary to evaluate each data set to arrive at a judicious estimate of its capability in mapping lithologic units and structures.

In the Canadian Shield, a prime characteristic of many lithologic units and structures is a pronounced azimuthal trend and a narrow spatial distribution. This is particularly true in highly deformed areas such as the Churchill-Superior Boundary zone straddled by the Wabowden test site. Comparing the gravity, stretched aeromagnetic and satellite data (Figures 3.1, 3.4, and 3.9 through 3.12), it is evident that the anomalies in the gravity and aeromagnetic data show prominent northeast trends. Therefore, in a subjective ranking of importance these two data sets take precedence over the satellite data.

Several factors need to be considered to select a front-runner between the gravity and aeromagnetic data. Original digital data from the gravity surveys could not be obtained. Therefore, a regional gravity survey map prepared by Gibb (1968), was digitised. Smoothing operations in the compilation of the map may have eliminated local variations. On the other hand, the aeromagnetic anomaly maps used in this study were derived from the original digital data. They are therefore more reliable than the gravity data.

For the Wabowden test site, the stretched aeromagnetic anomaly data were judged to be the most effective and were assigned global probability values from 0.1 to 0.5. Gravity data were evaluated as being moderately effective and were assigned values between 0.1 and 0.3. For satellite MSS data, the visible and near infrared bands (Band 4, 5 and 6) contain less spatial information than the mid-infrared Band 7 (Chavez, 1992). Here only Band 7 data were used in the integration procedure. In comparison to the stretched and gravity data the satellite image data were least effective and were assigned a probability of 0.05 and 0.1.

The next step is to assign local probabilities to the anomalies (grey levels) in each of the data sets. Here, traditional photo-interpretation methods are invoked to assess the geological significance of each grey level in the data set. Besides traditional photo-interpretation elements such as tone, shape, and size, the grey level must exhibit, as discussed earlier, the requirement of a narrow spatial distribution and an azimuthal trend. In the gravity data (Figure 3.1), grey levels 4 through 8 show an obvious linear trend of which 4 and 6 being narrower are the most likely to represent lithologic units.

At this juncture let us consider the stretched aeromagnetic anomaly data (Figure 3.4). Here too there are several grey levels that show a prominent trend, of which grey levels 6 and 7 have a narrower spatial distribution. On comparing we find that grey level 4 in the gravity data and some areas of grey level 7 in the aeromagnetic data have the same spatial location and are therefore of more significance. Therefore, grey level 4 in the gravity data is assigned a higher local probability of 0.3. Similarly grey level 7 in the aeromagnetic data is assigned local probabilities of 0.3 and 0.5. Furthermore, intuitively we know that, as we move away from grey level 7 towards adjacent higher and lower grey levels, the significance of these levels decreases progressively. Therefore successive higher and lower grey levels are assigned progressively lower local probabilities of 0.2, 0.1, 0.05, and 0.01.

In the MSS Band 7 satellite data (Figure 3.12), water bodies represented by grey levels 1, 2 and 3 are readily identifiable. It must now be decided if the rest of the grey levels represent rock exposures or some other surface features. Although the spectral reflectance of rock types and, by extension, the grey levels which represent them, is not known, intuitively we look for prominent irregular polygonal clusters, a defining characteristic of lithological units. The higher grey levels 10 through 16 occur ubiquitously throughout the image. Previous experience of the author suggests that these are more likely to be surficial features such as vegetation or soil cover. The lower grey levels 4 through 7 are not clearly identifiable on the image. Grey levels 8 and 9 form well defined, sporadically scattered, irregular polygons and are most likely to represent rock outcrops. Grey levels 8 and 9 are accorded higher local probabilities of 0.3.

Both global and local probabilities have a range of possible values. Thus, to test the effectiveness of the integration process and the validity of the probability assignments, various test cases were tried with different values of global and local probabilities. The data sets were integrated according to Equation (6.1) using different combinations of probability values. These tests, termed experiments 1 through 8, are presented in Table 6.1.

6.2.1 Interpretation of results

The results of the integration in the form of grey level plots are shown in Figures 6.1 through 6.8. Each pixel in these results has an associated unique probability value indicated by the linear grey scale bar. This value is the probability that the target proposition, a lithologic or tectonic feature exists at that pixel location. The maximum possible value is 1.0 (white) and the minimum is 0.0 (black). Except in one case (Figure 6.7, Expt. 7), the results show a pronounced trend. In the northern half of the image the trend is NNE-SSW; a similar, albeit curvilinear trend is seen in the southern half of the image. The curvilinear trend is an artifact of the integration process and is strongly influenced by the contours in the gravity anomaly map (Figure 3.1).

It is noteworthy that both high and low probability values show distinctive trends (e.g. Figures 6.3, 6.4 and 6.8). However, probability theory suggests that the high probability values are more likely to reflect the target proposition than the low value ones. The trend is clearly seen in six of the eight experiments.

In cases where the global probability assigned to the aeromagnetic data is higher

	GLOBAL PROBABILITY			LOCAL PROBABILITY											
	Promag (Aeromag.)	Prograv (Gravity)	Prosat (MSS Bnd7)	Aeromag					Gravity					Satellite (MSS Bnd 7)	
Greylev * Num.				7	6,8	5,9	4,10	Other	4	3,5	2,6	1,7	8	8,9	Other
Expt. Num.															
1	0.2	0.2	0.05	0.3	0.2	0.1	0.05	0.01	0.3	0.2	0.1	0.05	0.01	0.3	0.05
2	0.2	0.1	0.05	0.3	0.2	0.1	0.05	0.01	0.3	0.2	0.1	0.05	0.01	0.3	0.05
3	0.3	0.1	0.05	0.3	0.2	0.1	0.05	0.01	0.3	0.2	0.1	0.05	0.01	0.3	0.05
4	0.3	0.1	0.05	0.5	0.3	0.2	0.1	0.01	0.3	0.2	0.1	0.05	0.01	0.3	0.05
5	0.3	0.3	0.05	0.5	0.3	0.2	0.1	0.01	0.3	0.2	0.1	0.05	0.01	0.3	0.05
6	0.5	0.3	0.1	0.3	0.2	0.1	0.05	0.01	0.3	0.2	0.1	0.05	0.01	0.3	0.05
7	0.1	0.1	0.1	0.3	0.2	0.1	0.05	0.01	0.3	0.2	0.1	0.05	0.01	0.3	0.05
8	0.3	0.1	0.05	0.3	0.5	0.3	0.05	0.01	0.2	0.3	0.1	0.05	0.01	0.3	0.05

* Grey levels separated by a comma (,) indicates probability assignment to individual grey levels

* Grey levels separated by a hyphen (-) indicates probability assignment to a group of grey levels

Table 6.1 List of probability values assigned to data sets, Wabowden test site

than that assigned to the gravity data and satellite data (Figures 6.2, 6.3 and 6.4; Expts. 2,3 and 4 respectively), the zone of high probability is unmistakable; where global probabilities for aeromagnetic and gravity data are equal (Figure 6.1; Expt. 1), the zone of high probability merges with the intermediate probability value grey levels. This is also true when satellite data global probability is increased slightly (Figure 6.6, Expt. 6). Where all three global probabilities are equal (Figure 6.7; Expt. 7) no zones of high probability are visible. Variation in the assignment of the local probabilities does not make a significant difference. For instance, in Experiments 3 and 4, where global probabilities remain unchanged but the local probability assignment is altered, there is little difference between the two results (Figures 6.3 and 6.4).

The results of the experiments using different global probabilities leads to the inference that the aeromagnetic data has a higher geological information content, followed by gravity and finally by satellite data. In other words, the original deduction based on visual interpretation, which led to the aeromagnetic data being accorded higher global probability, has been reinforced.

The similarity of the results of the various experiments is illustrated by three profiles constructed for five experiments (Figures 6.2, 6.3, 6.4, 6.6 and 6.8). These profiles (Figures 6.9 through 6.11), show that high and low values occur in the same spatial location for the different experiments although absolute values differ from experiment to experiment. Also indicated on the profiles is the location of the boundary between the Churchill and Superior provinces as mapped by Gibb (1968). Subsequent research has shown that the boundary is a broad zone rather

than a sharp contact (e.g. Weber, 1990), but Gibb's position of the boundary is well within the broad zone and is therefore used in the profiles, simply as corroborative evidence without commenting upon or refuting subsequent research.

Comparing the results of the eight experiments with the existing, albeit poorly constrained geological map (Figure 2.9), confirms that the rock types exhibit similar trends as those shown by the algebraic probability integration. Also, the broad zone of higher probability values in the northwestern part of the area coincides with the boundary between the tonalite migmatite gneiss of the Thompson Belt on the northeast, and the amphibolite facies gneiss of the Superior Province on the southwest. This can be clearly seen in Figures 6.2, 6.3, 6.4, 6.5, 6.6 and 6.8. The result of the integration process has served to map a lithologic boundary that may be related to tectonic interaction between the Churchill and Superior Provinces.

The most significant result of the algebraic probability method is the NE trending zone of high probability values. This zone is, as just discussed, of geological significance and may be the boundary between the Churchill and Superior Provinces, or at least a lithologic boundary that parallels, and may be genetically related to, the suturing process. It is therefore treated as an *a priori* indicator in the next two methods (Chapters 7 and 8). For the purpose of integration the corresponding anomaly in the gravity map is treated as an *a priori* reference feature. In the gravity map this is the grey level 4 (Figure 3.1), and this grey level lies in the approximate centre of the broad zone of higher probability values obtained by the algebraic probability method.

At this stage it is possible to formulate a set of ideal combinations of data sets

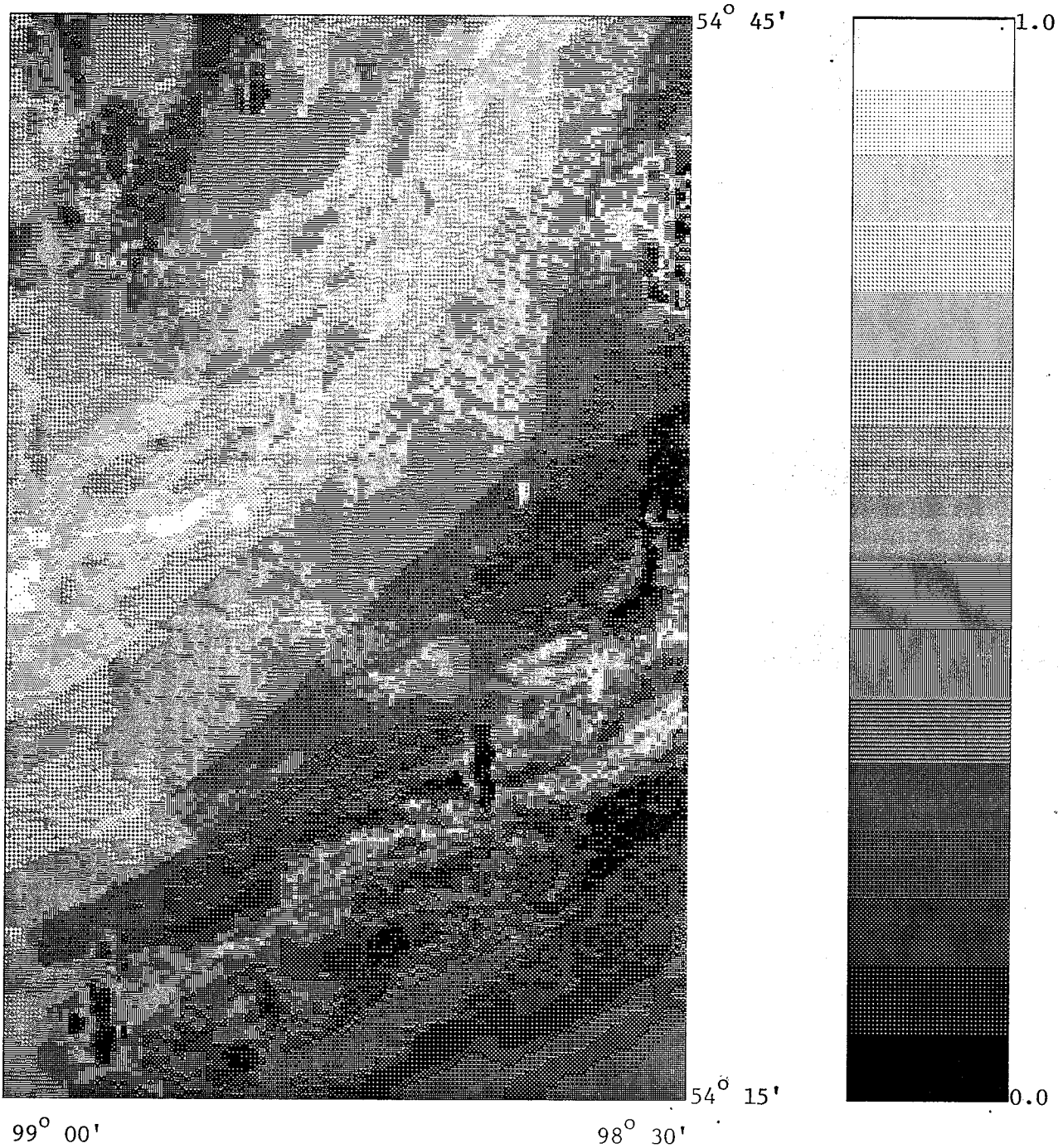


Figure 6.1 Result of algebraic probability integration (Expt.1)

Distance = 55250 m (N-S), 32750 m (E-W)

Pixel size = 216 m (N-S), 257 m (E-W)

Grey scale bar is linear

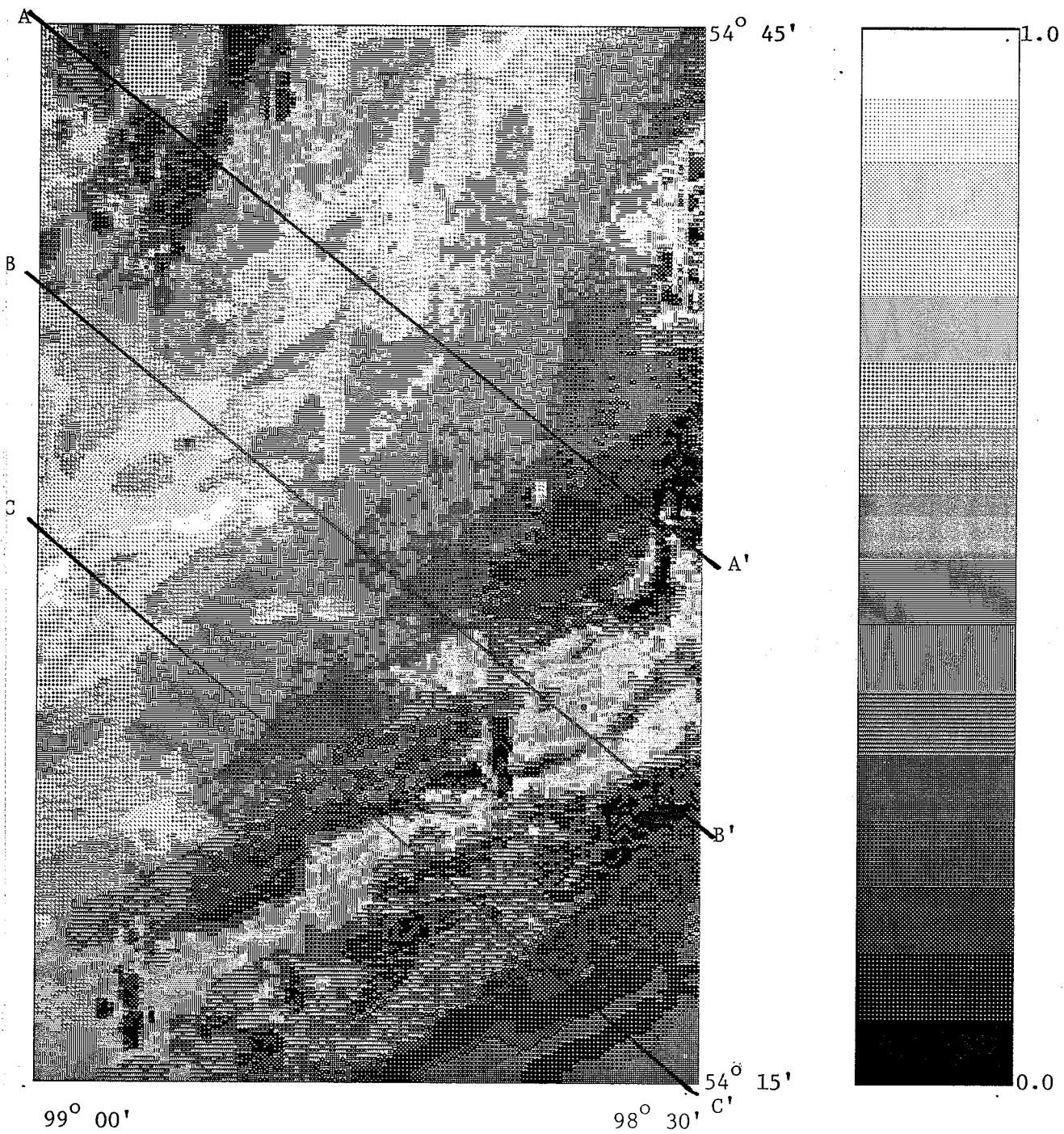


Figure 6.2 Result of algebraic probability integration (Expt. 2)

Distance = 55250 m (N-S), 32750 m (E-W)

Pixel size = 216 m (N-S), 257 m (E-W)

Grey scale bar is linear

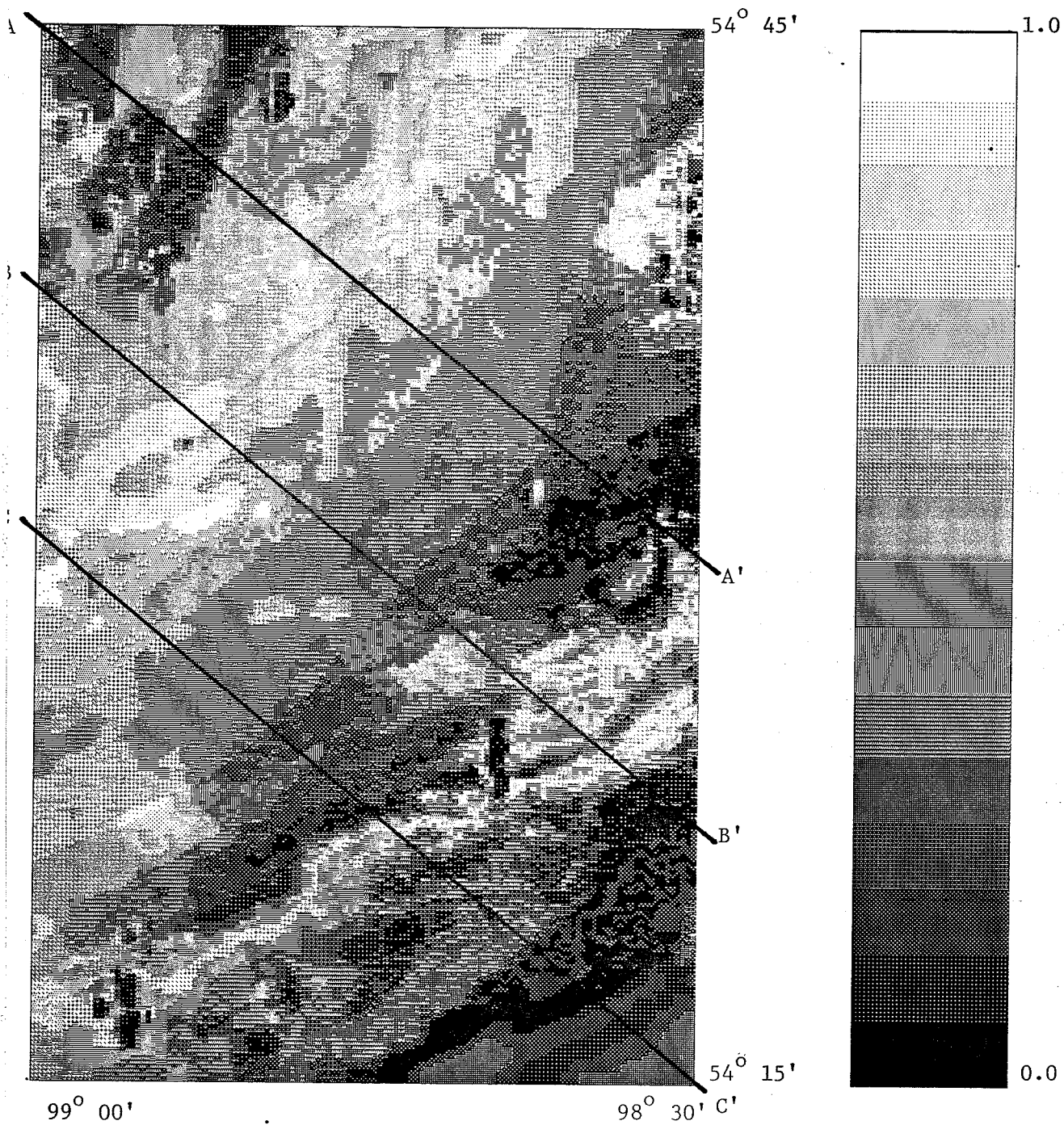


Figure 6.3 Result of algebraic probability integration (Expt. 3)

Distance = 55250 m (N-S), 32750 m (E-W)

Pixel size = 216 m (N-S), 257 m (E-W)

Grey scale bar is linear

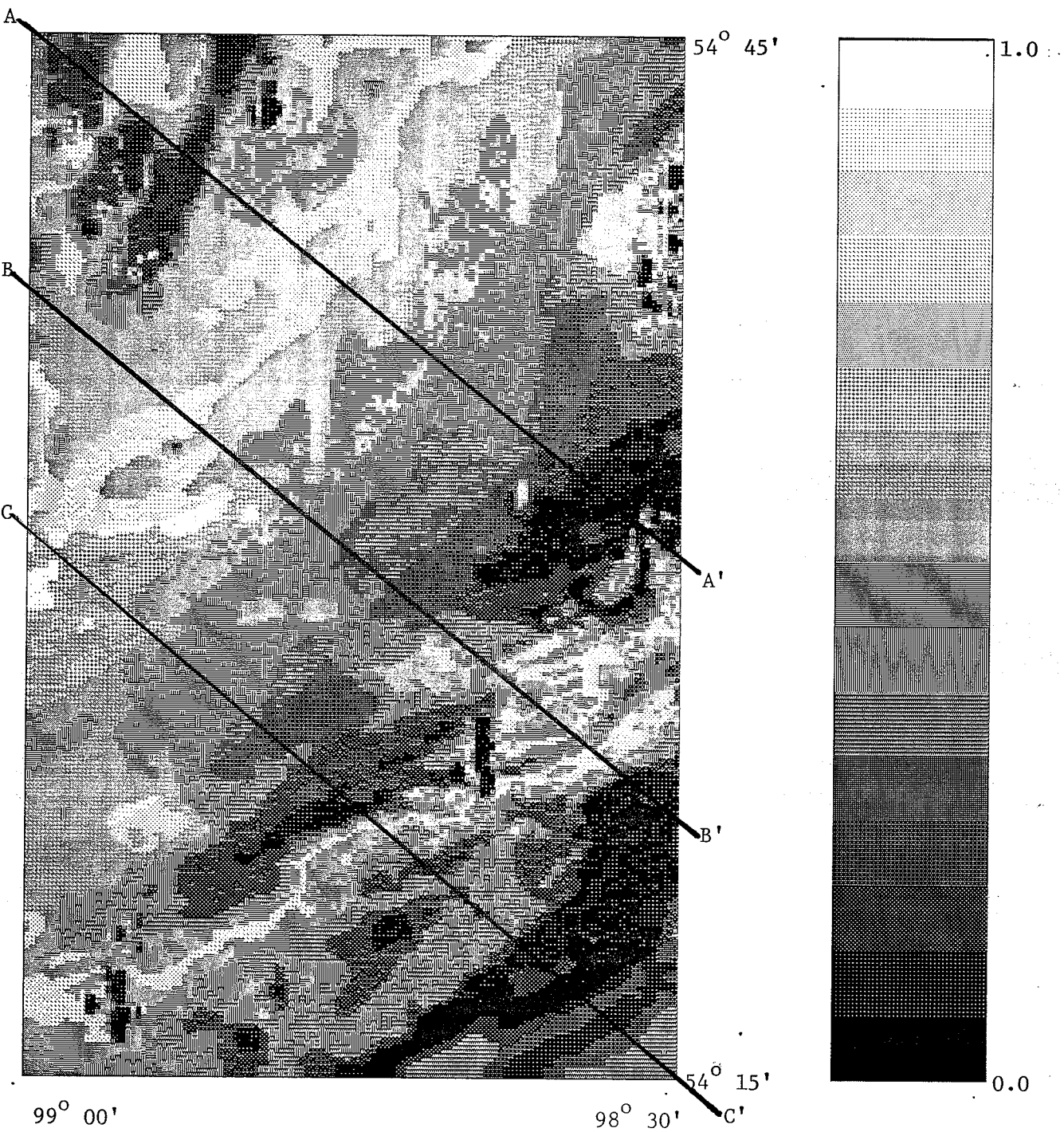


Figure 6.4 Result of algebraic probability integration (Expt. 4)

Distance = 55250 m (N-S), 32750 m (E-W)

Pixel size = 216 m (N-S), 257 m (E-W)

Grey scale bar is linear

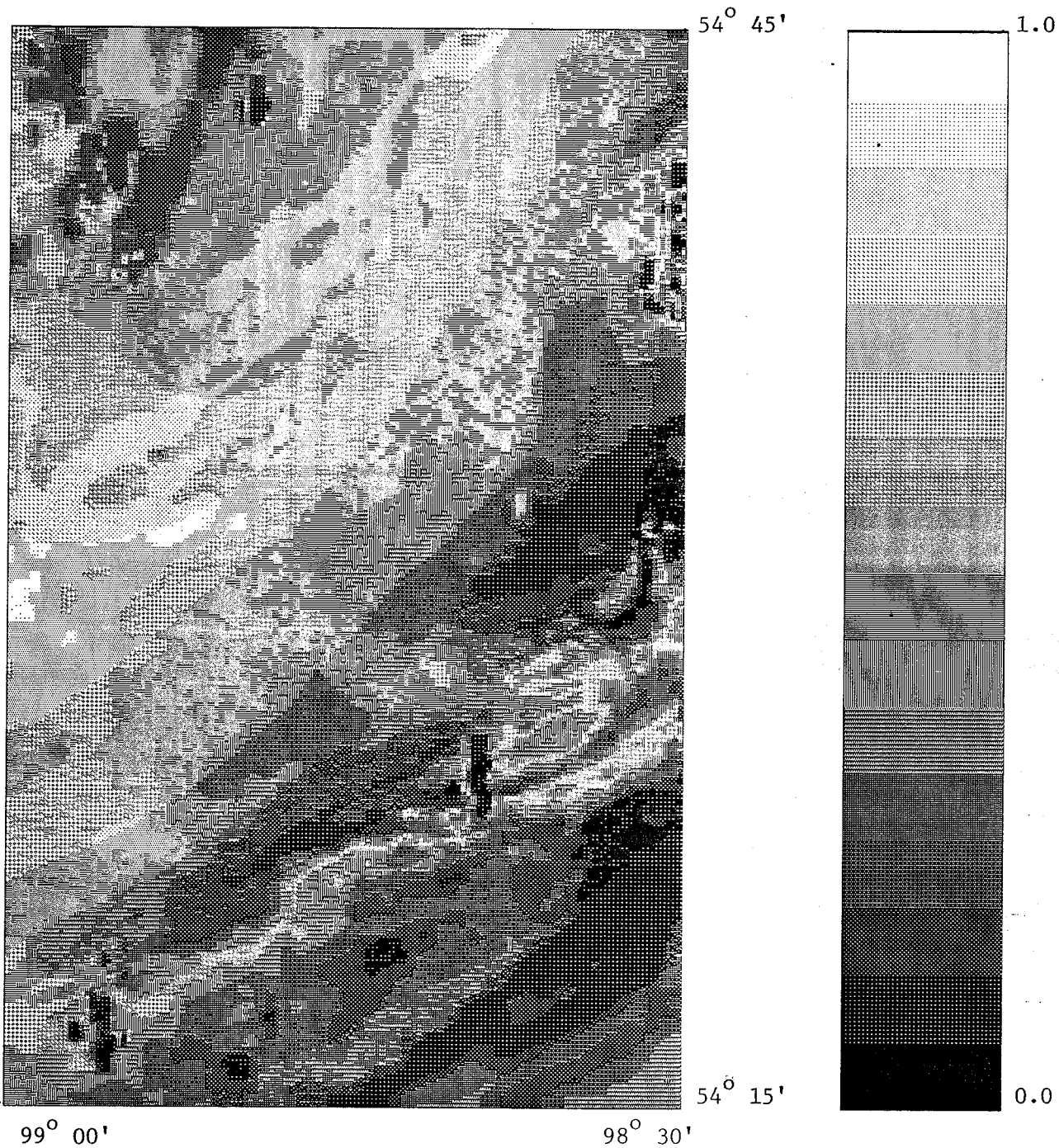


Figure 6.5 Result of algebraic probability integration (Expt. 5)

Distance = 55250 m (N-S), 32750 m (E-W)

Pixel size = 216 m (N-S), 257 m (E-W)

Grey scale bar is linear

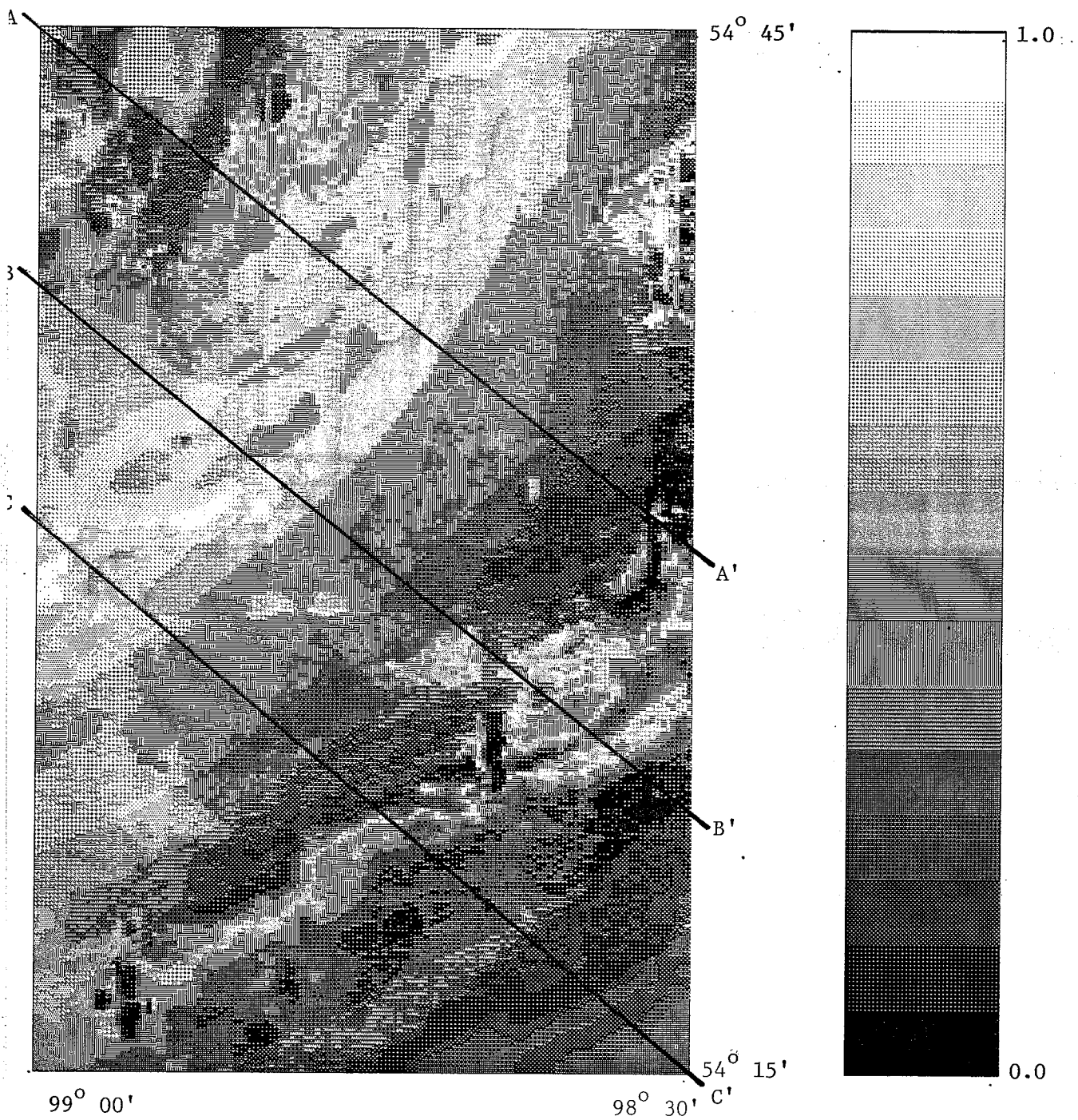


Figure 6.6 Result of algebraic probability integration (Expt. 6)

Distance = 55250 m (N-S), 32750 m (E-W)

Pixel size = 216 m (N-S), 257 m (E-W)

Grey scale bar is linear

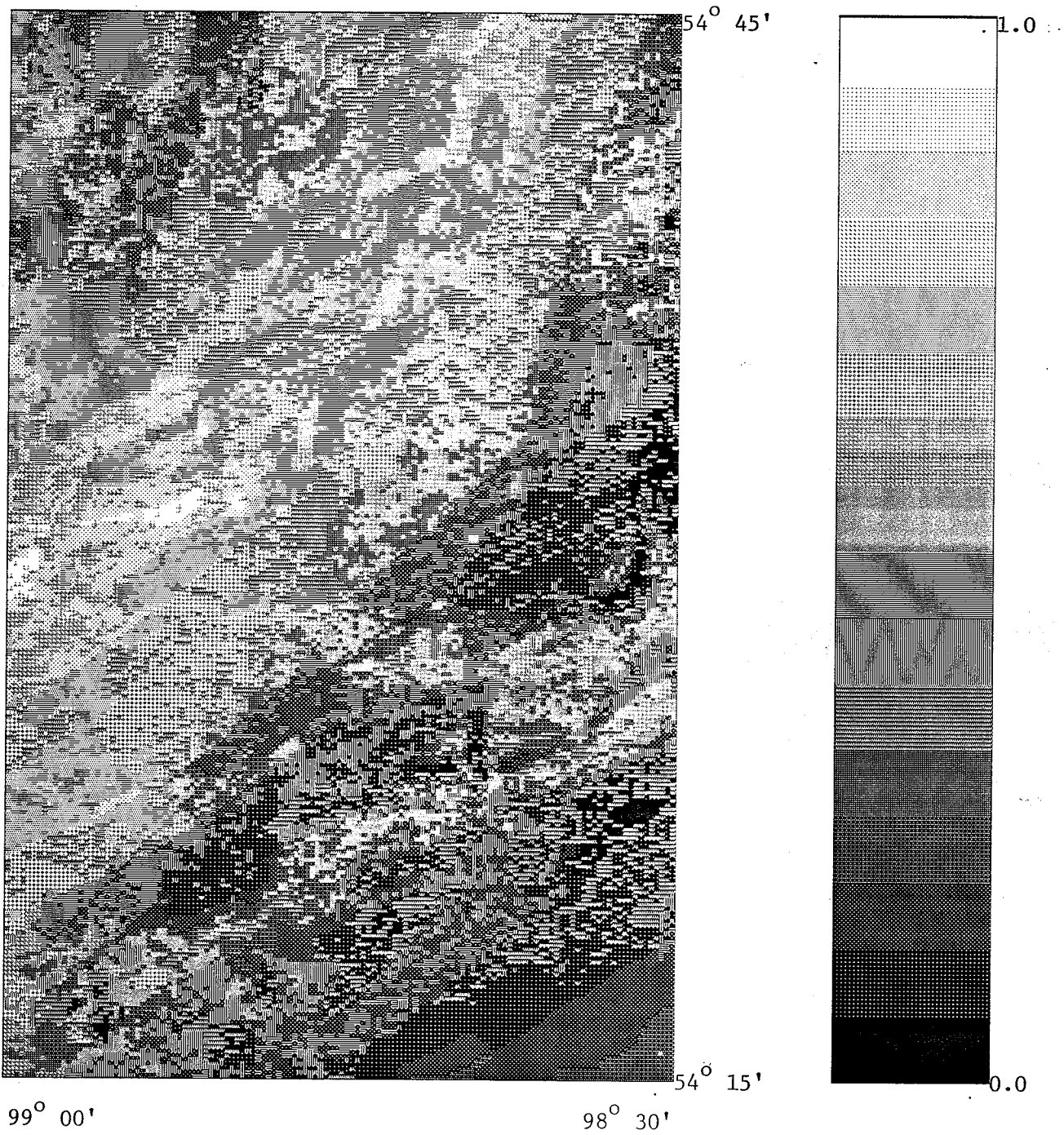


Figure 6.7 Result of algebraic probability integration (Expt. 7)

Distance = 55250 m (N-S), 32750 m (E-W)

Pixel size = 216 m (N-S), 257 m (E-W)

Grey scale bar is linear

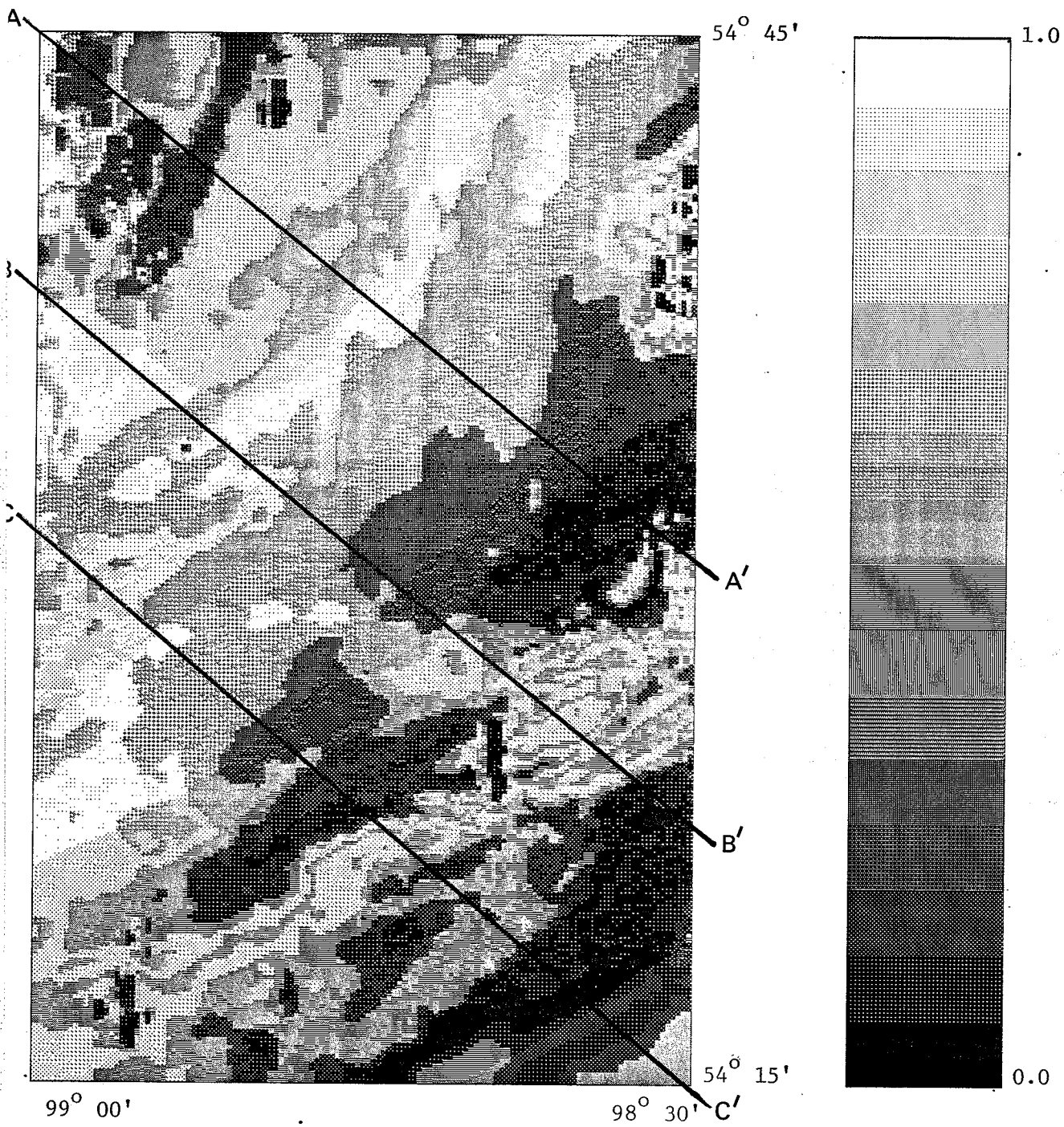


Figure 6.8 Result of algebraic probability integration (Expt. 8)

Distance = 55250 m (N-S), 32750 m (E-W)

Pixel size = 216 m (N-S), 257 m (E-W)

Grey scale bar is linear

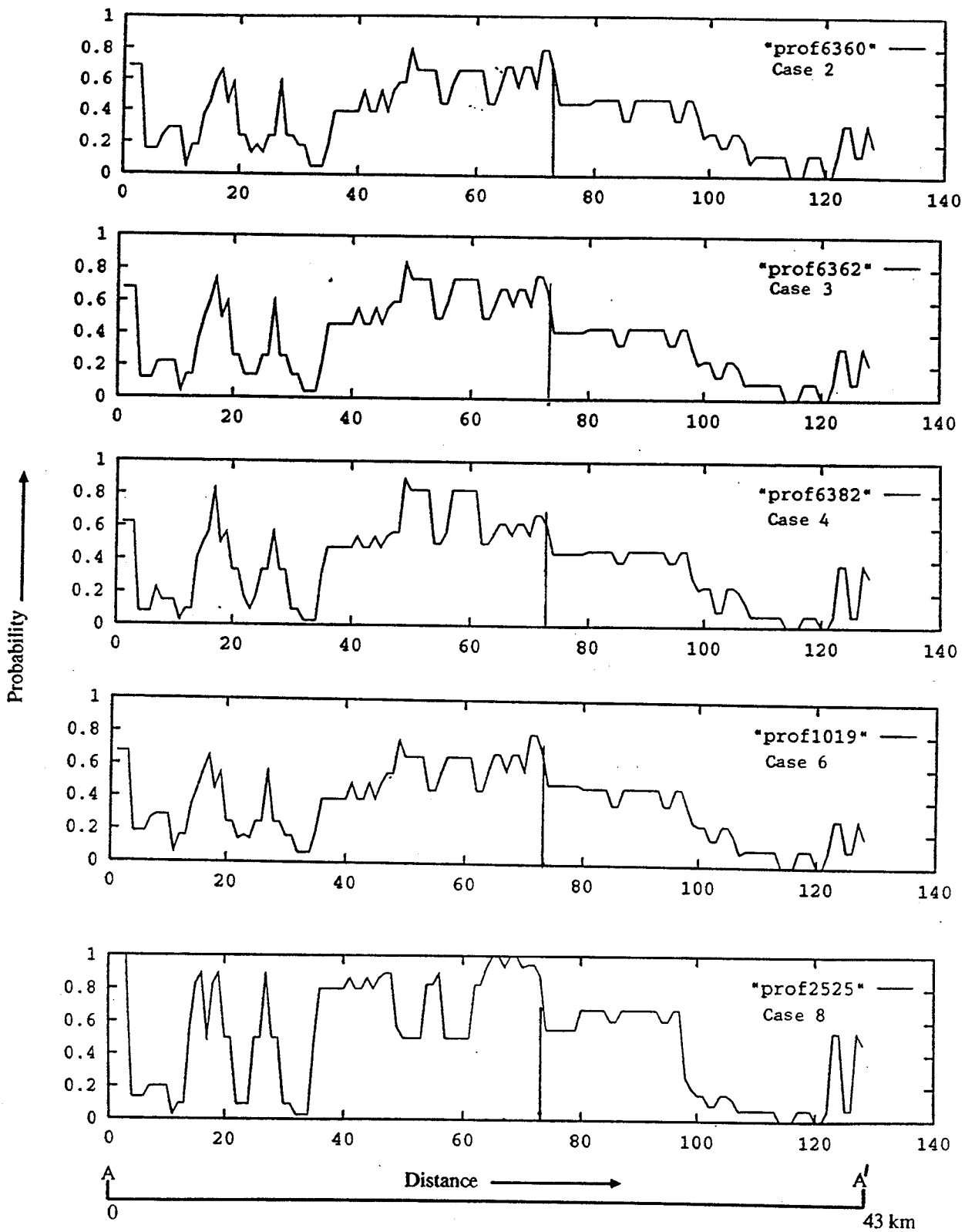


Figure 6.9 Profiles along Line A-A

Vertical line shows position of C-S boundary as mapped by Gibb (1968)

Vertical axis = probability; Horizontal axis = distance

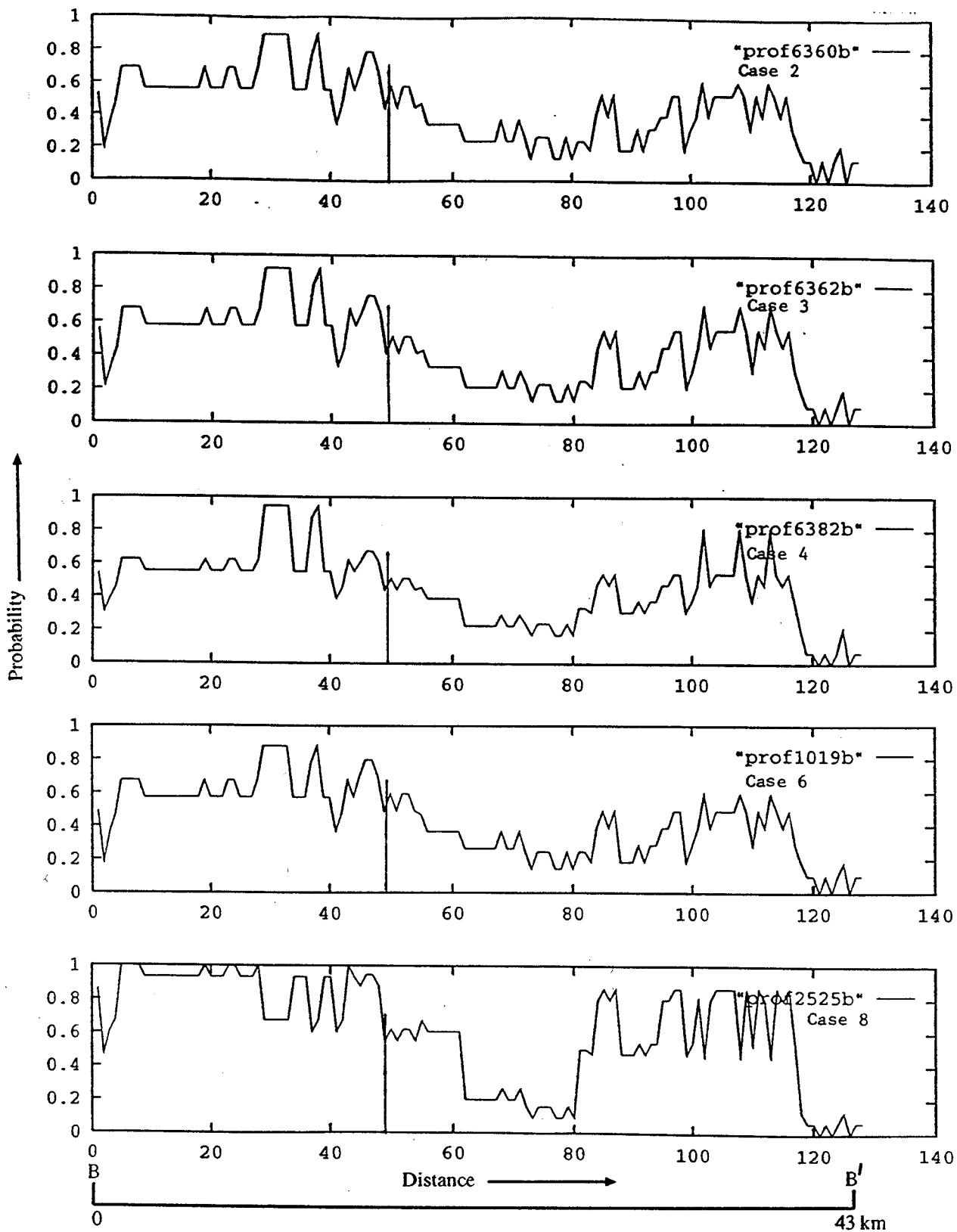


Figure 6.10 Profiles along Line B-B

Vertical line shows position of C-S boundary as mapped by Gibb (1968)

Vertical axis = probability; Horizontal axis = distance

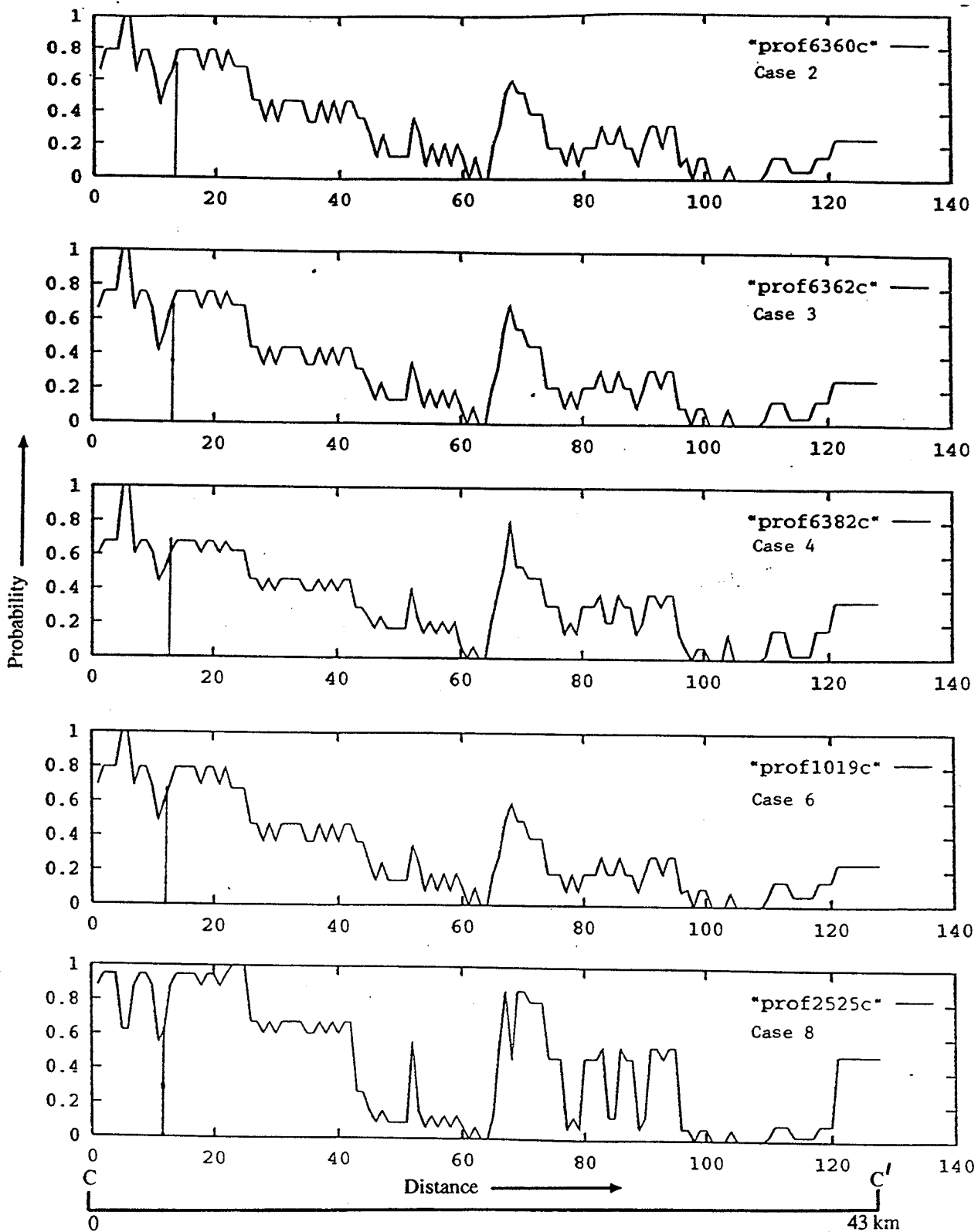


Figure 6.11 Profiles along Line C-C

Vertical line shows position of C-S boundary as mapped by Gibb (1968)

Vertical axis = probability; Horizontal axis = distance

and pertinent probability assignments for use in other study areas. However, the quality of the data, the nature of the terrain, and the target proposition will bear heavily on the combination. For instance in arid and semi-arid regions, by virtue of their sparse canopy cover, satellite data may well be more useful. Likewise, greater outcrop density would be another influencing factor. It is therefore prudent to apply essentially the same principles with appropriate modifications to other areas such as the Lake Wekusko test site.

This is illustrated in the next section where a different study area is selected, and the same principles applied for a different target proposition; that of mapping the geological structure and lithological units. If the results obtained match closely with the known geology then the algebraic probability method is validated.

6.3 Validation of the Method

The Lake Wekusko test site was chosen to test the algebraic probability method. In comparison to the Wabowden test site, the Lake Wekusko site has much better surface exposure of rock types. This provides greater control for geological mapping. Therefore the geology of this site is well documented. The objective is to apply the same principles but with a different target proposition. Here the algebraic probability method is used to map the lithological units and their associated structures. Once again the method is to visually interpret each data set and assess its applicability in mapping lithological units. This is translated into the assignment of global probabilities. Then the individual anomalies in each data set are assessed and assigned local probabilities.

The data sets available for this test site are the gravity anomaly data (Figure 3.2), the aeromagnetic anomaly data (Figure 3.5), and the original and filtered TM data in Band 3, Band 5 and Band 7 (Figures 3.13 through 3.18). A relative comparison of all these data sets shows a great deal of spatial variation in the grey levels for the aeromagnetic data and the satellite TM data. However, the gravity data does not show such a detailed variation. This is mainly because the gravity data have been obtained from a regional survey (Gibb, 1968). Local variations in the gravity anomaly have not been effectively recorded in the survey. It becomes readily apparent that the gravity data will not provide much information about the lithological composition of the site and can be safely discarded without detracting from the integration process.

As discussed earlier (§3.4), the original TM Band 3, 5 and 7 data contain salt-and-pepper noise that was significantly reduced by the application of a low-frequency pass filter. It is these filtered images (Figures 3.16, 3.17 and 3.18) that are considered in this step of the integration. Visual examination reveals that Band 3 data has a lower degree of spatial variability than Band 5 and Band 7. In other words, the rate of change in grey level along a given transect is lower for Band 3. Independent studies (e.g. Chavez, 1992), show that, in general, visible band images (such as TM Band 3) have a lower degree of spatial variation than the infrared band images (such as TM Band 5 and TM Band 7). Therefore in the present case only filtered TM Band 5 and TM band 7 are used.

6.3.1 Integration of Aeromagnetic and Filtered Satellite Data

As before, the process involves assigning relative probabilities to each of the input data sets as a whole (global probability) and each of the grey levels in the individual data sets (local probability). A series of experiments are conducted to test the effect of assigning different probability values (Table 6.2). These values are estimated by intuitive reasoning based on visual analysis. This analysis is also influenced by the target proposition which is the mapping of lithological units. The first series of four experiments used aeromagnetic and TM Band 5 data sets. A second series of four experiments used aeromagnetic and TM Band 7 data sets. Additional experiments were also tried but they did not significantly improve the results and are not reported here.

In the first experiment of both series both the aeromagnetic and satellite data are assigned equal global probabilities of 0.3 each. In other experiments, each data set are successively assigned higher and lower global probabilities of 0.5 and 0.3 respectively (Expt. 2, 3 and 4 of each series in in Table 6.2). For assigning the local probability we look for well defined irregular polygons which are most likely to represent rock units. In the aeromagnetic data, grey levels 13 through 16 satisfy this requirement and are assigned local probabilities of 0.3 and 0.5. Grey levels 6, 7, 10, 11, 12 also occur as irregular polygons but are spatially widespread. These are assigned values of 0.2 and 0.3. Grey level 8 and 9 are less effective and are assigned low values of 0.05 and 0.1.

Similarly in the filtered TM Band 5 data, grey levels 12 through 16, which have

the best defined irregular polygons, are assigned values of 0.3 and 0.5; grey level 8, seen as less well defined polygons, is assigned intermediate values of 0.2 and 0.3; grey level 11, with least well defined polygons, is assigned 0.1 and 0.2; and the rest, which mostly represent water bodies, are assigned very low values of 0.05 and 0.1. A set of four experiments are conducted for the aeromagnetic and filtered TM band 5 data sets. For filtered TM Band 7, a different set of grey levels were interpreted as being geologically significant using the same criteria as for filtered TM Band 5 data. The values assigned to these levels are shown in Table 6.2.

The results of the four experiments for the integration of aeromagnetic with TM Band 5, and an additional four experiments for integration with TM Band 7 are shown in Figures 6.12 through 6.19.

The results of the integration can be improved by using some classification technique on the satellite data, such as clustering. This algorithm is a form of unsupervised classification that takes advantage of the natural grouping of pixels in spectral space to form clusters. These clusters are representative of surficial features.

The simplest form of clustering does not require prior information, such as training areas. Since it is a non-parametric classifier with fewest assumptions it is a very powerful technique (Sabins, 1987). Therefore it can be applied without introducing bias in the result.

The various rock types must exhibit varying spectral signatures for them to form natural clusters. In the Wabowden test site, the spectral signature of vegetation and glacial deposits overpowers the spectral signature of the rock types. Hence,

the clustering process when applied to the MSS data of Wabowden test site, did not result in a significant improvement and the results are not presented here.

6.3.2 Integration of Aeromagnetic and Clustered Satellite Data

The scheme of clustering adopted in this study is a one-pass method. The very first pixel is assigned to a class. The second pixel is then compared with the first and the inter-spectral distance is computed. If this distance is less than a specified threshold the second pixel is considered to belong to the same cluster as the first pixel. The spectral mean of the class is computed as the average of the two pixels.

If the distance is greater, the second pixel is assigned to a new class. In this manner several clusters (or classes) are generated. Whenever a new unclassified pixel is encountered it is compared with all classes generated up to that point. Furthermore, with addition of pixels into a class a new mean or class center is computed. This process is repeated for all the pixels until the entire image is classified.

The clustered outputs for the filtered Band 5 and Band 7 are shown in Figures 6.20 and 6.21. The clustering process resulted in the identification of 12 classes in TM Band 5 data, and 11 classes in TM Band 7 data. The classes shown as sequentially numbered grey levels in the figures, do not represent spectral reflectance values. Once again a series of experiments are conducted in which relative global and local probabilities are assigned using the same criteria as for previous experiments. Table 6.3 lists the probabilities. Four experiments are conducted for each data set. Figures 6.22 - 6.29 show the result of the eight experiments.

	GLOBAL PROB.		LOCAL PROBABILITY													
	Promag	Prosat	Aeromagnetic						Satellite (Filtered TM Band 5)							
Greylev* Num			6,7	8	9	10-12	13-16	Other	6,7	8	9,10	11	12,13	14-16	Other	
Expt 1	0.3	0.3	0.3	0.1	0.05	0.3	0.5	0.01	0.1	0.3	0.1	0.2	0.3	0.5	0.05	
Expt 2	0.3	0.5	0.3	0.1	0.05	0.3	0.5	0.01	0.1	0.3	0.1	0.2	0.3	0.5	0.05	
Expt 3	0.3	0.5	0.2	0.05	0.05	0.2	0.3	0.01	0.05	0.2	0.1	0.1	0.5	0.3	0.05	
Expt 4	0.5	0.3	0.2	0.05	0.05	0.2	0.3	0.01	0.05	0.2	0.1	0.1	0.5	0.3	0.05	
									Satellite (Filtered TM Band 7)							
									6	7,8	9	10	11	12	13-16	Other
Expt 1	0.3	0.3	0.3	0.1	0.05	0.3	0.5	0.01	0.05	0.3	0.1	0.05	0.2	0.3	0.5	0.01
Expt 2	0.3	0.5	0.3	0.1	0.05	0.3	0.5	0.01	0.05	0.3	0.1	0.05	0.2	0.3	0.5	0.01
Expt 3	0.3	0.5	0.2	0.05	0.05	0.2	0.3	0.01	0.05	0.2	0.05	0.05	0.2	0.1	0.5	0.01
Expt 4	0.5	0.3	0.2	0.05	0.05	0.2	0.3	0.01	0.05	0.2	0.05	0.05	0.2	0.1	0.5	0.01

* Grey levels separated by comma (,) indicates probability assignment to individual grey levels

* Grey levels separated by hyphen (-) indicates probability assignment to a group of grey levels

Table 6.2 Probability values for aeromagnetic and filtered satellite data, Lake Wekusko test site

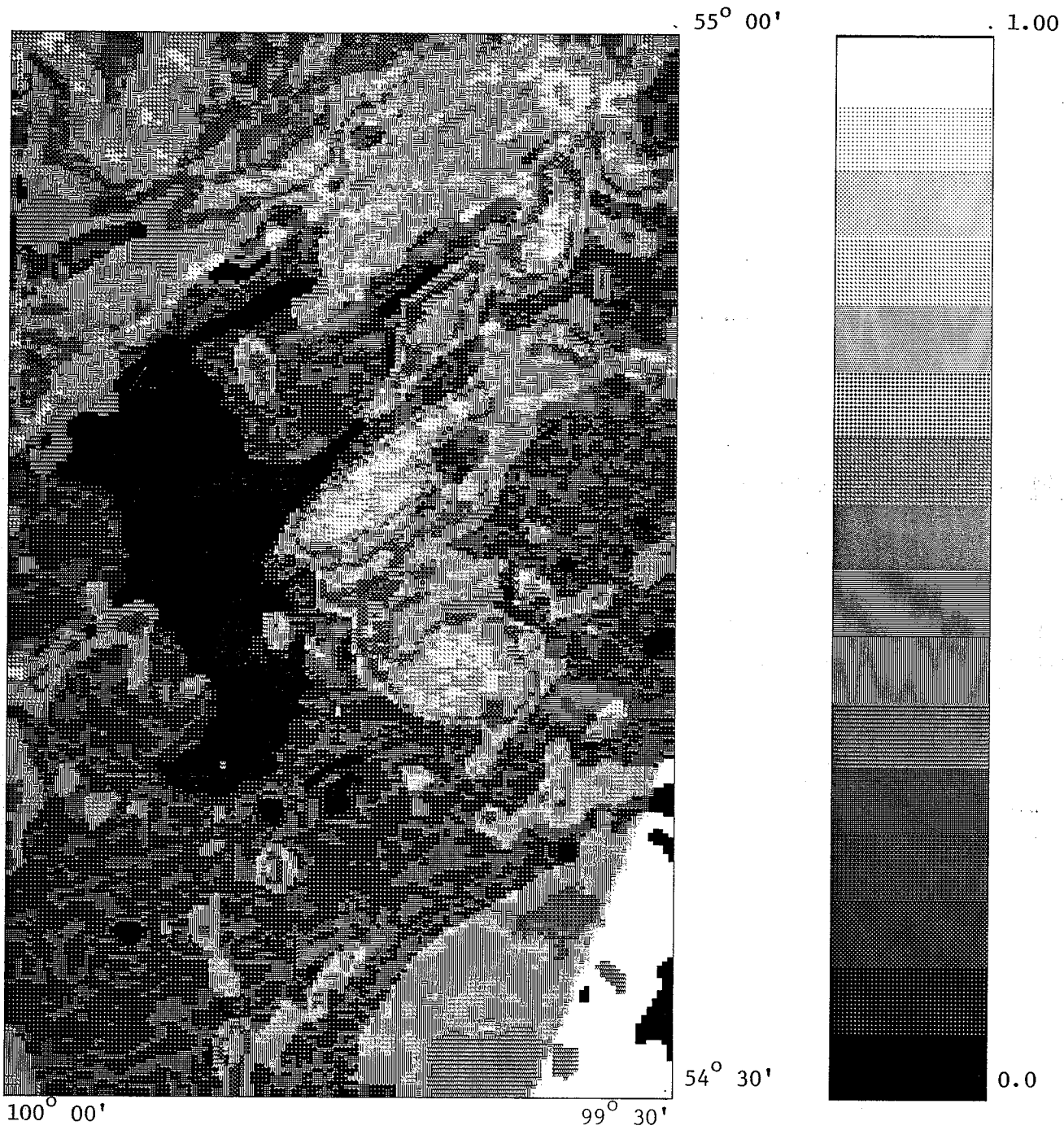


Figure 6.12 Integration of aeromagnetic with filtered TM Band 5 (Expt. 1)

Distance = 55250 m (N-S), 32750 m (E-W)

Pixel size = 216 m (N-S), 257 m (E-W)

Grey scale bar is linear

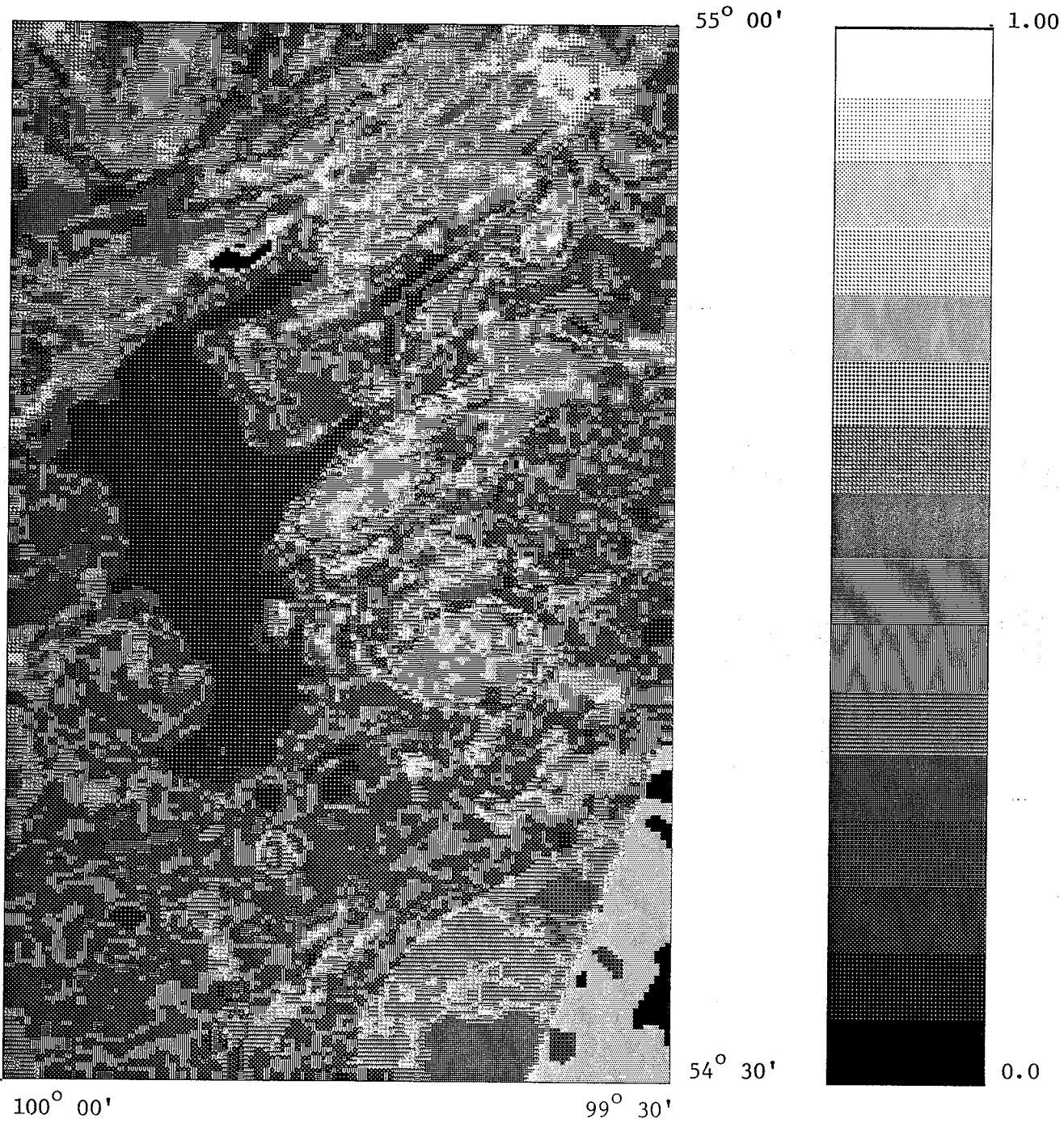


Figure 6.13 Integration of aeromagnetic with filtered TM Band 5 (Expt. 2)

Distance = 55250 m (N-S), 32750 m (E-W)

Pixel size = 216 m (N-S), 257 m (E-W)

Grey scale bar is linear

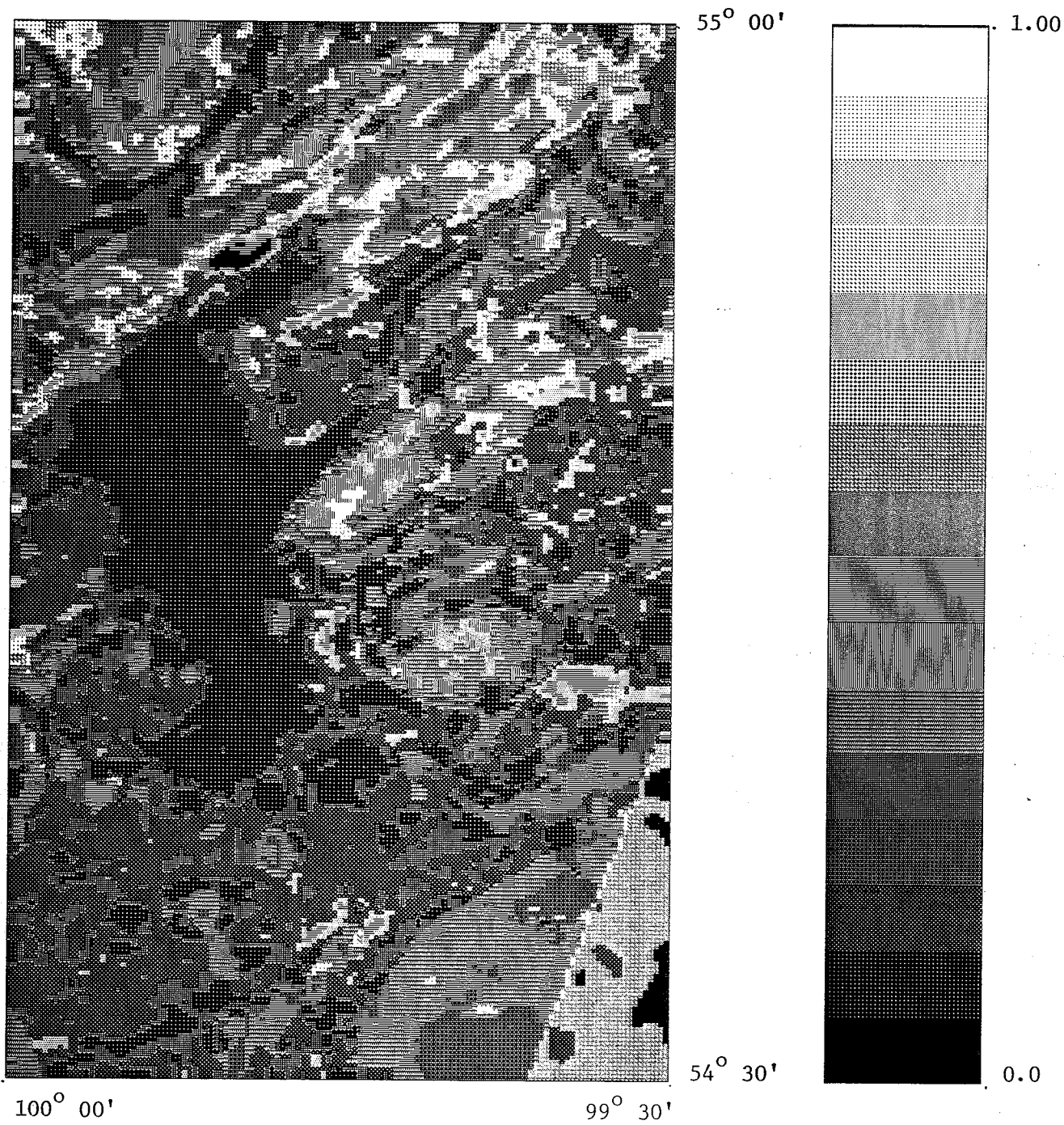


Figure 6.14 Integration of aeromagnetic with filtered TM Band 5 (Expt. 3)

Distance = 55250 m (N-S), 32750 m (E-W)

Pixel size = 216 m (N-S), 257 m (E-W)

Grey scale bar is linear

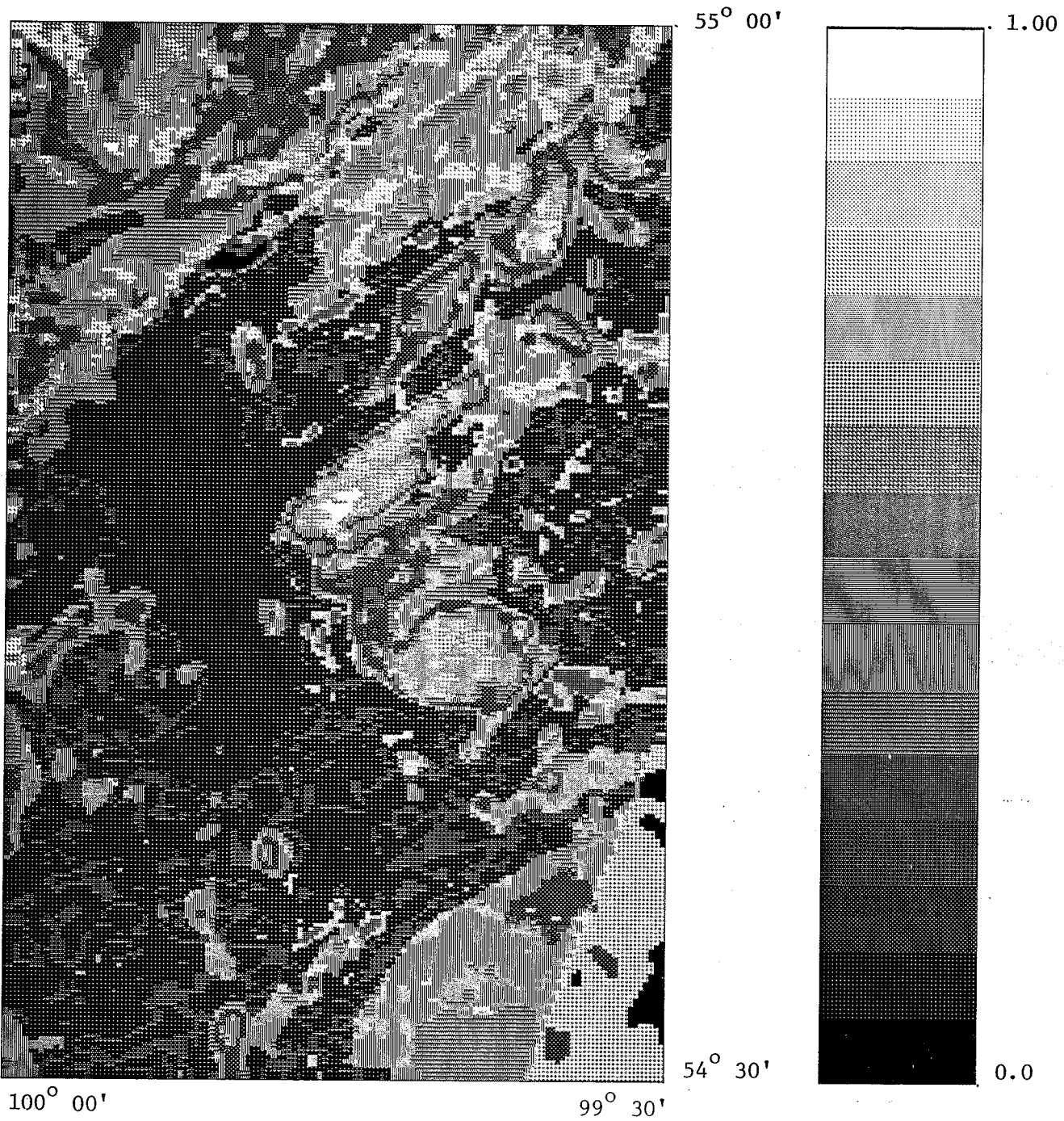


Figure 6.15 Integration of aeromagnetic with filtered TM Band 5 (Expt. 4)

Distance = 55250 m (N-S), 32750 m (E-W)

Pixel size = 216 m (N-S), 257 m (E-W)

Grey scale bar is linear

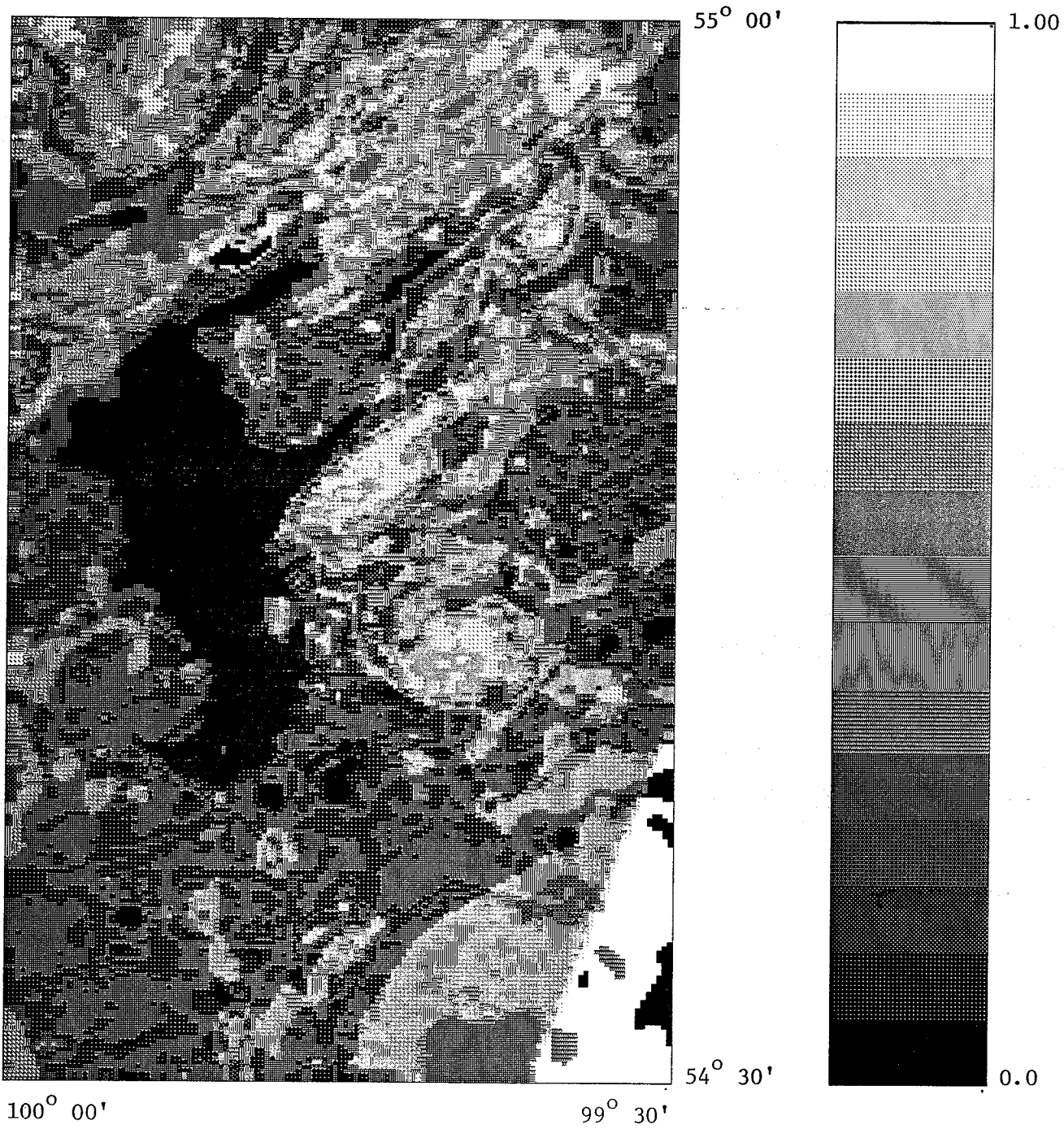


Figure 6.16 Integration of aeromagnetic with filtered TM Band 7 (Expt. 1)

Distance = 55250 m (N-S), 32750 m (E-W)

Pixel size = 216 m (N-S), 257 m (E-W)

Grey scale bar is linear

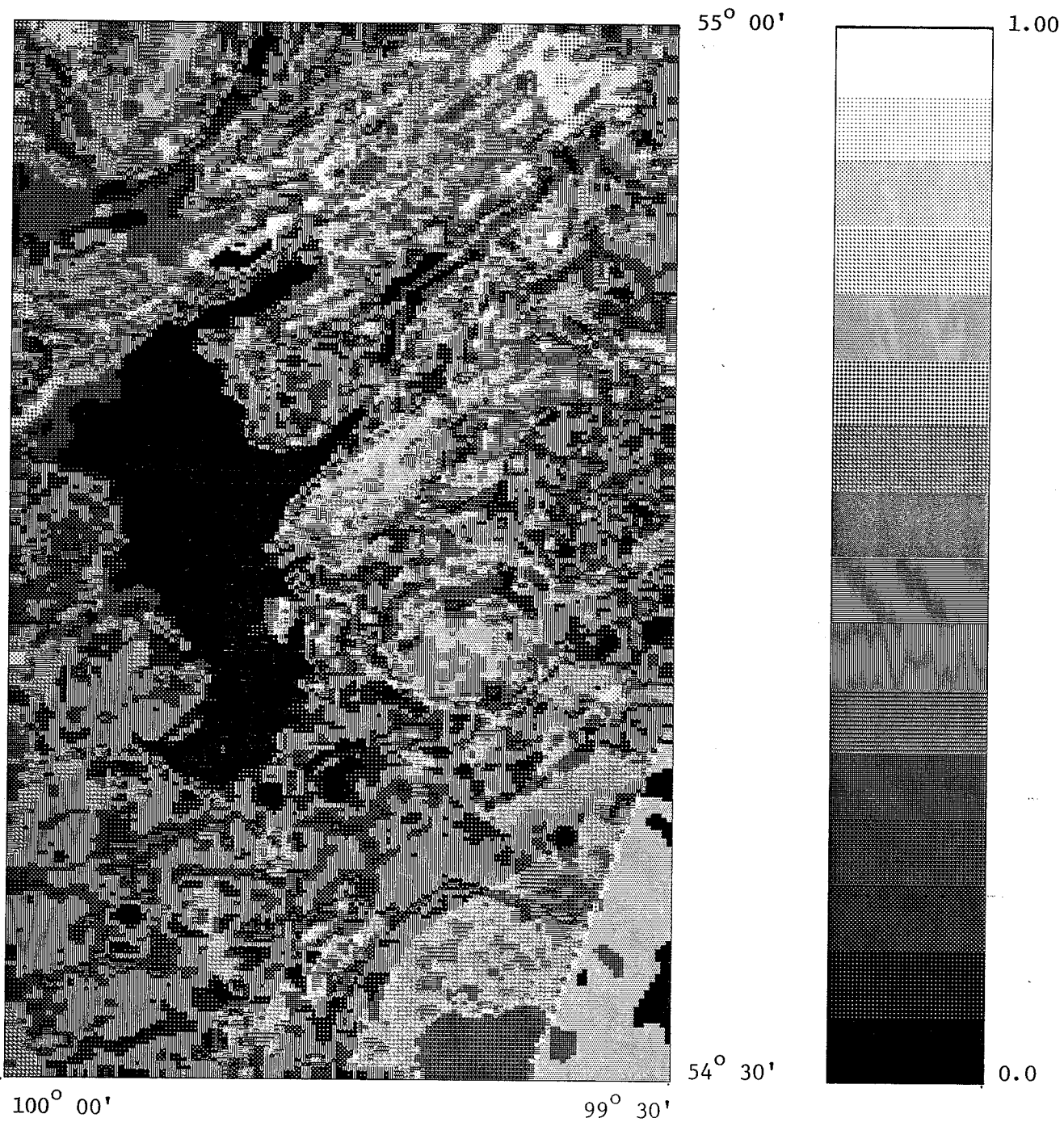


Figure 6.17 Integration of aeromagnetic with filtered TM Band 7 (Expt. 2)

Distance = 55250 m (N-S), 32750 m (E-W)

Pixel size = 216 m (N-S), 257 m (E-W)

Grey scale bar is linear

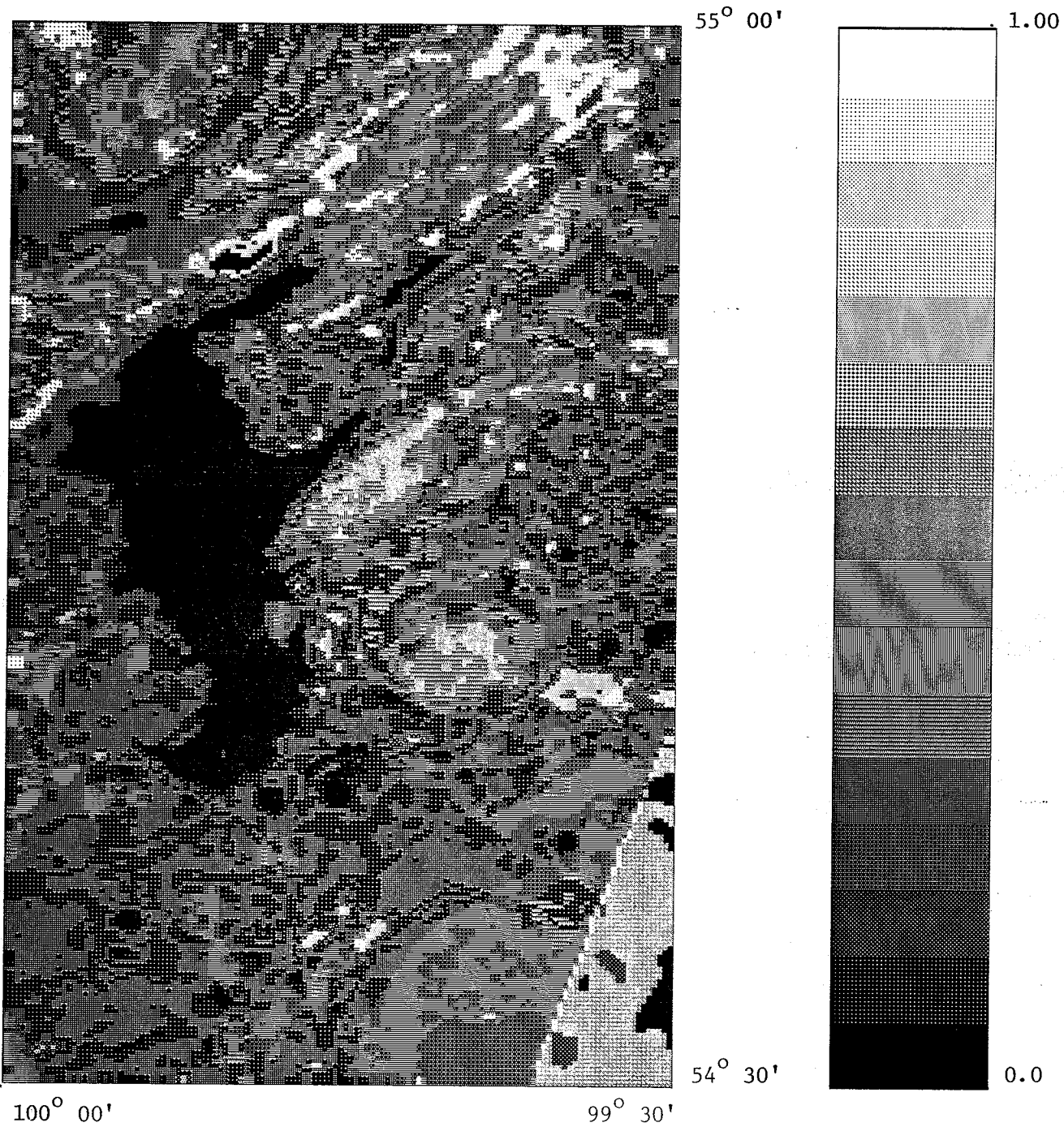


Figure 6.18 Integration of aeromagnetic with filtered TM Band 7 (Expt. 3)

Distance = 55250 m (N-S), 32750 m (E-W)

Pixel size = 216 m (N-S), 257 m (E-W)

Grey scale bar is linear

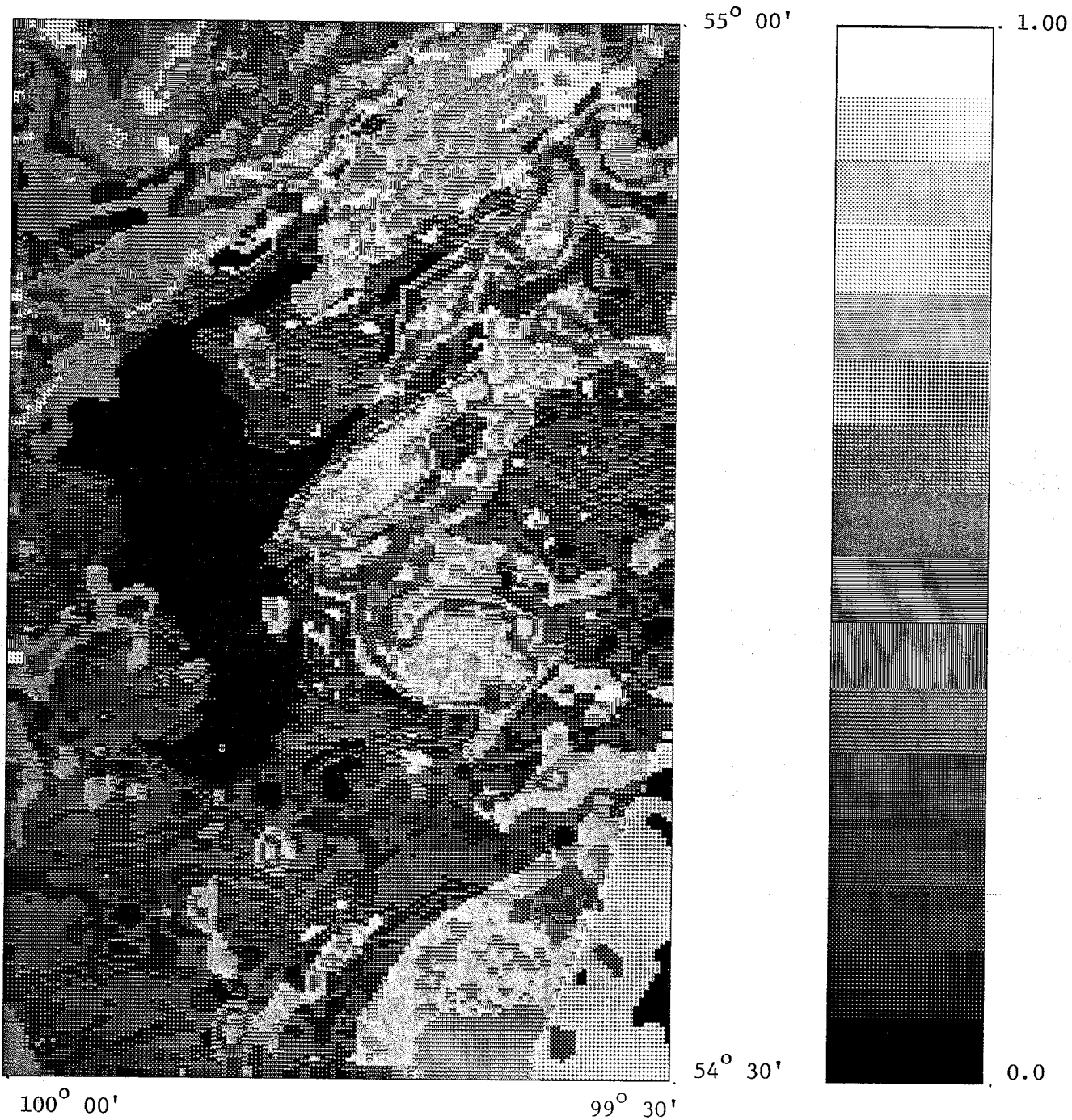


Figure 6.19 Integration of aeromagnetic with filtered TM Band 7 (Expt. 4)

Distance = 55250 m (N-S), 32750 m (E-W)

Pixel size = 216 m (N-S), 257 m (E-W)

Grey scale bar is linear

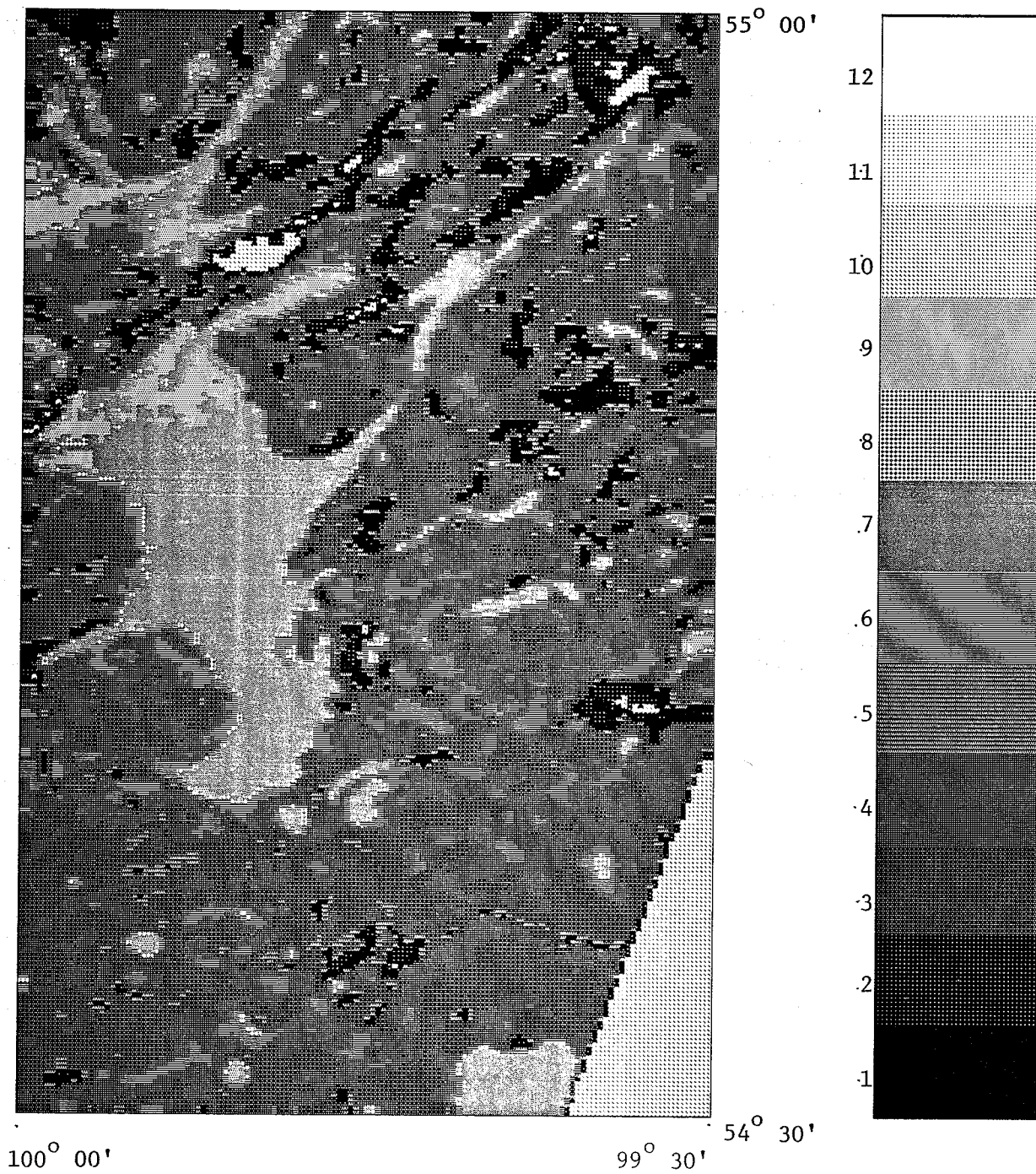


Figure 6.20 TM Band 5 image (After clustering)

Distance = 55250 m (N-S), 32750 m (E-W)

Pixel size = 216 m (N-S), 257 m (E-W)

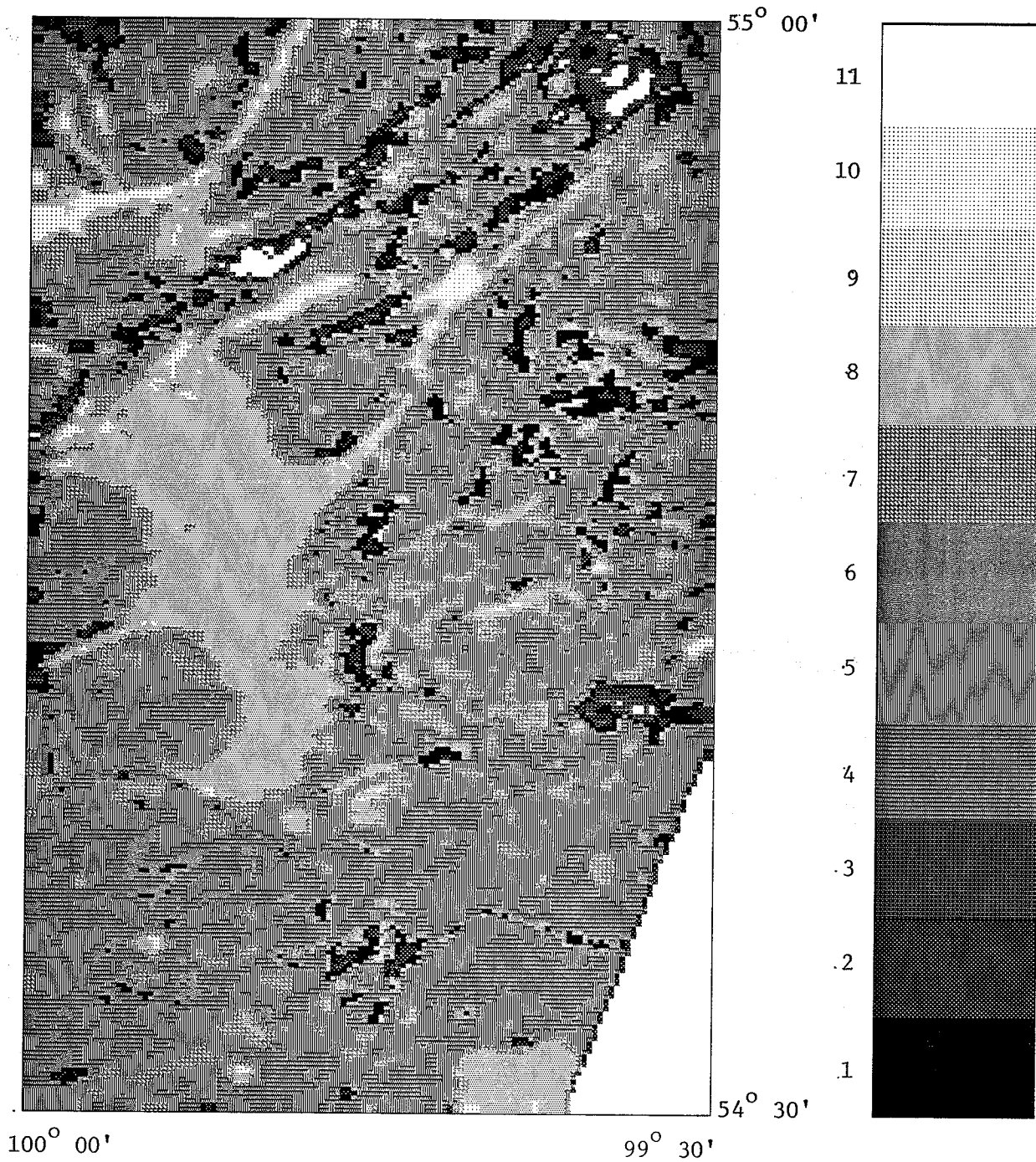


Figure 6.21 TM Band 7 image (After clustering)

Distance = 55250 m (N-S), 32750 m (E-W)

Pixel size = 216 m (N-S), 257 m (E-W)

	GLOBAL PROBABILITY		LOCAL PROBABILITY												
	Promag	Prosat	Aeromagnetic						Satellite (Clustered TM Band 5)						
Greylev* Num			6,7	8	9	10-12	13-16	Other	1	2	3	4	5,6	7-12	
Expt 1	0.3	0.3	0.3	0.1	0.05	0.3	0.5	0.01	0.2	0.01	0.5	0.3	0.3	0.01	
Expt 2	0.3	0.5	0.3	0.1	0.05	0.3	0.5	0.01	0.2	0.01	0.5	0.3	0.3	0.01	
Expt 3	0.3	0.5	0.2	0.05	0.05	0.2	0.3	0.01	0.2	0.01	0.5	0.2	0.2	0.01	
Expt 4	0.5	0.3	0.2	0.05	0.05	0.2	0.3	0.01	0.2	0.01	0.5	0.2	0.2	0.01	
									Satellite (Clustered TM Band 7)						
									1	2,3	4	5	6	7	8-11
Expt 1	0.3	0.3	0.3	0.1	0.05	0.3	0.5	0.01	0.2	0.01	0.3	0.3	0.1	0.2	0.01
Expt 2	0.3	0.5	0.3	0.1	0.05	0.3	0.5	0.01	0.2	0.01	0.3	0.3	0.1	0.2	0.01
Expt 3	0.3	0.5	0.2	0.05	0.05	0.2	0.3	0.01	0.2	0.01	0.5	0.3	0.1	0.2	0.01
Expt 4	0.5	0.3	0.2	0.05	0.05	0.2	0.3	0.01	0.2	0.01	0.5	0.3	0.1	0.2	0.01

* Grey levels separated by comma (,) indicates probability assignment to individual grey levels
 * Grey levels separated by hyphen (-) indicates probability assignment to a group of grey levels

Table 6.3 Probability values for aeromagnetic and clustered satellite data, Lake Wekusko test site

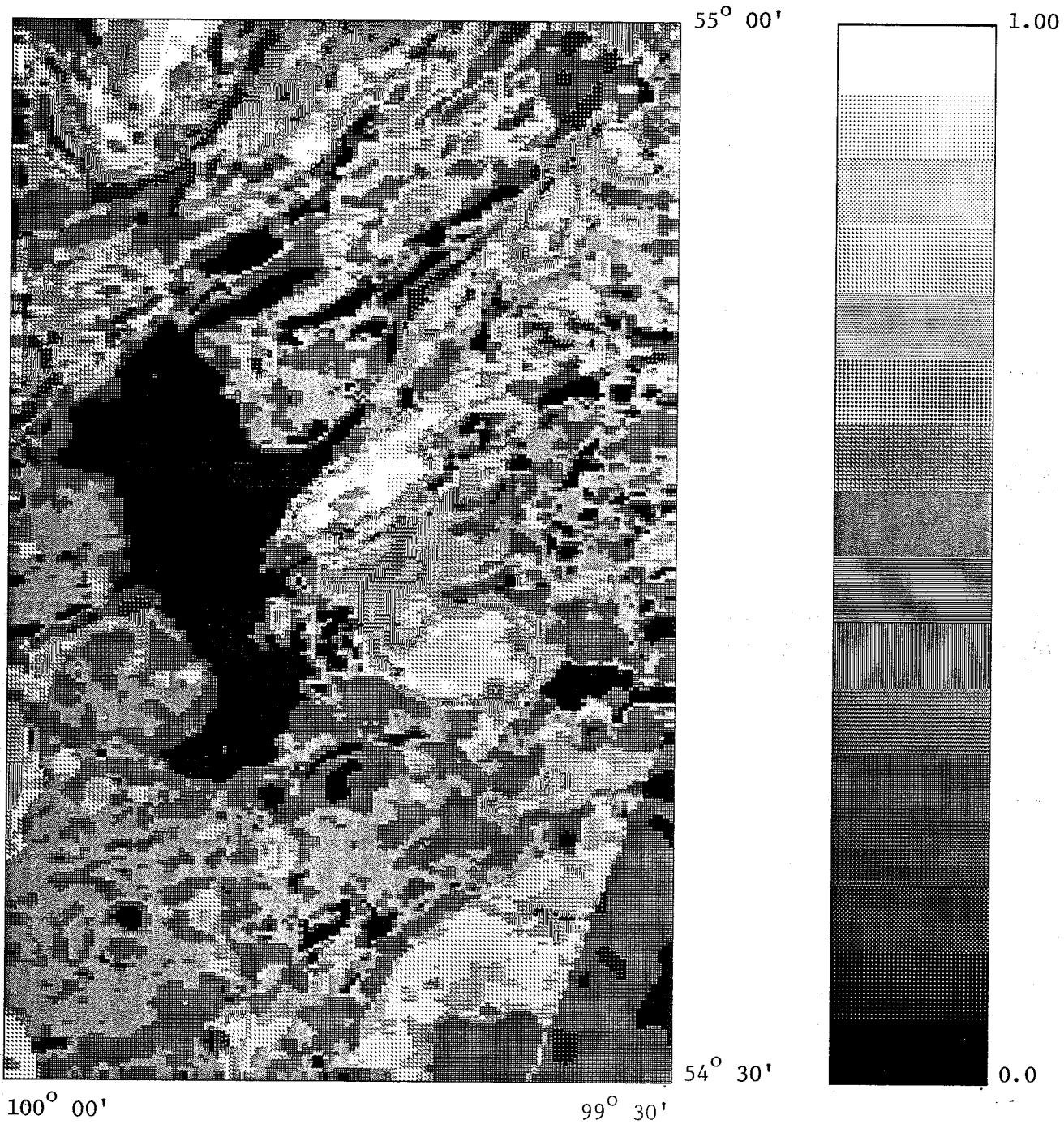


Figure 6.22 Integration of aeromagnetics with clustered TM Band 5 (Expt. 1)

Distance = 55250 m (N-S), 32750 m (E-W)

Pixel size = 216 m (N-S), 257 m (E-W)

Grey scale bar is linear

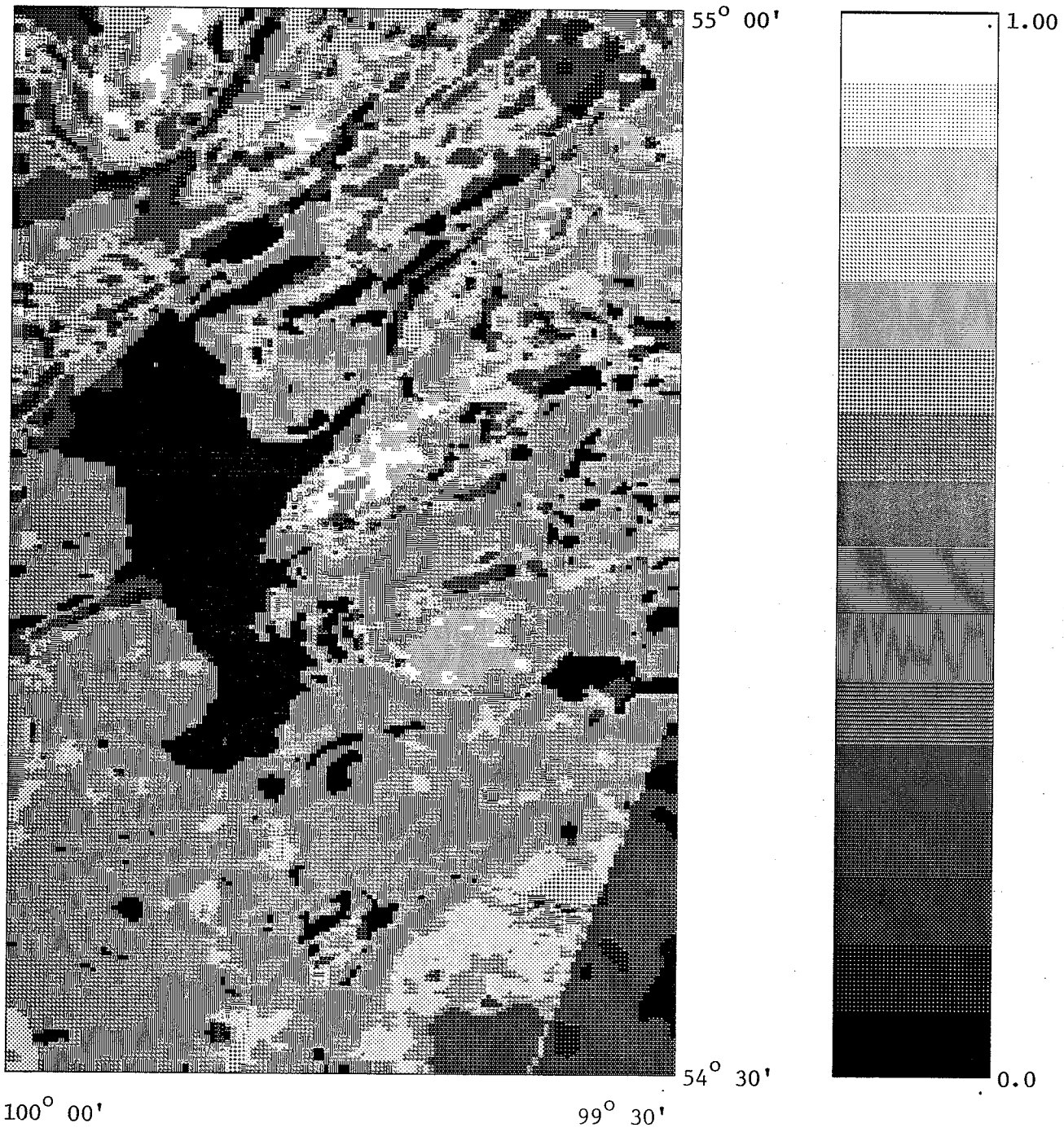


Figure 6.23 Integration of aeromagnetics with clustered TM Band 5 (Expt. 2)

Distance = 55250 m (N-S), 32750 m (E-W)

Pixel size = 216 m (N-S), 257 m (E-W)

Grey scale bar is linear

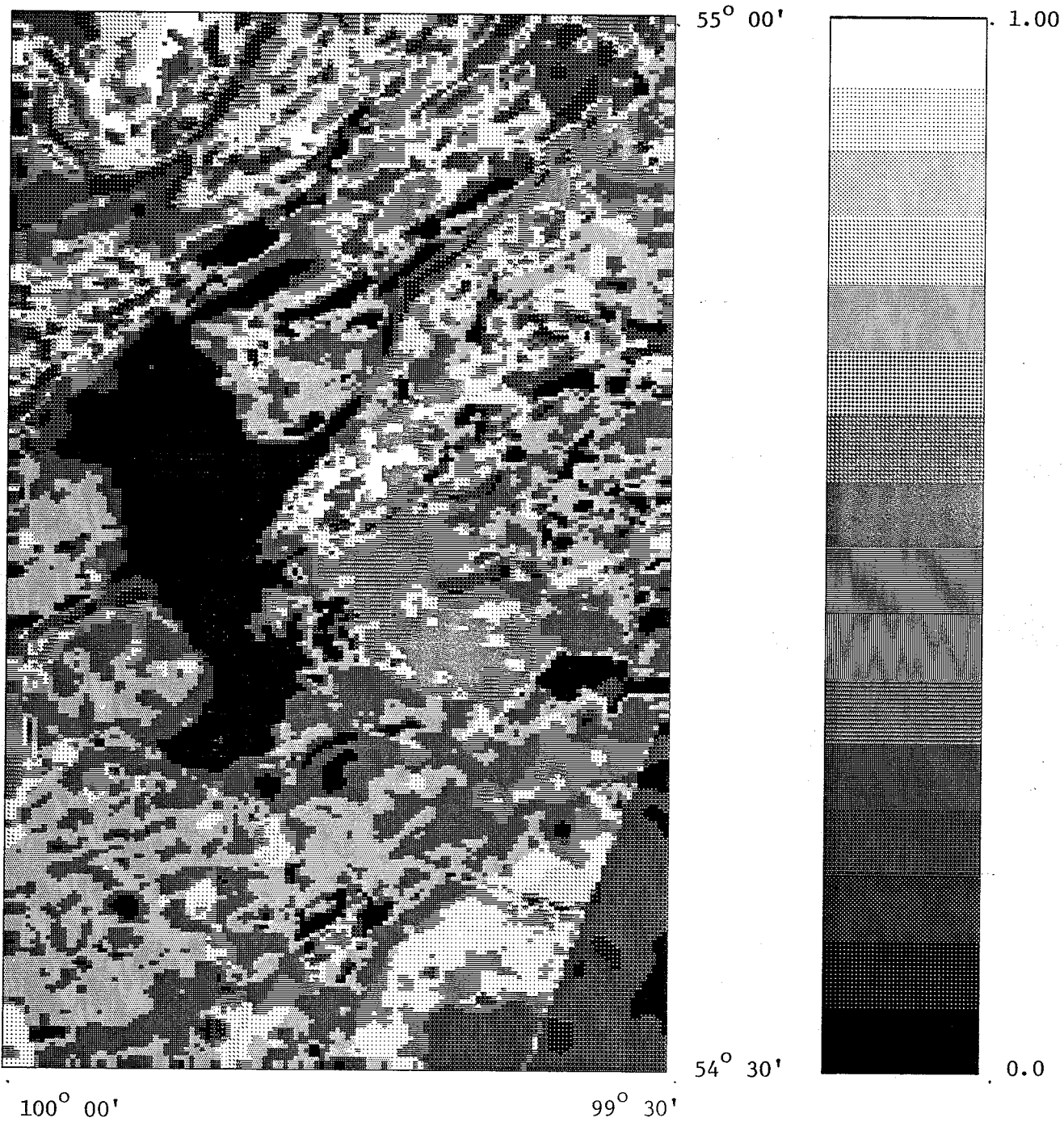


Figure 6.24 Integration of aeromagnetics with clustered TM Band 5 (Expt. 3)

Distance = 55250 m (N-S), 32750 m (E-W)

Pixel size = 216 m (N-S), 257 m (E-W)

Grey scale bar is linear

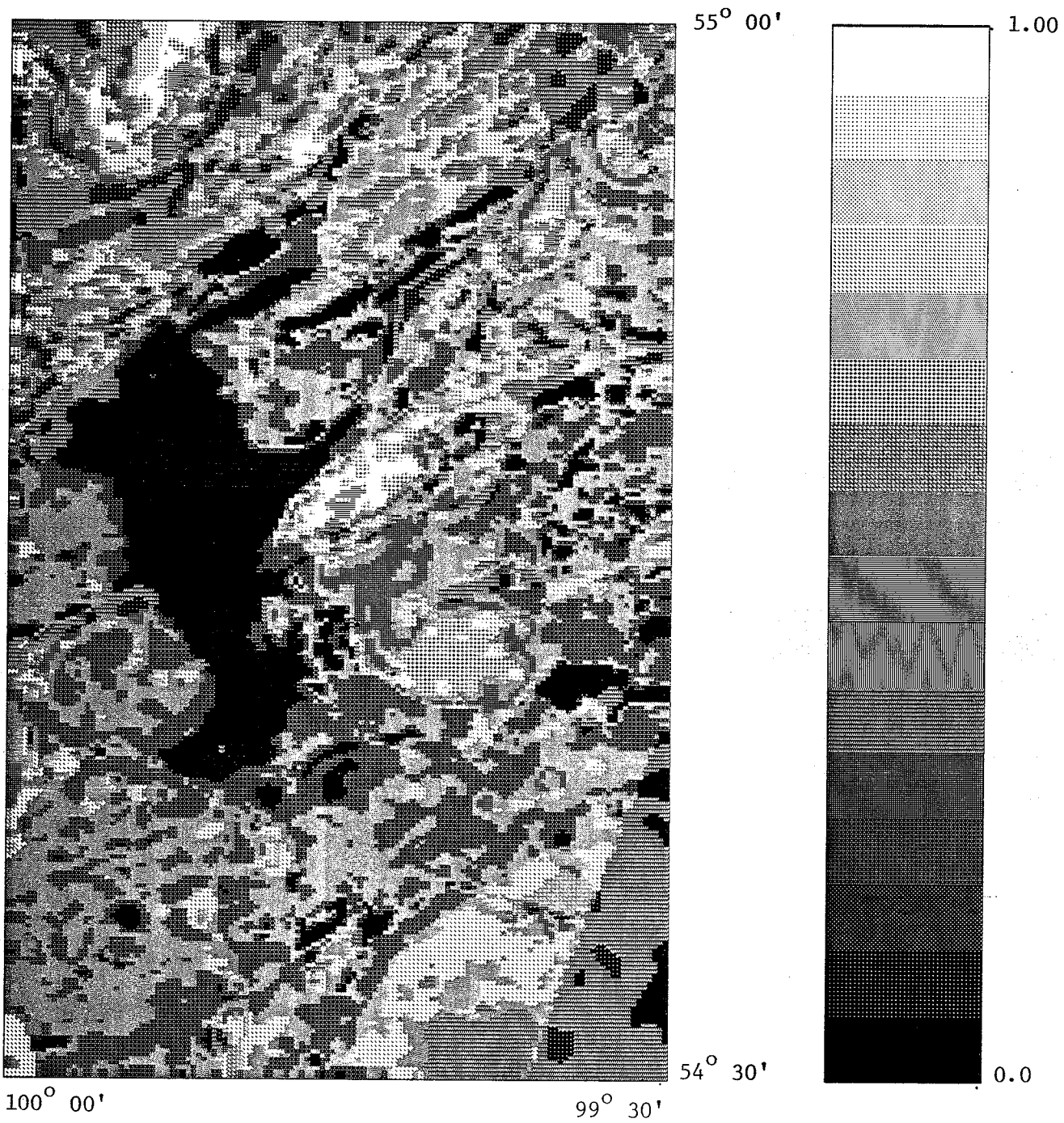


Figure 6.25 Integration of aeromagnetics with clustered TM Band 5 (Expt. 4)

Distance = 55250 m (N-S), 32750 m (E-W)

Pixel size = 216 m (N-S), 257 m (E-W)

Grey scale bar is linear

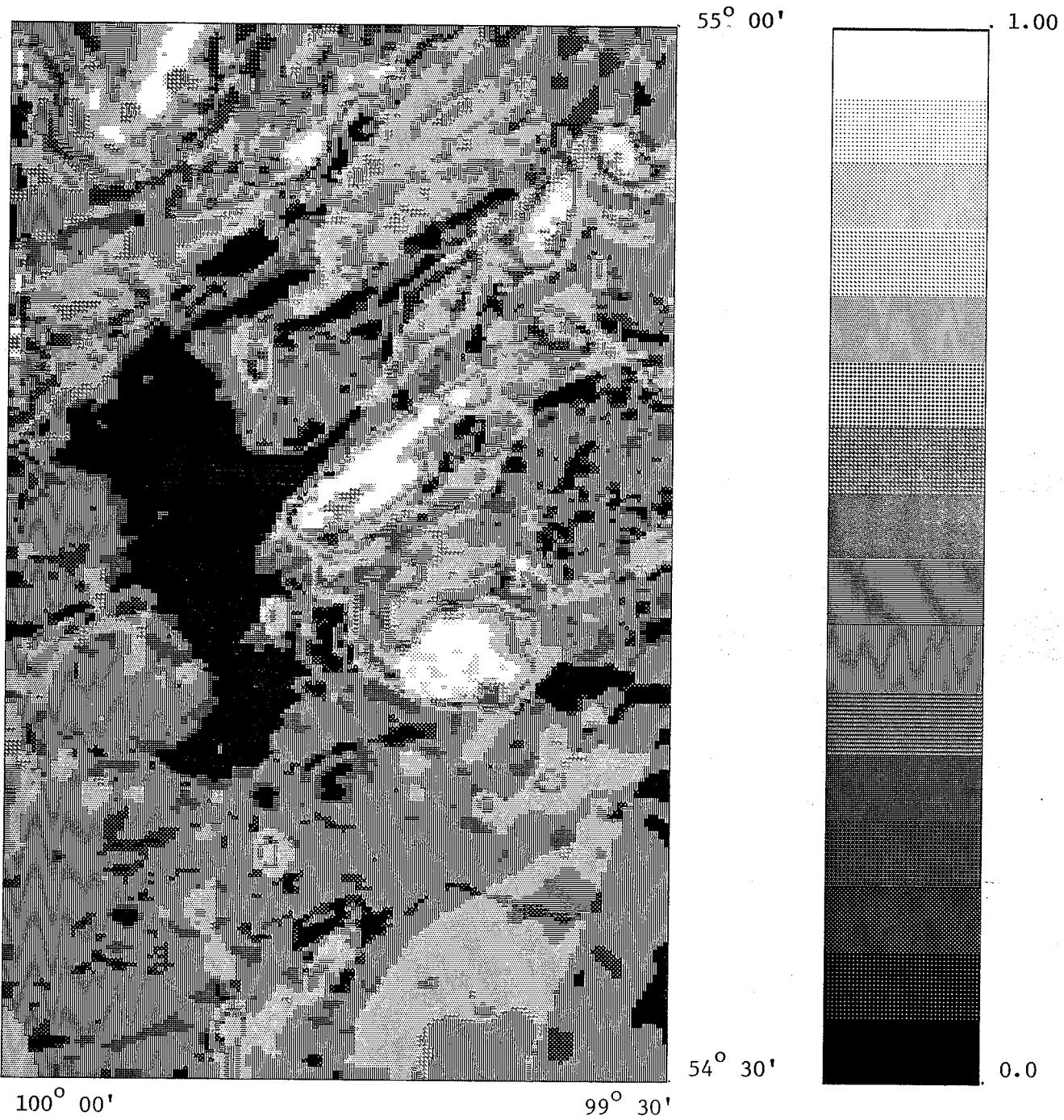


Figure 6.26 Integration of aeromagnetics with clustered TM Band 7 (Expt. 1)

Distance = 55250 m (N-S), 32750 m (E-W)

Pixel size = 216 m (N-S), 257 m (E-W)

Grey scale bar is linear

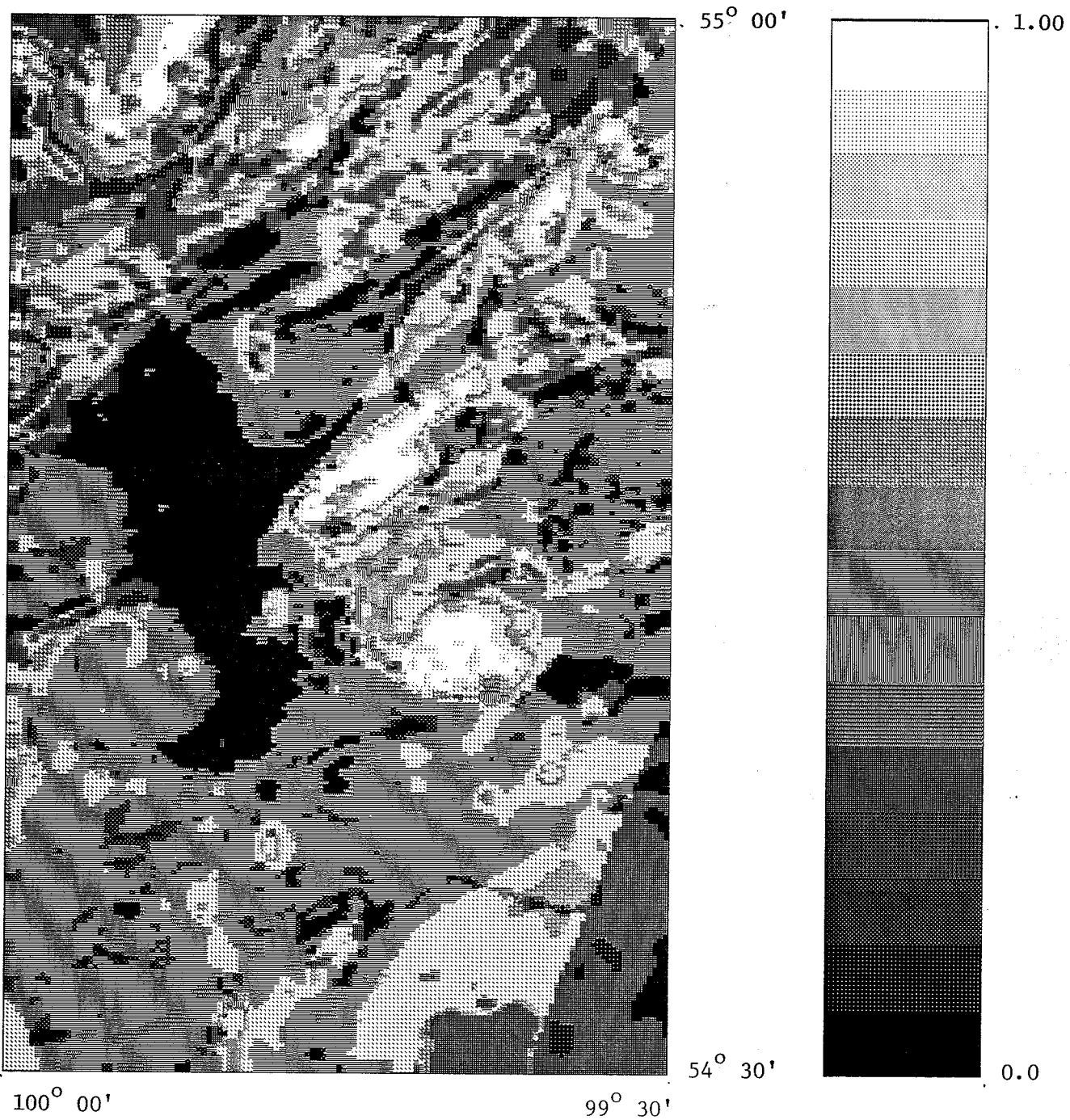


Figure 6.27 Integration of aeromagnetics with clustered TM Band 7 (Expt. 2)

Distance = 55250 m (N-S), 32750 m (E-W)

Pixel size = 216 m (N-S), 257 m (E-W)

Grey scale bar is linear

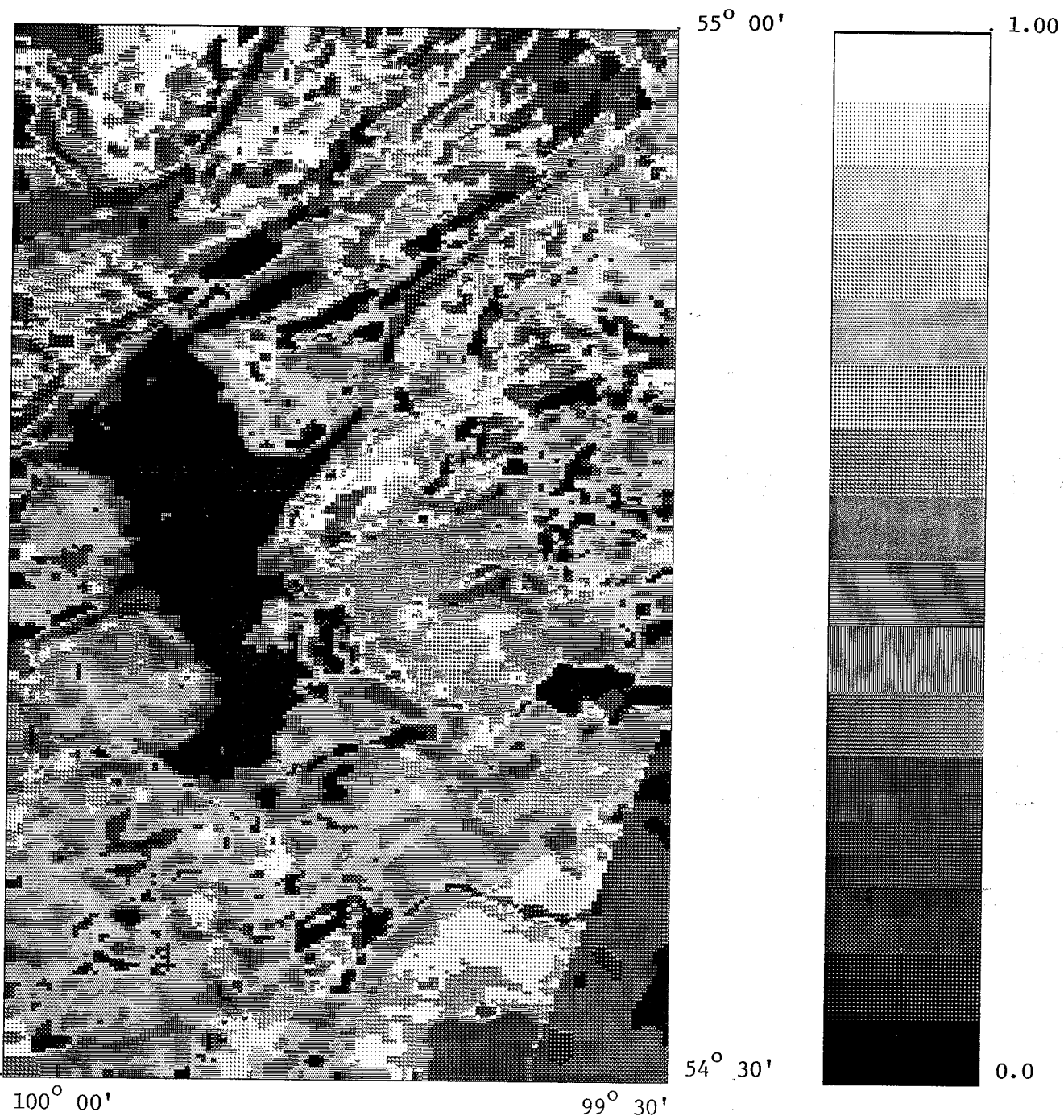


Figure 6.28 Integration of aeromagnetics with clustered TM Band 7 (Expt. 3)

Distance = 55250 m (N-S), 32750 m (E-W)

Pixel size = 216 m (N-S), 257 m (E-W)

Grey scale bar is linear

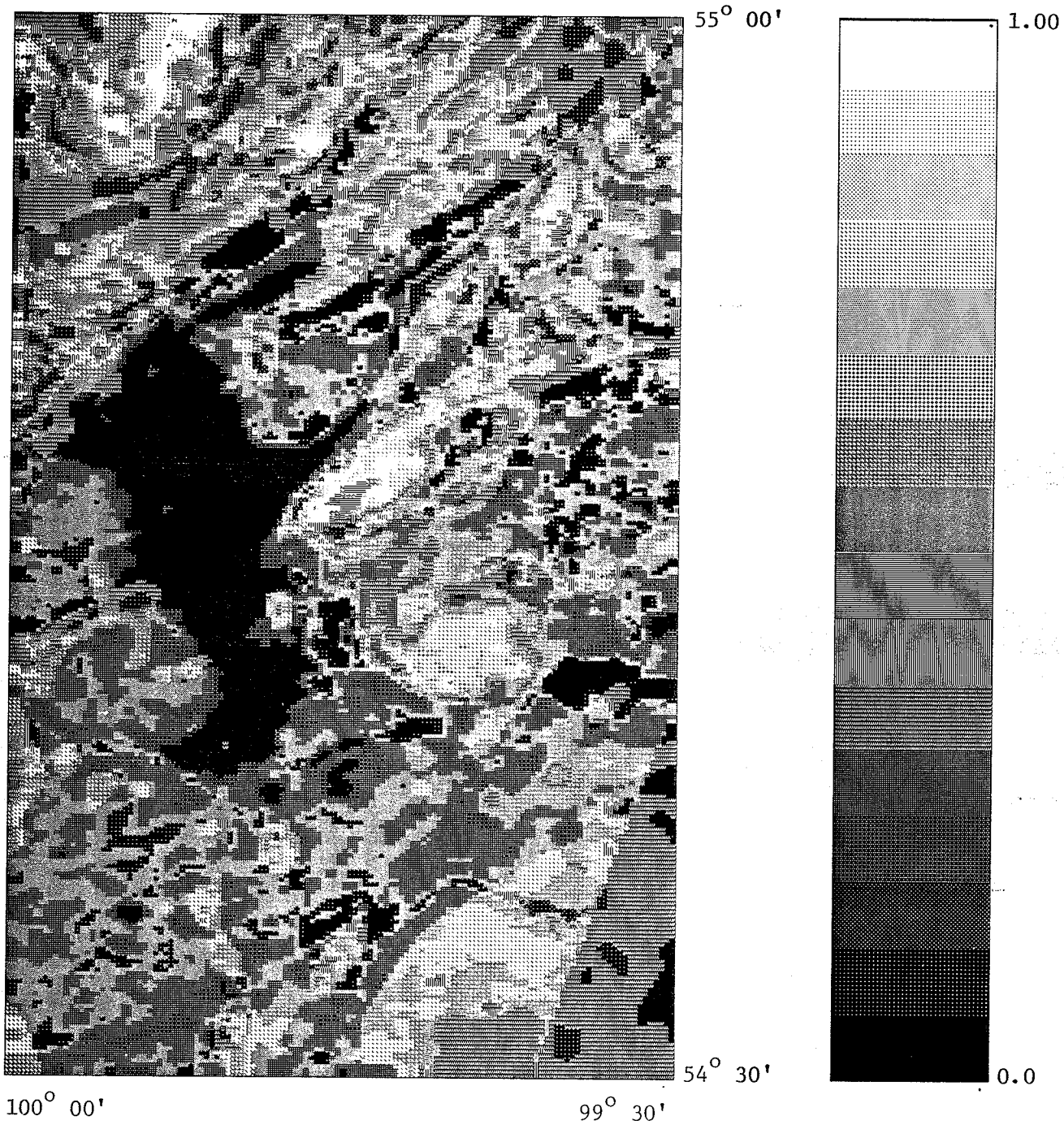


Figure 6.29 Integration of aeromagnetics with clustered TM Band 7 (Expt. 4)

Distance = 55250 m (N-S), 32750 m (E-W)

Pixel size = 216 m (N-S), 257 m (E-W)

Grey scale bar is linear

6.3.3 Interpretation of Results

Comparing the results obtained from the integration process with the known geology and deducing the level of agreement between the results and the geology serves to validate or refute the integration process as an interpretive tool. Here, detailed interpretations of two representative results, from the preceding set of experiments, are presented. The results of integration with the clustered data are selected because clusters represent an unbiased natural grouping of pixels. Also, Expt. 1 of the integration with clustered Band 5 and of integration with clustered Band 7 are chosen because equal global probabilities were assigned to both the aeromagnetic and satellite data. Thus the results are least influenced by the analyst's subjective reasoning. The integration of aeromagnetic data with clustered Band 5 is reproduced in Figure 6.31, and that of aeromagnetic data with clustered Band 7, in Figure 6.32. Both figures are annotated with the corresponding interpretation.

It is important to note that the interpretation is not dependent on the actual values of the probabilities. Rather, well defined areas, regardless of their actual values (grey levels), are interpreted as being representative of lithological units. This is a natural consequence of the local probability assignment discussed earlier. That is, since varying probabilities were assigned to the grey levels in the input data sets, the result of integration will also show varying probabilities. Furthermore, since local probabilities were estimated on the basis of likelihood of that grey level representing a lithological unit, the result will also be so influenced and is interpreted accordingly.

The Amisk Group metavolcanic and metasedimentary rocks are a major lithol-

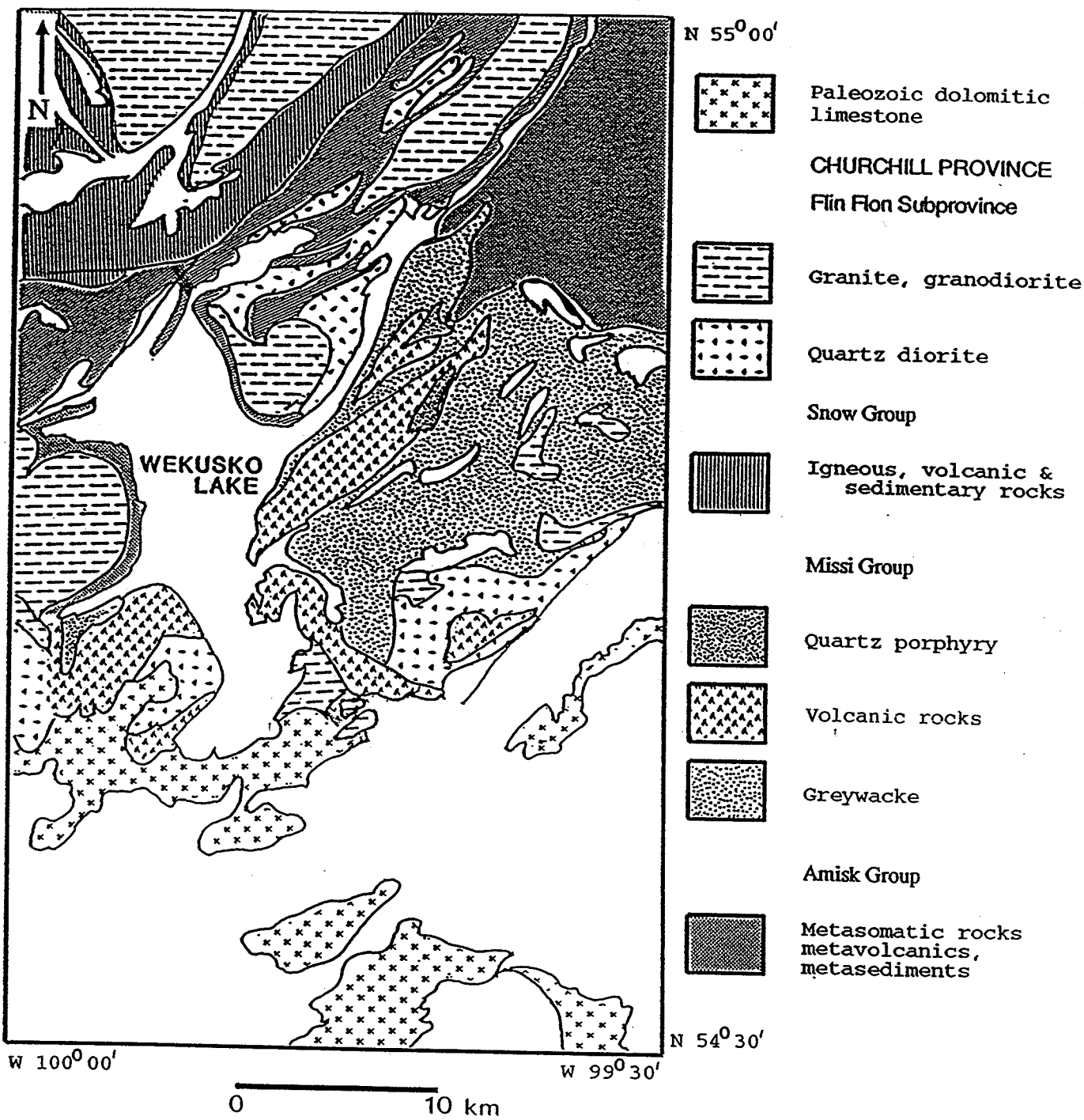


Figure 6.30 Geology of Lake Wekusko test site

Figure 2.10 is reproduced here for comparison with Figures 6.31 and 6.32

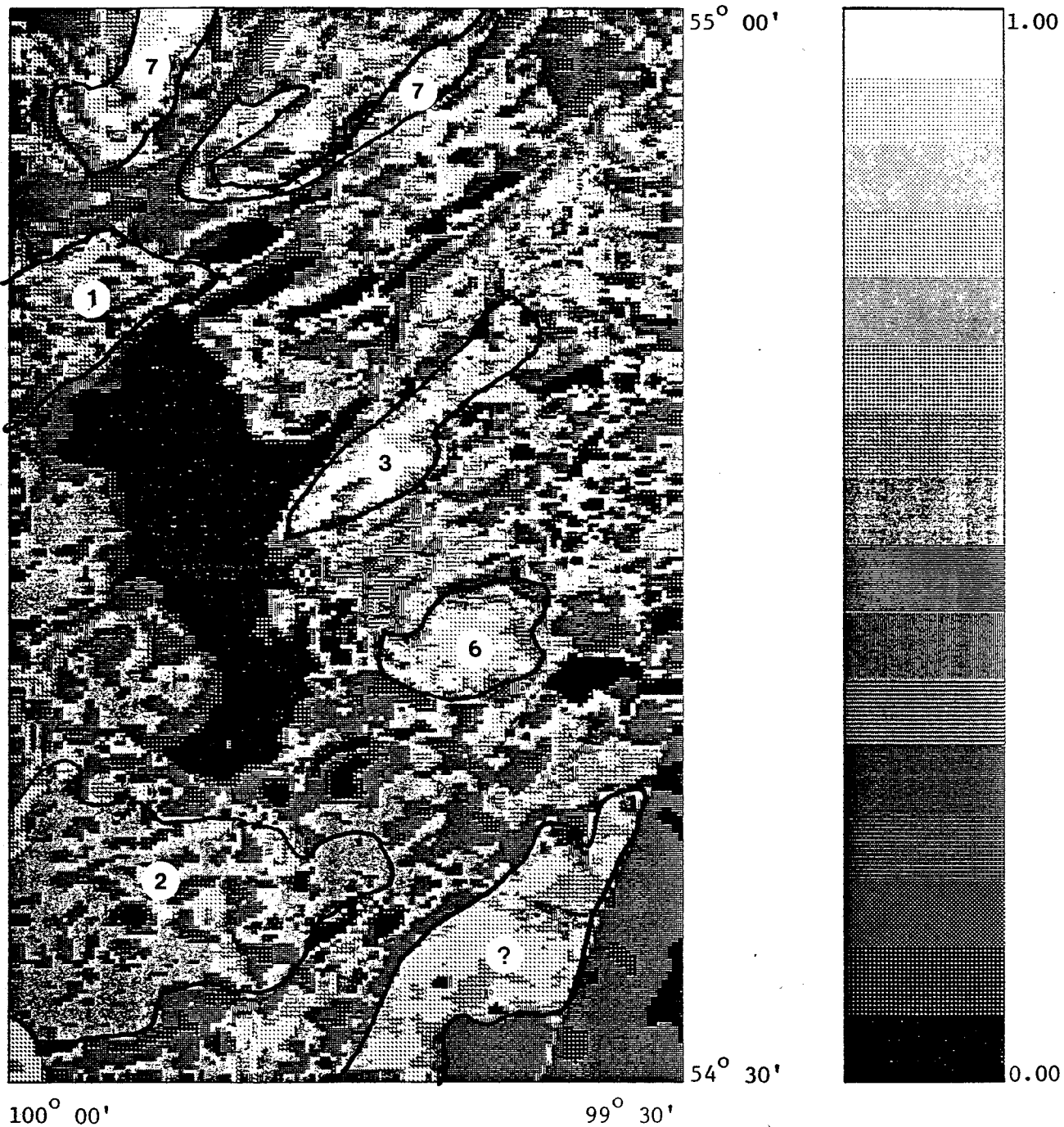


Figure 6.31 Interpretation of integration results (Aeromag. and Clustered TM 5; Expt. 1)

See text for explanation
 Distance = 55250 m (N-S), 32750 m (E-W)
 Pixel size = 216 m (N-S), 257 m (E-W)
 Grey scale bar is linear

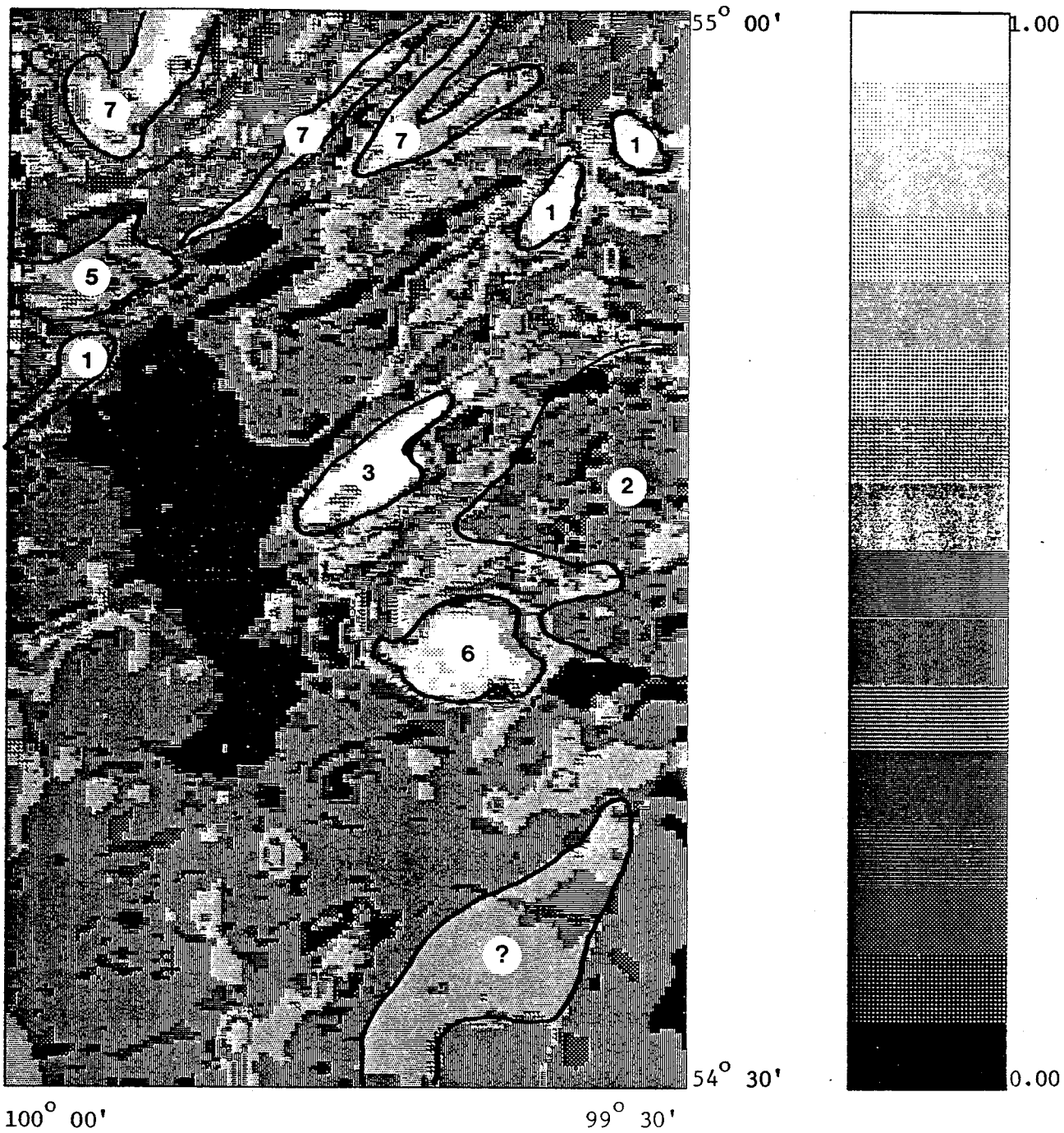


Figure 6.32 Interpretation of integration results (Aeromag. and Clustered TM 7; Expt. 1)

See text for explanation

Distance = 55250 m (N-S), 32750 m (E-W)

Pixel size = 216 m (N-S), 257 m (E-W)

Grey scale bar is linear

ogy in the northern part of the area (Figure 2.10; reproduced here as Figure 6.30 for ease of comparison with integrated data). Some parts of the Amisk Group can be recognized by areas of high probability using Band 5 satellite data (Figure 6.31, Label 1), but are not readily recognizable when Band 7 data are used (Figure 6.32). On Figure 6.31, only the most obvious area of Amisk Group rocks is indicated immediately northwest of Lake Wekusko. However, when the geological map (Figure 6.30) is compared with Figure 6.31, all areas of Amisk Group rocks can be delineated by areas of intermediate to high probabilities. However, these areas merge with other areas of intermediate to high probability, corresponding to other lithologies, and no boundaries can be drawn between the lithologies using the integration results.

Of the three lithologic units in the Missi Group, the quartz porphyry unit cannot be identified in either case, but these are relatively small units. Although the greywacke unit is areally large (Figure 6.30), it is readily identifiable (Label 2) only when Band 7 data are used, as seen in the central eastern part of Figure 6.32. When Band 5 data are used, this delineation is not possible due to the merging of the low to intermediate probabilities (Figure 6.31), making it difficult to infer contacts. Some of the volcanic rocks (Label 3) are unmistakable. In both integration cases they are small, well defined, similarly shaped areas of high probabilities.

Some areas of the Snow Group rocks (Label 5) are identifiable as a cluster of intermediate to high probabilities, to the northwest of Lake Wekusko, when Band 7 data are used (Figure 6.32). But in Figure 6.31, this area tends to merge with intermediate to high probabilities of the Amisk Group. A similar range of values

occurs in the northwest corner of Figure 6.32, where, according to the geology map, a strip of Snow Group rocks are exposed. But the areas are not defined well enough to allow for a delineation.

One of the quartz diorite plutons of the Flin Flon Subprovince is very clearly seen (Label 6) as an area of high probability, to the southeast of Lake Wekusko in both integrations, but other plutons are not easily recognizable. Similarly some of the granite-granodiorite rocks of the Flin Flon Subprovince are easily identifiable (Label 7) on both figures by high to intermediate probabilities.

In the southern part of the Lake Wekusko test site, Paleozoic rocks and glacial deposits overlie the Proterozoic rocks. In Figure 6.31, there is a large area of low to intermediate probabilities that is very similar to the east-central part of the image which is underlain by Missi Group units. Therefore, this is likely an occurrence of the Missi Group (Label 2) under the Paleozoic rocks. This is only identifiable when Band 5 data are used (Figure 6.31); this area cannot be delineated when Band 7 data are used (Figure 6.32).

Another noteworthy feature is the large area of intermediate to high probabilities in the southeast corner, which occurs in both experiments. The probability values of this feature, in Figure 6.31, are comparable to both the Missi Group volcanic rocks (Label 3) and to the quartz diorite of the Flin Flon Subprovince (Label 6). In Figure 6.32, the values are comparable to the granite-granodiorite (Label 7) of the Flin Flon Subprovince. In view of this ambiguous correspondence, unequivocal identification is not possible (Label '?').

The results presented herein show that the algebraic probability can be used

in the mapping of lithological units. It must be stressed, however, that the identification of the units is based on a comparison with known geology. Therefore, it is not suggested that this method, when applied to an unknown area, will help in categorizing or classifying rock units. Rather, the purpose was to demonstrate that various well defined probability areas do correlate with known geology, albeit imperfectly; only the general extent of some rock units could be identified, and one area was shown to have an ambiguous correspondence with the known geology. Further, the relative probabilities are not quantitative indicators of rock units. It is simply the occurrence of probabilities as spatially well defined areas that makes the technique useful. In addition it validates the integration process as well as the probability assignment scheme. Thus, being validated, the results can be used as an *a priori* input in the spatial index method and in the Bayesian approach.

CHAPTER 7

Spatial Indexing Method

7.1 Development and Application

In this method a quantitative assessment of the correlation between maps is obtained by first selecting a reference map. All input data sets are then compared with this reference map. The spatial distribution of each of the grey levels in the input data and that of the reference grey level in the reference map is compared, and this can be readily quantified as the number of pixels common to both. This is a quantitative measure of the spatial correlation or area correlation (Moore and Gregory, 1989) and is used in the computation of the spatial index. Figure 7.1 is a schematic flow chart of this method.

The input data sets in this case are the stretched aeromagnetic data (Figure 3.4) and MSS Band 7 satellite data (Figure 3.12), both for the Wabowden test site. As discussed in the previous chapters these are the two data sets that have the highest information content. Hence the other data sets (MSS Bands 4, 5 and 6) are

Spatial Indexing

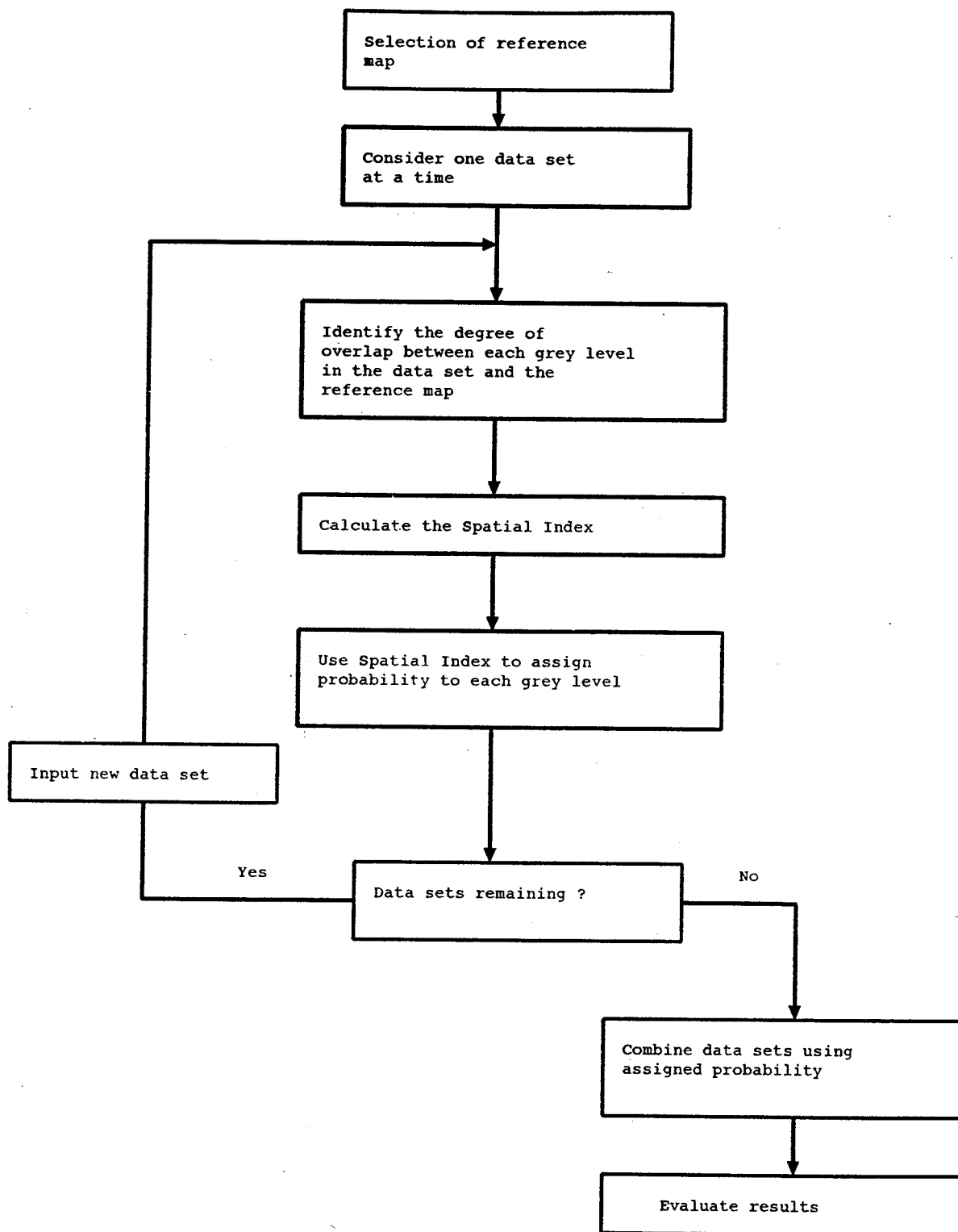


Figure 7.1 Flowchart for the Spatial Index method

not considered.

The digital data integration experiment using spatial indexing involves the following steps:

- 1) In this experiment the gravity anomaly map is used as a reference map. The choice of the -30 to -25 milligal grey level (Grey level 4, Figure 3.1) in the gravity map as the reference zone is based on the results from the algebraic probability method (§6.2.1). Further, Gibb (1968), used gravity data to locate the approximate boundary between the Churchill and Superior Provinces. He placed the boundary at the northwestern edge of the Nelson River high (Figure 2.3), which was produced by granulitic rocks of the Pikwitonei Subprovince. On the gravity map of Figure 3.1, Gibb's boundary corresponds approximately with the zone between -30 and -25 milligals (grey level 4). This gravity zone is selected as the reference feature.
- 2) The degree of overlap between each grey level in the input data set and the specific reference grey level in the gravity map is a measure of the spatial correlation between the two data sets. This is expressed as a percentage using the relation:

$$\text{Spatial Index} = \text{S. I.} = \frac{100 \times \frac{a_{\alpha}}{n}}{\sum 100 \times \frac{a_{\alpha}}{N}} \quad (7.1)$$

where a_{α} is the number of common pixels between the grey level α in the input data and the reference grey level in the gravity map,

n is the number of pixels in the reference grey level of the gravity anomaly map (= 3073),

and N is the total number of pixels in the data set (= 32768).

- 3) This formulation is based on the premise that it provides a ratio of the percentage overlap measured with respect to both the reference grey level as well as the whole image. Thus when no pixels overlap this ratio will equal zero and when a number of pixels overlap the ratio will consequently be large.
- 4) It should be noted that this method does not produce negative values and is analogous to, but not identical to, statistical correlation.
- 5) The final integration is achieved by summing the spatial index pixel by pixel

$$\sum_{k=1}^K = SI_{(i,j,k)} \quad (7.2)$$

where k represents the input data set (out of a total of K) and (i, j) are the row and column indices.

Table 7.1 shows the values of the spatial index for the aeromagnetic and MSS Band 7 data of the Wabowden test site. The grey level numbers of the aeromagnetic and MSS Band 7 satellite data are shown in Figures 3.4 and 3.12 respectively.

As can be seen from Table 7.1, grey level 6 has the highest spatial index for the aeromagnetic data (= 3.638); and grey level 10 has the highest value for MSS Band 7 satellite data (= 3.088). These two grey levels are thus most likely to be spatially associated with the reference grey level in the gravity map. In other words the two grey levels have the highest probability of representing the same geological feature as does the reference grey level in the gravity map. Therefore the two grey levels are assigned a probability of 1.0. Using this as a maxima, the probability of the other grey levels can be readily calculated as a simple proportion thereof. The calculated probabilities are also listed in Table 7.1.

<i>Grey Level Number</i>	<i>Aeromag. Spat. Ind.</i>	<i>Aeromag. Prob.</i>	<i>Band 7 Spat. Ind</i>	<i>Band 7 Prob.</i>
16	0.244	0.070	0.034	0.011
15	0.244	0.070	0.034	0.011
14	0.244	0.070	0.034	0.011
13	0.244	0.070	0.190	0.062
12	0.244	0.070	0.583	0.189
11	0.244	0.070	2.222	0.720
10	0.244	0.070	3.088	1.000
9	0.244	0.070	2.470	0.800
8	0.244	0.070	0.990	0.321
7	0.475	0.130	0.228	0.074
6	3.638	1.000	0.062	0.020
5	3.380	0.930	0.038	0.012
4	0.244	0.070	0.034	0.011
3	0.244	0.070	0.048	0.016
2	0.244	0.070	0.162	0.052
1	0.244	0.070	0.445	0.144

Table 7.1 Spatial Index values, Wabowden test site

The two data sets are then integrated according to Equation 7.2. Here the value of K, the total number of data sets is 2 and the calculated probabilities are substituted for SI(i,j). The result of this integration process is shown in Figure 7.2.

7.2 Interpretation of Results

In Figure 7.2 there is a zone of relatively high probability extending from the northeast corner to the southwest corner. It is approximately 10 km wide in the northeast widening to about 15 km in the southwest. This change in width may reflect the 3 to 6.5 km width of the reference grey level in the gravity map, which, in turn, may correspond with a southwestward widening lithologic unit. If Gibb's

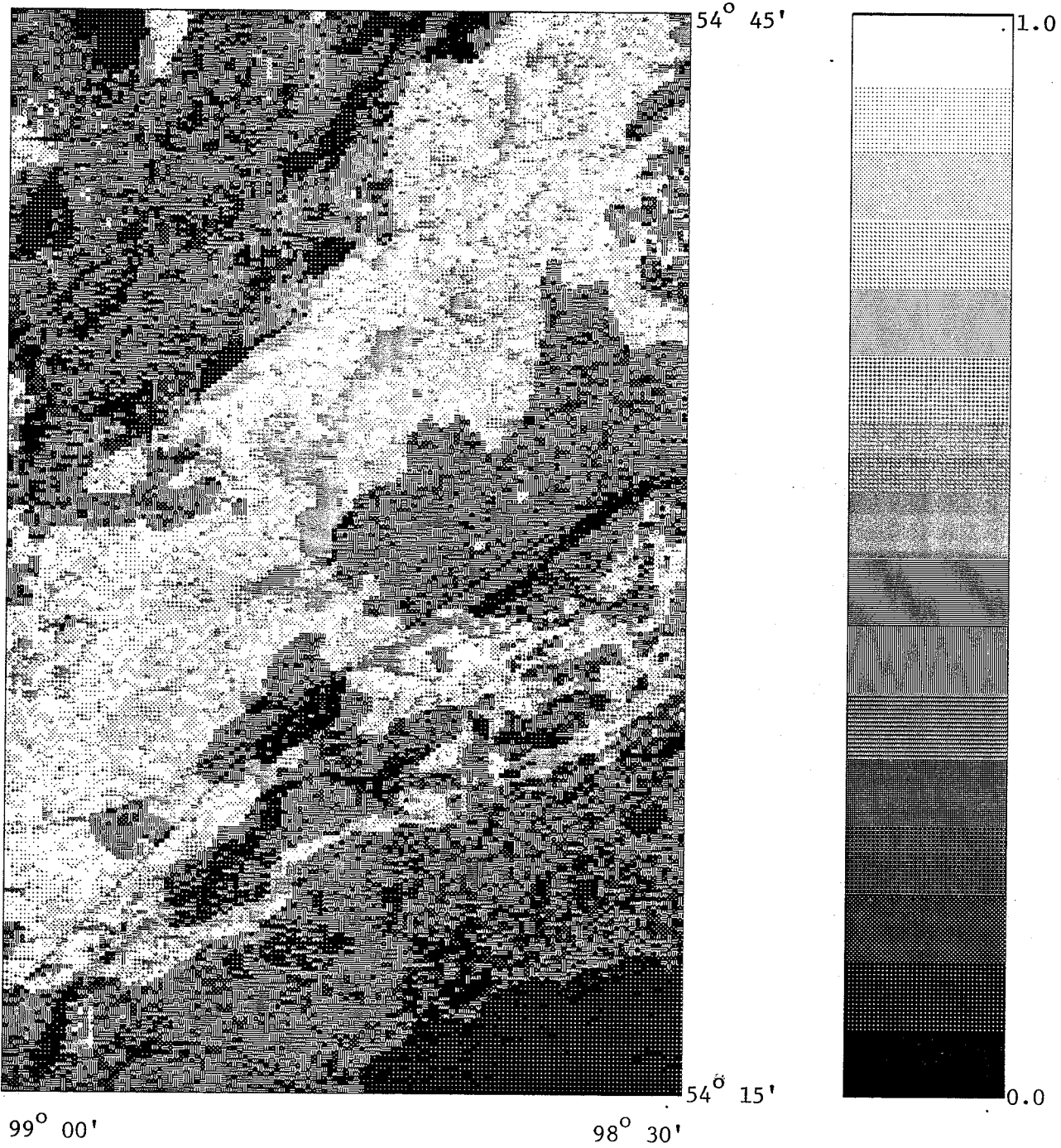


Figure 7.2 Result of integration using spatial index method

Distance = 55250 m (N-S), 32750 m (E-W)

Pixel size = 216 m (N-S), 257 m (E-W)

Grey scale bar is linear

(1968) interpretation of the location of the Churchill-Superior province boundary is correct, then the zone of relatively high probabilities on Figure 7.2 could be mapping a wide zone of tectonic overlap between the two structural provinces. Recent bore-hole core logs show that the boundary zone increases in width southwestward beneath the Paleozoic rocks (McGregor *et al.*, 1992, Pers. Comm.), in much the same way as the zone of high probabilities increases in width.

More recent research (e.g. Weber, 1990) equates the Thompson Belt with the boundary zone between the Churchill and Superior provinces. A comparison between Figure 7.2 and the geological map of the Wabowden test site (Figure 2.9) shows that the possible boundary zone as mapped by the spatial index method has very little overlap with the Thompson Belt. Indeed, for the most part, the high probability zone is southeast of the Thompson Belt.

This aspect is discussed in greater detail in subsequent chapters. For the present it is prudent to test other methods to see if the results can be further refined. The next method of integration that is tested is the method of Bayesian Probability.

CHAPTER 8

Bayesian Probability Method

8.1 Introduction

The main objective of statistical analyses is making inferences (predictions, decisions) about a population based upon information contained in a sample. Statistical analyses are characterised by five elements, (a) specification of the problem and related population, (b) sampling procedure, (c) analysis of samples, (d) using the sample data to make an inference about the population, and (e) estimating the reliability of the inference (Canavos, 1984). In classical statistics, sample evidence provides the sole information about the parameter of interest. Bayesian statistics, on the other hand, is based on the premise that some prior information is almost always available and must be taken into account. Thus Bayesian Inference is a function of both sample evidence and other information. In both types of statistics, the ultimate aim is quantification of information and evaluation of uncertainties in the final inference based on probability. That is, “the central function of Bayesian

statistics is the provision of probabilities to quantify prospective uncertainties given a current state of knowledge" (Dempster, 1985). Further, classical statistics assumes that a given parameter has a single value to be estimated. Bayesian statistics assumes that the parameter has a probability distribution rather than a single value.

The classical definition of probability (Press, 1989) was developed in relation to games of chance, in which outcomes of certain events are mutually exclusive as well as equally likely. This means that the probability of occurrence of an event is equal to the probability of occurrence of any other event and that both cannot occur simultaneously. In reality, however, these conditions are seldom met. Therefore, the probability is approximated by the relative frequency of the outcomes derived from a number of repeated performances of the experiment under identical conditions. The underlying principle being that, after a sufficiently large number of repetitions, the estimated probability of an event approaches the true probability. Again, there are a number of instances where it may not be possible to repeat an experiment a sufficient number of times, nor to do so under identical conditions. In such cases a subjective interpretation of probability is used where the analyst's conviction about the occurrence of an event provides an estimate of the probability. The assumed probability distribution (*a priori* probability) can be combined with additional evidence to form a new modified distribution (*a posteriori* probability) by means of Bayes' Theorem.

Thus given a set of n mutually exclusive events $B_1, B_2, B_3, \dots, B_n$, Bayesian theory relates the *a priori* and the additional information to the *a posteriori* prob-

ability as (Canavos, 1984):

$$P(B_j|A) = \frac{P(B_j)P(A|B_j)}{\sum_{i=1}^n P(B_i)P(A|B_i)}, \quad j = 1, 2, 3, \dots, n \quad (8.1)$$

where

$P(B_j)$ is the *a priori* probability of event B_j ,

$P(A|B_j)$ is the conditional probability of event B_j , computed on the basis of evidence provided by data A, observed under a specific alternative B_j ,

and $P(B_j|A)$ is the *a posteriori* probability of the event B_j .

The implication of this theorem is that it provides a means to update the state of knowledge. In other words, as more data become available the *a posteriori* probability can be progressively revised in sequential stages to form new estimates of the probability distribution. Also, the *a posteriori* probability obtained at the end of the first stage becomes the new *a priori* probability for the commencement of the second stage and so on.

Agterberg *et al.*, (1972), using a cell-based approach, demonstrated the application of Bayesian probability to mapping potential zones of copper and zinc mineralisation, and Favini and Assad (1979) applied a similar approach to massive sulphide exploration. Lindley (1991) cited illustrations of the effect of each successive stage of accumulated evidence on an initial subjective probability and its implications in reaching a verdict in a court of law.

8.2 Application of Bayesian Probability Theory

As indicated earlier, Bayesian statistical inference can be used to minimize the uncertainties resulting from multiple data integration. To start with, an independent data set can be used to estimate the *a priori* probability of the occurrence of the target proposition, which, in the Wabowden test site is the boundary zone. Then the available data sets are treated as additional evidence to compute its revised *a posteriori* probability.

Initially the *a priori* probability of the occurrence of the boundary between the Churchill and Superior Provinces is obtained from the gravity anomaly map as a ratio of the number of pixels in the -30 to -25 milligal range to the total number of pixels in the image. The selection of this particular zone is based on the results obtained from the algebraic probability method. The spatial location of the zone of high probability, as mapped by this method, coincides largely with the -30 to -25 milligal range in the gravity anomaly map. Further, an independent study (Gibb, 1968) showed that the location of the boundary corresponds with the zone between -30 and -25 milligals (Grey level 4) of Figure 3.1. Areal measurements of grey levels are obtained by a simple count of the number of pixels in that grey level. In the next step, the intersection of each grey level with the gravity anomaly of interest is computed by finding the number of common pixels between the two. This is a measure of the spatial relationship between the grey levels in different data sets and the reference grey level in the gravity anomaly map.

Table 8.1 lists the parameters derived from the different data sets and used in

the integration procedure. Some grey levels in the aeromagnetic and satellite data do not intersect with the reference grey level in the gravity map, i.e. the number of common pixels is zero. Therefore these are assigned extremely low values in columns (e) and (h) of Table 8.1. This was done to eliminate the need to store extremely small values in the buffer memory during program execution. This limitation on floating point storage capacity is hardware dependent.

The sequence of the analysis is as shown in Figure 8.1, where a pair of data sets is considered in each step. The *a posteriori* probability obtained from the first pairwise integration is used in the next stage of integration. Theoretically any number of additional data sets can be integrated in this manner. Usually, the sequence is terminated when no significant improvement is perceived. In the present case, the stretched aeromagnetic data (Figure 3.4) and MSS Band 7 satellite data (Figure 3.12) form the integration pair with the gravity data (Figure 3.1) providing the *a priori* information. If more data sets were available, such as finer resolution TM or SPOT data, they would in turn be subjected to a pairwise integration. In the absence of such additional data, the current experiment can only be done once.

8.2.1 Bayesian Integration

Referring to the Bayes' Rule (Equation 8.1), in the present analysis, $P(B_j)$ is the *a priori* probability of the occurrence of the Churchill-Superior boundary zone derived from the gravity anomaly map where it lies between -25 to -30 mgals (Gibb, 1968). In terms of grey level this is Unit 4 (Table 8.1) with an *a priori* probability of 3073.0/32768.0 .

Gravity Anomaly Fig. 3.1		Satellite (MSS 7) Fig. 3.12			Aeromagnetic Anomaly Fig. 3.4		
GryLev Num	Num of pixels	GryLev Num	Num of pixels	Num of common pixels	GryLev Num	Num of pixels	Num of common pixels
(a)	(b)	(c)	(d)	(e)	(f)	(g)	(h)
1	1017	1	2336	129	1	107	100
2	3669	2	623	47	2	91	100
3	3699	3	202	14	3	1129	100
4	3073 *	4	157	10	4	4097	100
5	5273	5	206	11	5	7201	1386
6	3566	6	415	18	6	5549	1492
7	6322	7	1076	66	7	3455	195
8	6149	8	3362	287	8	4133	100
		9	7288	716	9	2822	100
		10	8555	895	10	1751	100
		11	5896	644	11	1411	100
		12	1972	169	12	530	100
		13	531	55	13	225	100
		14	125	10	14	83	100
		15	20	10	15	89	100
		16	4	10	16	95	100
	32768		32768			32768	

* Grey level 4 in column (a) provides the value of $P(B_j)$

NOTE 1: Column (e) and (h) refer to the number of pixels common between the corresponding grey level and grey level 4 in column (a).

NOTE 2: Values less than 10 in column (e) and less than 100 in column (h) have been treated as equal to 10 and 100 respectively. See text for details.

Table 8.1 Table of parameters used in the Bayesian integration procedure

Bayesian Integration

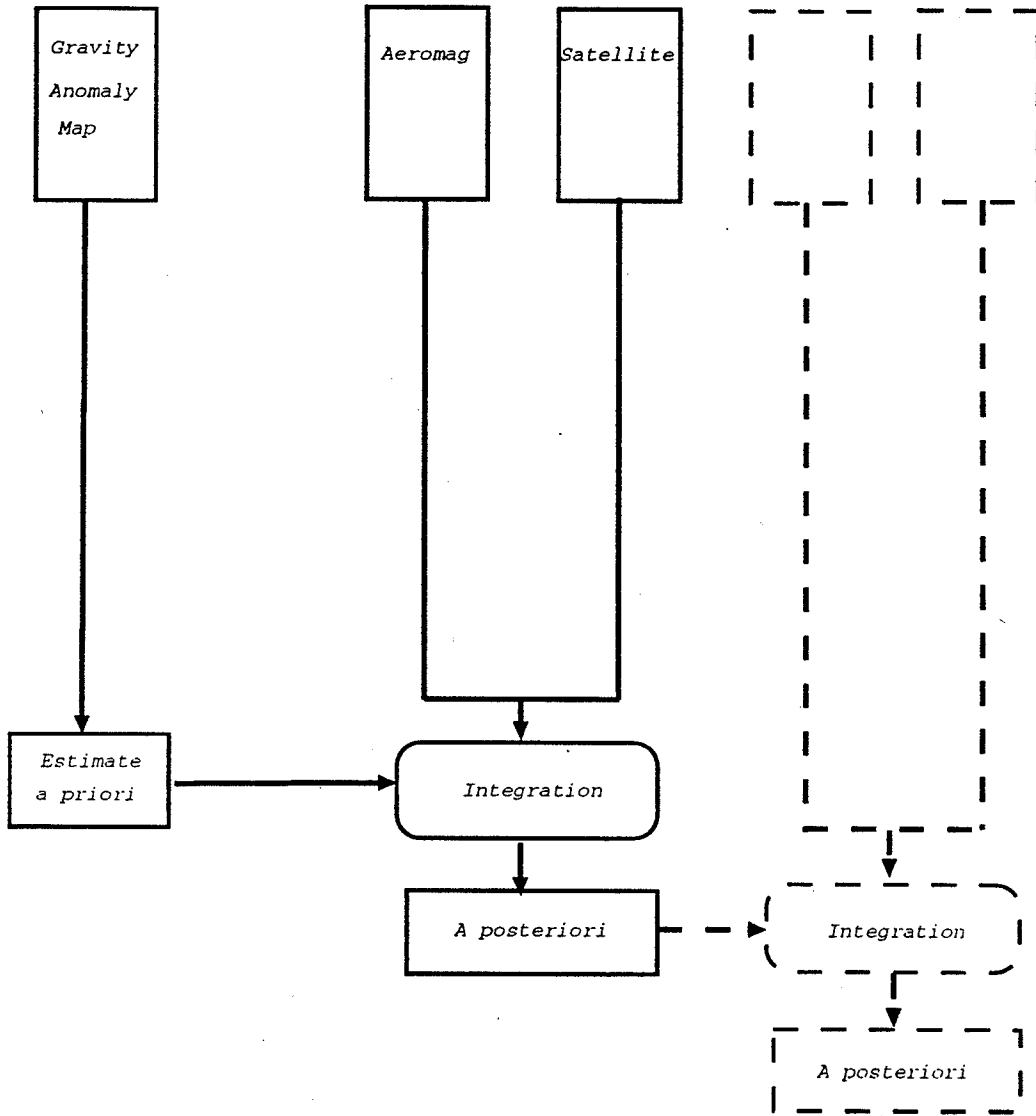


Figure 8.1 Flowchart for the Bayesian integration procedure

If A represents the additional evidence provided by say, the aeromagnetic map then $P(A|B_j)$ is the conditional probability that a given pixel in the aeromagnetic map belongs to the boundary zone given the condition that the boundary zone occurs with a certain *a priori* probability. The value of $P(A|B_j)$ is computed as the ratio of the joint probability to the marginal probability. To compute the joint probability the number of pixels that are common to the aeromagnetic anomaly pattern under consideration and the gravity pattern of the boundary are determined. The marginal probability is simply the ratio of the number of pixels in the pattern under consideration to the total number of pixels. This method of computation is done on a pixel by pixel basis for the aeromagnetic anomaly and the MSS Band 7 data and the *a posteriori* probability determined (Figure 8.2).

If an additional pair of data sets were available they would be similarly processed, but the *a posteriori* probability computed in the preceding stage then becomes the new *a priori* probability. Although MSS Band 4, 5 and 6 data are available for the test site, these were not used because a visual examination reveals that Band 4 and 5 are not of adequate quality to provide some improvement in the results. Band 6 and Band 7 are very similar in spectral signatures because they are both in the near infrared region. Further, amongst the four, Band 7 has the greatest spatial variation and therefore maximum information content (Chavez, 1992).

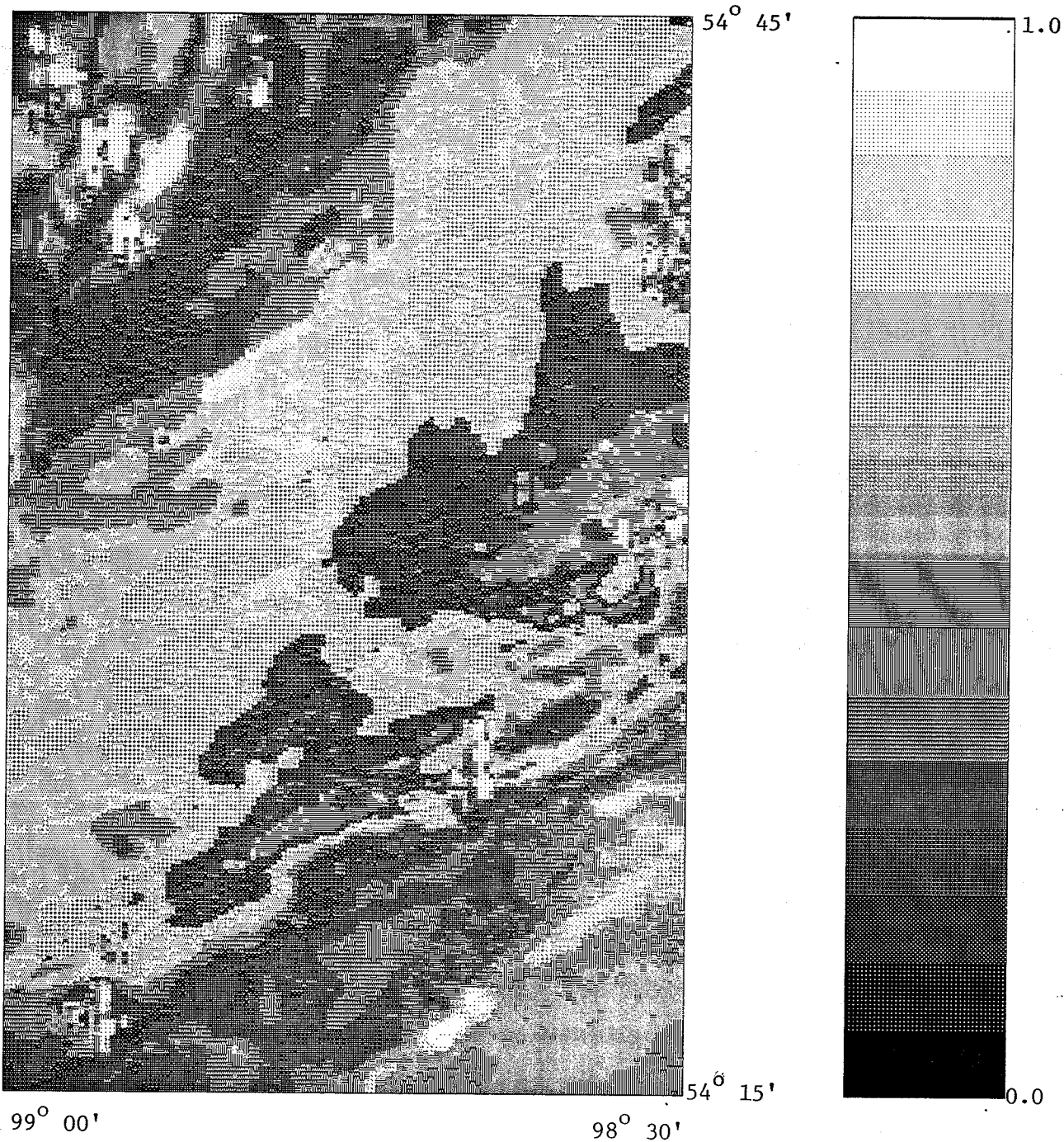


Figure 8.2 *A posteriori* probability map from the integration of aeromagnetic and MSS Band 7 data using gravity data as *a priori*

Distance = 55250 m (N-S), 32750 m (E-W)

Pixel size = 216 m (N-S), 257 m (E-W)

Grey scale bar is linear

8.3 Interpretation of Results

In Figure 8.2 a zone of relatively high probability trending NE is clearly seen. Although absolute values are different, the general patterns in Figure 8.2 and the results of the Spatial Index method (Figure 7.2) are very similar. If the *a priori* postulation is correct, and the assigned gravity corresponds to the boundary between the Churchill and Superior provinces, then the zone of high probabilities outlines the boundary zone. Once again it is evident that the boundary is a wide zone, extending much farther southeastward than the eastern edge of the Thompson Belt.

This result combined with recent work by other workers allows us to revise the known geology and produce an updated map, which is presented later. In essence, the fundamental purpose of using an integrated approach to revise and update existing information is fulfilled.

CHAPTER 9

Conclusions

The objective of this study was to develop a method by which diverse geological, geophysical and satellite data can be effectively utilized in combination to extract maximum possible information oriented towards automated mapping of geological features in the Wabowden and Lake Wekusko test sites. Considering the interdisciplinary nature of most modern earth science research (e.g. Welch *et al.*, 1988), the development of a method of integration of data sets is of crucial importance.

The method of integration demonstrated in the present study has several advantageous features:

- (1) The method is flexible and can be adapted for use with other data sets. Although raster format is preferred, the method can be modified to include other formats.
- (2) Including additional data sets as and when they become available is straight-

forward.

- (3) Implementation of the method requires standard hardware components such as a digitising table and a micro- or mainframe computer. Production of hard copy outputs may require some photo-optic reading/writing hardware.
- (4) The method is portable and can be readily transported between operating systems as well as programming languages.

One important consideration is that the algebraic probability, spatial index, and Bayesian integration form a natural progression of spatial data integration and information extraction. The algebraic probability method is the most flexible in that no initial field-based information is needed. The results from the algebraic probability method provide *a priori* information that can be used in a subsequent method.

The assignment of probabilities is, to some extent, based on the analyst's judgement of the geological significance of the anomalies in the data sets. Arguably, the need for an expert analyst to perform the visual interpretation makes the method dependent on the level of expertise of the analyst. This is no different from other artificial intelligence techniques where the rules are formulated by the expert. For example, in PROSPECTOR, an artificial intelligence program for mineral exploration, the link between rules is characterised by numbers, which are based on subjective guesses by experienced scientists (Agterberg, 1989b).

Initially, conventional digital image processing techniques were applied to satellite data of the Lake Wekusko test site. Principal Component Transform, which in

many cases is a very effective information extraction method (Chavez and Kwarteng, 1989; Fung and LeDrew, 1987), served to delineate the fold structures near Angus Bay (Figure 5.2b) in the northwestern part of Lake Wekusko test site. The combined C-SAR and TM data also helped identify some lineaments. This is useful because mineralisation is commonly related to lineament zones (Heyl, 1983). Although they were not attempted here, methods such as the IHS transform (Carper *et al.*, 1990; Harris *et al.*, 1990) may provide some improvement. These methods were not attempted partly due to lack of time and resources but mainly because the major thrust of the present work was the application of probability techniques to data integration.

In most studies involving integration of multiple data sets, some initial information is required, on the basis of which an integration procedure is developed. This information is compiled on the basis of field studies. However, such initial information may not be available, particularly in inaccessible areas. In such cases remotely sensed data can be readily acquired but the means to integrate the data sets must be constructed without benefit of initial field based investigations. In the present study a method was developed which addresses this problem.

The Churchill-Superior Boundary Zone

In the Wabowden test site the main objective of this work was to develop a statistically valid method of integration of geological and geophysical data sets, particularly a method that could be readily adapted to other areas of study as well as other applications. For instance, in this study, the application was to map

the area assuming no prior geological information was available. Three methods were developed: algebraic probability, spatial indexing, and Bayesian probability. In this sequence the output of the preceding step provided constraints that were incorporated in each successive step. All three methods consistently showed a zone of high probability. Comparison with published literature (Gibb, 1968) indicates that this zone of high probability could be the Churchill-Superior boundary zone. The location of this zone has been debated for several decades (Bell, 1971). Given the geological complexity of the area, the tectonic implications of this boundary zone, and its topical relevance to mineralisation, better understanding of the nature and position of the zone are crucially important. Boundaries of similar nature occur in several parts of the Precambrian Shield of Canada (Stockwell *et al.*, 1970). Hence the method used here can be applied to these boundaries as well and may lead to a better understanding of Precambrian tectonics.

Recent research (e.g. Weber, 1990) equates the Thompson Belt with the boundary zone between the Churchill and Superior Provinces. However, the results of the current research show that the high probability zone has very little overlap with the Thompson Belt. Indeed, for the most part, the high probability zone is southeast of the southeastern edge of the Thompson Belt.

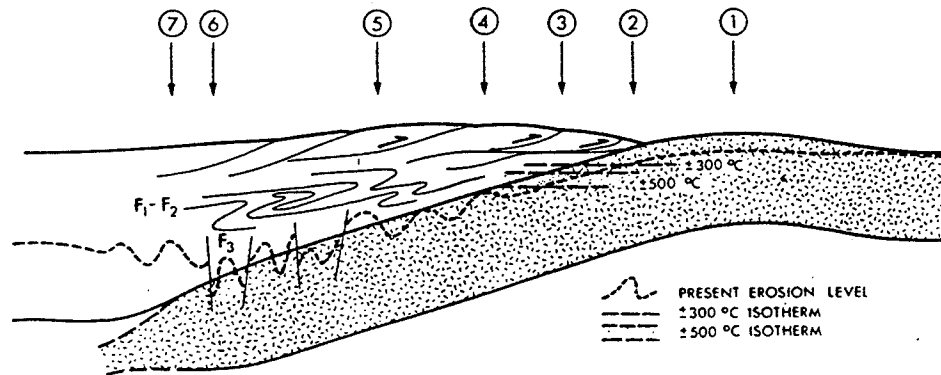
This disagreement between the present results and the generally accepted beliefs on the location of the boundary zone require further discussion. The location of the boundary has been one of the most extensively debated controversies in studies of the Canadian Precambrian Shield (Bell, 1971). Figure 9.1 illustrates one possible explanation (Bleeker, 1990) for the confusion in delineation of the boundary. In this

figure location 5 is the eastern edge of the Thompson Belt, and location 3 is the position of an extensive aeromagnetic low. This aeromagnetic low is represented by grey levels 5 and 6 in the aeromagnetic anomaly map (Figure 3.4). Further, both these levels have a high spatial index (Table 7.1). Therefore it is location 3 that has been mapped by the integration process developed in this research.

Kornik and MacLaren (1966) have interpreted location 3 as the eastern edge of the boundary zone. However, the results of the present investigation show the zone to extend much farther eastwards. This leads to the inference that the boundary zone is much wider than hitherto believed.

One of the inherent problems of comparing surface geology with geophysical information is the fact that the geophysical information is an integration over considerable crustal thickness. This is not a problem where rock units are dipping vertically. However, reconciling surface location of rock units with the subsurface attitudes, can pose a potential problem where rock units have a shallow dip. The disagreement between the previously mapped position of the boundary and the results from the present research could be a reflection of shallow dip.

Most recent workers interpret a shallow NW dip for the Thompson Belt, as shown in Figure 9.1 (Bleecker, 1990) and Figure 2.8 (Green *et al.*, 1985a). New seismic reflection studies across the Trans Hudson Orogen were carried out as a part of the LITHOPROBE program. More than 1000 km of vertical-incidence seismic reflection data were obtained, and the results indicate that the Thompson Belt has a shallow SE dip (Lucas *et al.*, 1993), as shown in Figure 9.2. Results from the present research tend to favour this new interpretation of the Thompson Belt



Generalized section through a collisional orogen, as applied to the TNB (section viewed toward the north-northeast). An overthrust/nappe pile, comprising detached basement slices and Aphebian supracrustals, is emplaced across the Superior plate margin. For simplicity, late, high-amplitude, upright F_3 folds and subsequent ductile reverse faults are restored. The present erosion level exposes a deep, cryptic section through the originally northwest-dipping plate contact. Seven "boundaries" can be defined, many of which have played a role in the "Churchill-Superior boundary debate" (cf. Bell, 1971): (1) Outer gravity high over much of the Pikwitonei granulite belt — the Nelson River high (Gibb, 1968). (2) Intersection between the present erosion level and the $\pm 300^\circ\text{C}$ (transient) Hudsonian isotherm; west of this boundary, K-Ar biotite systems show complete resetting. (3) Where the $\pm 500^\circ\text{C}$ isotherm is crossed, K-Ar hornblende systems show resetting and magnetite-consuming reactions in the granulites cause an extensive aeromagnetic low. This is the present (arbitrary) definition of the eastern boundary (Kornik and MacLaren, 1966). (4) Upright F_3 folds attain sufficient intensity to dominate the aeromagnetic fabric of the belt. (5) First Aphebian supracrustals — a fundamental boundary, but obscure in the TNB because of poor exposure, basement involvement in thrusting, and tight upright F_3 folding. (6) Most westerly occurrence of (reworked) basement gneisses at the surface. (7) Leading, thinned edge of the Superior plate in the subsurface, probably corresponding with the strong gravity gradient between the TNB low and the inner Burntwood River high (Gibb, 1968). The western boundary of the TNB has been defined by boundary (6), but data available at present suggest that the leading edge of the Superior plate may project farther west in the subsurface.

Figure 9.1 Significance of proposed locations of the boundary (After Bleeker, 1990)

exhibiting a SE dip. Further work, such as drilling, may help to resolve this aspect.

The results of the present work can also be used to revise the surface geology map as in the revised geological map of the Wabowden test site (Figure 9.3). As shown in this figure, the NE trends of the rock contacts change to a more southerly trend in the southern part of the area. This is crucial information for future mineral exploration programs. Target areas for detailed investigations can be localised along this trend and its extension under the Paleozoic cover. Thus the integration technique developed herein shows how geological maps can be readily updated with considerable savings in time and money. As more information becomes available, the integration process can be repeated to produce a current updated version of the map.

This research has shown that satellite data by itself has limited scope in areas where paucity of rock exposures on the surface, absence of differential relief, and vegetation cover detract from the quality of the satellite image. Ancillary data, such as aeromagnetic anomaly map used in this study are virtually indispensable in automated mapping. This was demonstrated by the analysis of the Wabowden and Lake Wekusko test sites. Processing steps such as removal of noise, unsupervised clustering etc, which require no prior information serve to maximise the information content of the satellite images.

Furthermore, this study demonstrates the ability to revise and update geological maps on the basis of the integration procedures. The extension of the Churchill-Superior boundary zone under the Paleozoic rock cover could be mapped. In the Lake Wekusko test site it was shown that the rocks of the Flin Flon subprovince

Inset map shows the location of the study area with respect to the Trans-Hudson and other >1.8-Gyr-old Proterozoic orogens (dark grey) and Archaean provinces (named) of continental North America, Greenland and western Scandinavia (after ref. 9). All younger orogens are shaded light grey and autochthonous platform cover has been removed. HBS, US: Hudson Bay and Ungava segments of the Trans-Hudson orogen. Main map: locations of the seismic reflection lines (numbered) in relation to the geology. 'W' indicates location of Archaean basement windows within the Reindeer zone. FFb: Fin Fion belt; GD: Glennie domain; KD: Kiseynew domain; LRD: La Ronge domain; RD: Rottenstone domain; TB: Thompson belt; TF: Tabbemor fault; WB: Wathaman-Chipewyan batholith; WD: Wollaston domain.

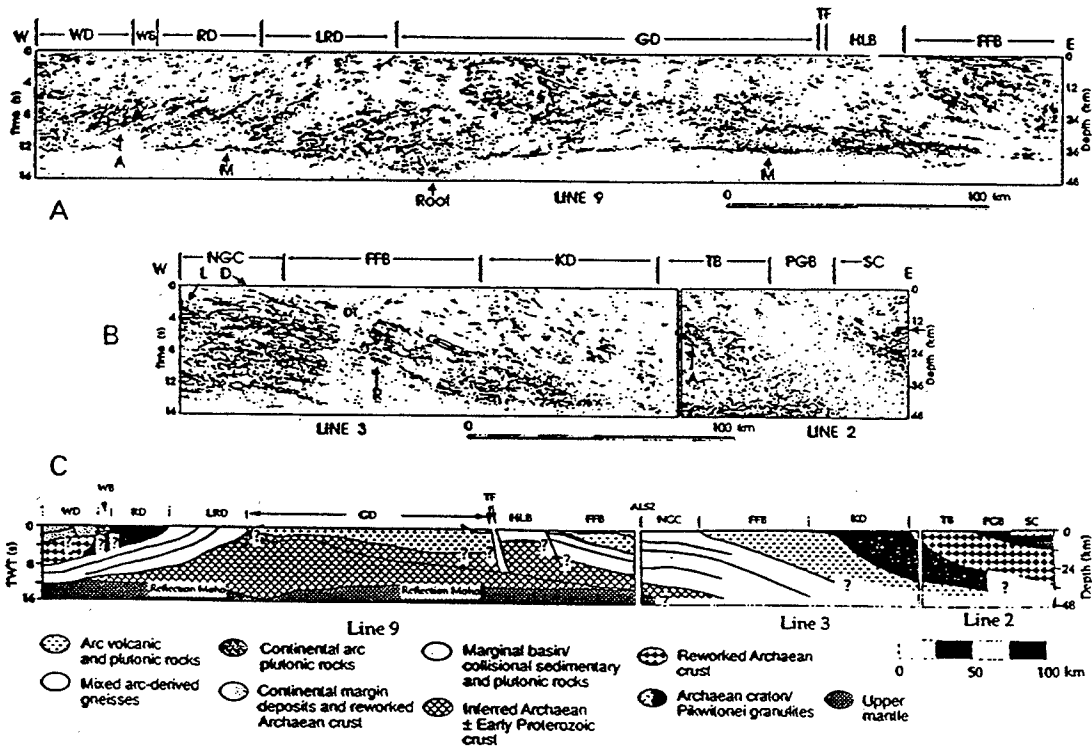
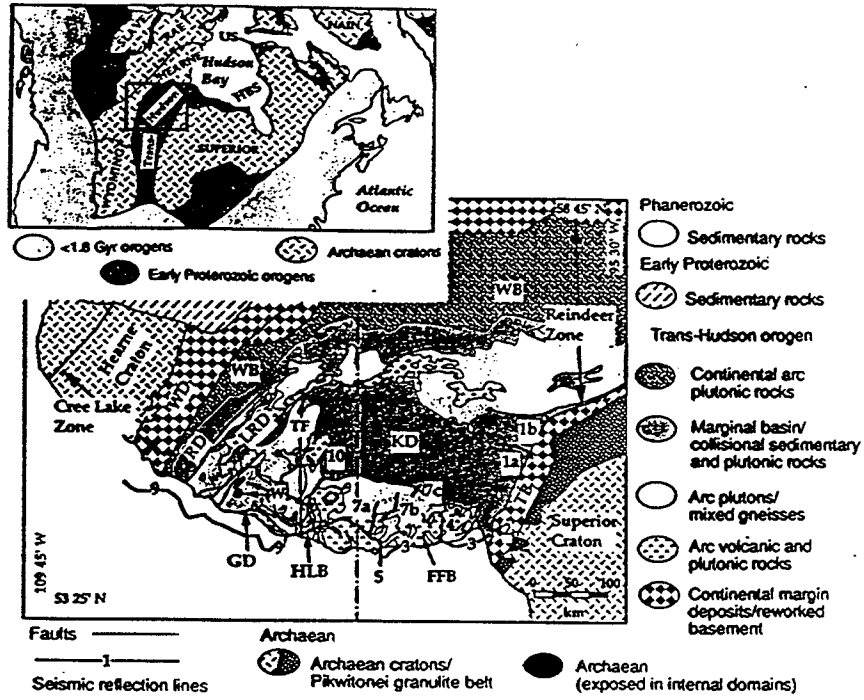


Figure 9.2 Geological section interpreted from LITHOPROBE data (After Lucas et al., 1993)

Line 2 in cross section C shows the SE dip of the Thompson Belt (TB)

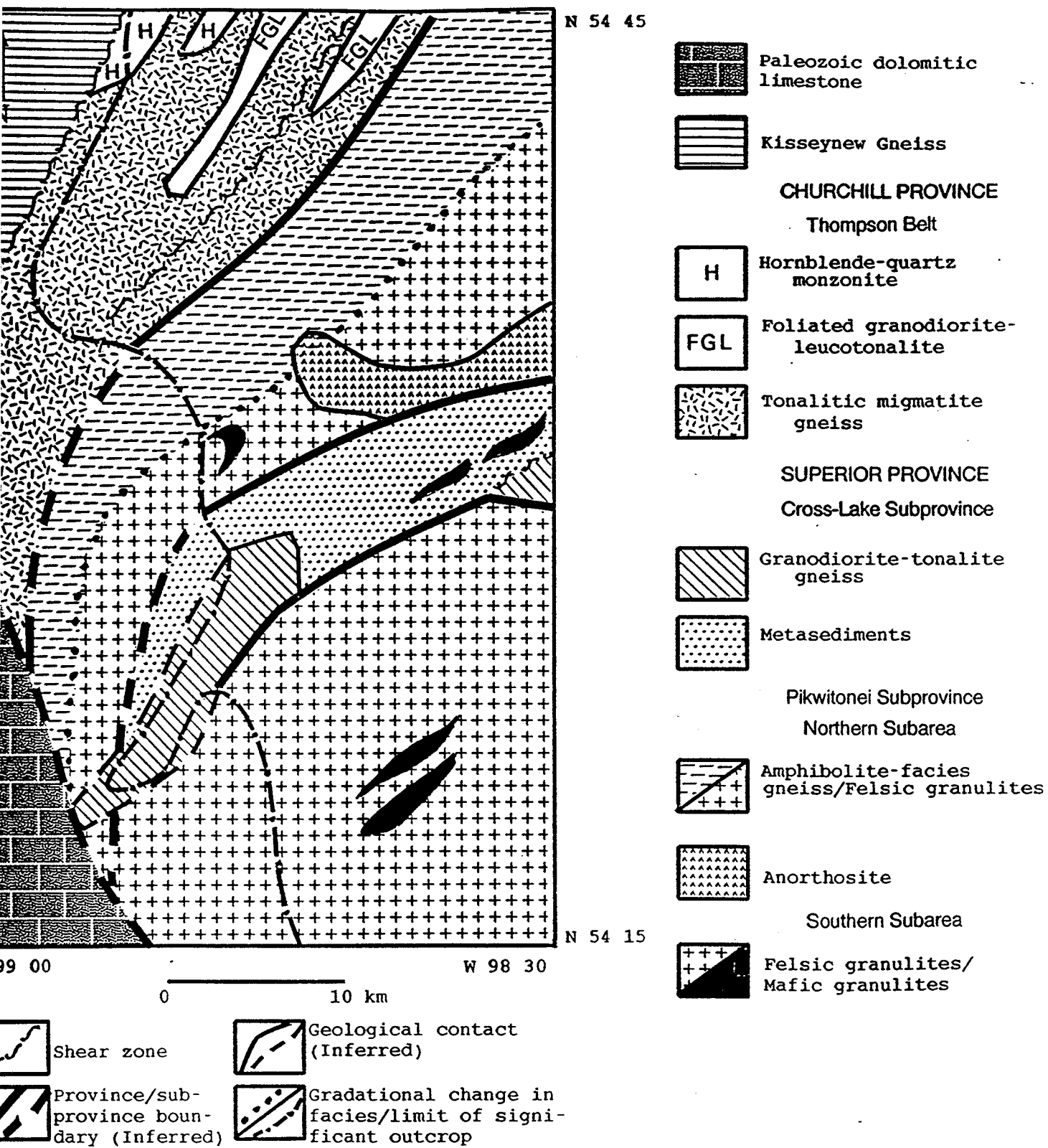


Figure 9.3 Revised geology map of Wabowden test site

occur below the Paleozoic cover. Hitherto, this kind of information could only be obtained by expensive seismic surveys or drilling.

As part of a future research program, other methods of integration can be tested and their results compared with the method developed herein. Some of the methods that are currently being investigated, in other study areas, include Fuzzy representation (Wang, 1990); neural networks (Hepner *et al.*, 1990; Ryan *et al.*, 1991); artificial intelligence (Egenhofer and Frank, 1990); and knowledge-based expert systems (van Cleynenbruegel *et al.*, 1990).

Bibliography

A.S.P.R.S. (1978); Usage of International System of units

Photogrammetric Engineering and Remote Sensing, 44(7), pp 923-938.

Agterberg, F.P. (1989a); Systematic approach to dealing with uncertainty of geoscience information in mineral exploration

in Weiss, A. (Ed.); *Proc. 21st symposium on Applications of Computers and Operations Research in Mineral Industry; Society of Mining Engineers, Colorado*, pp 165-178.

Agterberg, F.P. (1989b); Computer programs for mineral exploration

Science, 245, pp 76-81.

Agterberg, F.P. (1990); Estimating the probability of occurrence of mineral deposits from multiple map patterns

in Merriam, D.F. and H. Kurzl (Eds.); *Use of Microcomputers in Geology; Plenum Press, New York, U.S.A.*

- Agterberg, F.P., G.F. Bonham-Carter and D.F. Wright (1990); Statistical pattern integration for mineral exploration
in Gaal, G. (Ed.); *Proc. COGEO DATA Symposium on Computer Applications in Resource Exploration, July 1988, Espoo, Finland.*
- Agterberg, F.P., C.F. Chung, A.G. Fabbri, A.M. Kelly and J.S. Springer (1972); Geomathematical evaluation of copper and zinc potential of the Abitibi area, Ontario and Quebec
Geological Survey of Canada Paper 71-41, 55 p.
- Akima, H. (1978a); A method of bivariate interpolation and smooth surface fitting for irregularly distributed data points
ACM Transactions on Mathematical Software, 4(2), pp 148-159.
- Akima, H. (1978b); ALGORITHM 526 Bivariate interpolation and smooth surface fitting for irregularly distributed data points [E1]
ACM Transactions on Mathematical Software, 4(2), pp 160-164.
- An, P., W.M. Moon and A. Rencz (1991); Application of fuzzy set theory to integrated mineral exploration
Canadian Journal of Exploration Geophysics, 27(1), pp 1-11.
- Avery, T.E. and G.L. Berlin (1992); Fundamentals of Remote Sensing and Air-photo Interpretation
Macmillan Publ. Co., New York, 472 p.
- Bailes, A.H. (1980); Origin of early Proterozoic volcanoclastic turbidites, south margin of the Kiseynew sedimentary gneiss belt, File Lake, Manitoba
Precambrian Research, 12, pp 197-225.

- Baragar, W.R.A. and R.F.J. Scoates (1981); The Circum-Superior belt: A Proterozoic plate margin?
in Kröner, A. (Ed.); *Precambrian Plate Tectonics*; Elsevier, Chap.12,
pp 297–330.
- Barker, R. (1988); Remote Sensing: The unheralded component of geographic information systems
Photogrammetric Engineering and Remote Sensing, 54(2), pp 195–199.
- Bayes, T. (1764); An essay towards solving a problem in the doctrine of chances;
Philosophical Transactions of the Royal Society of London, Vol. 53
Reprinted in Press, S.J. (1989); *Bayesian Statistics*, John Wiley and Sons, NY,
USA, pp 189–217.
- Bell, C.K. (1966); Churchill-Superior province boundary in northern Manitoba
Geological Survey of Canada Paper 66-1, pp 133-136.
- Bell, C.K (1971); History of the Churchill–Superior boundary
in Turnock, A.C. (Ed.); *Geoscience Studies in Manitoba*; Geological Association of Canada Special Paper 9, pp 5–10.
- Bell, C.K. (1978); Geology, Wekusko Lake map-area, Manitoba
Geological Survey of Canada Memoir 384, 84 p.
- Bleeker, W. (1990); New structural-metamorphic constraints on Early Proterozoic oblique collision along the Thompson Nickel Belt, Manitoba, Canada
in Lewry, J.F. and M.R. Stauffer (Eds.); *The Early Proterozoic Trans-Hudson Orogen of North America*; Geological Association of Canada Special Paper 37,
pp 57–73.

Bolstad, P.V. and T.M. Lillesand (1992); Rule-based classification models: Flexible integration of satellite imagery and thematic spatial data

Photogrammetric Engineering and Remote Sensing, **58(7)**, pp 965–971.

Bonham-Carter, G.F., F.P. Agterberg and D.F. Wright (1988); Integration of geological datasets for gold exploration in Nova Scotia

Photogrammetric Engineering and Remote Sensing, **54(11)**, pp 1585–1592.

Burrough, P.A. (1986); Principles of Geographic Information Systems for Land Resources Assessment

Oxford University Press, U.K., 194 p.

Canavos, G.C. (1984); Applied Probability and Statistical Methods

Little, Brown and Co., Boston, U.S.A., 608 p.

Card, K.D. (1990); A review of the Superior Province of the Canadian Shield, a product of Archean accretion

Precambrian Research, **48**, pp 99–156.

Carper, W.J., T.M. Lillesand and R.W. Kiefer (1990); The use of Intensity-Hue-Saturation transformations for merging SPOT panchromatic and multispectral image data

Photogrammetric Engineering and Remote Sensing, **56(4)**, pp 459–467.

Chavez, P.S. Jr. (1992); Comparison of spatial variability in visible and near-infrared spectral images

Photogrammetric Engineering and Remote Sensing, **58(7)**, pp 957–964.

Chavez P.S. Jr. and A.Y. Kwarteng (1989); Extracting spectral contrast in Landsat Thematic Mapper image data using selective Principal Component

Analysis

Photogrammetric Engineering and Remote Sensing, 55(3), pp 339–348.

Colwell, R.N. (Ed.) (1983); *Manual of Remote Sensing*, Second Edition
American Society of Photogrammetry and Remote Sensing, Virginia, Two Volumes.

Corkery, M.T. (1987); *Geological Highway Map of Manitoba*
Geological Survey of Canada; Manitoba Energy and Mines, Scale 1:1,000,000

Cranstone, D.A. and A. Turek (1976); *Geological and geochronological relationships of the Thompson nickel belt, Manitoba*
Canadian Journal of Earth Sciences, 13, pp 1058–1069.

Crippen, R.E. (1989); *A simple spatial filtering routine for the cosmetic removal of scan line noise from Landsat TM P-Tape imagery*
Photogrammetric Engineering and Remote Sensing, 55(3), pp 327–331.

Dempster, A.P. (1985); *Probability, Evidence and Judgement*
in *Bernardo, J.M., M.H. DeGroot, D.V. Lindley and A.F.M. Smith (Eds.); Bayesian Statistics 2, Elsevier Science Publishers, B.V., North-Holland*, pp 119.

Drury, S.A. (1987); *Image Interpretation in Geology*
Allen and Unwin, London, U.K., 243 p.

Egenhofer, M.J. and A.U. Frank (1990); *LOBSTER: Combining AI and database techniques for GIS*
Photogrammetric Engineering and Remote Sensing, 56(6), pp 919–926.

Fabbri, A.G. and C.A. Kushigbor (1989); Relationships between integrated multisensor imagery, geophysical data and geological map patterns for mineral exploration east of Bathurst Inlet, N.W.T. Canada

Proc. IGARSS '89, Vancouver, Canada, 3, pp 1414–1420.

Favini, G. and R. Assad (1979); An optimised decision model for area selection in massive sulphide exploration

The Canadian Mining and Metallurgical Bulletin, 72(804), pp 118–126.

Fernandez-Alonso, M. and A. Tahon (1991); Lithological discrimination and structural trends in W-Rwanda (Africa) on images of airborne radiometric and aeromagnetic surveys, coregistered to a Landsat scene

Photogrammetric Engineering and Remote Sensing, 57(9), pp 1152–1162.

Ford, G.E. and C.I. Zanelli (1985); Analysis and quantification of errors in the geometric correction of satellite images

Photogrammetric Engineering and Remote Sensing, 51(11), pp 1725–1734.

Friedman, D.E., J.P. Friedel, K.L. Magnussen, R. Kwok and S. Richardson (1983); Multiple scene precision rectification of spaceborne imagery with very few ground control points

Photogrammetric Engineering and Remote Sensing, 49, pp 1657–1667.

Fung, T and E. LeDrew (1987); Application of principal components analysis to change detection

Photogrammetric Engineering and Remote Sensing, 53(12), pp 1649–1658.

Geological Survey of Canada (1987); Magnetic anomaly map of Canada, Map 1255A, Scale 1:5,000,000, Fifth Edition

- George, H. and G.F. Bonham-Carter (1989); Spatial modeling of geological data for gold exploration, Star Lake area, Saskatchewan
in Agterberg, F.P. and G.F. Bonham-Carter (Eds.); *Statistical Applications in the Earth Sciences; Geological Survey of Canada Paper 89-9*, pp 157-169.
- Gibb, R.A. (1968); A geological interpretation of the Bouguer anomalies adjacent to Churchill-Superior boundary in northern Manitoba
Canadian Journal of Earth Sciences, 5, pp 439-453.
- Gibb, R.A. (1983); Model for suturing of Superior and Churchill plates: An example of Double Indentation tectonics
Geology, 11, pp 413-417.
- Gibb, R.A. and M.D. Thomas (1976); Gravity signature of fossil plate boundaries in the Canadian Shield
Nature, 262, pp 199-200.
- Gill, J.E. (1949); Natural divisions of the Canadian Shield
Transactions of the Royal Society of Canada, 43(III), Sec. IV, pp 61-69.
- Goetz, A.F.H. and L.C. Rowan (1981); Geologic Remote Sensing
Science, 211, pp 781-791.
- Goetz, A.F.H., B.N. Rock and L.C. Rowan (1983); Remote sensing for exploration: An overview
Economic Geology, 78, pp 573-590.
- Goodacre, A.K., G.F. Bonham-Carter, F.P. Agterberg and D.F. Wright (1991); A statistical analysis of the spatial association of seismicity with drainage patterns and magnetic anomalies in the Papineau-Labelle-Laurentides region of

Western Quebec

Geophysics Division, Geological Survey of Canada, Unpublished Report

Goodenough, D.G. (1988); Thematic Mapper and SPOT integration with a Geographic Information System

Photogrammetric Engineering and Remote Sensing, 54(2), pp 167–176.

Gordon, T.M., P.A. Hunt, A.H. Bailes and E.C. Syme (1990); U-Pb ages from the Flin-Flon and Kiseynew Belts, Manitoba: Chronology of crust formation at an early Proterozoic accretionary margin

in Lewry, J.F. and M.R. Stauffer (Eds.); *The Early Proterozoic Trans-Hudson Orogen of North America; Geological Association of Canada Special Paper 37*, pp 177–199.

Green, A.G., G.L. Cumming and D. Cedarwell (1979); Extension of the Superior-Churchill boundary zone into southern Canada

Canadian Journal of Earth Sciences, 16, pp 1691–1701.

Green, A.G., Z. Hajnal and W. Weber (1985a); An evolutionary model of the western Churchill Province and western margin of the Superior Province in Canada and the North Central United States

Tectonophysics, 116, pp 281–322.

Green, A.G., W. Weber and Z. Hajnal (1985b); Evolution of Proterozoic terrains beneath the Williston Basin

Geology, 13, pp 624–628.

Haralick, R.M. and K.S. Fu (1983); Pattern recognition and classification in Colwell, R.N. (Ed.); *Manual of Remote Sensing, Vol. I*, pp 793–805.

Harris, J.F., R. Murray and T. Hirose (1990); IHS transform for the integration of radar imagery with other remotely sensed data

Photogrammetric Engineering and Remote Sensing, 56(12), pp 1631-1641.

Hepner, G.F., T. Logan, N. Ritter and N. Bryant (1990); Artificial neural network classification using a minimal training set: Comparison to conventional supervised classification

Photogrammetric Engineering and Remote Sensing, 56(4), pp 469-473.

Heyl, A.V. (1983); Some major lineaments reflecting deep seated fracture zones in the central United States and mineral districts related to the zones

Global Tectonics and Metallogeny, 2, Nos.1 and 2.

Hodgson, M.E., J.R. Jensen, H.E. Mackey Jr. and M.C. Coulter (1988); Monitoring Wood Stork foraging habitat using remote sensing and Geographic Information Systems

Photogrammetric Engineering and Remote Sensing, 54(11), pp 1601-1607.

Hoffman, P. (1988); United Plates of America, the birth of a craton: Early Proterozoic assembly and growth of Laurentia

Annual Review of Earth and Planetary Sciences, 16, pp 543-603.

Hook, S.J. (1985); Integrated Landsat-MSS and TM and Geophysical Data Applications in Geological Mapping and Mineral Exploration for Western Newfoundland

Unpublished M.Sc Thesis, University of Alberta, 131 p.

Hubregtse, J.J.M.W. (1980a); The Archean Pikwitonei granulite domain and its position at the margin of the northwestern Superior Province (Central Man-

itoba)

Manitoba Dept. of Energy and Mines, Geol.Paper GP80-3, 16 p.

Hubregtse, J.J.M.W. (1980b); Preliminary Geology Map Number 1980 N-2

Manitoba Dept. of Energy and Mines, Mineral Resources Divn.

Innes, M.J.S. (1960); Gravity and isostasy in Manitoba and northern Ontario

Publications of the Dominion Observatory 26(6).

Jensen, J.R. (1986); Introductory Digital Image Processing - A Remote Sensing Perspective

Prentice-Hall, New Jersey , 379 p.

Jensen, J.R. and M.E. Hodgson (1986); Appendix A: The SENSOR digital image processing programs

in *Jensen, J.R. (1986); Introductory Digital Image Processing - A Remote Sensing Perspective; Prentice-Hall, New Jersey , pp 272-363.*

Kahle, A.B. and A.F.H. Goetz (1983); Mineralogic information from a new airborne Thermal Infrared Multispectral Scanner

Science, 222, pp 24-27.

Kiss, F.G. (1989); Aeromagnetic total field, vertical gradient, VLF-EM and time domain-EM surveys in Manitoba and Saskatchewan

Geological Survey of Canada Open File 2133, pp 116-130.

Kornik, L.J. (1971); Magnetic subdivisions of Precambrian rocks in Manitoba

in *Turnock, A.C. (Ed.); Geoscience Studies in Manitoba; Geological Association of Canada Special Paper 9, pp 51-60.*

Kornik, L.J. and A.S. MacLaren (1966); Aeromagnetic study of the Churchill-Superior boundary in northern Manitoba

Canadian Journal of Earth Sciences, 3, pp 547-557.

Kowalik, W.S. and W. E. Glenn (1987); Image processing of aeromagnetic data and integration with Landsat images for improved structural interpretation

Geophysics, 52(7), pp 875-884.

Letts, P. (1978); Unsupervised classification in the ARIES image analysis system

Proceedings of the 5th Canadian Symposium on Remote Sensing, pp 61-71.

Lewry, J.F., D.J. Thomas, R. Macdonald and J. Chiarenzelli (1990); Structural relationships in accreted terranes of the Trans-Hudson Orogen, Saskatchewan: Telescoping in a collisional regime?

in Lewry, J.F. and M.L. Stauffer (Eds.); *The Early Proterozoic Trans-Hudson Orogen of North America, Geological Association of Canada Special Paper 37*, pp 75-94.

Lindley, D.V. (1991); Subjective probability, decision analysis and their legal consequences

Journal of the Royal Statistical Society, Series A, 154, Part I, pp 83-22.

Lucas, S.B., A. Green, Z. Hajnal, D. White, J. Lewry, K. Ashton, W. Weber and R. Clowes (1993); Deep seismic profile across a Proterozoic collision zone: surprise at depth

Nature, 363, pp 339-342.

Marble, D.F. and D.J. Peuquet (1983); Geographic Information Systems and remote sensing

in Colwell, R.N. (Ed.); *Manual of Remote Sensing, Vol. I*, pp 923–958.

Masouka, P.M., J. Harris, P.D. Lowman Jr. and H.W. Blodget (1988); Digital processing of orbital radar data to enhance geologic structure: Examples from the Canadian Shield

Photogrammetric Engineering and Remote Sensing, 54(5), pp 621–632.

Mather, P.M. (1987); Computer Processing of Remotely-Sensed Images An Introduction

John Wiley and Sons, Chichester U.K., 352 p.

McGregor, C.R., J.J. Macek and L. Chackowsky (1992); Location map of the relogged nonconfidential core from the SW extension of the Thompson Nickel Belt

Unpublished map, Manitoba Energy and Mines (Pers. Comm.)

Moon, W.M. (1993); On mathematical representation and integration of multiple spatial geoscience data sets

Canadian Journal of Remote Sensing, 19(1), pp 63–67.

Moore, H.D. and A.F. Gregory (1989); Weighting of geophysical data with SPANS for digital geological mapping

in Agterberg, F.P. and G.F. Bonham-Carter (Eds.); *Statistical Applications in the Earth Sciences; Geological Survey of Canada Paper 89-9*, pp 193–200.

Newton, G.D. (1985); Computer programs for common map projections

USGS Bulletin No. 1642, 33 p.

NOAA (1975 -); Landat Data Users Notes

NOAA Landsat Customer Services, Mundt Federal Building, Sioux Falls, SD,
USA 57198

Ojakangas, R.W. (1985); Review of Archean clastic sedimentation, Canadian
Shield: major felsic volcanic contributions to turbidite and alluvial fan-fluvial
facies associations

in Ayres, L.D., P.C. Thurston, K.D. Card and W. Weber (Eds.); *Evolution
of Archean Supracrustal Sequences; Geological Association of Canada Special
Paper 28*, pp 23-47.

Ortí, F. (1981); Optimum distribution of control points to minimize Landsat
image registration errors

Photogrammetric Engineering and Remote Sensing, 47(1), pp 101-110.

Patterson, J.M. (1963); Geology of the Thompson-Moak lake area

Manitoba Mines Branch Publication 60-4

Peredery, W.V. (1982); Geology and nickel sulphide deposits of the Thompson
Belt, Manitoba

in Hutchinson, R.W., C.D. Spence and J.M. Franklin (Eds.); *Precambrian
Sulphide Deposits; Geological Association of Canada Special Paper 25*, pp 165-
209.

Pereira, J.M.C. and R.M. Itami (1991); GIS-based habitat modeling using lo-
gistic multiple regression: A study of the Mt. Graham red squirrel

Photogrammetric Engineering and Remote Sensing, 57(11), pp 1475-1486.

- Press, S.J. (1989);** Bayesian Statistics; Principles, Models and Applications
John Wiley and Sons, New York, U.S.A., 237 p.
- Price, J.C. (1981);** The contribution of Thermal data in Landsat multispectral classification
Photogrammetric Engineering and Remote Sensing, 47(2), pp 229–236.
- Quirke, Jr., T.T., D.A. Carnstone, C.K. Bell and C.J.A. Coats (1970);** Geology of the Moak-Setting lakes area, Manitoba
Geological Association of Canada, Field Trip Report
- Rance, H. (1966);** Superior-Churchill structural boundary, Wabowden, Manitoba
Unpublished Ph.D. Thesis; Univ. of Western Ontario
- Reddy, R.K.T, G.F. Bonham-Carter and D.F. Wright (1991);** Computer modeling of VMS potential using artificial intelligence approaches, Snow Lake, Manitoba
Proceedings of the GIS Conference, Ottawa, Canada
- Richards, J.A. (1986);** Remote Sensing Digital Image Analysis - An Introduction
Springer Verlag, New York, 281 p.
- Richards, J.A., D.A. Landgrebe and P.H. Swain (1982);** A means for utilising ancillary information in multispectral classification
Remote Sensing of Environment, 12, pp 463–477.
- Robinove, C.J. (1986);** Principles of logic and the use of digital Geographic Information Systems
USGS Circular 977, 19 p.

- Rousell, D.H. (1965);** Geology of the Cross lake area
Manitoba Mines Branch Publication 62-4.
- Rowan, L.C. and A.B. Kahle (1982);** Evaluation of 0.46 to 2.36 μm Multi-spectral Scanner image of the East Tintic Mining District, Utah, for mapping hydrothermally altered rocks
Economic Geology, 77, pp 441-452.
- Ryan, T.W., P.J. Sementilli, P. Yuen and B.R. Hunt (1991);** Extraction of shore-line features by neural nets and image processing
Photogrammetric Engineering and Remote Sensing, 57(7), pp 947-955.
- Sabins, F.F. (1987);** Remote Sensing - Principles and Interpretation
W.H. Freeman and Co., New York, 449 p.
- Salomonson, V.V. (1984);** Landsat 4 and 5 status and results from Thematic Mapper data analyses
in *Klepfer, M.M. and D.B. Morrison (Eds); Proc. of the 10th Int. Symp. on Machine Processing of Remotely Sensed data with special emphasis on Thematic Mapper data and Geographic Information Systems; June 12-14, Purdue University, U.S.A.*, pp 13-18.
- Siegrist, A.W. and C.C. Schnetzler (1980);** Optimum spectral bands for rock discrimination
Photogrammetric Engineering and Remote Sensing, 46(9), pp 1207-1215.
- Snyder, J.P. (1978);** The Space Oblique Mercator projection
Photogrammetric Engineering and Remote Sensing, 44(5), pp 585-596.

- Snyder, J.P. (1981); Map projections for satellite tracking
Photogrammetric Engineering and Remote Sensing, 47(2), pp 205–213.
- Snyder, J.P. (1987); Map Projections – A working manual
USGS Professional Paper 1395, 383 p.
- Spiegelhalter, D.J. (1986); A statistical view of uncertainty in expert systems
in Gale, W.A. (Ed.); *Artificial Intelligence and Statistics*, Addison-Wesley Publishing Co., Massachusetts, U.S.A., pp 17–55.
- SPOT (1984); SPOT Simulation Applications Handbook—Proceedings of the
1984 SPOT Symposium, Aug. 20-23, Scottsdale, Arizona
American Society of Photogrammetry and Remote Sensing, Virginia, 274 p.
- Steneker, M and G.F. Bonham-Carter (1988); Computer program for converting
arc-node vector data to raster format
Geological Survey of Canada Open File 1767.
- Stevens, S.S. (1946); On the theory of scales of measurement
Science, 103, pp 677–680.
- Stockwell, C.H. (1964); Fourth report on structural provinces, orogenies, and
time-classification of rocks of the Canadian Precambrian Shield
Geological Survey of Canada Paper 64-17, Part II, pp 1–21.
- Stockwell, C.H., J.C. McGlynn, R.F. Emslie, B.V. Sanford, A.W. Norris, J.A.
Donaldson, W.F. Farhig and K.L. Currie (1970); Geology of the Canadian Shield
in Douglas, R.J.W. (Ed.); *Geology and Economic Minerals of Canada*, Geological Survey of Canada, *Economic Geology Report No. 1, Chapter IV*.

Stott, G.M. and F. Corfu (1991); Uchi subprovince

in Thurston, P.C., H.R. Williams, R.H. Sutcliffe and G.M. Stott (Eds.); *Geology of Ontario; Ontario Geological Survey Special Volume 4, Part 1*, pp 145-236.

Strahler, A.H., T.L. Logan and N.A. Bryant (1976); Improving forest cover classification accuracy from Landsat by incorporating topographic information
Proceedings of the 12th International Symposium on Remote Sensing of Environment, Phillipines.

Strahler, A.H., J.E. Estes, P.F. Maynard, F.C. Mertz and D.A. Stow (1980); Incorporating collateral data in Landsat classification and modelling procedures
Proceedings of the 14th International Symposium on Remote Sensing of Environment, Costa Rica, 2, pp 1009-1026.

Swain, P. H. and S.M. Davis (Eds.) (1978); *Remote Sensing: The Quantitative Approach*

McGraw-Hill Inc., New York, 396 p.

Swann, R., D. Hawkins, A. Westwell-Roper and W. Johnstone (1988); The potential for automated mapping from geocoded digital image data
Photogrammetric Engineering and Remote Sensing, 54(2), pp 187-193.

Telford, W.M., L.P. Geldart, R.E. Sherrif and D.A. Keys (1976); *Applied Geophysics*

Cambridge Univ. Press, Cambridge, 860 p.

Thomas, M.D. and R.A. Gibb (1985); Proterozoic plate subduction and collision: Processes for reactivation of Archean crust in the Churchill Province
in Ayres, L.D., P.C. Thurston, K.D. Card and W. Weber (Eds.); *Evolution*

of Archean Supracrustal Sequences; Geological Association of Canada Special Paper 28, pp 263–279.

Trevett, J.W. (1986); *Imaging Radar for Resources Surveys*
Chapman and Hall, New York, U.S.A., 313 p.

Van Cleynenbreugel, J., F.Fierens, P. Suetens and A. Oosterlinck (1990); Delineating road structures on satellite imagery by a GIS-guided technique
Photogrammetric Engineering and Remote Sensing, **56(6)**, pp 893–898.

Walsh, S.J., J.W. Cooper, I.E. Von Essen and K.R. Gallager (1990); Image enhancement of Landsat Thematic Mapper data and GIS data integration for evaluation of resource characteristics
Photogrammetric Engineering and Remote Sensing, **56(8)**, pp 1135–1141.

Wang, D.C.C., A.H. Vagnucci and C.C. Li (1983); Digital image enhancement: A survey
Computer Vision, Graphics, and Image Processing, **24**, pp. 363–381.

Wang, F. (1990); Improving remote sensing image analysis through fuzzy information representation
Photogrammetric Engineering and Remote Sensing, **56(8)**, pp 1163–1169.

Weber, W. (1990); The Churchill-Superior boundary zone, southeast margin of the Trans-Hudson orogen: A review
in *Lewry, J.F. and M.R. Stauffer (Eds.); The Early Proterozoic Trans-Hudson Orogen of North America; Geological Association of Canada Special Paper 37*, pp 41–55.

Welch, R. (1985); Cartographic potential of SPOT image data

Photogrammetric Engineering and Remote Sensing, 51(8), pp 1085–1091.

Welch, R., T.R. Jordan and M. Ehlers (1985); Comparative evaluation of the geodetic accuracy and cartographic potential of Landsat-4 and Landsat-5 Thematic Mapper image data

Photogrammetric Engineering and Remote Sensing, 51(11), pp 1799–1812.

Welch, R., M.M. Remillard and R.B. Slack (1988); Remote sensing and geographic information system techniques for aquatic resource evaluation

Photogrammetric Engineering and Remote Sensing, 54(2), pp 177–185.

Wilson, H.D.B. and W.C. Brisbin (1961); Regional structure of the Thompson–Moak Lake nickel belt

The Canadian Mining and Metallurgical Bulletin, 54, pp 815–822.

Wilson, H.D.B. and W.C. Brisbin (1962); Tectonics of the Canadian Shield in northern Manitoba

in Stevenson, J.S. (Ed.); *Royal Society of Canada Special Publication No. 4*, pp 60–75.

Wilson, J.T. (1949); Some major structures of the Canadian Shield

Bulletin of the Canadian Instt. of Mining and Met., 42, pp 543–554.

Wilson, M.E. (1939); The Canadian Shield

Geology der Erde, Geology of North America I

Wright, D.F., G.F. Bonham-Carter and P.J. Rogers (1988); Spatial data integration of lake-sediment geochemistry, geology and gold occurrences, Meguma Terrane, Eastern Nova Scotia

Proceedings of the CIMM Meeting, Halifax, Canada, pp 501–515.

Zhou, Qiming (1989); A method for integrating remote sensing and Geographic Information Systems

Photogrammetric Engineering and Remote Sensing, **55(5)**, pp 591–596.